CLUSTERING OF HALL EFFECT THRUSTERS FOR HIGH-POWER ELECTRIC PROPULSION APPLICATIONS

by

Brian Eric Beal

A dissertation submitted in partial fulfillment
of the requirements for the degree of
Doctor of Philosophy
(Aerospace Engineering)
at The University of Michigan
2004

Doctoral Committee:

Associate Professor Alec D. Gallimore, Chair
Professor Iain D. Boyd
Professor Ronald M. Gilgenbach
Dr. William A. Hargus, Jr., United States Air Force Research Laboratory

ACKNOWLEDGEMENTS

Although I have had the privilege of taking credit for most of it, the research presented in this dissertation would not have been possible without the support of a great many people. First, I would like to sincerely thank my advisor and dissertation committee chairman, Professor Alec Gallimore, for his guidance and mentorship throughout the course of this project. Alec has created an environment in which graduate students are able to work on projects that are interesting, challenging, and relevant to the scientific community while retaining the freedom to pursue our own interests. Under his leadership, PEPL has become one of the world's preeminent laboratories for electric propulsion research and an institution that I am proud to have been a part of. Amazingly, Alec has achieved all of this while maintaining the personality of someone with whom I enjoy having a beer and talking football. Thanks, Boss.

I am also grateful for the contributions of the other members of my committee, Professor Iain Boyd, Professor Ron Gilgenbach, and Dr. William Hargus, Jr. of the Air Force Research Laboratory. Their experience and insight have been invaluable benefits to the completion of this thesis. In particular, I would like to thank Bill, who has done double duty by serving on my committee and, along with Dr. Ron Spores, has funded a great deal of this research. I also gratefully acknowledge the assistance of the technical and administrative staff of the Aerospace Engineering department: Margaret, Sue, Sharon, Tom, Dave, and especially Terry, whose excellent work in fabricating both the energy analyzer and the LGIT made a significant portion of my research possible.

Of course, one of the factors separating a good university from a great one is the quality of the students, and I have been fortunate to work with some of the best. Thanks to those who were here before me and helped me to get my feet wet in this field: George, Tim, Farnk, Matt, Colleen, Jon, and James. Thanks for sharing your experience with me, I've learned a lot. Then there's my generation of PEPL people: Rich, Peter, Mitchell, Dan, and Allen. Thank you for the good times at the lab and the better times at conferences. As we old guys graduate, we will be leaving the lab in the capable hands of the newer people in the group: Josh, Jesse, Rob, Dave "Floppy" Kirtley, and Kristina "Hurry up and graduate so I can have your desk" Lemmer. It has been a pleasure working with all of you. Keep up the good work. I would especially like to thank James Haas for teaching me most of what I know about Hall thrusters. In addition to being a great friend, Dr. Jimmy has been a huge benefit to my research by allowing me to use his RPA and providing me with a place to stay during my stints at AFRL. Just make sure that vacuum doesn't get out of the chamber and hurt somebody.

Most importantly, I would like to thank my parents for the love, encouragement, and upbringing they've given me throughout my life. From watching countless little league games to trying to understand my Ph.D research, they've gone out of their way to help me succeed. Thanks also to my little sister, Bridget, for dragging me out of the lab and forcing me to have some fun once in a while. Good luck finishing pharmacy school; we're all proud of you. I'm very lucky to have the best family that anyone could ask for and, despite all of the awards I've been fortunate enough to receive over the years, the times that I've made you proud have been my most rewarding achievements.

Last, but certainly not least, I'd like to say thank you to my wonderful fiancée, Olivia. Living on opposite sides of the country for the last three years has been tough for both of us, but your love, support, and most of all patience, have made it worthwhile. Knowing that we will finally be able to start our life together once I finish grad school has been the best motivation imaginable as I've written this dissertation. We're almost there! Thank you.

Brian Beal
January 7, 2004

PREFACE

This thesis presents research aimed at understanding the technical issues related to operating multiple Hall effect thrusters in close proximity to each other in order to achieve electric propulsion systems capable of operating at power levels well beyond the current state of the art. This knowledge is essential to allow clusters of Hall thrusters to be developed in existing vacuum facilities while minimizing costs and development risks.

An extensive array of plume data was obtained using a variety of plasma diagnostics including the triple Langmuir probe, floating emissive probe, Faraday cup, and retarding potential analyzer, as well as several others. Measurements were taken downstream of a cluster of four thrusters, each of which was coupled to its own hollow cathode and operated from its own set of power supplies. Data obtained in this nominal configuration were compared to parameters recorded in the plume of a single thruster. It was found that three of the most basic properties in the cluster plume: plasma density, electron temperature, and plasma potential, could be predicted based solely on knowledge of the characteristics of a single thruster and the geometric location of each device in the array. Predictions made using the methods presented in this dissertation appear to be accurate to within the margin of error of typical plasma diagnostics.

Secondary properties such as the ion current density and ion energy spectrum were also studied in the cluster plume. It was found that the beam profile of a cluster is slightly narrower than predicted by linear superposition of the contributions from each individual engine. A particle tracking algorithm revealed this behavior to be the result of low-energy ions being preferentially deflected downstream due to the unique plasma potential profiles in the cluster plume. Measurements of the ion energy spectrum showed a significant increase in ions at energy to charge ratios below the main peak in the distribution when multiple thrusters were operated. This appears to indicate an increase in elastic scattering due to clustering.

Finally, several alternative cluster configurations have been studied to examine parallel and shared cathode operation. It was found that parallel operation generally caused one cathode to dominate the discharge thus introducing a new criterion that must be considered when designing a cluster intended for parallel operation. When multiple thrusters were coupled to a single cathode, the plume properties could no longer be predicted using simple analytical formulas. This is because the operating characteristics of a single thruster depended on the location of the hollow cathode. The dramatic changes in plume properties observed in this configuration are the result of poor cathode coupling caused by operation with a distant cathode.

TABLE OF CONTENTS

LIST OF FIGURES

LIST OF TABLES

LIST OF APPENDICES

NOMENCLATURE

A_c	Collector area	[m^2]
A_{exit}	Thruster exit plane area	[m^2]
A_P	Probe surface area	[m^2]
$\mathbf{B}$, $\vec{B}$	Magnetic field vector	[T]
B	Scalar magnetic field strength	[T]
D	Electron diffusion coefficient	[m^2/s]
d	Plate separation (in both ESA and ExB probes)	[m]
dx	Distance between adjacent electrodes	[m]
e	Electron charge	[1.6×10^{-19} C]
$\mathbf{E}$, $\vec{E}$	Electric field vector	[V/m]
E	Scalar electric field strength	[V/m]
$f_e(v)$	Electron velocity distribution function	[-]
f(E)	Electron energy distribution function (EEDF)	[-]
$f_i(v)$	Ion velocity distribution function	[-]
f(V)	Ion energy per charge distribution function	[-]
$\mathbf{F}$, $\vec{F}$	Force vector	[N]
g	Earth's gravitational constant	[9.81 m/s^2]
I_B	Ion beam current	[A]

I_{coll}	RPA collector current	[A]
I_D	Discharge current	[A]
$I_{i,sat}$	Ion saturation current	[A]
I_j	Current due to species j	[A]
I_p	Probe current	[A]
I_{sp}	Specific impulse	[sec]
$\mathbf{j}$, $\vec{j}$	Current density vector	[A/m^2]
j	Current density scalar	[A/m^2]
K_{45}	ESA spectrometer constant	[-]
k_b	Boltzmann's constant	[1.38 x 10^{-23} J/K]
L	Distance from cathode to the measurement point	[m]
L_{ch}	Acceleration channel length	[m]
m_e	Electron mass	[9.11 x 10^{-31} kg]
m_{final}	Final spacecraft mass (after maneuver)	[kg]
m_i	Ion mass	[kg]
$m_{initial}$	Initial spacecraft mass (before maneuver)	[kg]
m_p	Proton mass	[1.67 x 10^{-27} kg]
m_{prop}	Propellant mass load	[kg]
$\dot{m}$	Propellant mass flow rate	[kg/sec]
$\dot{m}_{anode}$	Propellant mass flow rate through the anode	[kg/sec]

$\dot{m}_{in}$	Rate of background gas ingestion into engine	[kg/sec]
n_e	Electron number density	[m^{-3}]
n_i	Ion number density	[m^{-3}]
n_j	Number density of ions with charge multiple j	[m^{-3}]
n_n	Neutral number density	[m^{-3}]
n_{target}	Number density of the collision target population	[m^{-3}]
p_B	Background pressure	[Torr]
p_e	Electron pressure	[Torr]
P_t	Thrust power	[watts]
P_{in}	Input power	[watts]
q	Electric charge	[C]
q_i	Ion charge state (1, 2, 3, …)	[-]
q_{eff}	Effective charge state	[-]
$r_{L,e}$	Electron Larmor radius (gyroradius)	[m]
$r_{L,I}$	Ion Larmor radius (gyroradius)	[m]
r_p	Probe electrode radius	[m]
R	Radius of arc on which measurements were taken	[m]
T	Thrust	[N]
T_e	Electron temperature	[K] or [eV]
T_i	Ion temperature	[K] or [eV]
T_n	Neutral temperature	[K]

$\overline{u}_e$	Mass averaged exhaust velocity	[m/s]
V	Voltage	[V]
V_b	Beam voltage	[V]
V_D	Discharge voltage	[V]
V_{grid}	Repelling grid voltage	[V]
V_{ExB}	Voltage between electrodes of ExB probe	[V]
V_R	ESA ion repeller plate voltage	[V]
v_{crit}	Critical velocity	[m/s]
v_{ExB}	**ExB** drift speed	[m/s]
v_i	Ion velocity	[m/s]
v_{rel}	Interparticle speed before collision	[m/s]
$v_{th,e}$	Electron thermal speed	[m/s]
$v_{th,i}$	Ion thermal speed	[m/s]
W	Characteristic discharge channel dimension	[m]
Δv	Velocity increment	[m/s]
α	Shock divergence angle	[deg.]
α_j	Fraction of ions with charge multiple j	[-]
β	Ratio of thermal pressure to magnetic pressure	[-]
∇	Gradient operator	[m^{-1}]
γ_j	Secondary electron yield for species j	[-]

κ_1	Electron velocity of the first Xe ionization energy	[m/s]
κ_2	Electron velocity of second Xe ionization energy	[m/s]
Δ	Characteristic length scale of significant change	[m]
ϕ	Plasma potential	[V]
ϕ_T	Thermalized potential	[V]
Ψ	Ratio of electrons with speeds > κ_1 to those > κ_2	[-]
η	Plasma resistivity	[Ohm · m]
η_a	Acceleration efficiency	[-]
η_t	Total efficiency	[-]
λ_C	Collision mean free path	[m]
λ_D	Debye length	[m]
Λ	Plasma parameter	[-]
ν	Total electron collision frequency	[s^{-1}]
ν_{ei}	Electron-ion collision frequency	[s^{-1}]
ν_{en}	Electron-neutral collision frequency	[s^{-1}]
ν_{ii}	Ion-ion collision frequency	[s^{-1}]
Ω_j	Current fraction due to species j	[-]
σ	Collision cross section	[m^2]
σ_{CEX}	Charge exchange collision cross section	[m^2]
σ_{EL}	Elastic collision cross section	[m^2]

σ_{ei}	Electron-ion collision cross section	[m^2]
σ_{en}	Electron-neutral collision cross section	[m^2]
σ_i	Ionization cross section	[m^2]
σ_{ii}	Ion-ion collision cross section	[m^2]
τ_{esc}	Characteristic escape time of a thermal neutral	[s]
τ_{ion}	Mean ionization time	[s]
μ_0	Permeability of free space	[$4\pi \times 10^{-7}$ N/A^2]
μ	Electron mobility	[m^2/V-s]
ω_c	Electron cyclotron frequency	[rad/s]

1. INTRODUCTION

As the name implies, electric propulsion (EP) involves the conversion of electrical energy into kinetic energy for the purpose of accelerating a spacecraft. The main advantage of using EP instead of conventional chemical propulsion was first pointed out by the famous rocket pioneer Robert Goddard in the early 1900's.[1] He noted that elimination of the fundamental limit imposed by a conventional rocket engine's reliance on chemical reactions as an energy source allows electrically accelerated particles to achieve a much higher velocity. The average exit velocity of the ejected propellant is directly related to a propulsive device's specific impulse, which is a measure of its thrust producing ability per unit propellant mass, i.e. its fuel efficiency. The relationship between a device's specific impulse, thrust produced, propellant mass flow rate, and average exhaust velocity is given in Eqn. 1-1. Although EP systems are incapable of producing the high thrust typical of chemical engines (at reasonable power levels), their much lower mass flow rate and higher specific impulse make them desirable for many missions.

$$I_{sp} \equiv \frac{T}{\dot{m} g} = \frac{\overline{u}_e}{g} \qquad \textbf{Eqn. 1-1}$$

The main advantage of using electric propulsion rather than chemical propulsion for spacecraft orbit raising and station keeping operations is demonstrated by the rocket equation given in Eqn. 1-2. This equation shows that the propellant mass needed for a maneuver requiring a given velocity increment, ΔV, decreases dramatically when accomplished at a high specific impulse. The resultant propellant mass saving translates into performance and financial gains for spacecraft operators and mission planners in at least three distinct ways. First, for a given spacecraft initial mass, a reduction in the required propellant mass load results in an equivalent increase in the allowable final mass of the spacecraft, as shown by Eqn. 1-3. This additional mass capacity can be used to include additional scientific instruments, transponders, or other useful payload aboard the spacecraft, thus increasing its capabilities. Alternatively, for a specified final spacecraft mass dictated by mission requirements, a reduction in the propellant mass load results in a lower spacecraft launch mass. In many cases, this mass savings may allow a spacecraft to be launched aboard a significantly smaller, and thus less costly, launch vehicle than would be possible using chemical propulsion. Finally, utilization of a high-I_{sp} system can dramatically enhance the capability of a spacecraft by increasing its potential ΔV while leaving other parameters unchanged. This can greatly increase the useful on-orbit lifetime of a spacecraft by allowing a larger number of station keeping and repositioning maneuvers to be accomplished using a given amount of propellant. The increased capability provided by electric propulsion is often said to be "mission enabling," since some high-ΔV interplanetary and deep space missions currently under consideration cannot be accomplished with other presently available propulsion technologies.[2]

$$\frac{m_{prop}}{m_{initial}} = 1 - e^{-\Delta V / g I_{sp}} \qquad \textbf{Eqn. 1-2}$$

$$m_{initial} = m_{final} + m_{prop} \qquad \textbf{Eqn. 1-3}$$

An example of the mass savings possible using EP is illustrated in Fig. 1-1, which shows the propellant mass fraction needed for north-south station keeping (NSSK) of a geosynchronous satellite as a function of specific impulse and mission duration. This plot assumes an annual ΔV requirement of 51.3 m/s for NSSK, which is a typical value for spacecraft in geosynchronous earth orbit (GEO).[3] As this figure shows, an increase in specific impulse from 225 seconds, which is typical of monopropellant systems,[4] to 1300 seconds, which is easily achievable using low-power EP systems,[5] causes the NSSK propellant mass fraction to decrease from over 20% to less than 4% for a 10-year mission. Alternatively, for a spacecraft in which the NSSK propellant mass fraction is capped at 10% due to mission or launch constraints, the same increase in specific impulse can extend the lifetime of the spacecraft from less than 5 years to more than 20 years.

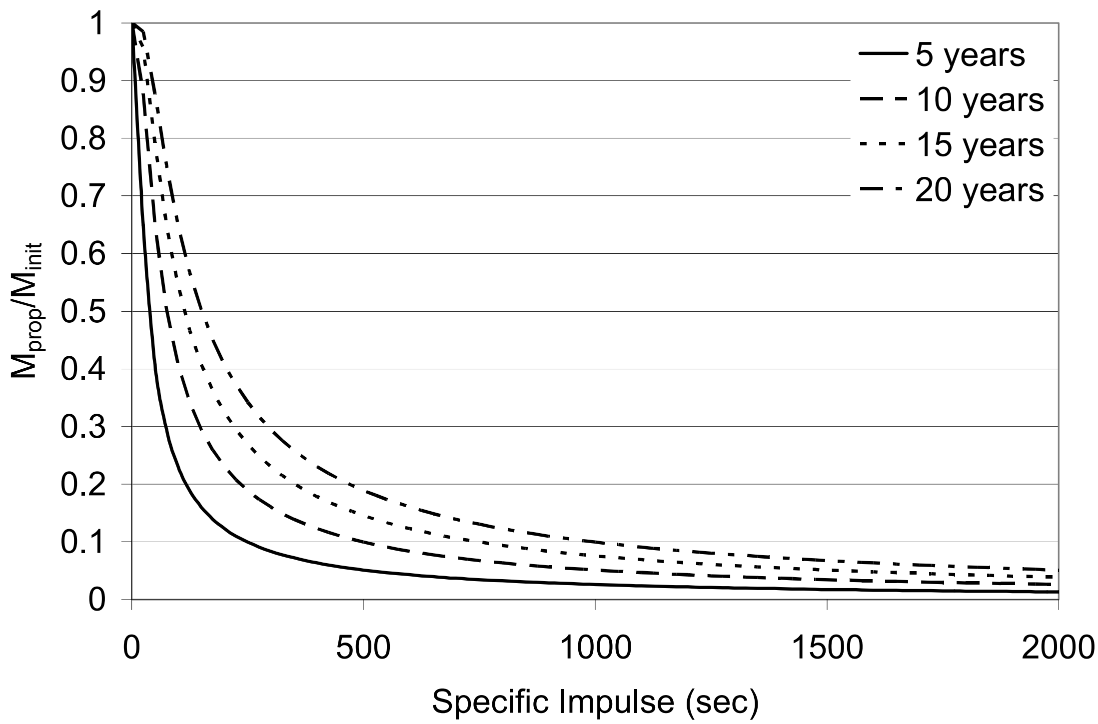

Figure 1-1: Propellant mass fraction required for NSSK of a GEO satellite as a function of specific impulse and mission duration.

1.1 Electric Propulsion Overview

Although electric propulsion devices share the property of using electrical energy to accelerate a propellant to higher exhaust velocities than typical chemical systems, the manner in which this is accomplished varies widely between devices. Electric propulsion can be divided into three main categories: electrothermal, electromagnetic, and electrostatic. The devices comprising these categories vary in terms of governing physics, typical power levels, and flight qualification status, and are therefore worthy of independent discussion.

1.1.1 Electrothermal Propulsion

Of the three main types of EP, electrothermal propulsion is most closely related to chemical propulsion in that it involves expansion of a working fluid through a conventional, converging-diverging rocket nozzle. Instead of relying on chemical reactions to heat the working fluid, however, the heating is supplied either resistively, in the case of a resistojet, or via arc heating, as in an arcjet. These devices are compatible with a wide range of propellants and are often operated on hydrazine to provide commonality with standard propellant storage and delivery components used in monopropellant applications.[6] Operation on hydrazine generally results in specific impulses of about 300 seconds for resistojets and 400-550 seconds for arcjets.[7] Operation on lighter propellants, such as ammonia or hydrogen, can result in higher specific impulses, but at the cost of increased complexity in the propellant storage and delivery system.[6] Of the various types of EP, electrothermal systems generally produce the lowest values of specific impulse, although their performance in still significantly better than that of chemical systems using storable propellants. Resistojets and arcjets commonly operate at power levels ranging from several hundred watts up to a few kilowatts for NSSK,[8] although operation at higher power levels has been demonstrated.[9] Both resistojets and arcjets are fully flight-qualified and well over 100 satellites have been flown using this technology.[10]

1.1.2 Electromagnetic Propulsion

Electromagnetic propulsion, the second branch of EP, differs significantly from both conventional and electrothermal propulsion in that the propellant is accelerated by direct interaction with applied electric and magnetic fields rather than by heating and expansion through a nozzle. This category consists mainly of the magnetoplasmadynamic thruster (MPDT) and the pulsed plasma thruster (PPT). Both of these devices accelerate a plasma by driving a current through it. This current interacts with a magnetic field, which may be applied externally or created by the current itself, and creates a force on the plasma given by Eqn 1-4.

$$\vec{F} = \vec{j} \times \vec{B} \qquad \textbf{Eqn. 1-4}$$

The PPT and MPDT differ in terms of the propellant used, typical power ranges, and the missions for which each is suited. Pulsed plasma thrusters generally operate at power levels below a few hundred watts and function by ablating, and then accelerating, a solid propellant, such as Teflon.[6] The ability of the PPT to achieve a very small impulse bit, which is the thrust multiplied by the thrusting time, makes it a particularly attractive option for applications requiring precise maneuvering, such as in multi-spacecraft arrays currently under consideration for a variety of missions.[11] Pulsed plasma thrusters have been demonstrated in space and are currently planned for use on several upcoming flights.[8]

Unlike PPTs, magnetoplasmadynamic thrusters often operate at power levels as high as several hundred kilowatts to a few megawatts.[12] The most successful MPDTs to date have operated on lithium, although much of the recent work in this field has concentrated on alternative propellants.[12] Despite the fact that these devices have suffered from poor performance in the past and have therefore failed to achieve widespread use,[6] development of MPDTs has continued due to their capability to accommodate very high power throughputs, such as those required for piloted interplanetary flights, and their tendency toward improved performance at high power levels.

1.1.3 Electrostatic Propulsion

Electrostatic systems create thrust by accelerating a charged propellant through an electric field, which asserts a force on charged particles according to Eqn. 1-5. The most notable examples of electrostatic thrusters include gridded ion thrusters and Hall effect thrusters, although less common devices such as colloid thrusters and field-effect electric propulsion (FEEP) thrusters fall into this category as well. Hall effect thrusters (HETs) are the subject of the experiments presented in this dissertation and will be discussed in greater detail in Section 1.2.

$$\vec{F} = q\,\vec{E} \qquad \textbf{Eqn. 1-5}$$

Ion thrusters function by ionizing a propellant, accelerating the positively charged ions to a high velocity to produce thrust, and neutralizing the resultant ion beam with a stream of low-energy electrons.[13] Ionization of the propellant, usually a noble gas such as xenon, occurs in a discharge chamber whose outer wall serves as the positively biased anode for the discharge circuit. Electrons are emitted from a hollow cathode within the discharge chamber. An externally applied, cusped magnetic field impedes the flow of electrons toward the outer anode and facilitates ionization of the injected propellant via electron bombardment. The resulting ions then diffuse downstream where they encounter a strong electric field imposed between electrically biased grids. This electric field accelerates the ions to a high velocity and ejects them out the rear of the device to create thrust. Upon exiting the thruster, the ion beam is neutralized by electrons emitted from a second hollow cathode to maintain charge neutrality between the spacecraft and its surroundings.

Ion thrusters are currently one of the most popular forms of electric propulsion, in terms of both research and operation, with at least 19 communications satellites using them for station keeping and/or orbit raising as of 2002.[8] The current prominence of ion thrusters follows the success of NASA's Solar Electric Propulsion Technology Application Readiness (NSTAR) thruster, which served as primary propulsion for the Deep Space 1 mission.[14] The flight spare for this mission has demonstrated the durability of this engine by operating for more than 23,000 hours during a life test at NASA's Jet

Propulsion Laboratory.[2] The success of NSTAR provides mission planners with an "off-the-shelf" 2.5 kW, 3000 second propulsion option, while current work seeks to extend the performance of ion thrusters to 14,000 seconds of specific impulse and up to 100 kW of power.[2]

1.2 Hall Effect Thruster Overview

Like an ion thruster, a Hall thruster is a device in which a noble gas, usually xenon, is ionized and accelerated electrostatically to produce thrust. Unlike in an ion thruster, the electric field is supported perpendicular to an imposed magnetic field rather than between biased grids. The main components of a typical Hall thruster are shown in Figs. 1-2 and 1-3. As depicted in these sketches, most Hall thrusters are annular in geometry, although linear and racetrack geometries have been tested.[5,15,16] One such device with a nontraditional geometry is discussed in Appendix A.

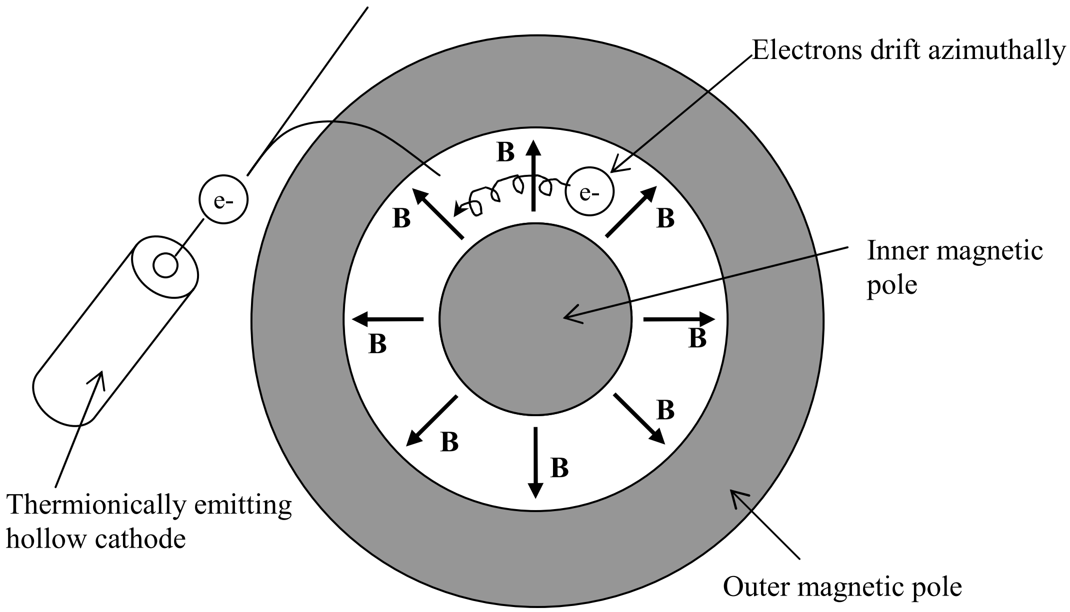

Figure 1-2: Components of a typical Hall thruster (front view).

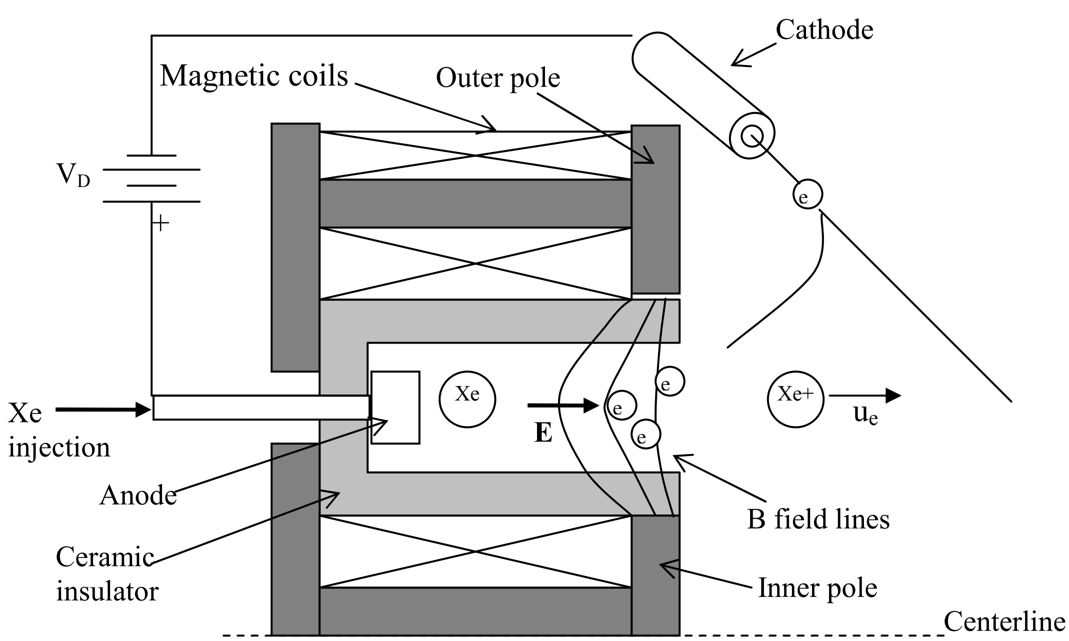

Figure 1-3: Components of a typical Hall thruster (side view).

In an HET, electrons emitted thermionically from an external hollow cathode stream toward the positively biased upstream anode, which often also serves as the propellant gas injector. The motion of the electrons is impeded by a magnetic field created by electromagnet coils and directed radially across the discharge channel by ferromagnetic pole pieces. The magnetic field strength is chosen such that the electron Larmor radius is much smaller than the characteristic width of the discharge channel, W, while the ion gyroradius is much larger as shown in Eqn. 1-6.[17]

$$r_{L,e} = \frac{m_e v_{th,e}}{eB} << W << r_{L,i} = \frac{m_i v_{th,i}}{eB} \qquad \textbf{Eqn. 1-6}$$

The applied magnetic field traps electrons in cyclotron motion and facilitates establishment of a strong axial electric field within the plasma. The resultant electron motion in the orthogonal electric and magnetic fields can be broken into two components: a fast gyration about the magnetic field lines and an azimuthal drift in the **ExB** direction with velocity given by Eqn. 1-7. The azimuthal drift of electrons, without a corresponding motion of ions, results in a closed-drift Hall current from which this device derives its name.

$$v_{ExB} = \frac{E}{B} \qquad \textbf{Eqn. 1-7}$$

Although the applied magnetic field tends to impede the axial motion of electrons, they do diffuse slowly toward the anode due to collisions (both with other particles and the discharge channel walls) and plasma turbulence. As these electrons approach the anode, they collide with and ionize neutral xenon atoms. The resulting ions are sufficiently massive that their motion is not significantly affected by the magnetic field and they are accelerated axially by the electric field. Additional electrons emitted by the hollow cathode maintain neutrality of the ejected beam. An important point to note about the acceleration mechanism is the quasineutral plasma in which it occurs. This allows Hall thrusters to avoid the space-charge limitations that occur when a net buildup of positive charge distorts the local electric field and restricts ion motion into the region. Hall thrusters are thus able to achieve much higher current densities than gridded ion thrusters are capable of.

1.3 Historical Perspective and Recent Trends

Although Hall thrusters are currently one of the main types of EP in use and under further development, this was not always the case. Research and development of Hall thrusters began in the United States in the early 1960's at a time when the primary range of specific impulse of interest for EP was 5,000-10,000 seconds based on the expected availability of lightweight, high-power energy sources.[18] At the discharge voltages required to achieve these specific impulses, the electron backflow was sufficiently energetic to cause difficulties in ion production.[18] The associated energy loss led to an unacceptably low thruster efficiency, which is defined as the fraction of applied electrical energy that is converted to useful thrust and is quantified by Eqn. 1-8. Hall thruster research in the United States was largely abandoned in favor of more efficient gridded ion thruster technology by about 1970.[18]

$$\eta_t = \frac{P_t}{P_{in}} = \frac{\frac{1}{2} T\overline{u}_e}{V_D I_D} \qquad \textbf{Eqn. 1-8}$$

Although largely neglected in the United States, Hall thruster research continued in what was then the Soviet Union. It is there that two distinct variants of the Hall thruster reached maturity, the stationary plasma thruster (SPT) developed under the direction of A. I. Morozov and the thruster with anode layer (TAL), which was studied by a group under the leadership of A.V. Zharinov.[19] The main difference delineating these categories is in the nature of the discharge channel walls. The TAL features short, metallic walls, while the discharge channel of the SPT is longer and constructed from a ceramic such as boron nitride.[20] This distinction is important primarily due to the different secondary electron emission (SEE) characteristics of these two materials.[21]

As electrons within the thruster annulus diffuse toward the anode, their energy increases monotonically due to interaction with the electric field. These electrons, being free to flow along the radial magnetic field lines, experience frequent collisions with the discharge chamber walls. In the case of a ceramic insulator, which has a high SEE coefficient, the energetic electrons striking the wall are replaced by low-energy secondary electrons and the electron temperature, T_e, within the plasma remains low.[22] In a TAL, on the other hand, the low SEE yield and negative bias of the metallic walls cause the average electron energy, and hence T_e, to be higher in this device than in an otherwise similar SPT. The higher electron temperature leads to stronger electric fields within the plasma.[21] Since the boundary conditions on the potential are set by the applied discharge voltage, the result is a shorter acceleration zone in a TAL compared to in an SPT operating at the same voltage. It is for this reason that the SPT is sometimes referred to in the literature as a closed drift thruster with an extended acceleration zone (CDEA). Although the internal plasma structure differs between the TAL and the SPT, the performance, operating characteristics, and plume structure of these devices are very similar.[18] For this reason, the results discussed throughout the remainder of this dissertation apply to both variants unless otherwise noted.

In the last 15-20 years, Hall thrusters have seen a major resurgence in popularity due primarily to their potential advantages over other types of EP for near-Earth missions such as the low-earth orbit (LEO) to GEO transfer.[23] During this time, these devices have generally been regarded as 1-5 kW devices operating at specific impulses between 1,000 and 2,000 seconds. It is in this range that they have exhibited efficient operation (typically 45%-65% anode efficiency). In recent years, the range of specific impulses at which efficient operation has been demonstrated has expanded to well beyond 3,000 seconds for xenon propellant[24] and to at least 4,500 seconds for krypton.[25] Even more striking than the gains in specific impulse that have been achieved is the degree to which the thruster power envelope has expanded. Recent work has demonstrated Hall thruster operation at power levels as low as 100 watts[5] and as high as 74 kW.[25] These values are included in Table 1, which summarizes the typical performance parameters of various types of in-space propulsion with planned or demonstrated extremes included for comparison.

Thruster Type	Min. I_{sp} (sec.)	Max. I_{sp} (sec.)	Min. Power (kW)	Max. Power (kW)	Typical Efficiency	Ref.
Chemical Monopropellant	150	225	N/A	N/A	N/A	4
Chemical Bipropellant	300	450	N/A	N/A	N/A	4
Resistojet	150	700	0.5	1.5	80%	4,6
Arcjet	450	1,500 (1,970 demonstrated)	0.3	30 (100 demonstrated)	25-40%	4, 6, 9
PPT	1,000	1,500	0.001	200	8-13%	6
MPD	2,000	5,000	1	4,000	<50%	6
Gridded Ion	2,800	5,000 (14,000 planned)	0.2	10 (100 planned)	55-65%	2, 6
Hall*	1,000	2,000 (4,500 demonstrated)	0.1	20 (74 demonstrated)	45-65%	5, 24, 25

Table 1-1: Typical performance parameters of various in-space propulsion systems.

The expansion of the EP power range noted above, particularly for ion and Hall thrusters, seems to be driven by two factors: evolving mission requirements and greater power availability in space. From 1996 to 2002, the average end-of-life power available aboard commercial GEO satellites more than tripled to greater than 10 kW.[26] Both the United States Air Force (USAF) and NASA have initiated programs to increase available power even more dramatically. The USAF push toward higher power consists mostly of research into advanced solar arrays and large, flexible power sails. NASA has recently initiated Project Prometheus, formerly known as the Nuclear Systems Initiative, in an effort to develop lightweight nuclear reactors suitable for spaceflight.[27] The commencement of these programs significantly increases the likelihood that tens or even hundreds of kilowatts of power will be available for electric propulsion in the foreseeable future.

* These values exclude Hall thrusters operating on liquid metal propellants, such as bismuth, which can dramatically increase the specific impulse attained.

The increase in available power responds to perceived needs for EP systems capable of operating at power throughputs in excess of 100 kW. The USAF foresees a need for such high-power propulsion for use in orbit transfer vehicles and rescue vehicles capable of repositioning assets that have exhausted their propellant load or failed to reach their intended orbit.[28,29] NASA, on the other hand, predicts that high-power EP systems will be used in both a high-thrust mode to reduce mission trip times and in a high-I_{sp} mode to enable missions requiring very large velocity increments.[2,30]

1.4 Clustered Hall Thrusters for High-Power Missions

The most suitable form of electric propulsion for accomplishing many of the high-power, near-Earth missions of interest to the USAF is the Hall thruster due to its favorable combination of low specific mass (mass per unit of power throughput), high thrust density, and high reliability. The recent improvements in the specific impulse range of these devices also make them applicable to the deep space missions of primary concern to NASA. Although the envisioned power level is somewhat beyond the current state of the art, two obvious approaches exist for attaining this level. The first, known as the monolithic approach, is to design a single thruster capable of operating at the desired power level. The second, complementary approach involves clustering several moderately powered devices together to reach the total throughput desired.

The clustered approach may be expected to result in a slightly lower total efficiency and higher dry mass than a comparable monolithic thruster since larger devices have historically outperformed smaller engines in these regards. A cluster of thrusters, however, has several advantages over a single unit including improved reliability due to the inherent redundancy of operating multiple devices, as well as the ability to throttle the system by simply turning on or off the appropriate number of thrusters. Throttling the system in this way allows a cluster to perform at lower powers without operating any of the individual thrusters at off-design conditions. This aspect of a cluster may prove beneficial on missions where either the available power or the propulsive needs change as a function of time. For example, a high-power cluster of thrusters could be used to accomplish the previously mentioned LEO-GEO transfer of a geosynchronous communications satellite. Upon reaching its final destination, one element of the cluster could then be used for NSSK while the unused electrical power capacity remains available for other spacecraft operations.

In addition to the advantages mentioned above, multi-thruster arrays also offer a high degree of system scalability. In principle, once the technical issues associated with operating multiple thrusters in close proximity to each other are understood, a single engine could support a wide range of missions requiring varying power levels by simply clustering the appropriate number of thrusters. This reduces the overall cost of developing high-power EP options by reducing the number of engine designs that must be flight qualified. Rather than performing tedious and expensive life tests on different thruster designs for each power range desired, a minimal number of "building block" thruster designs are required to support a wide variety of missions with a reasonable number of clustered thrusters.

Another factor that may dramatically affect the cost of developing high-power EP systems, and thus the choice between monolithic and clustered approaches, is the power level of the individual thrusters being tested. There are very few vacuum facilities in the world capable of maintaining an adequate background pressure while supporting the propellant mass flow rate required for operation of a 100-kW Hall thruster. The cost of constructing and operating ground facilities to test very high-power thrusters could easily overshadow the cost of thruster development. Clusters of thrusters, on the other hand, can be developed in many existing vacuum facilities by using a two-stage approach. First, a cluster of low-power thrusters can be used to study the technical issues related to clustering and to develop analytical methods for predicting critical cluster operating parameters. The moderately-powered "building block" thrusters needed for high-power clusters can then be developed, tested, and flight qualified individually without the need to ground test an entire high-power cluster. The relative merits of clustered and monolithic high-power Hall thruster systems are summarized in Table 1-2.[29] In general, clustering sacrifices a small amount of performance in favor of improved reliability, scalability, and flexibility.

Criteria	Monolithic	Cluster
Performance		
Efficiency	Approximately the Same†	Approximately the Same†
Specific Impulse	Approximately the Same†	Approximately the Same†
System Dry Mass	Lower	Higher
Reliability		
Individual Thruster	Same	Same
Overall System	Lower	Higher (redundancy)
Operational Flexibility		
Throttling Range	Lower	Higher
Suitability for Orbit Raising	Same	Same
Suitability for Station Keeping	Lower (Off-design operation)	Higher
Development Flexibility	Lower	Higher
Development Cost	Higher	Lower
Suitable Test Facilities	Few	Many

Table 1-2: Relative merits of monolithic and clustered high-power Hall systems.[29]

1.5 Contribution of Research

Although using a cluster of moderately-powered Hall thrusters appears to be advantageous for many high-power missions, there are a number of issues that must be addressed before this can occur.[28,29] For example, the neutralization process must be examined to determine whether a single hollow cathode can be used to neutralize the entire assembly or if an individual cathode is required for each thruster. The possibility of thruster cross-talk through the plasma plumes must be studied to determine the potential impact of clustering on the design of power processing units (PPUs). Perhaps the most pressing issue is the need to understand the interaction of the plasma plumes with each other and with the spacecraft. The research discussed in subsequent chapters of this dissertation is part of a collaborative effort between the U.S. Air Force Research

† Monolithic thrusters may be expected to have a slight advantage in terms of both specific impulse and efficiency due to lower wall losses and power consumed by the electromagnets compared to the smaller thrusters of a cluster. The difference, however, is likely to be small.

Laboratory (AFRL) and the University of Michigan's Plasmadynamics and Electric Propulsion Laboratory (PEPL) to address these issues.

To the author's knowledge, the only research into clustering of Hall thrusters, other than that at AFRL and PEPL, has been funded by the USAF European Office of Aerospace Research and Development (EOARD) and conducted at the Russian Central Research Institute of Machine Building (TSNIIMASH).[31,32] That work was conducted using a cluster of three D-55 TAL thrusters and has demonstrated that multiple thrusters can be operated from a single cathode with little or no effect on the cumulative thrust produced.[31] Operation of three thrusters from a single power supply was also demonstrated with no significant increase in the level of discharge current oscillations and no apparent coupling among the devices.[31]

Unlike the Russian research mentioned above, which concentrated mainly on characterizing the basic performance of different operational configurations, the main focus of the research presented in this dissertation is on the plasma properties in the cluster plume. In particular, a method is presented for predicting the plasma number density, electron temperature, and plasma potential in the cluster plume based on knowledge of similar properties downstream of a single thruster unit. This ability is critical for spacecraft designers who need to determine the interaction between the chosen electric propulsion system and potentially sensitive spacecraft components, such as solar arrays. Additionally, this work has implications for the thruster modeling community. Most current Hall thruster simulation tools are two-dimensional and axisymmetric in nature. Due to the annular shape of most engines, these tools are able to capture the important geometry as well as the relevant plasma physics. When one considers a cluster of thrusters, however, axisymmetry of the system cannot be guaranteed. Thruster modelers are therefore faced with the prospect of either developing complex, costly, fully three-dimensional simulations or adapting existing axisymmetric simulations to a three-dimensional environment. The methods presented in this dissertation facilitate the latter.

In addition to the basic plume properties discussed above, several other important aspects of clustering are also addressed. The ion energy spectra downstream of a cluster have been measured using two different diagnostic techniques. These spectra show rather dramatic differences between single- and multi-thruster operation, which may impact calculations of spacecraft surface sputtering. Additionally, the effect of cathode number and placement on basic cluster operating characteristics and plume properties has been studied. Measurements show that cathode placement can greatly influence the plasma plume properties, particularly when operating individual thruster units rather than the entire cluster. The results of this work will enable future spacecraft designers to determine the optimal configuration of a cluster of Hall thrusters and to analytically predict the most important plume properties downstream of the system. This will facilitate studies of thruster/spacecraft interactions and allow high-power clusters of Hall thrusters to be implemented with minimal development cost and risk.

2. EXPERIMENTAL APPARATUS

As alluded to in Chapter 1, the research presented in this dissertation has utilized a multitude of experimental facilities and diagnostic techniques. This chapter discusses the relevant details of the thrusters studied and the experimental facilities in which they were operated. The theories used to implement the various diagnostic techniques, as well as details regarding the construction and operation of various instruments, are also presented.

2.1 Hall Thruster Cluster

The cluster studied in this experiment consists of four Busek model BHT-200-X3 Hall thrusters, which operate at a nominal power throughput of 200 watts. An earlier version of this thruster was reported to operate at an anode efficiency of 42% and specific impulse of 1300 seconds while providing 12.4 mN of thrust at the nominal operating conditions.[5] Each thruster has a mean diameter of 21 mm and is operated on xenon propellant. The thrusters are arranged in a 2x2 grid with approximately 11.5 centimeters between the centerlines of adjacent thrusters. Typical operating conditions for the BHT-200 are given in Table 2-1.

Parameter	Typical Value
Discharge Voltage (V)	250 ± 0.5
Discharge Current (A)	0.80 ± 0.03
Cathode Potential (V)	-8.5 ± 1.0
Electromagnet Current (A)	1.0 ± 0.03
Keeper Current (A)	0.5 ± 0.05
Keeper Voltage (V)	13 ± 1
Anode Mass Flow Rate (sccm)	8.5 ± 0.85
Cathode Mass Flow Rate (sccm)	1.0 ± 0.1

Table 2-1: Typical operating parameters of the BHT-200 thruster.

In the nominal configuration, each thruster is completely independent of the others, although other configurations were studied and will be discussed in subsequent chapters of this dissertation as appropriate. Nominally, each thruster has a separate 3.2 mm (1/8") diameter hollow cathode whose potential is allowed to float independently of the other three. Each thruster uses four separate laboratory power supplies to power the main discharge circuit, the electromagnet coil, the cathode heater, and the cathode keeper electrode. Relevant operating parameters are measured using a multi-channel data logger and recorded by a PC running Labview software. A schematic of the thruster power circuit is given in Fig. 2-1. Note that the BHT-200 uses only one electromagnetic winding, unlike the two or more coils typically used by larger thrusters.

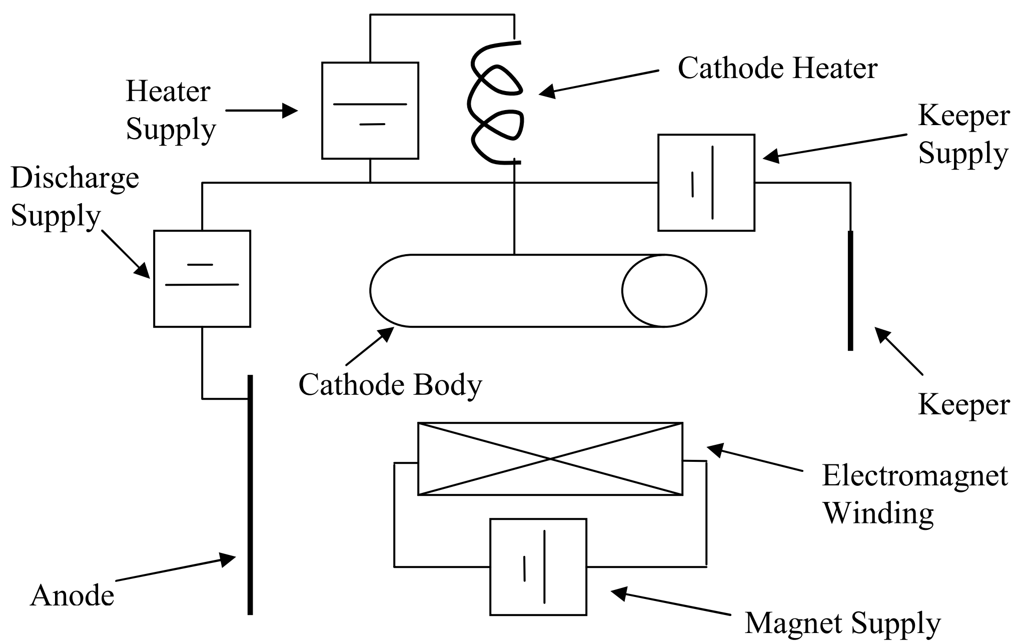

Figure 2-1: Simplified electrical schematic for the BHT-200.

The coordinate system and thruster naming convention referred to throughout this dissertation are shown in Fig. 2-2. As shown, the thrusters are labeled TH 1-4 starting in the upper left-hand corner (when viewed from the front) and proceeding counterclockwise from there. In the orthogonal coordinate system, X is to the right, Y is up, and Z measures the distance downstream of the cluster exit plane. The origin of the coordinate system is at the center point of the cluster and distances are typically measured in millimeters such that the centerline of each thruster is located at X = ±57.5, Y = ±57.5. The object seen in the center of Fig. 2-2 is the triple probe discussed later in this chapter. Figure 2-3 shows two views of the cluster during operation.

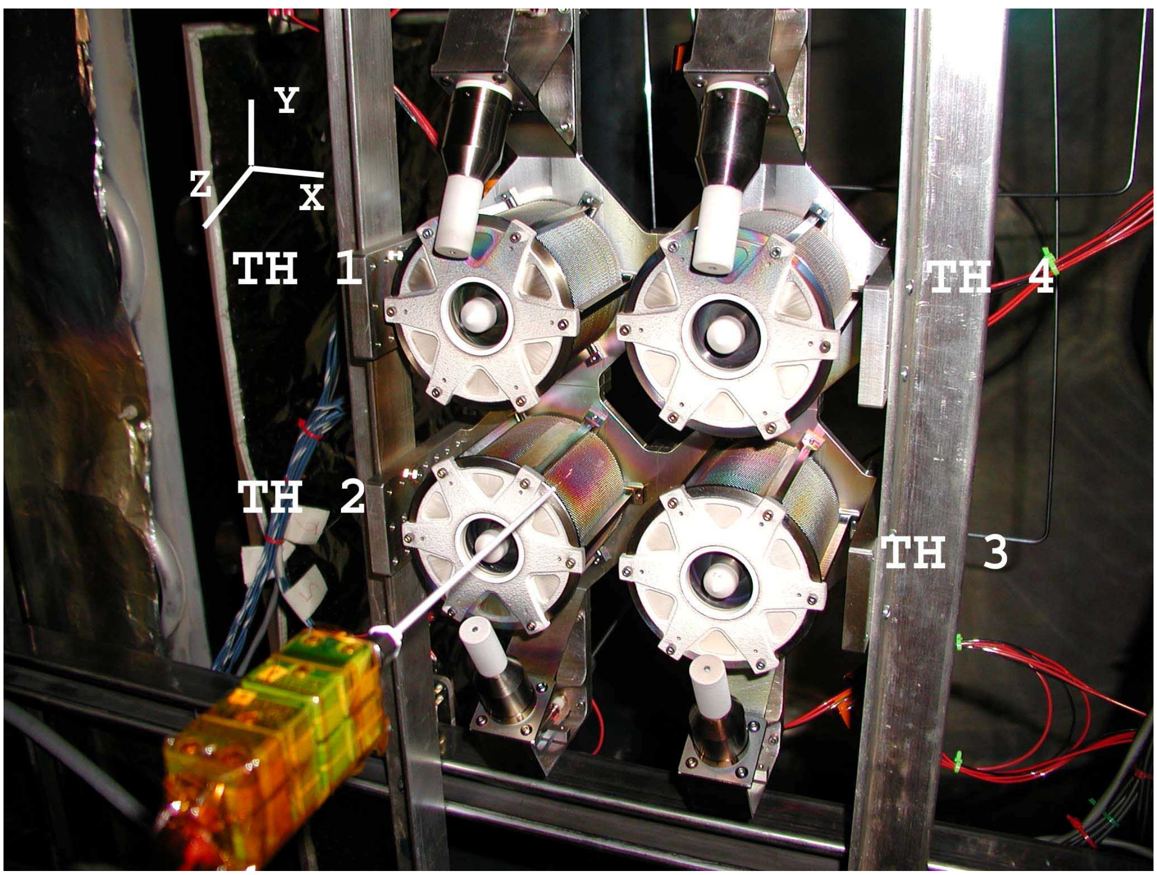

Figure 2-2: Cluster naming convention and coordinate system.

Figure 2-3: Two views of the Hall thruster cluster during operation.

2.2 Langmuir Probe

The Langmuir probe is a commonly used plasma diagnostic device that consists simply of a conducting electrode of a known size immersed in a plasma. The probe used in these experiments consisted of a 1.58 mm stainless steel sphere spot welded to a wire lead that was coated with an alumina insulating paste. This device is capable of measuring electron number density, electron temperature, and plasma potential by observing the current collected by the probe as a function of its potential with respect to a reference electrode such as the vacuum chamber ground. A comprehensive discussion of Langmuir probes under various plasma conditions has been compiled by Schott.[33] The discussion below is limited to the basic theory used in the present experiments.

The main operating principle behind the Langmuir probe involves the realization that the current collected by the electrode is composed of two components: ions and electrons. The ions, being much more massive, are only weakly affected by the relatively low voltages applied to the probe and, as a first approximation, the ion flux to the probe can be considered nearly constant. Consideration of the electron response to the applied potential allows the characteristic trace to be divided into three distinct regions, as shown in Fig. 2-4. At applied voltages sufficiently negative with respect to the local plasma potential, electrons are repelled and the resultant current is due almost exclusively to the collected ion flux. This condition corresponds to the ion saturation region shown in Fig. 2-4. At higher potentials, slow electrons are repelled by the applied voltage while faster electrons are able to overcome the repelling potential and reach the probe. At voltages above the plasma potential, nearly all electrons reaching the edge of the thin sheath that forms around the probe are collected and the current plateaus at the electron "saturation" current. The term "saturation" is somewhat of a misnomer since, as seen in Fig. 2-4, the collected current tends to increase with voltage as a result of sheath expansion.[33]

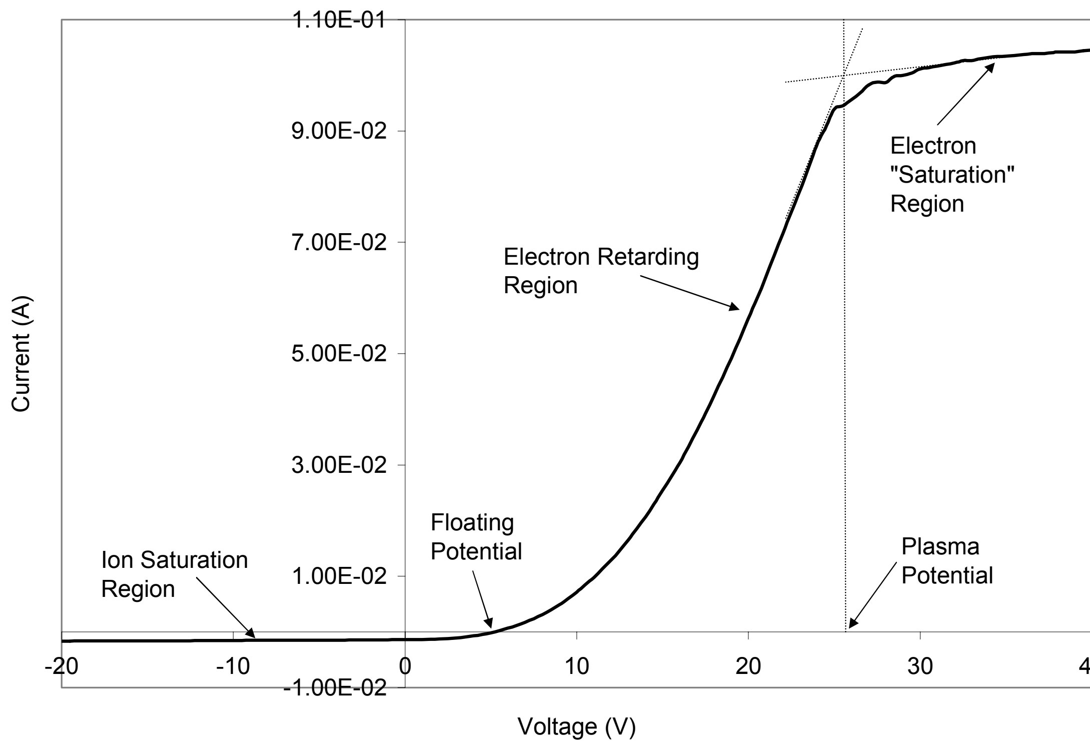

Figure 2-4: Typical Langmuir probe characteristic.

For a Maxwellian electron velocity distribution, the plasma density and electron number density can be calculated using simple formulas. In the electron retarding region, the exponential increase in collected current is affected by the local electron temperature, which can be inferred using Eqn. 2-1.[33] After the electron temperature has been determined, the Bohm sheath criterion and the standard assumption of quasineutrality can be exploited to determine the electron number density via Eqn. 2-2.[17] The plasma potential is taken to be the "knee" in the characteristic, as shown in Fig. 2-4.

$$\frac{k_b T_e}{e} = \left(\frac{d \ln(I_p)}{dV} \right)^{-1} \qquad \textbf{Eqn. 2-1}$$

$$n_e = \frac{I_{i,sat}}{\exp\left(\frac{-1}{2} \right) e A_p \left({k_b T_e}/{m_i} \right)^{1/2}} \qquad \textbf{Eqn. 2-2}$$

Unfortunately, implementation of the Langmuir probe as a useful diagnostic is rarely as simple as the above discussion implies, particularly in a flowing plasma such as the one found in the plume of a Hall thruster. First, expansion of the non-neutral sheath causes the collected ion current to continue increasing as the probe is biased to increasingly negative potentials. The square of the collected ion current has been shown to increase linearly with applied voltage.[34] Although the error introduced by this phenomenon is relatively minor in the present case, the noted trend is used to correct for sheath expansion effects by fitting a line to the square of the current collected at the most negative potentials measured, i.e. -20 to -10 volts in Fig. 2-4. The ion "saturation" current is then taken to be the value of the extrapolated fit line at zero applied potential, thus providing a consistent means of determining the plasma density. The electron temperature is derived from the slope of the current trace taken at the floating potential.

In addition to the difficulties associated with determining the appropriate ion saturation current, determination of the plasma potential can be somewhat ambiguous because the “knee” in the current trace is often poorly defined. Finally, the results obtained from this diagnostic suffer from the probe’s need to collect current from the plasma. In many cases, the collected current can significantly perturb the local plasma thus introducing significant errors in the derived parameters. Due to the multiple sources of error associated with this diagnostic, as well as the tedious nature of the data analysis, the macroscopic plasma parameters derived from Langmuir probe data are used in this study primarily as a check on the values obtained by other means, such as the triple probe discussed in the next section.

An additional characteristic of the Langmuir probe that is taken advantage of in this work is its ability to measure the electron energy distribution function (EEDF). This is accomplished by smoothing the collected data numerically and taking the second derivative of the current with respect to voltage. The EEDF is then calculated from the Druyvestein formula given by Eqn. 2-3.[35]

$$f(E)\Big|_{E=-e(V-\phi)} = -\frac{4}{A_p e^2}\sqrt{\frac{m_e(\phi-V)}{2e}}\frac{d^2 I_p}{d(V-\phi)^2} \qquad \textbf{Eqn. 2-3}$$

2.3 Triple Probe

The symmetric triple probe, originally developed by Chen and Sekiguchi,[34] is a convenient plasma diagnostic to use in Hall thruster plumes due to the elimination of the voltage sweep required by other electrostatic probes. Additionally, since the probe as a whole floats, the disturbance to the ambient plasma is minimized compared to single Langmuir probes, which draw a net current from the discharge.

The triple probes used for this experiment consisted of three cylindrical tungsten electrodes insulated from each other by an alumina rod. Two separate probes were used. For the larger probe, the diameter of each electrode was 0.50 mm (0.02") and the length extending past the end of the alumina was 5.0 mm (0.20"). A smaller probe consisting of 0.38 mm (0.015") diameter, 3.8 mm (0.15") long electrodes was used in areas of the plume where improved spatial resolution was desired. In each case, the electrodes were aligned parallel to the thruster axis and spaced approximately two electrode diameters apart. The probes were sized to criteria that allowed the standard thin sheath assumptions of probe theory to be applied.[33] These criteria are summarized in Eqns. 2-4 through 2-8 below and are necessary to ensure that all ions entering the probe sheath are collected by the probe rather than being deflected by magnetic fields or collisions. Further, it was assumed that the electrodes were far enough apart to avoid interaction with each other and that the spatial gradients of plasma properties were sufficiently small such that all three electrodes were exposed to identical plasmas. Additionally, the plasma was assumed to be quasineutral and the electron velocity distribution was taken to be Maxwellian. In the relations that follow, Δ is a characteristic length scale over which plasma properties change significantly. The data collected in this experiment obeyed Eqns. 2-4 through 2-8 throughout most of the sampled volume. The small regions of the plume where Eqn. 2-8 was not strictly satisfied are discussed in Chapter 3.

$$r_{Li} >> r_{Le} >> \lambda_D \qquad \textbf{Eqn. 2-4}$$

$$\lambda_D < r_p \qquad \textbf{Eqn. 2-5}$$

$$\lambda_c >> r_p \qquad \textbf{Eqn. 2-6}$$

$$dx >> \lambda_D \qquad \textbf{Eqn. 2-7}$$

$$\Delta >> dx > r_p \qquad \textbf{Eqn. 2-8}$$

A schematic of the triple probe circuit is shown in Fig. 2-5. As shown, electrode 2 was allowed to float while the voltage, V_{d3}, was applied by a laboratory power supply with floating outputs. For the tests reported here, V_{d3} was set to 12 volts. The voltages V_{d2} and V_f were measured using a computer controlled data logger. The electrodes were numbered in order of decreasing potential such that electrode 2 was at the floating potential while electrodes 1 and 3 were biased above and below the floating potential, respectively.

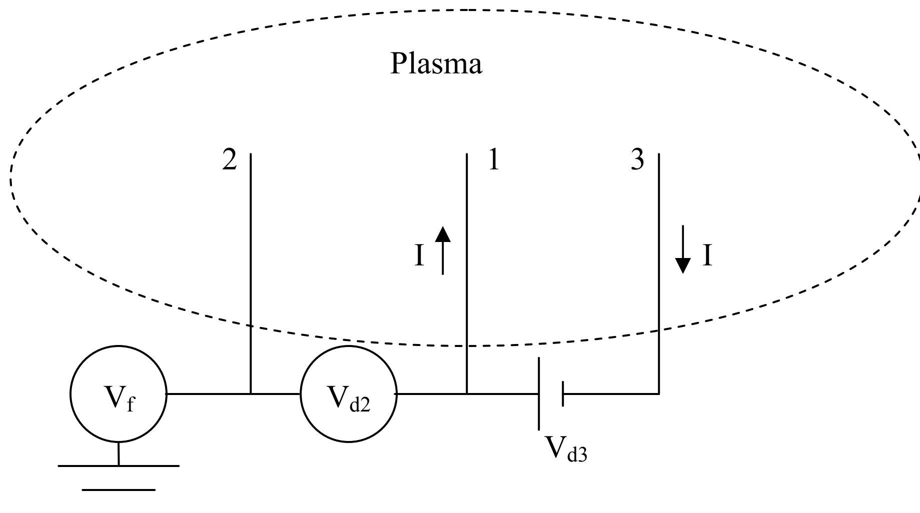

Figure 2-5: Triple probe circuit showing the applied voltage, V_{d3}, and the measured potentials, V_{d2} and V_f.

Three distinct methods were evaluated to calculate the electron number density and electron temperature from the raw triple probe data. The first is the original method derived by Chen and Sekiguchi, which assumes that the sheath thickness is negligible compared to the radius of the probe and that each electrode collects an equal ion saturation current. With these assumptions, the electron temperature and number density can then be calculated using Eqns. 2-9 and 2-10, respectively.[34]

$$\frac{1-\exp\left(\frac{-eV_{d2}}{k_bT_e}\right)}{1-\exp\left(\frac{-eV_{d3}}{k_bT_e}\right)}=\frac{1}{2} \qquad \textbf{Eqn. 2-9}$$

$$n_e=\left(\frac{em_i}{k_bT_e}\right)^{1/2}\frac{I_p\exp\left(\frac{1}{2}\right)}{A_pe^{3/2}\left[\exp\left(\frac{eV_{d2}}{k_bT_e}\right)-1\right]} \qquad \textbf{Eqn. 2-10}$$

The second method follows the mathematically rigorous derivation employed by Tilley,[36] which takes into account the slight variations in ion current collected by the three electrodes as a result of their differing voltages.[37] Unfortunately, the Peterson-Talbot method used to calculate the current to each electrode requires knowledge of the ion to electron temperature ratio, T_i/T_e.[37] Since this ratio is unknown in most practical situations, it is usually assumed to be a constant throughout the plume and to have a value somewhere between 0 and 1. While this assumption may be justified under certain plasma conditions in the devices for which it was originally applied, in the present situation it is equivalent to dictating that the ion temperature must evolve in exactly the same way as the electron temperature throughout the plume. This assertion is not supported by previously published laser induced fluorescence (LIF) measurements, which show the ion temperature to remain nearly constant over a large area of the plume while the electron temperature varies considerably over a comparable region.[22,38] Considering the ambiguity associated with the changing temperature ratio, this method was determined to be of varying validity over the sampled plume region and therefore unsuitable for determining the electron temperature and number density profiles.

The third method is very similar to the first, except that the physical probe area shown in Eqn. 2-10 is replaced with an effective collection area, which is defined as the surface area of the sheath surrounding each electrode. An estimate of the sheath thickness is given by Eqn. 2-11 and is approximately five Debye lengths for a xenon plasma.[39] For cylindrical electrodes, such as the ones comprising the triple probe, the sheath area is then given by Eqn. 2-12.

$$\delta = 1.02\lambda_D \left[\left(\frac{1}{2}\ln\left(\frac{m_i}{m_e}\right)\right)^{1/2} - \frac{1}{\sqrt{2}}\right]^{1/2} \left[\left(\frac{1}{2}\ln\left(\frac{m_i}{m_e}\right)\right)^{1/2} + \sqrt{2}\right] \qquad \textbf{Eqn. 2-11}$$

$$A_S = A_P\left(1 + \frac{\delta}{r_p}\right) \qquad \textbf{Eqn. 2-12}$$

The relations above allow the calculation method to proceed by first estimating the density according to Eqn. 2-10 and using this estimate to calculate a value of the sheath thickness. The updated collection area from Eqn. 2-11 is then used to determine an updated value of the density and the procedure continues iteratively until the solution converges. This method is preferred over the other two for several reasons. Unlike the procedure that depends on assuming an ion to electron temperature ratio, this method is believed to be of essentially constant validity over the entire plume region because it accounts for changing plasma conditions by explicitly taking into account the effect of the variable Debye length on the derived parameters. Accounting for the sheath thickness is also believed to make the results presented in this dissertation quantitatively more accurate than measurements presented previously by the current author, which neglected the effect of the sheath thickness and therefore reflected an upper bound on the actual density value.[40, 41] It should be noted, however, that the conclusions drawn in those publications are largely unaffected by implementation of the more precise analysis procedure and therefore remain valid.[40, 41] Various error analyses have shown the absolute error in the electron temperature and plasma density measurements derived from the triple probe to be generally less than 30% and 50%, respectively.[34, 36] The relative uncertainty between multiple data points measured using the same probe is believed to be significantly lower than the absolute uncertainty.

2.4 Emissive Probe

Plasma potential measurements were conducted using a floating emissive probe similar to the one described by Haas *et al*.[42] The emitting portion of the probe consisted of a loop of 0.127 mm (0.005”) diameter tungsten filament, the ends of which were inserted into double bore alumina tubing along with 0.508 mm (0.020”) diameter molybdenum wire leads. Short lengths of tungsten wire were inserted into the alumina tube to ensure contact between the emitting filament and molybdenum leads. The diameter of the emitting filament loop was approximately 3 mm. Figure 2-6 shows a sketch of the emissive probe. The normal to the plane of the loop formed by the emitting filament was oriented in the X direction shown in Fig. 2-2.

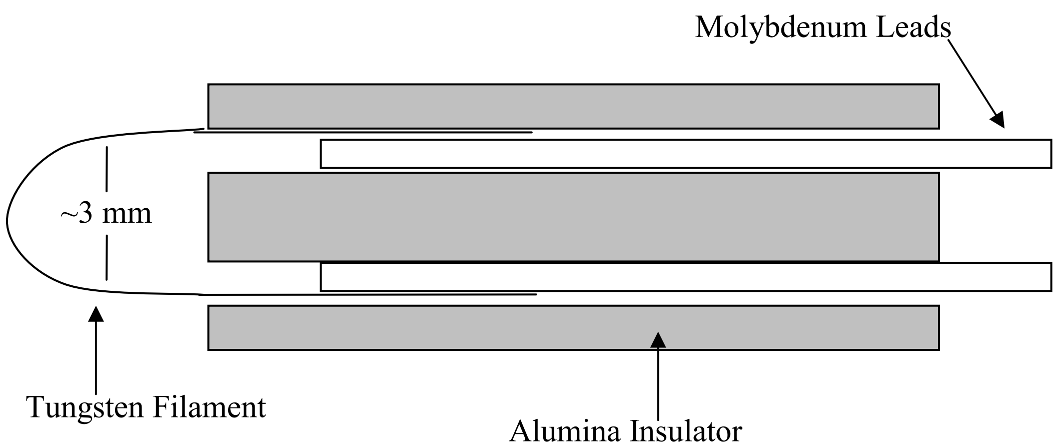

Figure 2-6: A sketch of the floating emissive probe.

The theory of the emissive probe is well established and results in the conclusion that a thermionically emitting filament will approach the local plasma potential when its emitted electron current is sufficient to neutralize the plasma sheath.[43] For the experiments reported here, the current necessary to heat the probe was provided by a programmable power supply with floating outputs. At each location in the plume, the filament current was steadily increased and the potential with respect to ground at the negative terminal of the power supply was recorded. This method allowed for verification of a well-defined plateau in the voltage-current trace indicating neutralization of the plasma sheath. The shape of a typical trace, such as the one shown in Fig. 2-7, can be explained as follows. At zero applied current, the probe assumes the local floating potential. As the current to the probe is increased, the measured potential initially decreases as a resistive voltage drop appears across the probe causing the potential at the negative terminal to move below the floating potential. As the probe current is increased further, the filament begins to emit electrons causing the measured potential to rise sharply before approaching an asymptote at the local plasma potential.

The main source of uncertainty in the emissive probe technique stems from the varying potential across the length of the emitting filament. Considering that the voltage drop across the probe never exceeded 6 V in the present study, the maximum uncertainty due to this factor is estimated to be ±3 V. A second potential source of error relates to an assertion by some authors that the potential of the emitter tends to remain below the true plasma potential by approximately $k_b T_e/e^2$.[44] Since the electron temperature in Hall thruster plumes rarely exceeds 3 eV (except in the very near field) the maximum uncertainty due to this factor is estimated to be +3, -0 volts. It should be noted, however, that previously published plasma potential measurements taken inside an operating Hall thruster using an emissive probe show no evidence of the probe floating below the true plasma potential despite the high electron temperature, which approached 40 eV.[22] The total uncertainty in the absolute value of plasma potentials reported in this dissertation is therefore conservatively estimated to be +6, -3 volts, although the relative uncertainty between adjacent points is considerably smaller.

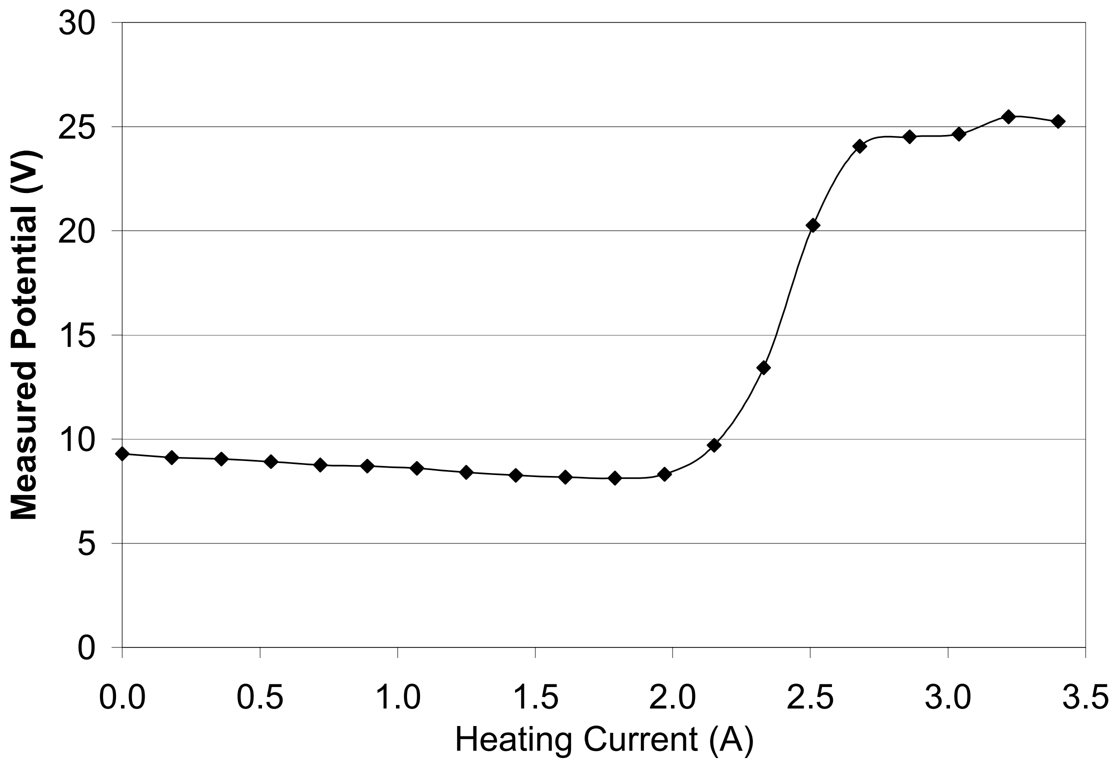

Figure 2-7: A typical emissive probe characteristic. At sufficiently high heating current, the probe potential approaches the local plasma potential.

2.5 Faraday Probe

The Faraday probe is a commonly used tool for measuring the ion beam profile downstream of a thruster. It is very similar in operation to a Langmuir probe except that it is generally used to measure the directed ion flux while the Langmuir probe seeks to collect the random ion flux due to thermal motion and use that quantity to determine plasma density. In its simplest form, the Faraday probe is simply a planar electrode oriented perpendicular to the flow of the ion beam from the thruster. The electrode is biased to a sufficiently negative potential to repel electrons and limit the collected current to that due to the directed ion flux, i.e. the probe operates in the ion saturation regime shown in Fig. 2-4.

Two separate Faraday probes were used in the cluster experiments. The first is a standard nude probe, which consists of a 19.0 mm diameter collector disc surrounded by a 43.2 mm outer diameter annular guard ring as sketched in Fig. 2-8. The purpose of the guard ring is to minimize the adverse effects of the growing sheath discussed previously in conjunction with the triple probe. This is accomplished by biasing the guard ring to the same negative potential as the collector to form an essentially flat sheath in front of the probe. As the sheath expands away from the probe with increasingly negative bias voltage, the projected collection area remains nearly constant and the ion current density can be obtained by dividing the collector current by the area of the electrode. As shown in Fig. 2-9, the collected ion current at a given location remains very nearly constant for bias voltages beyond approximately -5 to -10 volts. The collector and guard ring are biased through resistor strings and the current to the collector is obtained by the voltage drop across the resistor as shown in the diagram below.

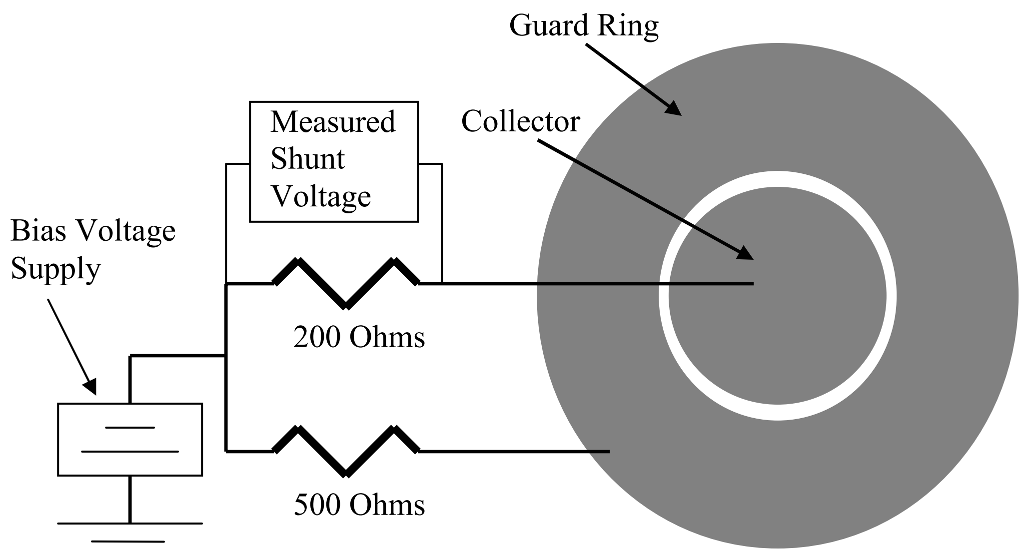

Figure 2-8: Sketch of the nude Faraday probe and biasing circuit.

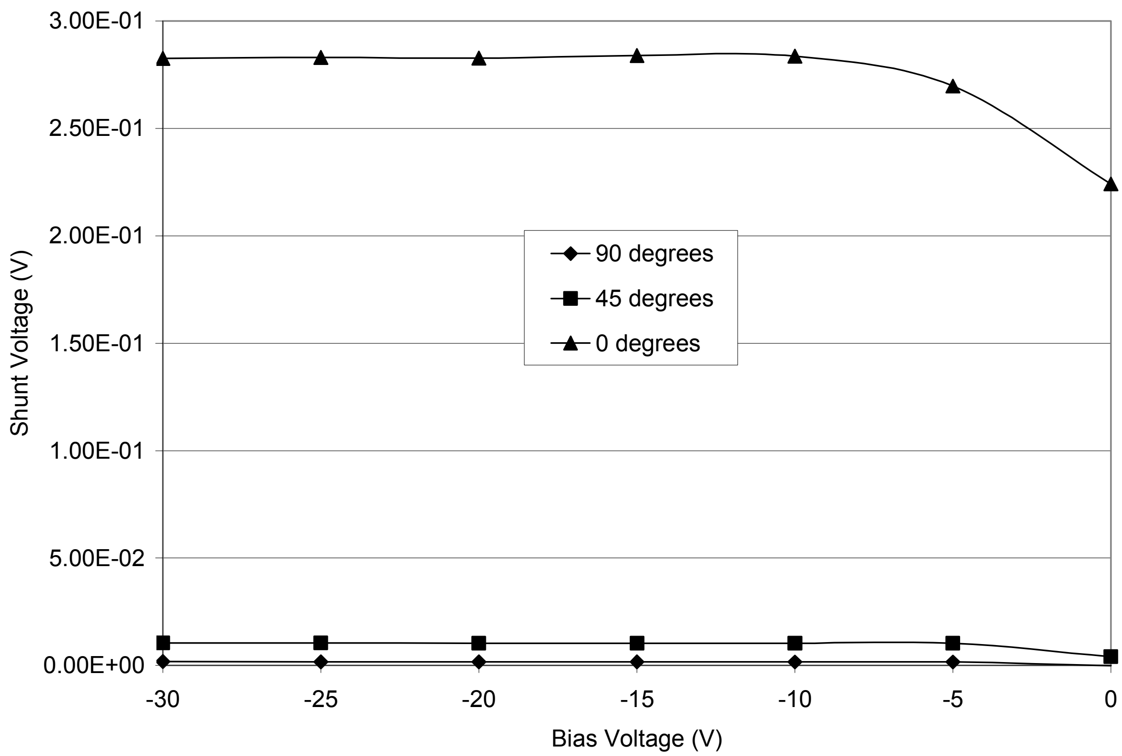

Figure 2-9: Saturation characteristics of the nude Faraday probe at three different angles off the centerline of thruster 3. The measured shunt voltage is directly proportional to the ion current density.

One shortcoming of nude Faraday probes is that ion current density measurements derived from them are often highly dependent on the pressure in the vacuum facility.[45] This is because a portion of the high velocity ions exiting the thruster collide with background neutrals resulting in resonant charge exchange (CEX) between the particles. Charge exchange occurs when an electron is transferred from one particle to another without significant momentum transfer. In the present case, this process results in a fast moving ion and a slow moving neutral being converted into a fast moving neutral and a so-called CEX ion with a random velocity equal to that of the original low-energy neutral. The presence of CEX ions has been shown to result in a large increase in the current collected by a nude Faraday probe, particularly at large angles off the thruster centerline.[46] This leads to an overprediction of both the total current flux from the thruster and the beam divergence, which is a figure of merit characterizing how well a device directs ions in the preferred, axial direction.

To mitigate the adverse effects of CEX ions, a gridded Faraday probe was used in conjunction with the nude probe for some of the current density measurements. This device consists of an inlet grid in front of the collector surface. The grid is biased approximately 30 volts above ground to reflect CEX ions while permitting the faster beam ions to be collected. Physically, this device is simply the retarding potential analyzer described in the next section with the center two grids removed.

2.6 Retarding Potential Analyzer

The retarding potential analyzer (RPA) provides a means of measuring the ion energy spectra in the plasma plume of a Hall thruster. Similar in concept to the gridded Faraday probe, the RPA uses a biased grid to exclude ions with a directed velocity below some critical value, v_{crit}. When these ions are excluded, the current to the collector is described by Eqn. 2-13 where f(v) is the ion velocity distribution function and the subscript j refers to species of different charge states (singly-charged, doubly-charged, etc.). The value of v_{crit} is related to the grid bias voltage through Eqn. 2-14.

$$I_{coll} = A_c e \sum_j n_j q_j \int_{v_{crit}}^{\infty} v f_j(v) dv \qquad \textbf{Eqn. 2-13}$$

$$v_{crit} = \sqrt{\frac{2 q_j e V_{grid}}{m_i}} \qquad \textbf{Eqn. 2-14}$$

As Eqn. 2-14 shows, the critical velocity below which ions are rejected depends on both the mass and charge state of the sampled ions. In a Hall thruster plume, nearly all ions are of equal mass depending only on the molecular mass of the propellant, but there is likely to be a significant fraction (on the order of 10%) of multiply-charged ions present.[47] For this reason, it is generally convenient to define an equivalent ion voltage, which is the ion's kinetic energy per unit charge. Applying this definition and substituting variables allows the collected current to be written directly in terms of the retarding grid potential and the ion voltage according to Eqn. 2-15, where the effective charge state, q_{eff}, is given by Eqn. 2-16. Differentiation of Eqn. 2-15 leads to Eqn. 2-17, which shows that the ion voltage distribution is directly proportional to the derivative of the collected current with respect to the retarding grid voltage. It must be emphasized that although the RPA is commonly referred to as an energy diagnostic, it is actually only capable of measuring the energy per charge distribution because a singly-charged ion traveling with a given kinetic energy is indistinguishable from a doubly-charged ion possessing twice the kinetic energy.

$$I_{coll} = A_c \frac{n_e e^2 q_{eff}^2}{m_i} \int_{V_{grid}}^{\infty} f(V) dV \qquad \textbf{Eqn. 2-15}$$

$$q_{eff}^2 = \frac{\sum_j \left(n_j q_j^2\right)}{\sum_j n_j} \qquad \textbf{Eqn. 2-16}$$

$$\left.\frac{dI}{dV}\right|_{V=V_{grid}} = -A_C \frac{n_e q_{eff}^2 e^2}{m_i} f(V) \qquad \textbf{Eqn. 2-17}$$

The RPA used in this experiment is based on the multi-gridded energy analyzer design of Hutchinson.[39] It consists of three grids and is shown schematically in Fig. 2-10. The outer body of the RPA is constructed of 316 stainless steel (SS) tubing, which is held at ground potential. A phenolic sleeve placed inside the body provides electrical isolation of the grids. All grids are identical and are cut from 316 SS, photochemically machined sheet with a thickness of 0.127 mm (0.005”). The grid openings are 0.2794 mm (0.011”) in diameter with a total open area fraction of 38%. Grid spacing is achieved using Macor washers machined to provide correct separation. The collector is a simple copper disc. Electrical connections are accomplished by spot welding stainless steel wire to each grid.

The wires are then routed along the inner edge of the phenolic sleeve and out the rear of the body. The washers and grids are compressed by a spring placed behind the collector and held in place by a rear cover. Relevant dimensions are summarized in Table 2-2.

Washer	1	2	3	4	5
Thickness (mm)	1.07	3.35	1.73	6.55	6.55
Inner Diameter (mm)	18.54	21.54	21.54	21.16	21.23

Table 2-2: RPA spacer dimensions.

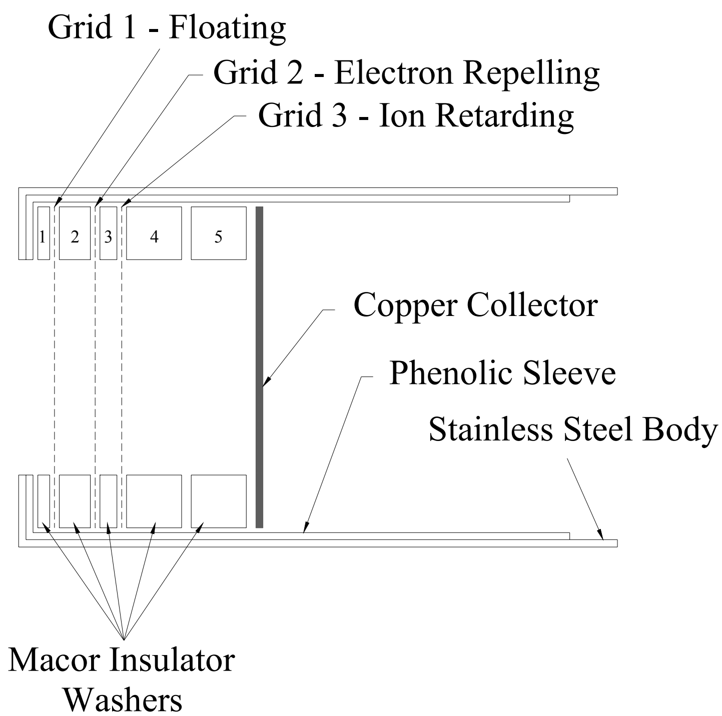

Figure 2-10: Schematic of the retarding potential analyzer (RPA).

During operation, grid 1 is allowed to float in order to provide a non-perturbing interface between the probe and the plasma while a laboratory power supply is used to bias the second grid 30 volts below ground to repel electrons. Grid 3 is swept from 0 to 600 volts relative to ground using a sourcemeter. The resulting current to the collector is measured using a picoammeter and the entire data acquisition routine is controlled by a computer running Labview software.

One factor that is not taken into account in the present implementation of this diagnostic is secondary electron emission from the copper collector. In theory, the variable SEE yield of the collector material as a function of ion impact energy could cause an overestimate of the fraction of ions occurring at energies for which the SEE yield of copper is high. Fortunately, for impact energies below 1 keV, the SEE yield of copper is less than 0.1 electrons per ion.[48] Considering the low secondary electron emission expected from the copper collector, as well as the relatively narrow ion velocity distributions in the Hall thruster plume, this potential source of error is thought to be negligible in the present case. This claim is supported by previous, unpublished tests with this instrument, which included the addition of an electron suppression grid upstream of the collector (between washers 4 and 5 in Fig. 2-10). This grid was biased below ground such that secondary electrons were reflected back to the collector. Successive tests with and without the suppression grid in place yielded no discernible change in the measured data.[49] In the study presented in this dissertation, the suppression grid was omitted in order to maximize the open area fraction of the grid system and ensure an adequate signal to noise ratio at the low current densities present in the far-field plume of the BHT-200.

RPA data are processed by fitting a cubic spline to the raw data and using 11 point box smoothing in order to reduce numerical noise. The resulting spline is then numerically differentiated to obtain the ion energy per charge spectrum. Figure 2-11 shows a sample fit along with the raw data and the resulting voltage spectrum. At each location, multiple traces were taken to verify the repeatability of the obtained spectra. Figure 2-12 shows the results of three separate data traces taken at the same location and demonstrates the excellent repeatability exhibited by this diagnostic. The traces shown in Figs. 2-11 and 2-12 were taken 0.5 m downstream of thruster 3, 5º off centerline.

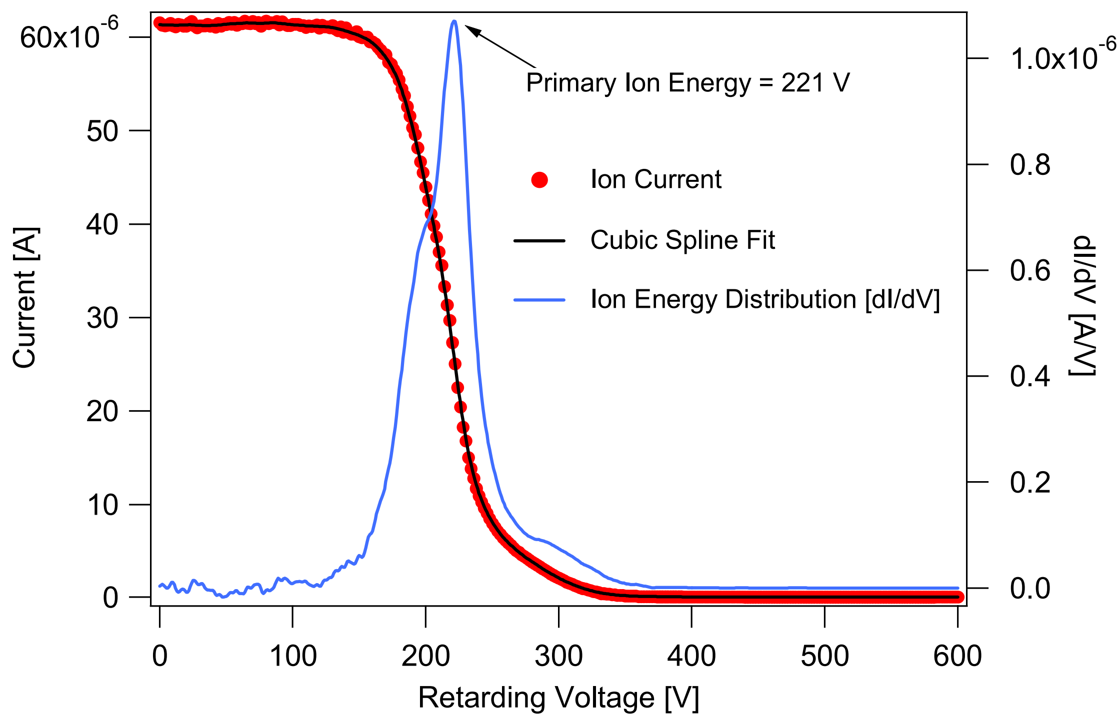

Figure 2-11: Sample RPA raw data, a cubic spline fit, and the resulting ion voltage distribution.

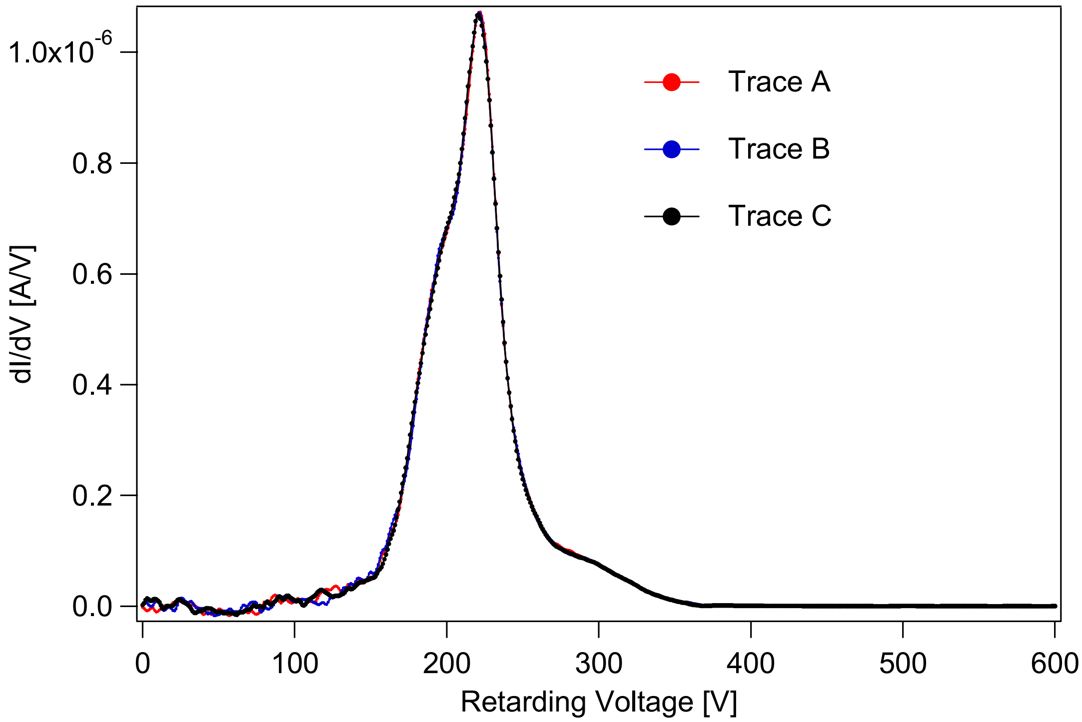

Figure 2-12: Multiple RPA data traces taken at the same location. Note the excellent repeatability.

2.7 Parallel-Plate Electrostatic Energy Analyzer

The second instrument used in this work to study the plume ion energy spectra was a 45° parallel-plate electrostatic analyzer (ESA). The operation of an ESA can be explained with the help of Fig. 2-13. The device consists of two parallel plates separated by a distance, d. One of the plates is electrically grounded while the other is biased to a positive potential, V_R, to reflect ions admitted through a slit in the grounded base plate. Ions entering the area between the plates experience a constant electric field of magnitude V_R/d in the Y direction shown in Fig. 2-13. The X and Y equations of motion for the admitted ions can then be written as Eqns. 2-18 and 2-19, respectively.

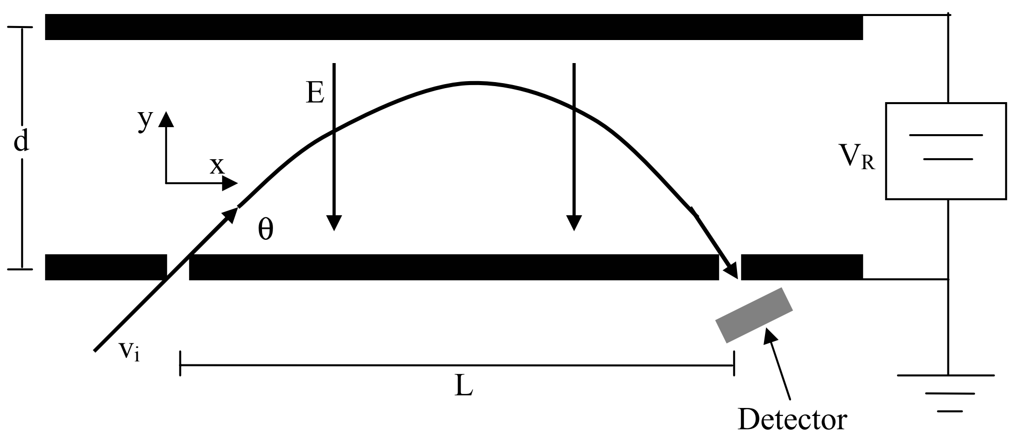

Figure 2-13: Schematic of parallel-plate energy analyzer operation.

$$m_i \frac{d^2 x}{dt^2} = 0 \qquad \textbf{Eqn. 2-18}$$

$$m_i \frac{d^2 y}{dt^2} = -\frac{q_i e V_r}{d} \qquad \textbf{Eqn. 2-19}$$

Integrating Eqns. 2-18 and 2-19 twice, eliminating the time variable, and applying the boundary conditions dictated by the ion injection angle, θ, allows the ion trajectory to be written as Eqn. 2-20, where the spatial coordinates are measured from the inlet slit. Since only ions exiting the second slit (at x=L, y=0) are collected by the detector, the equivalent voltage of the collected ions can be correlated with the dimensions of the device and the voltage applied to the repelling plate as given by Eqn. 2-21. In Eqn. 2-21, the ion injection angle has been taken to be 45° and the ion voltage has been defined as the ion kinetic energy per unit charge as was the case for the RPA discussed in the previous section.

$$y = x\tan(\theta) - \frac{q_i e V_r x^2}{2 m_i v_i^2 d \cos^2(\theta)}$$ **Eqn. 2-20**

$$V_i = \frac{L}{2d} V_R = K_{45} V_R$$ **Eqn. 2-21**

The resulting current to the detector can be expressed as the sum of the currents associated with ions of various charge states as given by Eqn. 2-22. The current due to each component can, in turn, be written as Eqn. 2-23, where q_j is the charge multiple of each ionic species. Summing the components of Eqn. 2-23, explicitly calculating the factors involving charge state raised to the 3/2 power, and combining constants into a single factor, k, allows the current to be written according to Eqn. 2-24, where we have introduced the charge state fractions defined by Eqn. 2-25. Finally, we note that the ion density at a given voltage, $n_i(V_i)$ is just the ion energy per charge distribution. Assuming that the term in brackets in Eqn. 2-24 is constant at a given location allows the ion voltage distribution to be expressed directly in terms of the collected current and the ion voltage as in Eqn. 2-26. It must be pointed out that use of Eqn. 2-26 amounts to implicitly assuming that the charge state fractions are independent of the ion voltage. In situations where the fractions change significantly as a function of voltage, the energy per charge distribution would need to be modified by the bracketed term in Eqn. 2-24 where the charge state fractions would be specified at each value of ion voltage.

$$I_C = \sum_j I_j$$ **Eqn. 2-22**

$$I_j = A_c n_j(V_i) v_j q_j e = A_c n_j(V_i) q_j^{3/2} e^{3/2} \sqrt{\frac{2V_i}{m_i}}$$ **Eqn. 2-23**

$$I_C = k\sqrt{V_i}\, n_i(V_i)\left[\alpha_1 + 2.83\alpha_2 + 5.20\alpha_3 + \ldots\right]$$ **Eqn. 2-24**

$$\alpha_j \equiv \frac{n_j}{\sum_k n_k}$$ **Eqn. 2-25**

$$f(V_i) \propto \frac{I_C}{\sqrt{V_i}}$$ **Eqn. 2-26**

Several ESAs of varying sizes have been used to study electric propulsion devices both at the University of Michigan and elsewhere.[47,50,51,52,53] The instrument used for the measurements in this dissertation is very similar in size to one used successfully by Pollard, *et al.*, to study a Hall thruster plume.[53] The main body of the ESA consists of a cube constructed of mica dielectric and measuring approximately 300 mm (12”) in each dimension. A dielectric material was chosen to reduce the disturbance to the plasma plume compared to that caused by the more common grounded devices. The inner surfaces of the box are coated with grounded aluminum foil to prevent charge accumulation within the instrument. Vent slots have been machined into the mica box to prevent an elevated pressure from occurring inside the device and causing collisions that would adversely influence the measurements. Grounded aluminum baffles prevent ions from entering through the vent holes while allowing neutral atoms to escape.

The parallel plates are constructed of 1.588 mm (0.0625") thick aluminum and are separated by a distance of 76.2 mm (3.0"). The rectangular slits in the base plate measure 1.5 x 15 mm (0.06" x 0.6") and are 152.4 mm (6.0") apart. Two field correction electrodes are placed between the main plates and biased by resistor strings to reduce the adverse effects of fringing electric fields. The field correction electrodes can be seen in Fig. 2-14, which shows the results of a computer simulation conducted using the software program Simion. The red arcs in Fig. 2-14 depict the trajectories of ions having various energy to charge ratios. Note that only ions of a specific voltage pass through the exit slit to be collected by the detector. The detector in this case is a steel disc, which was coated with tungsten in order to minimize secondary electron emission. A material with varying secondary electron emission characteristics over the range of ion energies studied could potentially skew the energy per charge spectra measured by the ESA by causing an inordinately high current to be collected at energies for which the SEE yield of the material is high. Fortunately, the SEE yield of tungsten due to impacting xenon ions is low (<0.04 electrons per ion for Xe^+) and nearly constant over the energy range of interest to the present study.[54] Figure 2-15 shows the completed ESA installed in the vacuum chamber along with the RPA and both the gridded and nude Faraday probes.

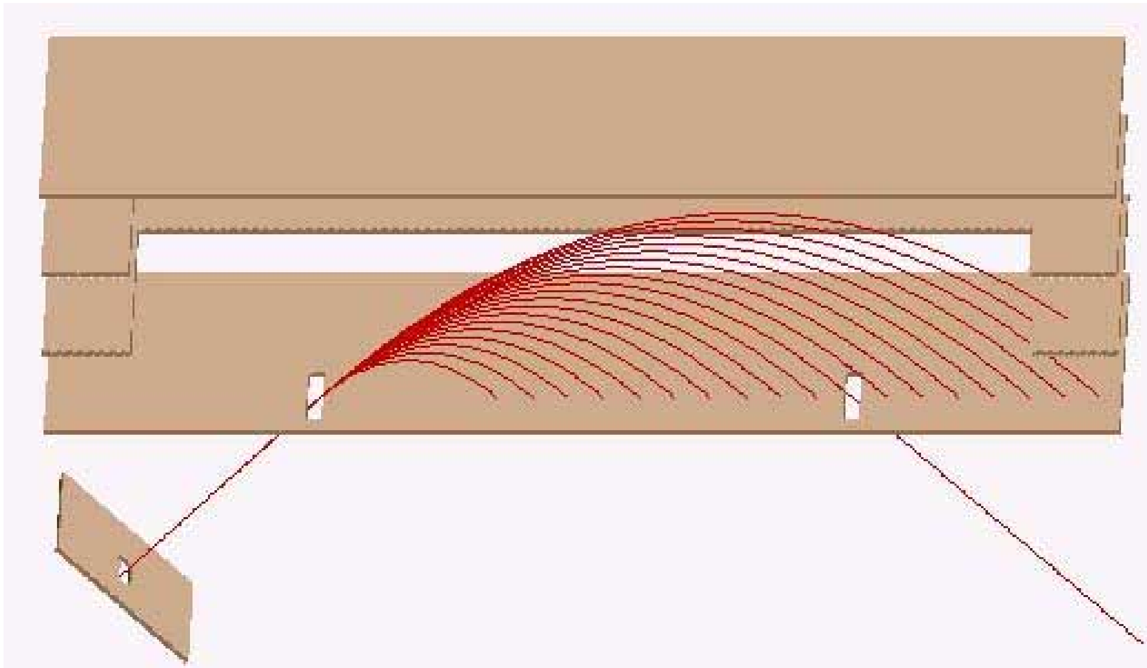

Figure 2-14: Simulation results showing the dispersion of ions with different energy to charge ratios within the ESA.

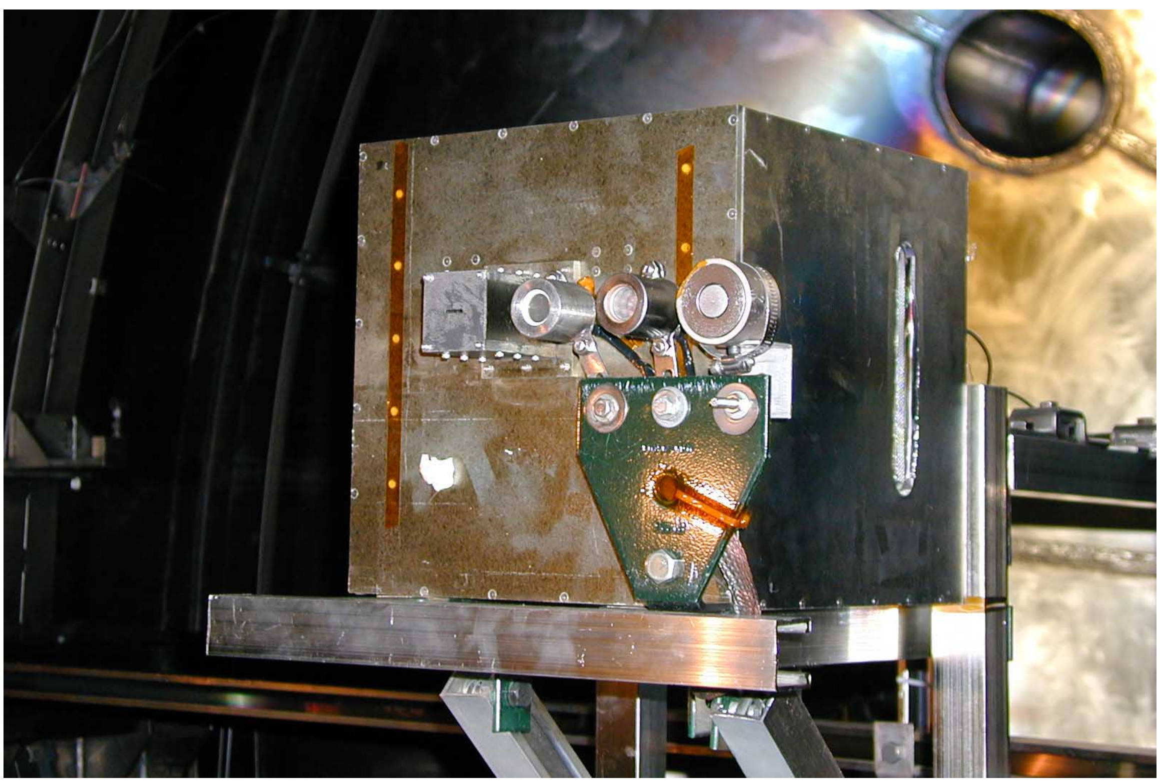

Figure 2-15: The parallel-plate energy analyzer installed in the vacuum chamber along with (from left to right) the RPA, the gridded Faraday probe, and the nude Faraday probe.

During data collection, the repelling plate voltage, V_R, was swept from 0 to 600 volts using a sourcemeter. The ion current collected at the detector was measured using a picoammeter. Both the plate voltage and the collected current were recorded by a PC running Labview software. Multiple ESA traces were obtained at each data point to verify the repeatability of the collected data. Figure 2-16 shows two sets of data collected 5° off centerline for a single thruster. Note the very good repeatability of the traces, particularly at ion energies above 100 volts.

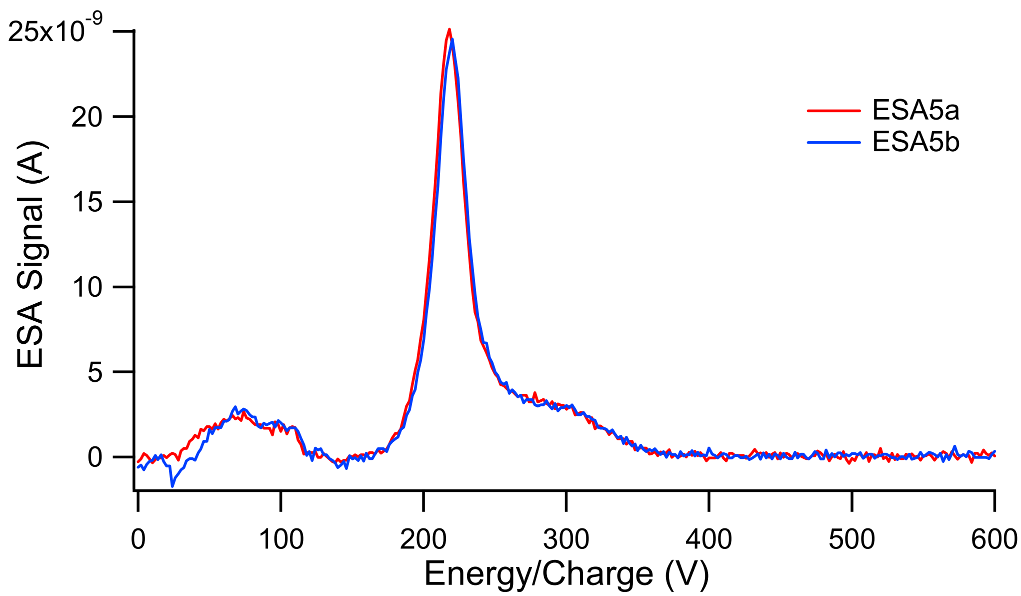

Figure 2-16: Two ESA traces recorded under identical conditions. Note the very good repeatability of the data.

It has been pointed out that the ion voltage distributions measured by both the ESA and RPA can be affected by the plasma potential at the location where the plume is sampled, thus causing the measured spectra to be shifted to higher voltages.[55] In the current experiments however, the measurements were taken at a distance of 0.5 meters from the thrusters where the plasma potential is sufficiently low (< 5 volts) so as to be negligible in its effect on the measured ion voltage spectra.

2.8 ExB Probe

As pointed out in the previous two sections, both the RPA and ESA are unable to distinguish between ions of different charges. One diagnostic that can be used to garner information about the charge state fractions in the plasma plume is an ExB probe, also commonly referred to as a Wien filter.[56] This device takes advantage of the well-known Lorentz force given by Eqn. 2-27, which shows the force on a moving ion due to both electric and magnetic fields. As the name implies, the ExB probe employs crossed electric and magnetic fields that are mutually perpendicular to the ion velocity vector as depicted in Fig. 2-17. This configuration results in a situation where only ions for which the Lorentz force vanishes are able to pass through the crossed field region and reach the collector. The velocity of the collected ions, v_{coll}, is thus related to the magnitude of the electric and magnetic fields through Eqn. 2-28.

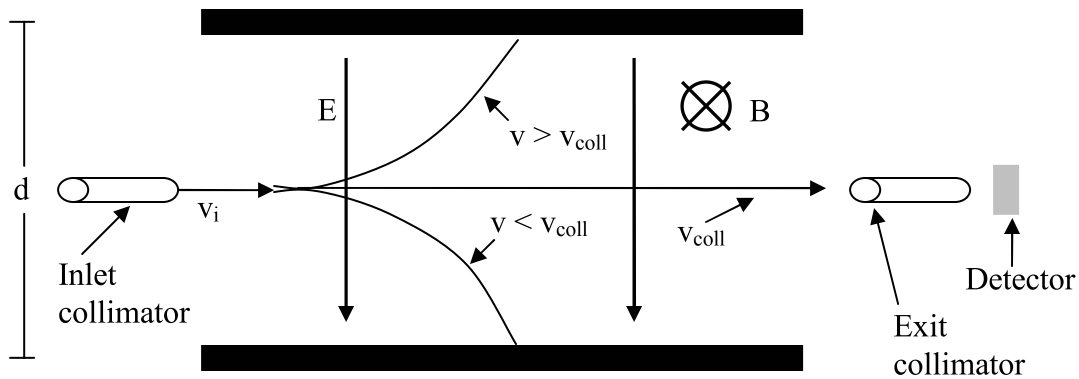

Figure 2-17: Operation of an ExB probe. Only ions of a selected velocity reach the detector.

$$\vec{F} = q_i e\left(\vec{E} + \vec{v}_i \times \vec{B}\right) \qquad \textbf{Eqn. 2-27}$$

$$v_{coll} = \frac{E}{B} \qquad \textbf{Eqn. 2-28}$$

As Eqn. 2-28 shows, the ExB probe acts purely as a velocity filter and the criterion determining whether or not an ion is detected is therefore independent of ion mass and charge state. This allows the charge state fractions to be determined by considering the relationship between ion velocity and voltage given by Eqn. 2-29, which can be combined with Eqn. 2-28 (for the collected particles) to provide an equation relating an ion's voltage and charge state to the probe voltage at which it will be detected. This relationship is shown in Eqn. 2-30 where the magnitude of the electric field has been replaced by the voltage between the electrodes of the ExB probe, V_{ExB}, divided by the distance between them. Since the ion voltage distribution in a Hall thruster plume is generally only a few tens of volts wide, multiply-charged ions will appear as distinct populations centered around a probe voltage of approximately $(q_i)^{1/2}$ times the probe voltage at which singly-charged ions are detected.

$$v_i = \sqrt{\frac{2q_i e V_i}{m_i}} \qquad \textbf{Eqn. 2-29}$$

$$V_{ExB} = Bd\sqrt{\frac{2q_i e V_i}{m_i}} \qquad \textbf{Eqn. 2-30}$$

The ExB probe used in this study was originally designed and built by Kim.[56] The magnetic field in this device is supplied by four ceramic permanent magnets. The resulting magnetic field strength in the crossed-field region averages 0.162 Tesla and the variation along the length of the device is less than 10%.[56] The electric field is applied between two rectangular aluminum electrodes measuring 27.9 x 3.8 cm and separated by a distance, d, of 1.90 cm. The current configuration differs from the one used by Kim in that the diameter of the inlet and exit drift tubes have been increased to improve the strength of the collected signal and increase the size of the imaged area. This change comes at the cost of probe resolution, which can be characterized by the degree to which an ion's theoretical collection voltage can vary from the applied one and still be detected. This parameter is given by w in Eqn. 2-31 and implies that ions with $V_{ExB} \pm w$ will be detected at a probe voltage of V_{ExB}.[56] The geometric properties used in Eqn. 2-31 are defined in Table 2-3 and the values used for the measurements described in this dissertation are included there as well. The geometry reflected in Table 2-3 results in an acceptance cone half angle of approximately 3.1 degrees and a probe resolution (in voltage) of approximately 2% for 200 volt ions.

$$w \le \frac{V_i d}{Z_f}\left(\frac{a_1 + a_2}{Z_c} + \frac{a_3 + a_4}{Z_M}\right)$$ **Eqn. 2-31**

Parameter	Symbol	Value
Diameter of Inlet Collimator Entrance	a_1	6.5 mm
Diameter of Inlet Collimator Exit	a_2	10.0 mm
Diameter of Collector Collimator Entrance	a_3	8.7 mm
Diameter of Collector Collimator Exit	a_4	8.7 mm
Length of Inlet Collimator	Z_c	152.4 mm
Distance Between Collimators	Z_f	254.0 mm
Length of Exit Collimator	Z_M	152.4 mm
Distance Between Electrodes	d	190 mm

Table 2-3: Relevant geometric properties determining the voltage resolution of the ExB probe.

The electrodes in the ExB probe are biased at equal voltages above and below ground by a Keithley sourcemeter and the circuit shown in Fig. 2-18. Ions that successfully traverse the crossed electric and magnetic fields are collected by a tungsten plate. A picoammeter records the current to the plate, which is given by Eqn. 2-32 for each species, where γ_j is the secondary electron emission coefficient given in electrons per ion.[57] Over the range of ion energies found in the Hall thruster plume, the secondary electron yield of tungsten has been reported to be 0.018, 0.216, and 0.756, for Xe^+, Xe^{2+}, and Xe^{3+}, respectively.[58]

$$I_j = A_c q_j e n_j u_j (1 + \gamma_j) = A_c q_j e n_j (1 + \gamma_j)\sqrt{\frac{2 e q_j V_i}{m_i}}$$ **Eqn. 2-32**

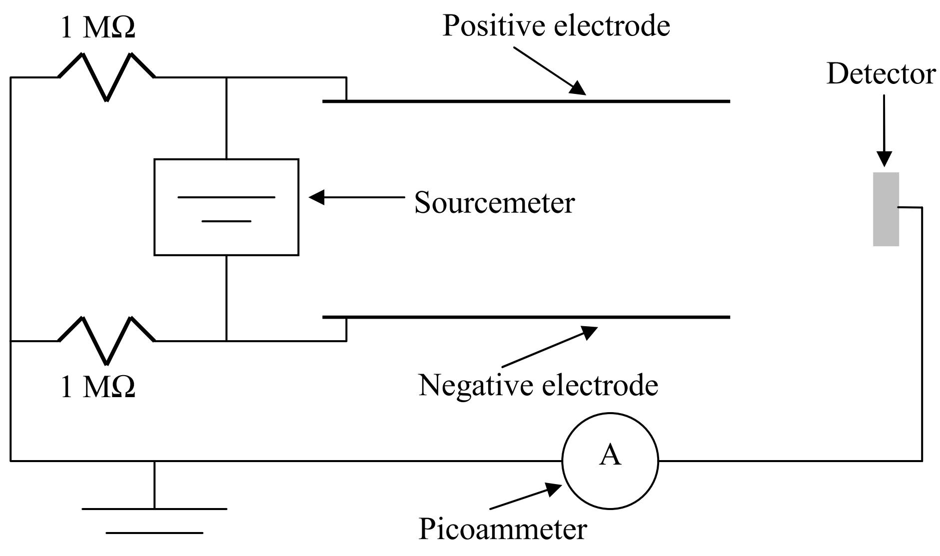

Figure 2-18: ExB probe circuit.

The current associated with each charge state, I_j, is equal to the area under the corresponding peak depicted in the sample ExB probe trace shown in Fig. 2-19. Determining the area under each curve is challenging due to the overlap that occurs between the various peaks. For example, the population visible between about 50 and 60 volts in the sample data of Fig. 2-19 is likely to contain contributions from both singly- and doubly-charged ions.

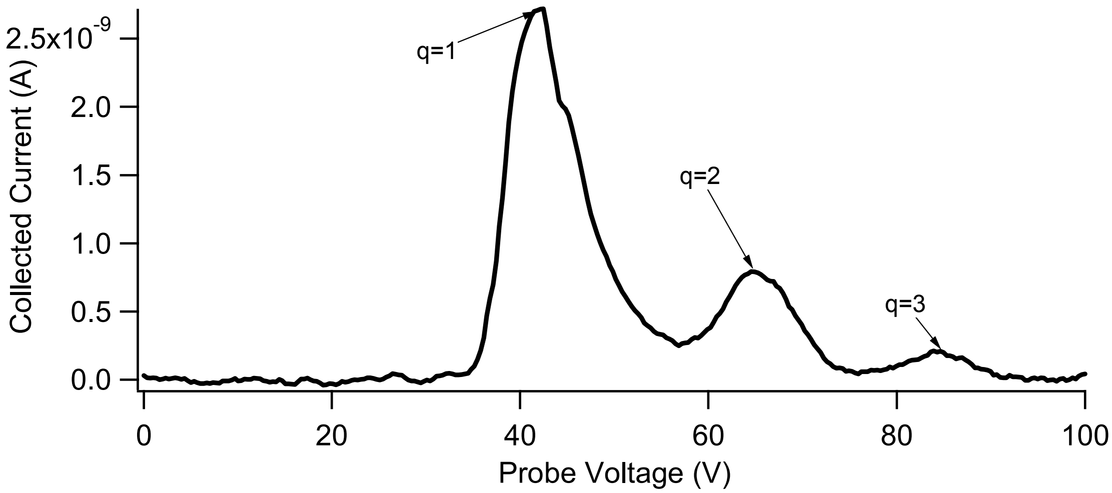

Figure 2-19: Sample ExB data showing the peaks due to various charge species.

One method that is sometimes used to estimate the current due to each species is to assume that it is proportional to the height of the corresponding peak in the probe trace. While this method avoids the ambiguity associated with the overlapping distributions, it is inherently flawed. The source of this flaw is illustrated by the following simple example. Consider a number of ions, N, originating with zero velocity in an area of potential gradient centered around ϕ such that the ion population is equally distributed between $\phi-\Delta\phi$ and $\phi+\Delta\phi$. The ions then fall from the potential at which they originated to ground, thus gaining kinetic energy. The resulting ion velocity distribution is related to the original number of ions through Eqn. 2-33. Since we previously specified that all of the ions originated in a certain potential range, we can write the expression for N in the simpler form of Eqn. 2-34. In writing Eqn. 2-34, we have made use of the fact that the velocity distribution for our simple case is constant between the velocities v_{min} and v_{max}, which correspond to the velocities of ions accelerated through $\phi-\Delta\phi$ and $\phi+\Delta\phi$, respectively. Outside of this range, the condition $f_i(v)=0$ holds.

$$N = \int_{-\infty}^{\infty} f_i(v)dv \qquad \textbf{Eqn. 2-33}$$

$$N = c(v_{\max} - v_{\min}) = 2c\Delta v \qquad \textbf{Eqn. 2-34}$$

Since the velocity difference in Eqn. 2-34 depends on the charge state of the ions, it is helpful to write it explicitly as a function of the applied potential as shown in Eqn. 2-35. This equation clearly shows that Δv is proportional to the square root of the ion charge. Since the number of ions, N, is constant regardless of the charge carried by each particle, Eqn. 2-34 shows that c, which represents the height of the velocity distribution, must decrease in inverse proportion to Δv as the charge state q is increased. This phenomenon is illustrated graphically in Fig. 2-20, which shows the velocity distribution that occurs when a group of ions is accelerated through the potential drop described above. The three traces in Fig. 2-20 represent three different charge states. Clearly the heights of the distributions differ even though the areas under the curves are equal. In analogy to this example, methods that use the height of the current peak in an ExB probe trace to represent the area under the curve tend to underestimate the current attributable to multiply-charged ions. The result is a concomitant overestimate of the singly-charged ion fraction.

$$\Delta v = (v_{\max} - v_{\min}) = \sqrt{q}\left[\sqrt{\frac{2e}{m_i}}\left(\sqrt{\phi + \Delta\phi} - \sqrt{\phi - \Delta\phi}\right)\right] \qquad \textbf{Eqn. 2-35}$$

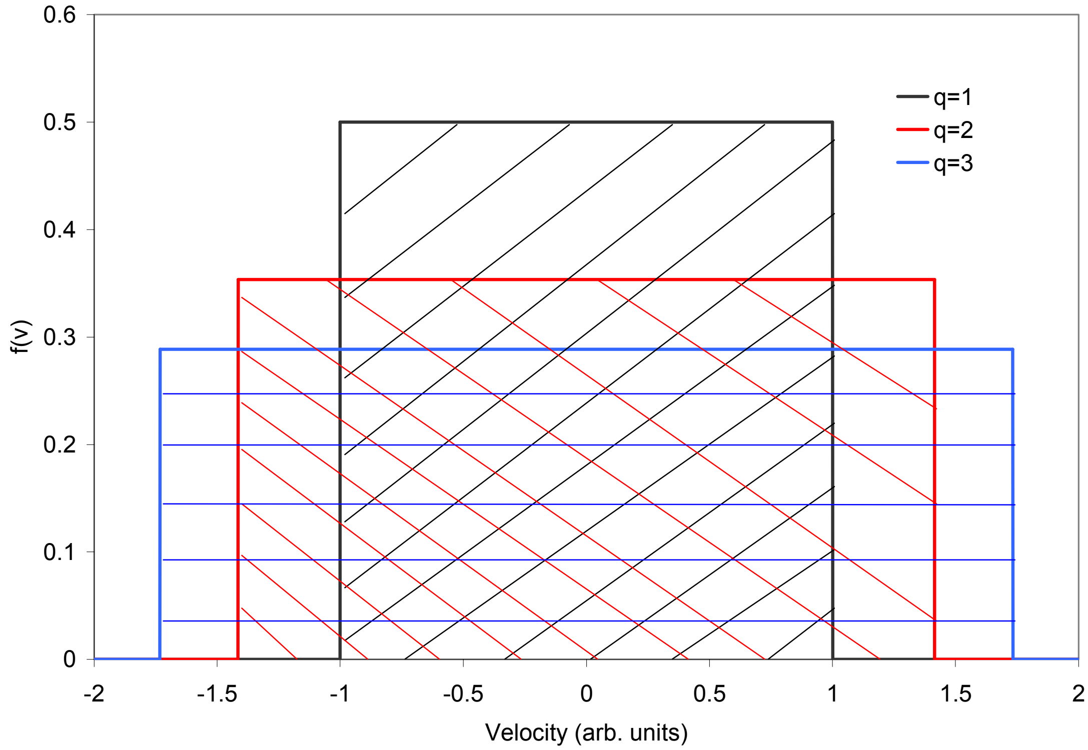

Figure 2-20: The velocity distributions resulting from ions of various charges accelerated through a range of potentials. Note that the height of the distributions varies as a function of charge state, but the product of the height and half-width remains constant for each species.

To avoid the inaccuracy discussed above, in the present work the current due to each species is taken to be proportional to the product of the peak height and the half width at half the maximum value (HWHM). Following the derivation of Hofer, *et al.*,[57] the measured current due to each species is then related to the corresponding current fraction through Eqn. 2-36. Substituting the expression in Eqn. 2-32 and the definition of the species fraction given by Eqn. 2-25, the measured current fractions can be related to the species fractions by Eqn. 2-37. Evaluating Eqn. 2-37 for each species and applying the condition stated in Eqn. 2-38 yields the charge state fractions.

$$\Omega_j = \frac{I_j}{\sum_j I_j}$$ **Eqn. 2-36**

$$\alpha_j = \frac{\Omega_j \sum_j \left[q_j^{3/2} \alpha_j \left(1+\gamma_j\right)\right]}{q_j^{3/2}\left(1+\gamma_j\right)}$$ **Eqn. 2-37**

$$\sum_j \alpha_j = 1$$ **Eqn. 2-38**

It should be pointed out that the derivation of Eqn. 2-37 requires an important, yet rarely noted, assumption. Namely, it was assumed that the $(V_i)^{1/2}$ term is constant for all charge states, as evidenced by the use of a single ion voltage, V_i, rather than a separate V_j for each species in Eqn. 2-32. This assumption is correct if all ions, regardless of charge state, are created at the same location in the thruster discharge chamber, accelerated through the same potential drop, and allowed to reach the probe without experiencing CEX collisions in the plume. For some unknown fraction of ions, however, this scenario may not be the correct one. For example, consider two ions, one with charge $q_1=1$ and the other with $q_2=2$, formed at the same location in the discharge chamber. Upon exiting the thruster, these ions would have the same energy to charge ratio, V_i, and their velocities would differ by a factor of $2^{1/2}$, as accounted for by the derivation above. If the doubly-charged ion now undergoes a CEX collision and becomes singly-charged, it will still reach the probe with its original velocity even though it now only carries a single charge. Since the ExB probe acts purely as a velocity filter, this ion would be "counted" as a doubly-charged ion. In other words, the charge state fractions derived from ExB probe data are really more closely related to the charge states of ions as they are accelerated through the electrostatic potential drop rather than the local species fractions that exist at the probe location. The distinction is probably not important for diagnosis of a single thruster, since ExB probes have been used successfully for this purpose in the past.[56, 57] In the case of a cluster, however, it must be noted that any changes in charge state that occur in the plume as a result of operating multiple thrusters cannot be detected by this instrument.

2.9 Current Interrupt Switch

The final device used in this study was a current interrupt switch similar to one discussed by Prioul, *et al.*[59] This switch represents a simple and effective method of studying both the transient response of a single thruster and the cross-talk between multiple thrusters of a cluster. The switch is used to open the discharge circuit for a specified time on the order of a few microseconds. Recording the discharge current of both the interrupted thruster and an adjacent one facilitates a search for perturbations to the surrounding thrusters, which would indicate cross-talk through either the plasma plume or the power circuit. This method was utilized in both the nominal configuration discussed in Chapter 4 and the alternative configurations presented in Chapter 5.

The circuit comprising the current interrupt switch is sketched in Fig. 2-21. The main component of the switch is a power field effect transistor (FET) wired in series with the discharge line. During normal operation, a 9 volt battery supplies the base current necessary to force the FET into a conducting mode and current flows freely through the FET to the anode. When a positive control signal is applied to the optocoupler shown in Fig. 2-21, however, the base (B) of the FET is shorted to the emitter (E) and conduction from the collector (C) to the emitter stops, thus deactivating the FET and preventing current flow to the anode. This process is depicted in Fig. 2-22 where a measured trigger control signal is shown along with the resulting current through the attached thruster. Note that when the control signal goes high in Fig. 2-22, the thruster discharge current drops to zero. Using an optocoupler to control the FET allows the control signal to come from a pulse generator referenced to ground, while the rest of the circuit floats near the thruster discharge voltage. The pulse generator used for the tests reported here was the Stanford Research Systems model DG535, and the switch allowed discharge current interruptions as short as 5 microseconds.

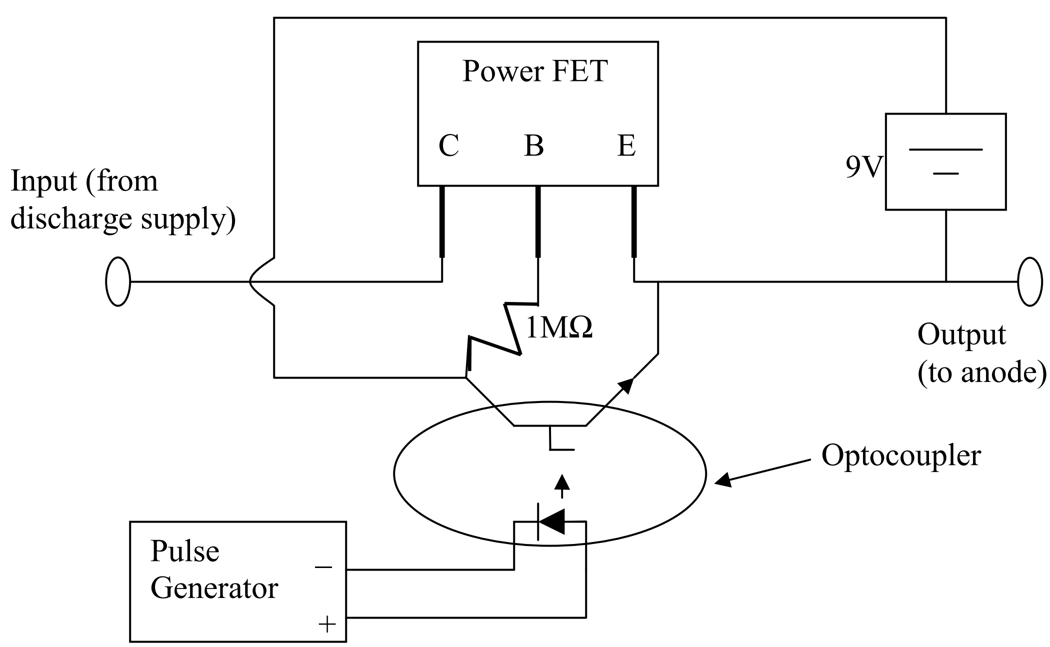

Figure 2-21: Circuit comprising the discharge current interrupt switch. The switch is connected in series with the anode power line and the cathode line is unaffected.

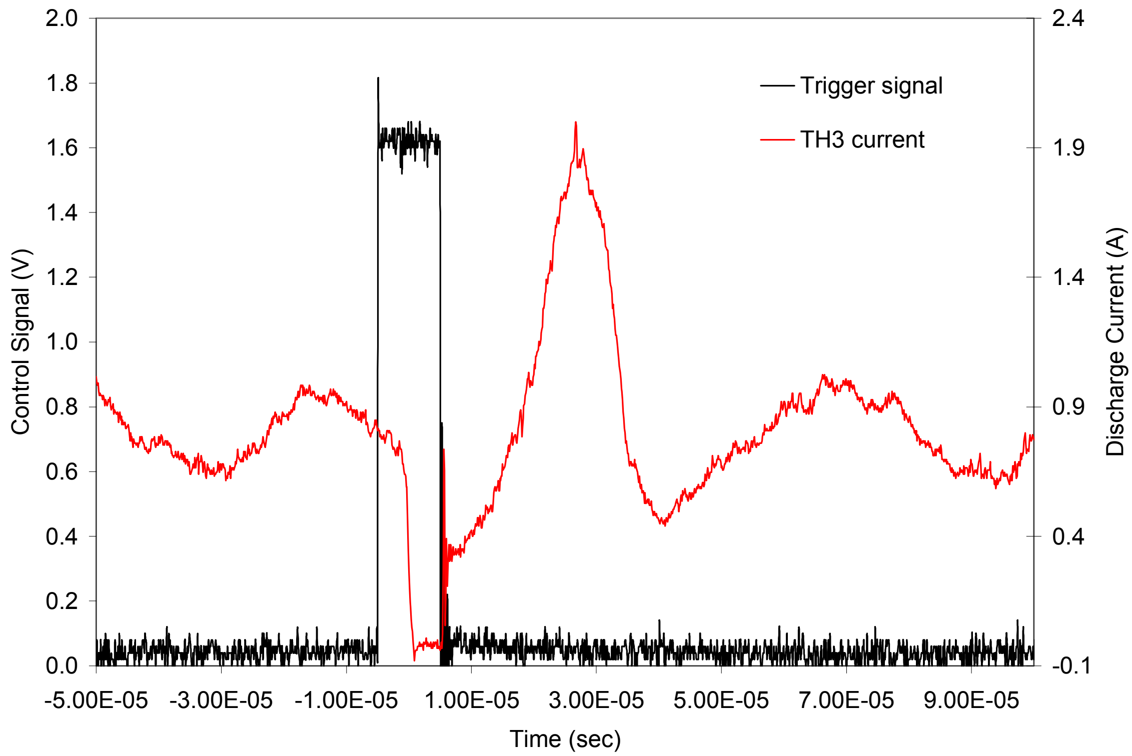

Figure 2-22: Sample data showing the operation of the current interrupt switch. Note that application of a positive trigger signal deactivates the FET and causes the thruster discharge current to drop to zero.

2.10 Vacuum Facilities

The experiments described in this dissertation were conducted in two separate vacuum facilities. The first was Chamber 6 at AFRL, which measures 1.8 meters in diameter and 3.0 meters in length. Figure 2-23 shows the layout of Chamber 6. Also shown in this figure is the location of a three dimensional positioning system used to move probes throughout the plume. A rough vacuum is provided by a Stokes roughing pump and blower system. Final evacuation of Chamber 6 is accomplished using four single-stage APD cryopanels maintained at approximately 25 Kelvin and one two-stage APD cryopump maintained at roughly 12 Kelvin. This system provides a measured pumping speed of 32,000 liters per second on xenon.[60] A typical base pressure of 8×10^{-7} Torr has been measured using an MKS Model 910 Ionization Gauge. During thruster operation, the background pressure typically rises to 6.1×10^{-6} Torr for single-thruster operation and to 2.3×10^{-5} Torr for four-thruster operation. Both pressures are corrected for xenon. Of the various diagnostics described previously, the Langmuir probe, triple probe, Faraday probe, current interrupt switch, and emissive probe were all used in Chamber 6.

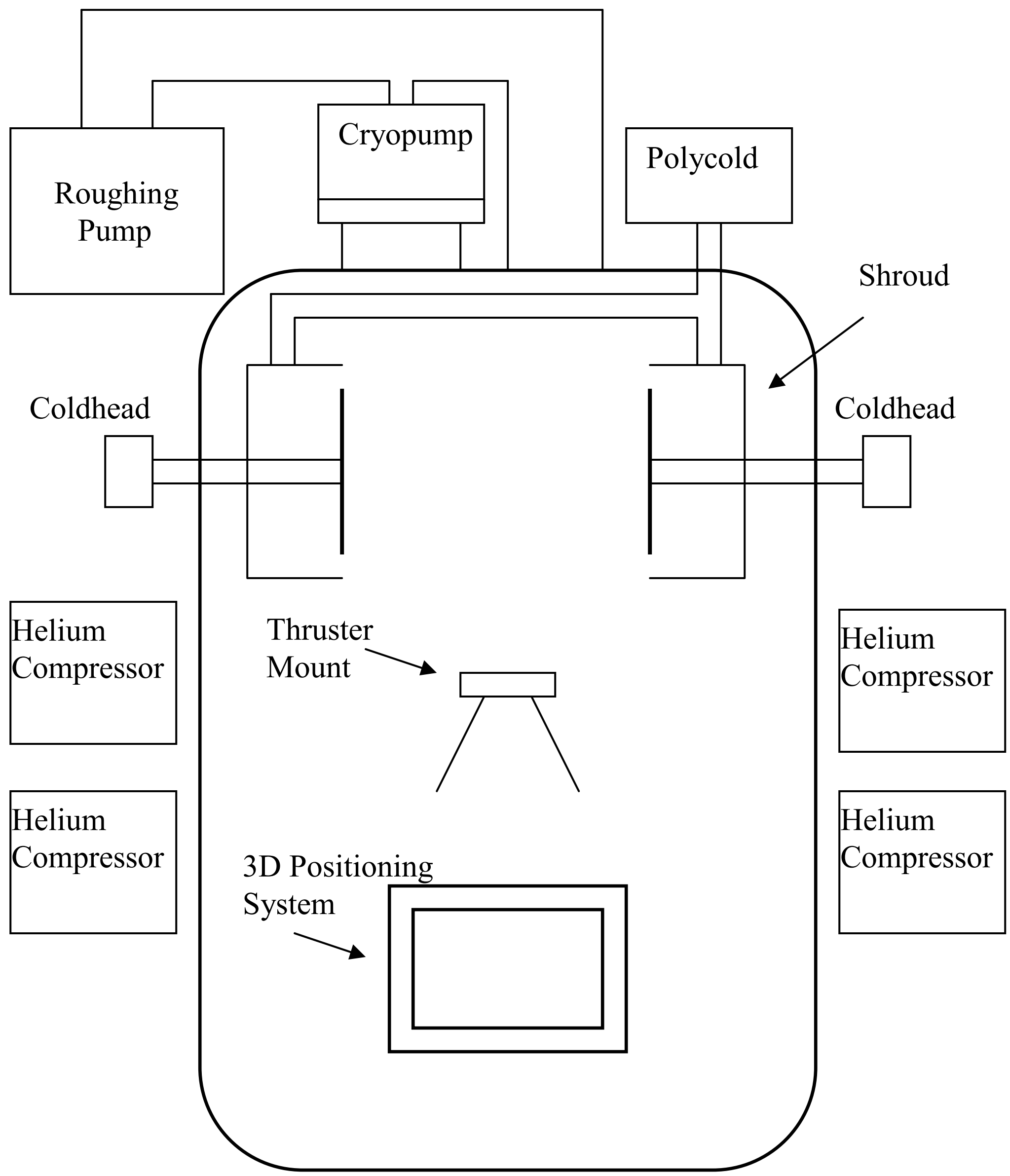

Figure 2-23: A sketch of Chamber 6 showing the locations of the pumping surfaces, thruster cluster, and probe positioning system.

The second chamber used for testing of the thruster cluster was the Large Vacuum Test Facility (LVTF) at the University of Michigan. The LVTF is a 6x9 meter, cylindrical, stainless steel clad vacuum chamber that is evacuated by seven CVI model TM-1200 cryopumps. The cryopumps provide a pumping speed of 500,000 liters per second on air and 240,000 liters per second on xenon for typical base pressures of approximately 2.5×10^{-7} Torr. For the experiments described here, only four cryopumps were used, thus resulting in chamber pressures of 1.1×10^{-6} and 3.6×10^{-6} Torr (corrected for xenon) during single- and four-thruster operation, respectively. The instruments used in this chamber include the ESA, RPA, ExB probe, triple probe, emissive probe, and both the nude and gridded Faraday probes. Figure 2-24 shows a sketch of the LVTF layout. The thruster positioning system allows linear motion in both horizontal axes and rotation about the vertical axis.

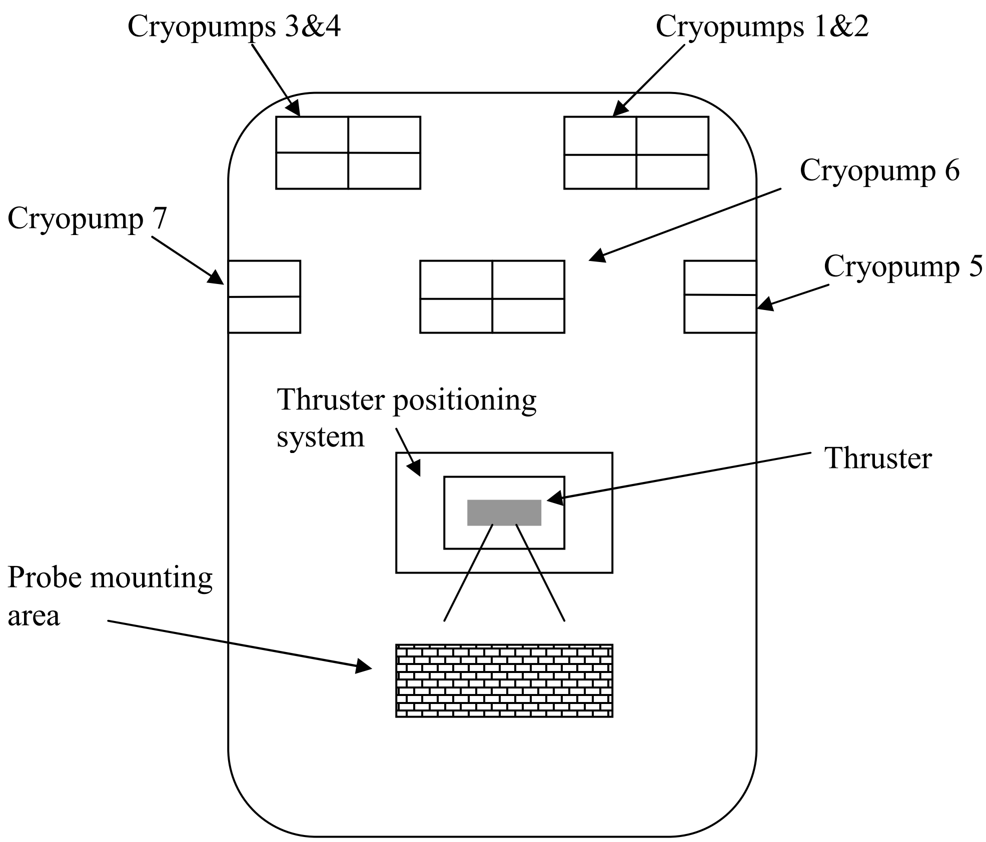

Figure 2-24: The layout of the Large Vacuum Test Facility at the University of Michigan.

3. SINGLE THRUSTER CHARACTERIZATION

Before studying the effects of clustering multiple thrusters on plasma plume properties, it is first necessary to examine the properties of a single thruster to establish a baseline from which clustering may cause perturbations. This chapter presents a thorough characterization of a single BHT-200 Hall thruster using the diagnostic techniques described in Chapter 2. Throughout this discussion, special emphasis is placed on unexpected properties observed along the engine centerline, and a possible explanation for these properties is discussed at the end of this chapter.

3.1 Discharge Current Characteristics

One of the most fundamental properties of a Hall thruster is the character of the discharge current. In the present case, the discharge current of a single BHT-200 was recorded using a Tektronix TDS 3012 oscilloscope and a TCP 202 current probe capable of measuring signals with characteristic frequencies as high as 50 MHz. Figure 3-1 shows two sample discharge currents, one of which was taken immediately after starting the thruster. The other was taken after the initial large-amplitude oscillations had decreased in magnitude to their steady-state value where departures from the nominal current (0.80 amps) were generally less than 10%. The initial large-amplitude oscillations were almost certainly due to water vapor desorption from the ceramic insulator in the thruster discharge channel, as evidenced by the fact that they only appeared after the thruster was exposed to atmospheric conditions.[61] This "startup phenomenon" is therefore of little concern to the on-orbit operation of Hall thrusters.

The characteristic frequency of both traces shown in Fig. 3-1 is approximately 25 kHz. This is consistent with the appearance of low-frequency oscillations noted in other thruster discharges and may be due to the so-called "breathing" mode resulting from unsteady ionization or azimuthally propagating density fluctuations.[62] While these oscillations represent an interesting field of study in their own right, they have been well characterized by other authors.[61,62] The present investigation is concerned with them only to the extent that they may be affected by multi-thruster operation thereby influencing cluster operation and the design requirements of power processing units. To study this, the traces shown in Fig. 3-1 will be compared to similar data recorded during cluster operation in Chapters 4 & 5.

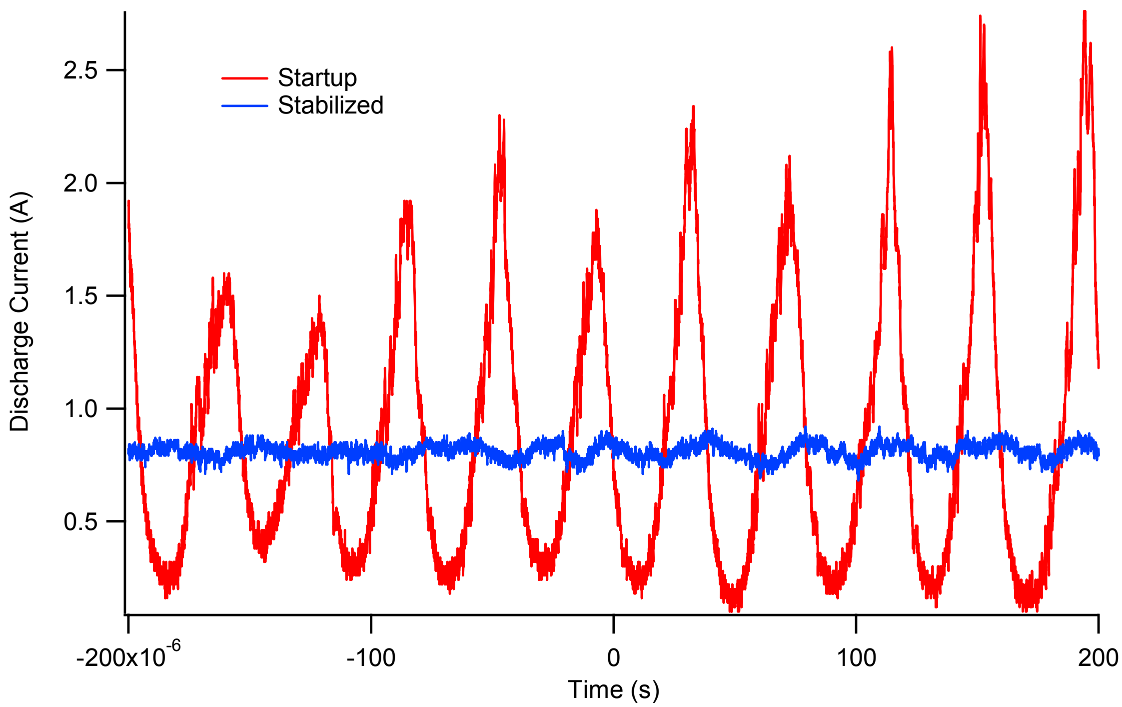

Figure 3-1: Discharge current characteristics of the BHT-200.

In addition to merely recording the natural oscillations of the discharge current, the current interrupt switch discussed in Chapter 2 was used to disrupt the current to the thruster anode for a short period of time while the response was recorded using the oscilloscope. The transient characteristics of the discharge are shown in Fig. 3-2 for two different values of disruption duration. When the current is switched back on, these data show a large overshoot in the current before it returns to its nominal value with the characteristic oscillation frequency of about 25 kHz. The magnitude of the current overshoot increases with increasing disruption time. This behavior is consistent with the trends observed by previous authors and is believed to be attributable to rapid ionization of neutrals that accumulate in the discharge channel during the current disruption.[63] Note the excellent repeatability of the traces recorded with a 10 microsecond interruption. This repeatability provides a second way of checking for interactions between thrusters because, in addition to disrupting the current to one thruster and checking for changes in the current characteristics of adjacent thrusters, it is also possible to determine whether the presence of the adjacent thrusters affects the response of the disrupted thruster. These effects are sought in the cluster data presented in Chapters 4 & 5.

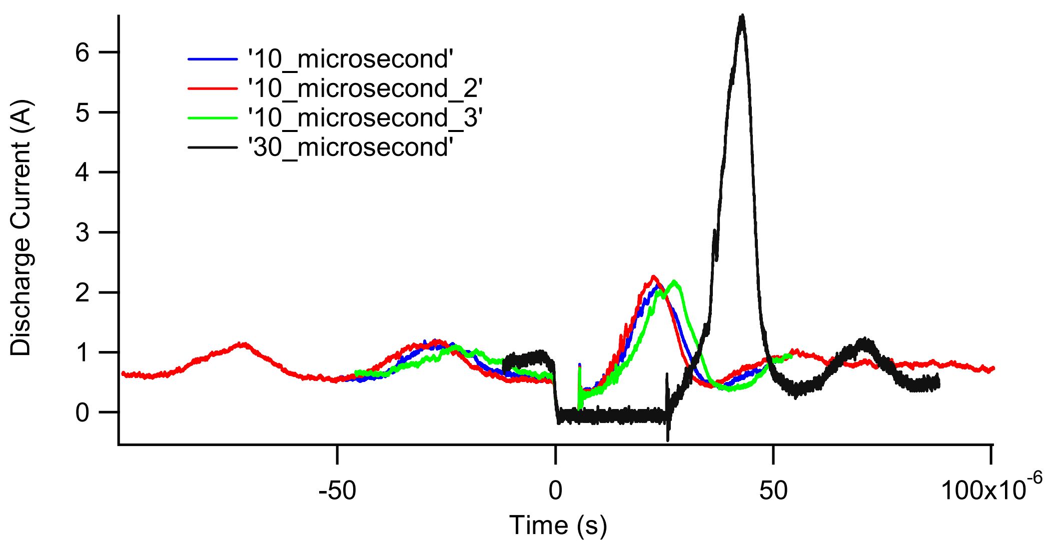

Figure 3-2: Response of the thruster discharge current to externally driven interruptions.

3.2 Plasma Density

The plasma density in the far-field plume of a single thruster was measured at 5 mm intervals using both the large triple probe and the Langmuir probe. Results of these measurements are shown in Figs. 3-3 and 3-4, respectively. Note that the density contours displayed in these figures are distributed exponentially rather than linearly for clarity. Also note that the coordinate system referenced in these plots is not the global system described previously but a local coordinate system whose origin is located at the intersection of the thruster centerline and exit plane.

Both Figs. 3-3 and 3-4 show a well-defined jet structure with a peak density near the thruster centerline. The plasma density is high near the thruster centerline and decreases rapidly in both the axial and transverse directions as the plume expands. The values of measured plasma density differ somewhat between the triple probe and the Langmuir probe with the triple probe showing consistently higher number densities. The peak density recorded by the triple probe was about 1.2×10^{18} m^{-3} while the Langmuir probe peaked at approximately 7.0×10^{17} m^{-3}. Although these variations are significant, they are within the 50% absolute uncertainty stated previously. The agreement between the diagnostics and the consistent shape of the profiles suggest that the values measured with the triple probe are valid to within the stated uncertainty. Due to the wider spatial range over which triple probe data were collected and the inherent ambiguity associated with Langmuir probe measurements, the results recorded with the triple probe are used for most of the analysis presented throughout the remainder of this chapter.

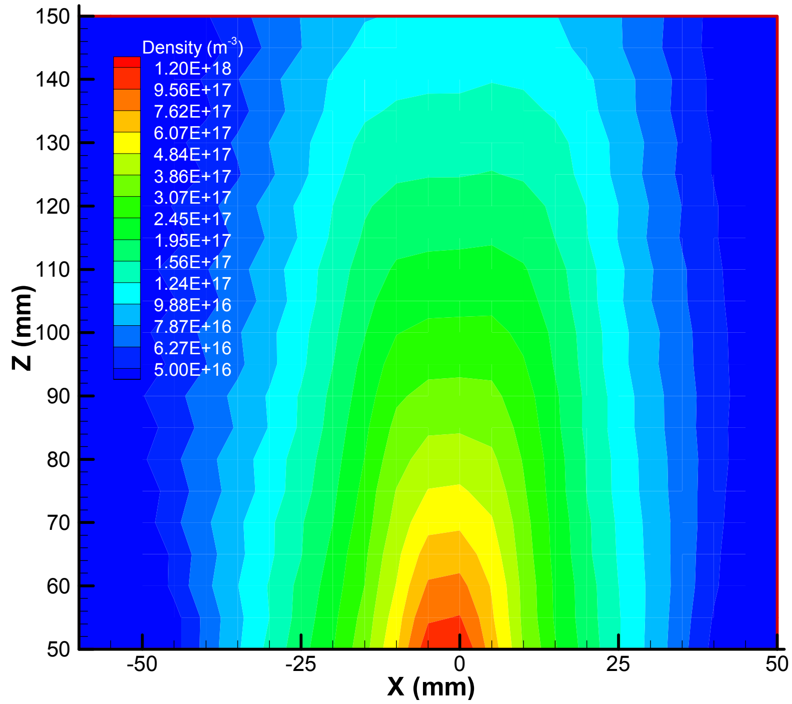

Figure 3-3: Plasma density in the far-field plume of a single thruster measured using a triple probe.

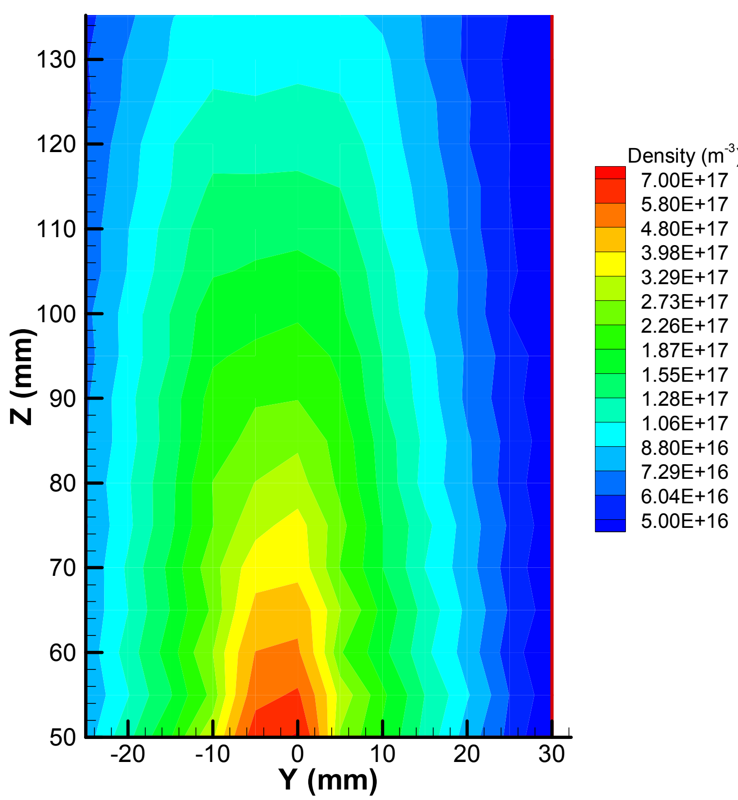

Figure 3-4: Far-field plasma density measured using a spherical Langmuir probe.

To study the processes occurring along the thruster centerline, measurements were taken in the near-field plume using both the large and small triple probe described previously. The data presented in Fig. 3-5 were taken at 2 mm intervals using the larger probe. Figure 3-6 shows measurements taken using the smaller probe at intervals of 1 mm in the X direction and 5 mm in the Z direction. As these figures show, the high density jet seen in the far-field data is very pronounced in the near-field and occurs in an area where a bright plasma core can be observed visually. This core is visible downstream of each thruster in Fig. 2-3. Although the densities measured by the two probes agree to within the 50% uncertainty mentioned previously, the results obtained using the smaller probe are believed to be more accurate for the reasons given in the next section regarding the electron temperature.

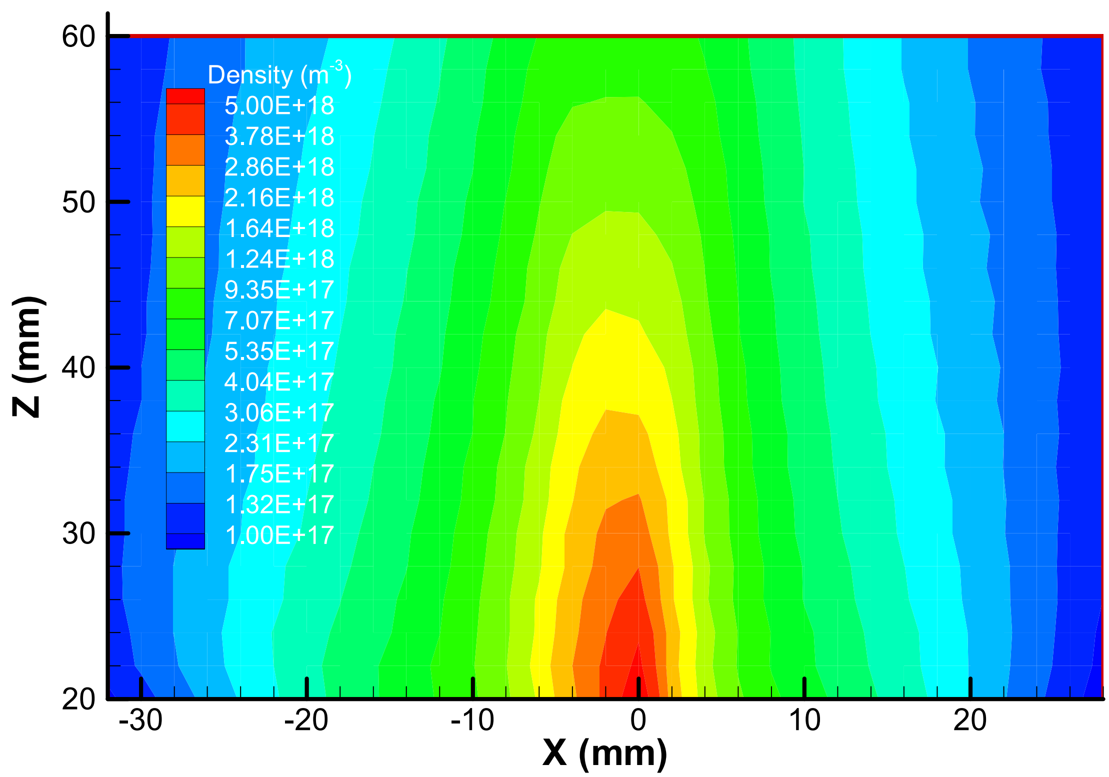

Figure 3-5: Near-field plasma density measured with the large triple probe.

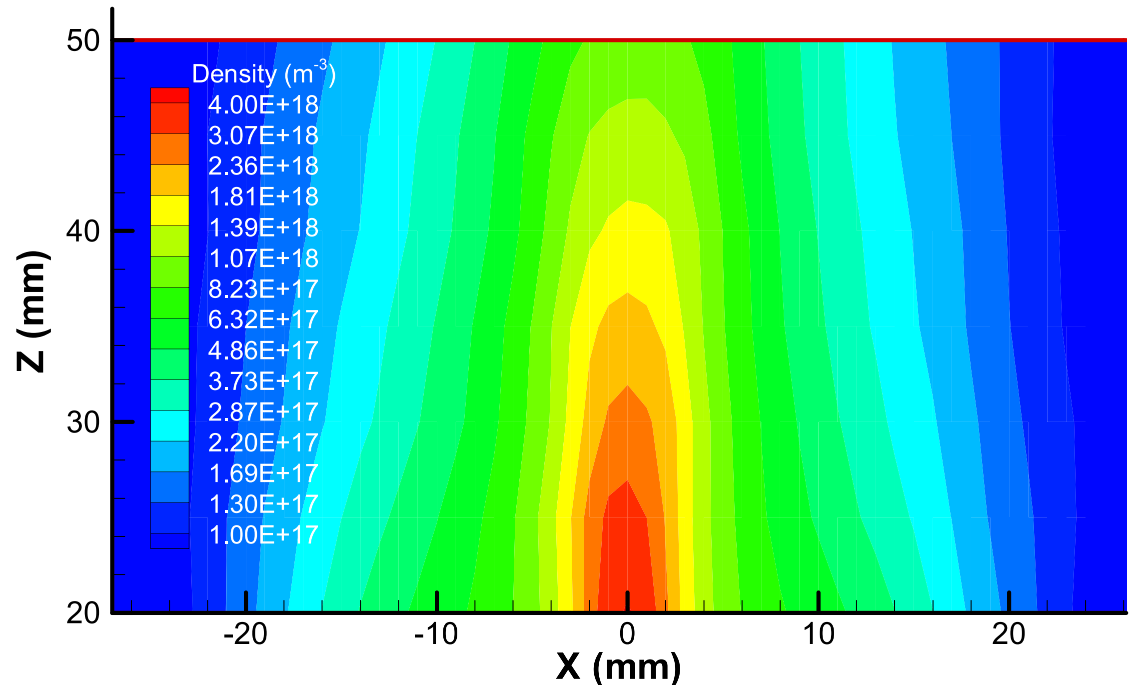

Figure 3-6: Near-field plasma density measured using a small triple probe.

3.3 Electron Temperature

The electron temperature in the far-field thruster plume was measured using both the large triple probe and the Langmuir probe. The results are shown in Figs. 3-7 and 3-8, respectively. The electron temperature distribution measured with the triple probe shows a similar structure to the plasma density with maximum temperatures occurring near the thruster centerline and decreasing in both the axial and transverse directions. The electron temperature varies between 1 and 2 eV over the majority of the displayed area and increases to nearly 3 eV along the thruster centerline at a distance of 50 mm. These numbers are verified by the Langmuir probe measurements shown in Fig. 3-8, which agree with the triple probe data to well within the stated 30% margin of error.

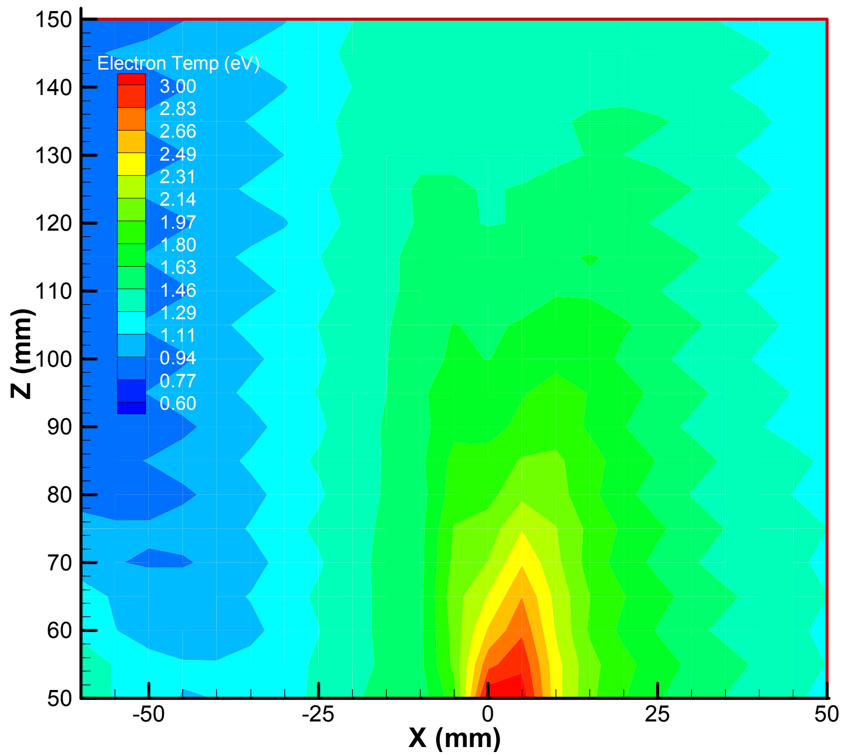

Figure 3-7: Electron temperature measured by the large triple probe in the far-field plume of the BHT-200.

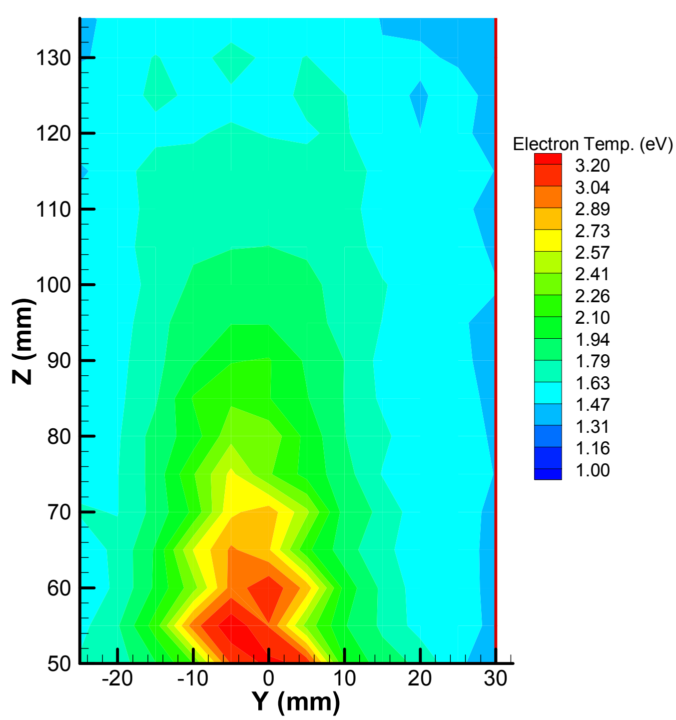

Figure 3-8: Electron temperature measured in the far-field plume using the spherical Langmuir probe.

The near-field electron temperature profiles measured with both the large and small triple probes are shown in Figs. 3-9 and 3-10, respectively. These data were recorded at the same spatial intervals as the number density and show several interesting features. The high electron temperature core alluded to previously is the dominant feature of both Fig. 3-9 and Fig. 3-10. The most notable features shown in these plots are the unexpectedly high level to which the electron temperature rises as the thruster centerline is approached from the radial direction and the relatively short distance (less than 10 mm) over which the increase occurs. Possible explanations for these phenomena are discussed near the end of this chapter.

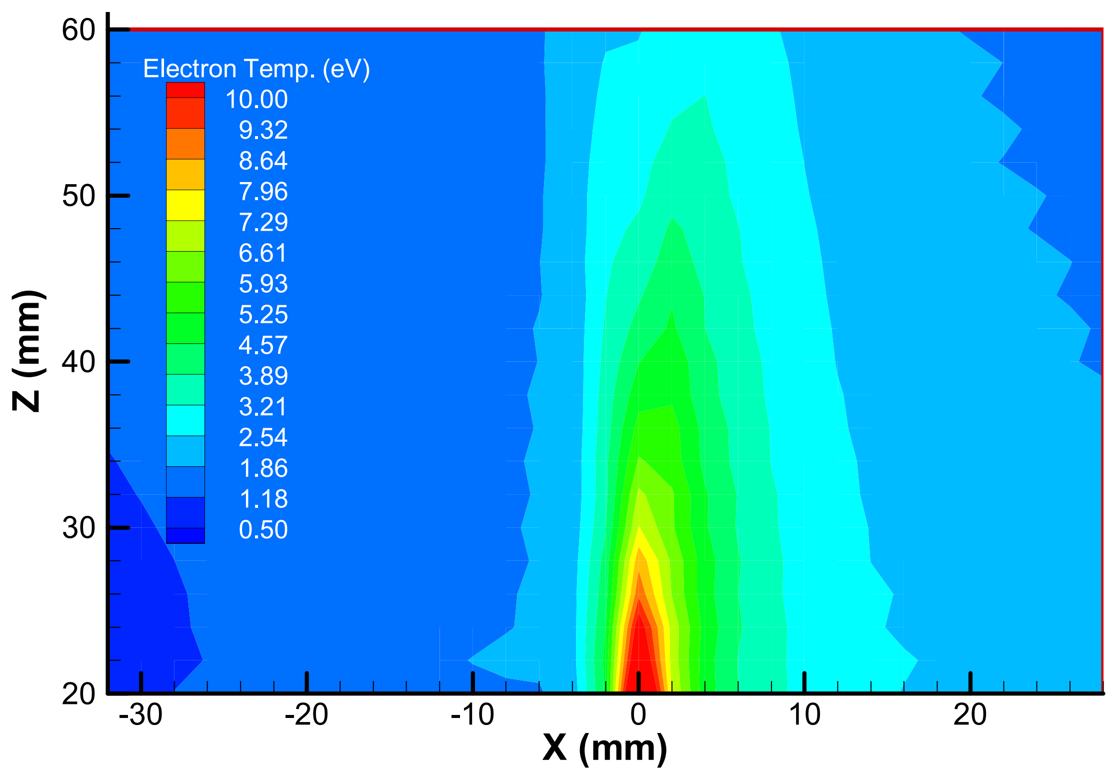

Figure 3-9: Electron temperature measured by the large triple probe.

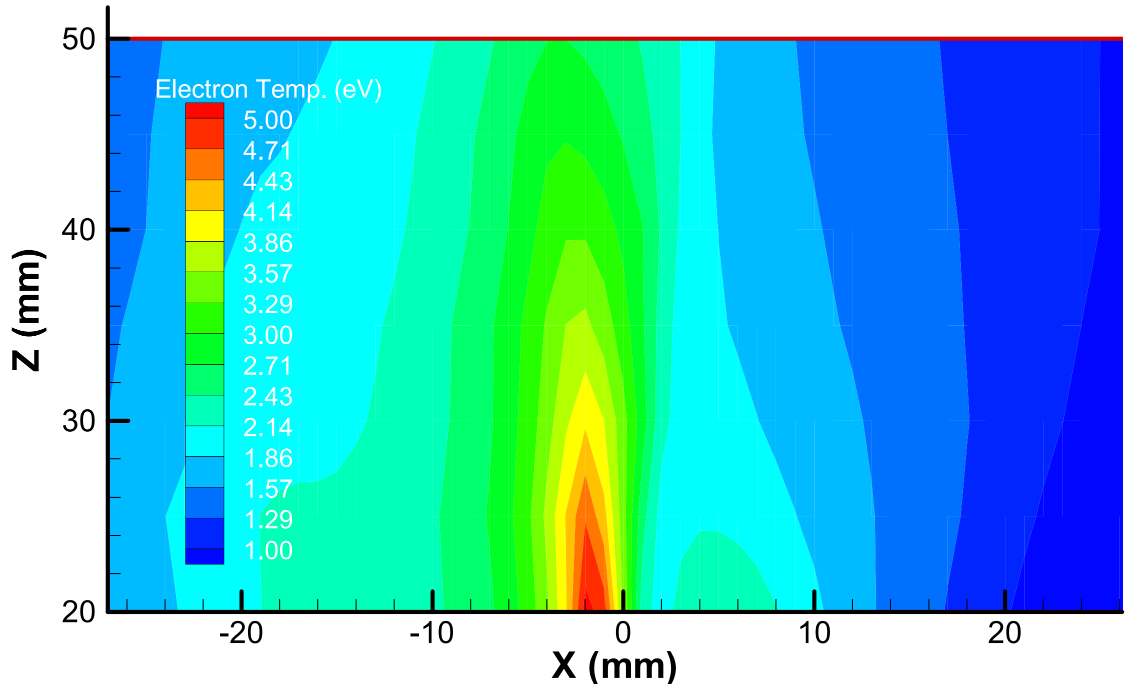

Figure 3-10: Electron temperatures measured by the small triple probe. Note both the high-temperature core and the significant disagreement with Fig. 3-9.

Although the near-field data taken with the large and small probes show similar trends, Fig. 3-9 and 3-10 reveal several discrepancies that must be explained. In particular, the maximum values of both density and electron temperature recorded by the larger probe are significantly higher than those measured by the smaller probe. The most obvious explanation for this discrepancy is the significant level of uncertainty inherent in all electrostatic probe measurements. Indeed the difference in the peak densities recorded by the two probes falls within the 50% margin of error stated previously. The electron temperature profiles shown in Figs. 3-9 and 3-10, on the other hand, show disagreement well in excess of the 30% margin of error typical of triple probes. This leads to the conclusion that there is a source of error in the measurements taken near the thruster centerline that is not taken into account by the standard triple probe theory.

One of the most basic assumptions in the derivation of the triple probe relations (Eqns. 2-9 and 2-10) is that all three electrodes comprising the triple probe are exposed to identical plasmas.[34] Near the thruster centerline, the measured electron temperature and number density change over such a short distance that this assumption is not justified for this region of the plume. Figures 3-11 and 3-12 show normalized traces of the electron number density and electron temperature, respectively, measured at various locations downstream of the thruster face using the small probe. The data in each curve are normalized by the maximum value recorded at the given axial location. These traces show that both the electron temperature and number density appear to change by as much as 20% over a distance of just 1 mm near the thruster centerline at the upstream end of the sampled region. Considering that the electrodes of the small probe are separated by approximately 2 mm, it is clear that the identical plasma assumption is not satisfied near the thruster centerline. Similar traces taken using the larger triple probe (not shown) indicate changes of plasma properties in excess of 50% over the roughly 4 mm diameter of the probe. Clearly, errors caused by gradients in plasma parameters should be more pronounced in data taken using the larger probe. This leads to the belief that the smaller probe more accurately depicts the plasma properties near the centerline than the larger probe, although even these data are subject to a significant degree of uncertainty. The idea that the discrepancies in the near-field data are caused by failure of the identical plasmas assumption is enhanced by the fact that both probes agree reasonably well in areas outside the central core. Differences in plasma properties between the two electrodes are also likely to be responsible for the asymmetry shown in the electron temperature data since the sign of the error would be reversed depending on which electrode, 1 or 3, is exposed to the higher density and electron temperature plasma. Although the absolute values measured in regions of large density and temperature gradients cannot be determined precisely, the data clearly indicate a significant rise in the electron temperature and electron number density near the thruster centerline. In fact, Fig. 3-11 shows the plasma density in the very near field to be about four times greater on centerline than it is just 5 mm off centerline.

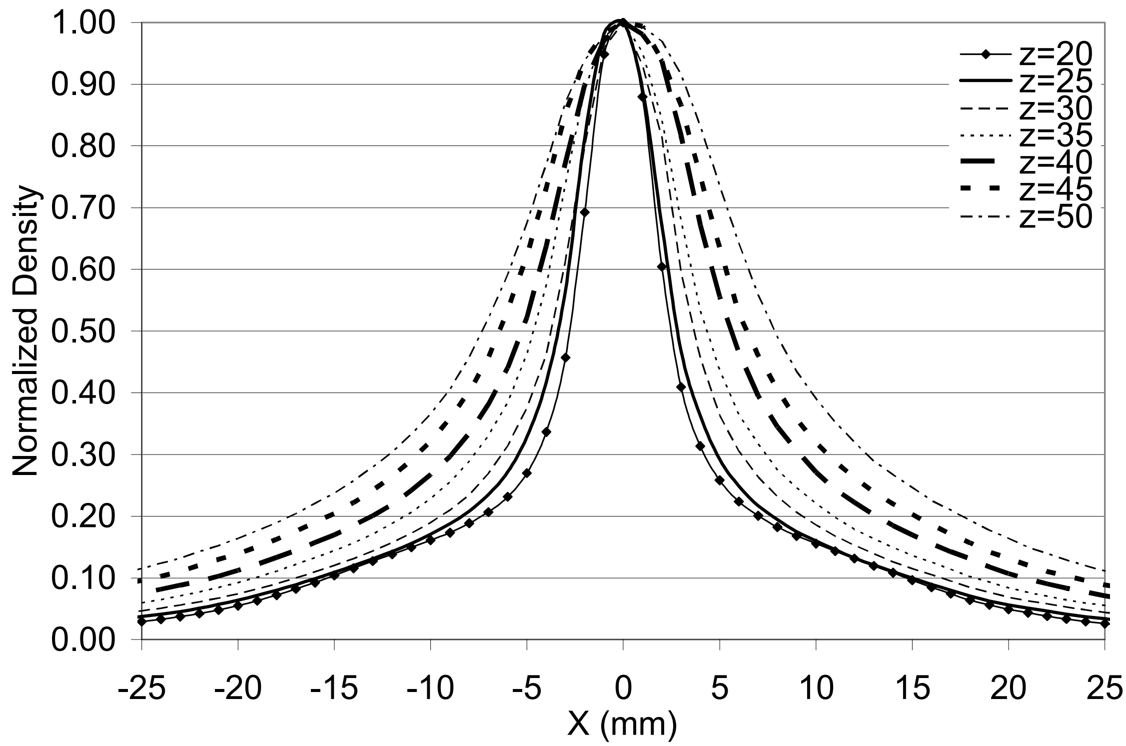

Figure 3-11: Normalized density profiles at various locations downstream of the thruster measured using the small triple probe. Note the large gradients near the centerline.

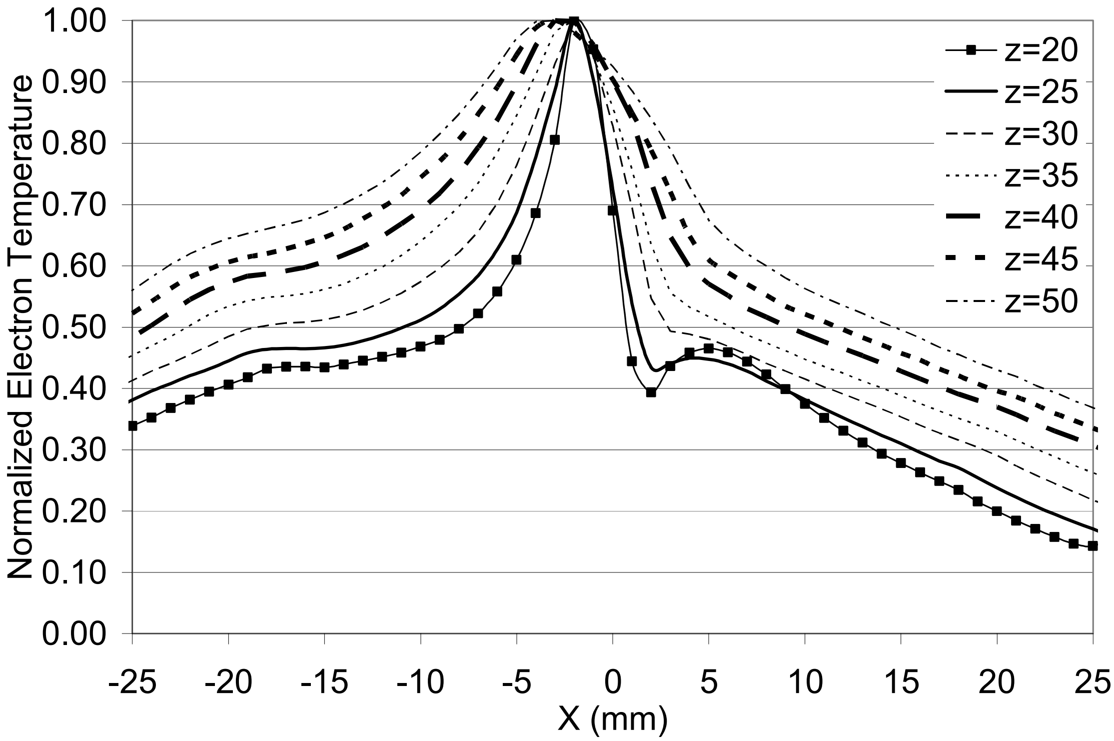

Figure 3-12: Normalized electron temperature data obtained with the small triple probe showing both a large temperature gradient near the thruster centerline and the apparent asymmetry resulting from it.

3.4 Plasma Potential

The emissive probe was used to measure the plasma potential in the XZ plane of thruster 3 at axial locations ranging from 50 to 150 mm downstream of the exit plane. These data were taken at 5 mm intervals in both the X and Z directions and are displayed in Fig. 3-13. Like the density and electron temperature, the plasma potential is highest near the thruster centerline and falls off rapidly in the radial, or X, direction. At 50 mm downstream, the plasma potential peaks at approximately 20 volts along centerline and falls to less than 5 volts at the boundaries of the sampled region. By 150 mm downstream, the peak plasma potential on centerline decreases to less than 10 volts.

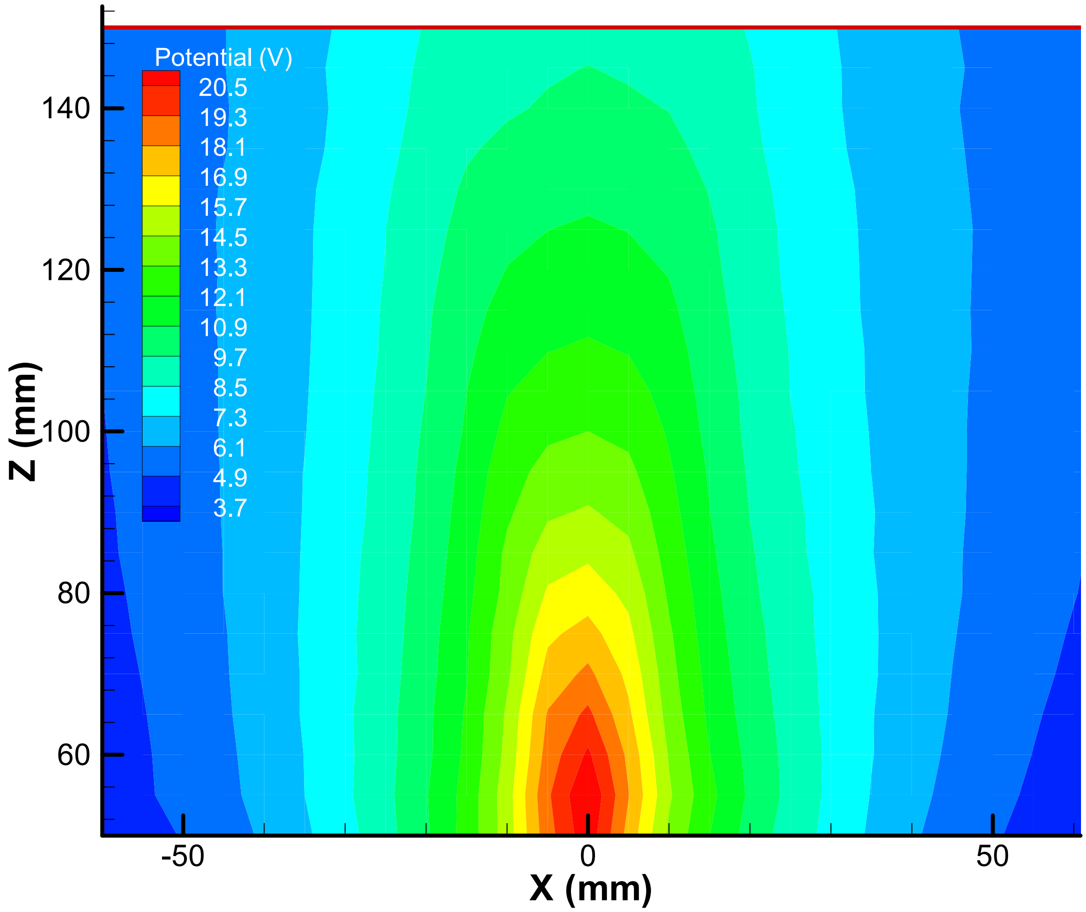

Figure 3-13: Plasma potential in the far-field of thruster 3.

An interesting insight can be obtained by examining the evolution of the plasma potential in the thruster plume. Along lines of force, the variation of the plasma potential is governed by the one dimensional generalized Ohm's law with terms involving the cross product of the magnetic field omitted. This result is given in Eqn. 3-1, where η represents the plasma resistivity, j is the current density, and p_e depicts the electron pressure, which is calculated according to the ideal gas law given by Eqn. 3-2. Generally, the first term on the right-hand side of Eqn. 3-1 is neglected and the plasma potential is estimated to be that which exactly cancels the electron pressure gradient. Figure 3-14 shows plasma potential values recorded along the thruster centerline and near the center of the discharge channel compared to those predicted in this manner. The curves labeled "predicted" in Fig. 3-14 were calculated according to the marching algorithm given by Eqn. 3-3, where the subscript k refers to the point index (k = 1, 2, 3…). In calculating the predicted plasma potential, the measured value at the furthest downstream location was used as a starting point and the incremental change given by the last term in Eqn. 3-3 was added to find the predicted value at the next point.

$$d\phi = -\eta j dz + \frac{1}{n_e e} dp_e \qquad \textbf{Eqn. 3-1}$$

$$p_e = n_e k_b T_e \qquad \textbf{Eqn. 3-2}$$

$$\phi_k = \phi_{k-1} + \frac{k_b \left(n_{e,k} T_{e,k} - n_{e,k-1} T_{e,k-1}\right)}{\frac{1}{2}\left(n_k + n_{e,k-1}\right) e} \qquad \textbf{Eqn. 3-3}$$

As shown in Fig. 3-14, the measured potential along the thruster centerline changes faster than predicted by a factor of approximately 2.5. This may indicate that the ηj term is not negligible in this region. If so, this would support the theory of Hruby *et al.* stating that the majority of the electrons emitted from the hollow cathode travel toward the anode along the thruster centerline rather than diffusing directly from the cathode through the annular discharge channel.[5] The increased local current density would thus cause the resistive term, ηj, to constitute a significant contribution to the electric field. Directly downstream of the discharge channel, which is outside of the bright plasma core, Fig. 3-14 shows the measured plasma potential to be in very good agreement with predictions. This further supports the claim that the change in plasma potential near the thruster centerline cannot be attributed solely to ambipolar effects. Although the data trace taken downstream of the discharge channel is not strictly along a line of force (see discussion in the next section), it can easily be shown that the magnetic field strength is sufficiently weak in this region to warrant omission from Eqn. 3-1.

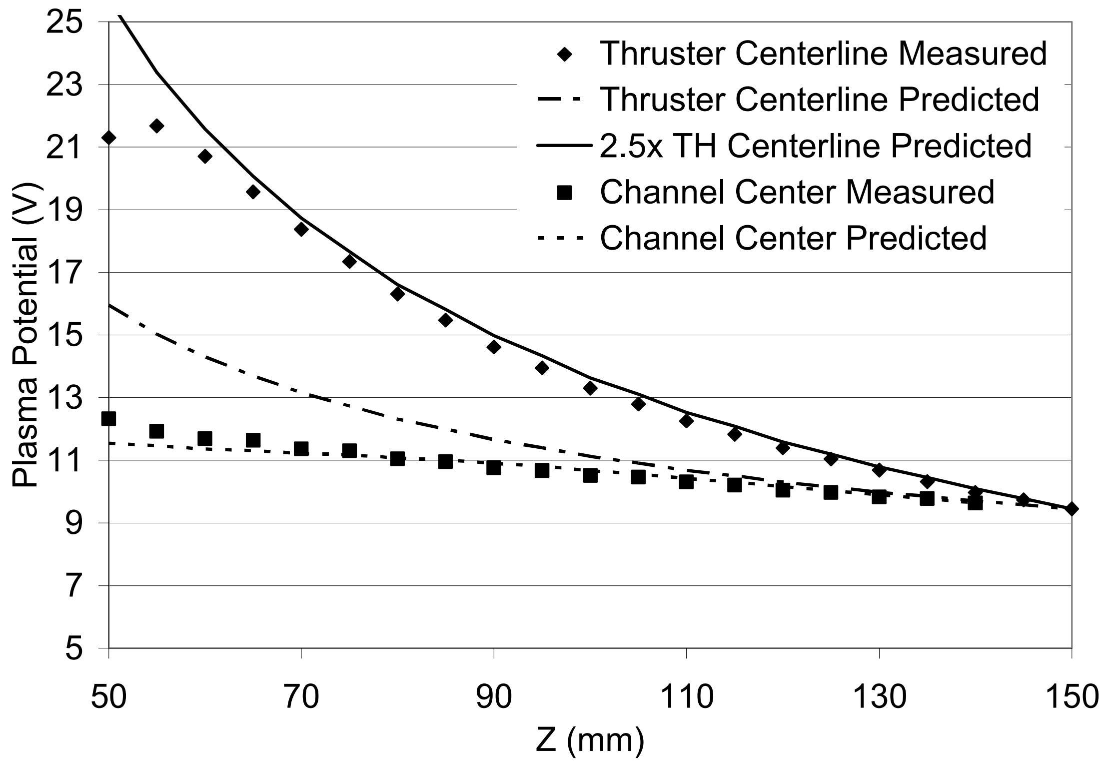

Figure 3-14: Evolution of the plasma potential in the thruster plume. Note that the potential along the thruster centerline changes faster than predicted.

Near-field plasma potential measurements recorded 20 to 40 mm downstream of the thruster exit plane are presented in Fig. 3-15. Due to the high plasma density in this region, the lifetime of the emitting filament was reduced compared to probes used for far-field measurements, and two separate probes were needed to collect the displayed data. The Z=20 trace was obtained with the first probe while the data at Z=30 and Z=40 were collected using a second identical probe. The plasma potential can be seen to increase sharply near the thruster centerline, especially at short distances downstream of the exit plane. The data taken 20 mm downstream, for example, show an increase of roughly 8 volts over a distance of approximately 2 mm. Assuming that this structure is axisymmetric, the physical size of the probe is again called into question. It should be noted that the diameter of the emitting filament loop is approximately 3 mm and hence is only marginally smaller than the width of the observed core. This does not qualitatively change the result that a region of high plasma potential appears along the thruster centerline and that the rise from the value in the surrounding plasma occurs over a relatively short distance. It does, on the other hand, imply that the apparent width of the core should be considered a rough approximation since slight misalignment of the probe in the Y direction could cause the core to appear narrower than it really is.

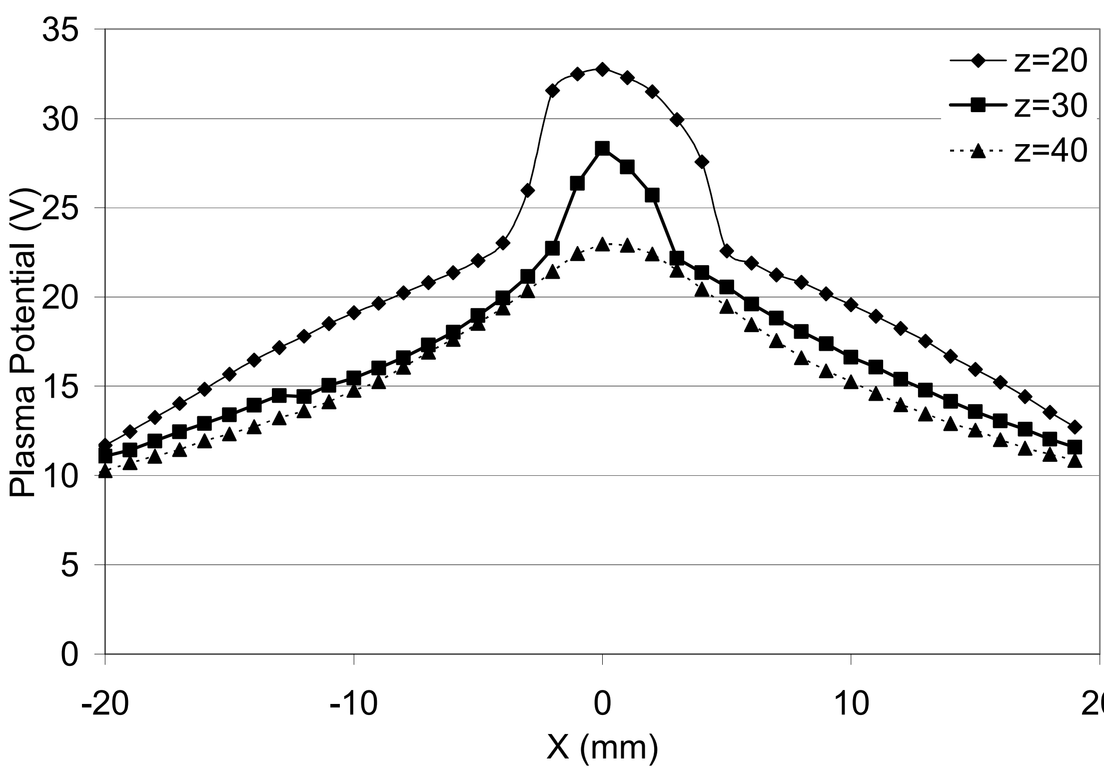

Figure 3-15: Plasma potential in the near field of thruster 3.

3.5 Magnetic Field Profile

The static magnetic field downstream of the BHT-200 was measured using a commercially available, Bell model 7030 three-axis gaussmeter. All data were recorded with the thruster electromagnet energized, but without the thruster in operation, i.e. with no plasma present. Although recent work has shown the magnetic field profiles inside an operating Hall thruster to deviate from the applied profiles due to fields induced by the azimuthal electron drift,[64] the difference in the plume region is expected to be negligible for the low-power thruster studied here because of the low current levels involved. The magnetic field profile displayed in Fig. 3-16 is, therefore, believed to be a realistic depiction of the one that occurs downstream of an operating thruster.

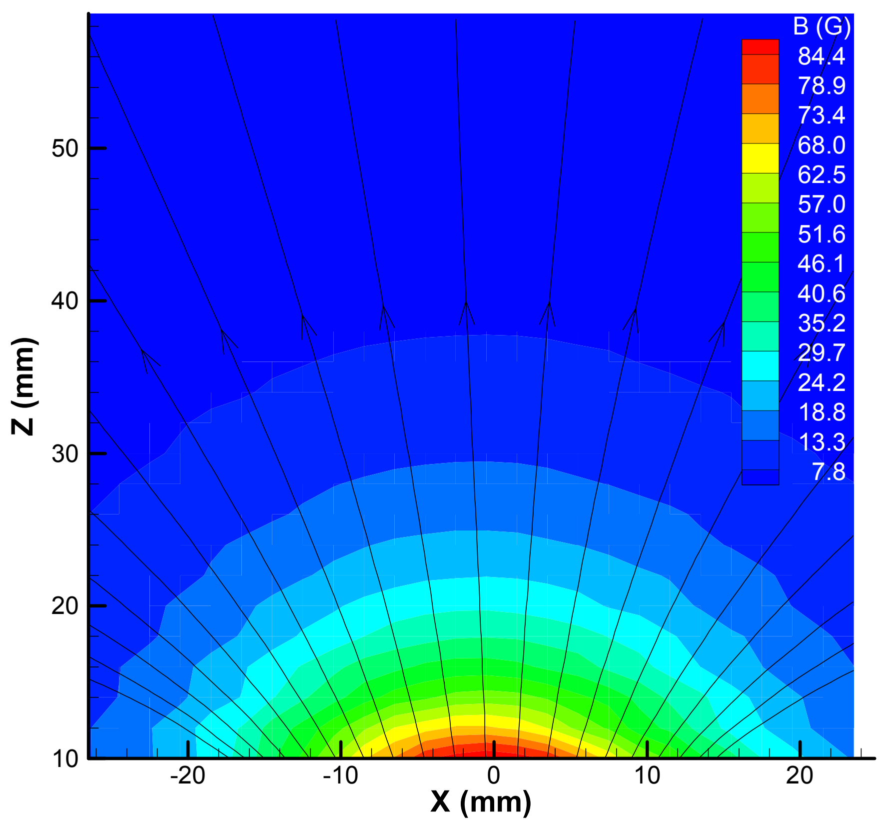

Figure 3-16: The magnetic field measured downstream of a single BHT-200.

As the figure above suggests, beyond about 50 mm downstream of the exit plane the magnetic field strength is less than 5 gauss. The significance of this field to the plasma physics can be quantified by the dimensionless parameter, β, which is defined as the ratio of the kinetic pressure to the magnetic pressure and is given by Eqn. 3-4. For a plasma with a density of 1×10^{18} m^{-3} and an electron temperature of 3 eV, which are typical values measured by the triple probe 50 mm downstream of the thruster exit plane, β is approximately 4.8 for a 5 gauss magnetic field. Since this ratio shows the forces due to particle pressure to be significantly higher than those due to magnetic forces, omission of the magnetic terms from Eqn. 3-1 is justified for areas in the far-field plume. The effects of the magnetic field may, on the other hand, be important when considering the dominant plasma wave modes that occur in the very near-field plume since the field strength is much higher in this region. For example, in areas where the magnetic field rises to just 50 gauss (15 mm downstream of the exit plane), the plasma β falls to less than 0.05 and the magnetic forces become significant. For this reason, magnetic effects are included in the discussion of plasma instabilities given at the end of this chapter.

$$\beta = \frac{n_e k_b T_e}{B^2 / 2\mu_0} \qquad \textbf{Eqn. 3-4}$$

3.6 Ion Current Density

The ion current density profile in the plume of a single thruster was measured along an arc of radius 0.5 meters using both the nude and gridded Faraday probes described in Chapter 2. Measurements with the nude probe were obtained in both

Chamber 6 at AFRL and in the LVTF at PEPL. The recorded beam profiles are shown in Figs. 3-17 and 3-18 on linear and logarithmic scales, respectively. In each case, the collector voltage was biased 20 volts below ground since this potential was shown to be well within the saturation region depicted in Fig. 2-9. The current densities reported for the nude probe were calculated by simply dividing the measured current by the physical area of the collector. The absolute current density recorded using the gridded probe is somewhat more ambiguous due to the effect of the retarding grid. Ideally, the grid, which was biased 30 V above ground, would simply exclude the low-energy CEX ions while allowing the beam ions to proceed unimpeded. In practice, however, the retarding grid has a certain open area fraction that restricts the flow of beam ions to the collector. The plasma sheath surrounding each grid wire causes the effective open area fraction to differ from the physical one, thus making the grid impediment difficult to account for analytically. The result is that a matching criterion must be used to put the data measured with the gridded probe on the correct absolute scale. In the present case, this was accomplished by equating the current collected by the gridded probe to the current density measured by the nude probe on the thruster centerline, where CEX products comprise a negligible fraction of the ion flux. The resulting correction factor was then applied to all measurements taken with the gridded Faraday probe. The current densities determined in this manner were approximately 11% higher than those calculated by taking the grid transparency to be equal to the physical open area fraction.

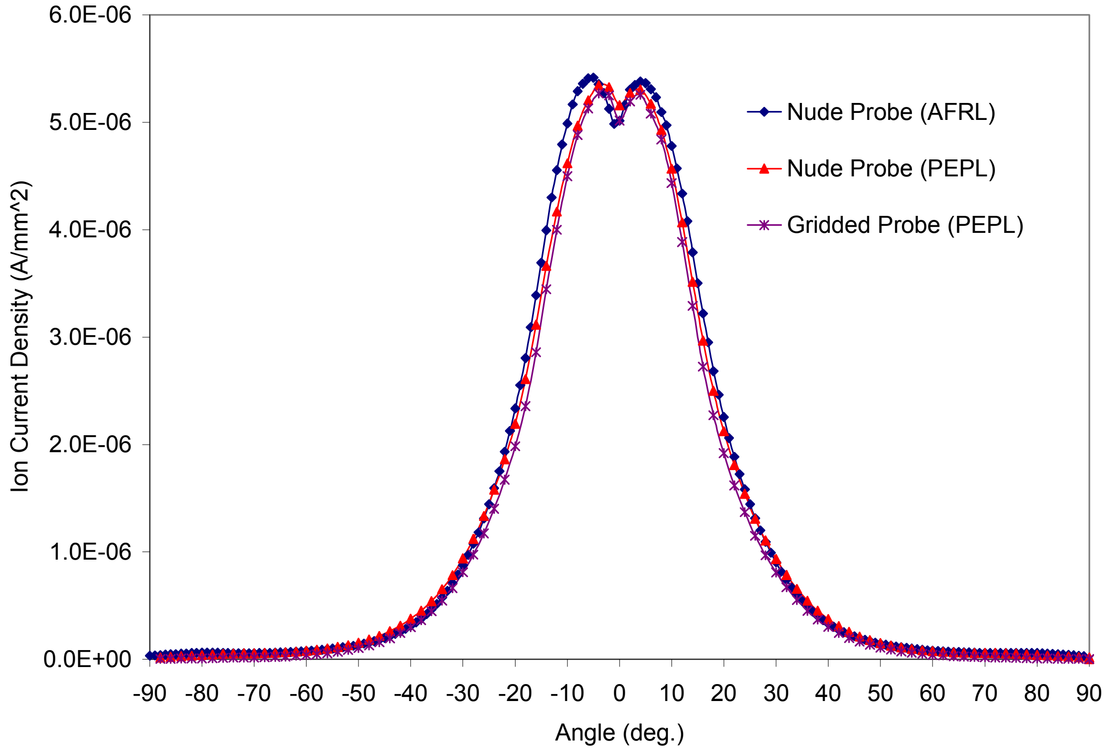

Figure 3-17: Current density recorded 0.5 m downstream of a single BHT-200 (linear scale).

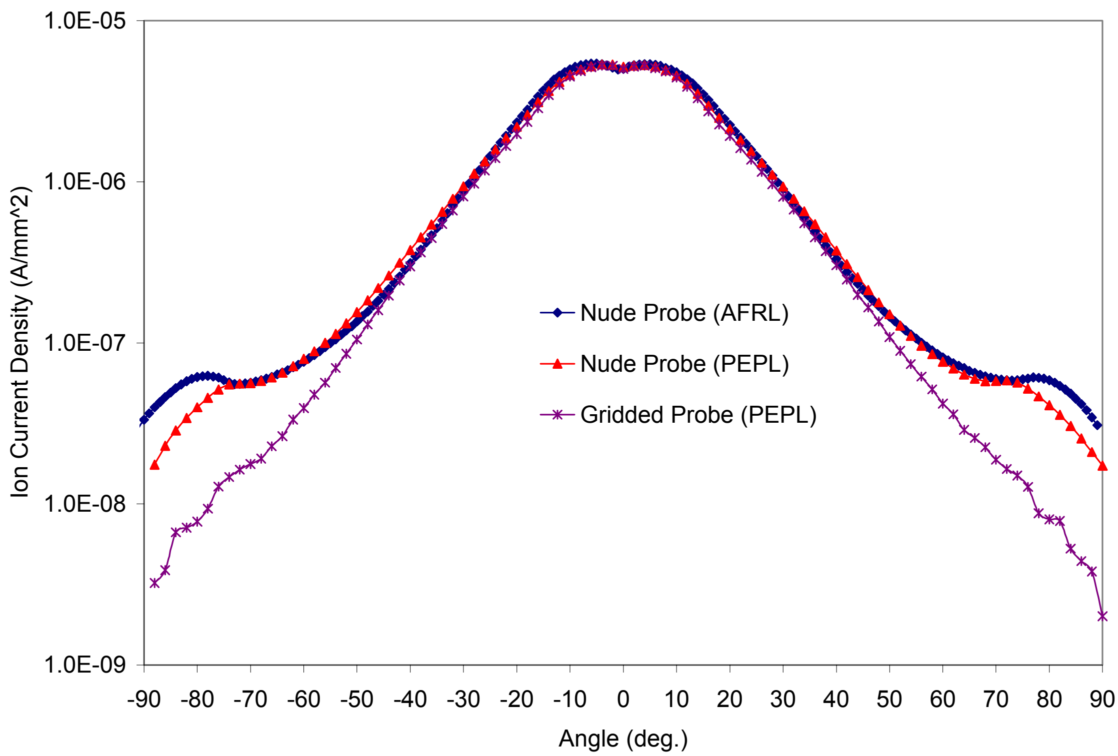

Figure 3-18: Ion beam profiles downstream of a single thruster. Note the CEX lobes visible in the nude probe data (log scale).

The data presented in Fig. 3-18 show several interesting features. The first is the excellent agreement between all three curves at angles below about 45° with respect to the thruster centerline. This agreement provides a great deal of confidence in the measurements and is consistent with the premise that the regions of high current density near the thruster centerline are largely unaffected by the presence of CEX ions. The effect of low-energy ions, on the other hand, can be seen clearly in the data taken at larger angles where the current densities recorded by the nude probe differ significantly from those taken with the gridded one. This suggests that a significant fraction of the current collected by the nude probe at angles greater than 45° is attributable to ions with kinetic energy to charge ratios below the 30 volt level set by the grid voltage. This is consistent with the measurements of energy spectra presented later in this chapter.

An additional feature observable in Fig. 3-18 is the effect of chamber pressure on the current densities recorded at high angles off centerline. The data recorded in Chamber 6 at AFRL were taken at a background pressure of approximately 6.1×10^{-6} Torr while the background pressure in the LVTF at PEPL was roughly 1.1×10^{-6} Torr. The increase in collected current at high angles with increasing pressure seen in this study is in good agreement with the previously published results of Manzella *et al*.[46] Since the appearance of the so-called "charge-exchange lobes" is clearly an effect of chamber background pressure, measurements taken in space conditions would not be expected to show these features. For this reason, the results of the gridded probe are likely to be more representative of the beam profiles that could be expected in space.

One measure that is often used to quantify the validity of beam profiles measured by Faraday probes is a comparison between the ion current resulting from integration of the current density profiles and the measured discharge current. The total ion flux from the thruster can be obtained by assuming axisymmetry of the beam and integrating the measured current density according to Eqn. 3-5. The results of this integration are shown in Table 3-1, which also shows the beam divergence half-angles reflected by each trace in Fig. 3-18. The beam divergence half-angle is calculated by determining an imaginary cone within which a specified percentage of the total current flux is contained. The uncertainties in the integrated ion currents and divergence half-angles due to the numerical integration scheme and slight asymmetry of the beam profiles are estimated to be 0.10 A and 1.0°, respectively. These estimates are determined by comparing the beam current and divergence angles calculated from first the positive and then the negative angles depicted in Figs. 3-17 and 3-18 assuming azimuthal symmetry. The values presented in Table 3-1 are the average of the two calculations.

$$I_i = 2\pi R^2 \int_0^{\pi/2} j(\theta)\sin(\theta)d\theta \qquad \textbf{Eqn. 3-5}$$

Current Trace	Integrated Ion Beam Current (A)	90% Divergence Half-Angle	95% Divergence Half-Angle	99% Divergence Half-Angle
Nude (AFRL)	0.732	48.4°	64.7°	83.5°
Nude (PEPL)	0.715	46.9°	60.4°	79.8°
Gridded (PEPL)	0.618	40.1°	48.2°	67.3°

Table 3-1: Ion beam currents and divergence angles inferred from Faraday probe data for a single thruster.

As Table 3-1 shows, the measurements obtained with the gridded Faraday probe result in a significantly lower value of ion beam current than the nude probe. An analytical estimate for the total ion beam current can be obtained by considering the total mass flux through the thruster (excluding the cathode flow) and assuming that each neutral is singly-ionized as expressed by Eqn. 3-6. For the 8.5 sccm (0.84 mg/sec) anode flow of the BHT-200, this results in a predicted ion current of 0.614 A, which is in very good agreement with the estimate obtained from the gridded probe data.[65] Further confidence in the validity of the gridded probe data is gained by comparing the calculated ion current to the measured discharge current, as suggested previously. The integrated current of 0.618 A constitutes approximately 77% of the 0.80 A discharge current, which is in good agreement with both the 74% reported by Kim[66] and the 77% measured by Hofer[67] in the plumes of larger Hall thrusters. The apparent validity of the gridded probe data implies that any prediction of thruster/spacecraft interactions based on nude Faraday probe measurements likely constitutes a "worst case scenario" of what could be expected in space. Since the gridded probe shows the beam divergence to be lower than that inferred from the nude probe, the actual impact of the thruster plume on spacecraft surfaces is likely to be less severe than that implied by traditional Faraday probe measurements.

$$I_B = \frac{e}{m_{Xe}} \dot{m}_{anode} \qquad \textbf{Eqn. 3-6}$$

3.7 Electron Energy Distribution Function

As mentioned in Chapter 2, the electron energy distribution function can be obtained from two successive differentiations of the Langmuir probe trace. The method by which this is accomplished in the present case is illustrated in Figs. 3-19 and 3-20. Figure 3-19 shows a sample Langmuir probe trace along with a smoothing spline fit to the data. In both traces, the ion saturation current has been subtracted to allow study of the electron component. The first and second derivatives calculated from the resulting spline are shown in Fig. 3-20.

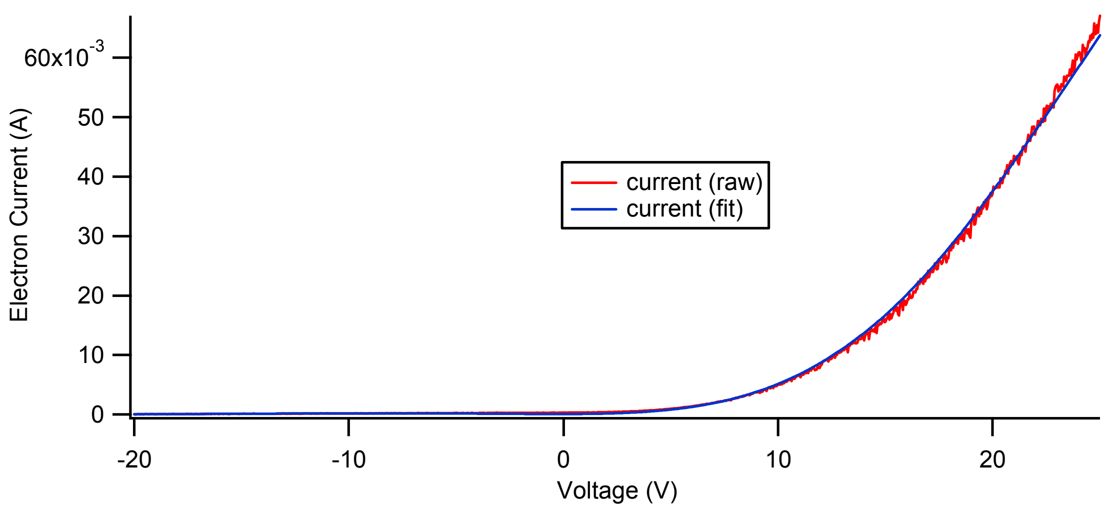

Figure 3-19: Sample Langmuir probe trace and smoothing spline fit to the data.

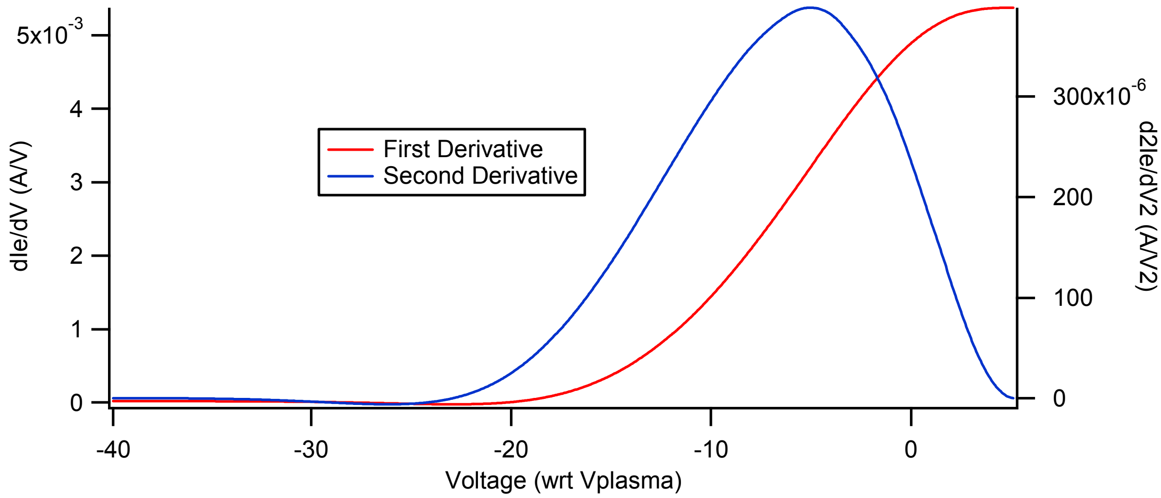

Figure 3-20: Sample first and second derivatives of a Langmuir probe trace. The second derivative is directly related to the EEDF.

One feature demonstrated by the current trace shown in Fig. 3-19 is the lack of electron current saturation encountered in many regions of the plume. This causes the plasma potential "knee" in these traces to be poorly defined. Since a value of plasma potential is required for implementation of Eqn. 2-4, it is estimated according to Eqn. 3-7, which is only strictly accurate for a perfectly Maxwellian plasma.[68] Using this estimate of plasma potential, the EEDF can then be calculated according to Eqn. 2-4. Examples of the resulting EEDF are shown in Fig. 3-21 for three different distances downstream of the exit plane along the thruster centerline.

$$\phi = V_f + \left| \left(\frac{k_b T_e}{e} \right) \ln \left[\left(\frac{2\pi m_e}{m_i} \right)^{1/2} \exp\left(-1/2\right) \right] \right| \qquad \textbf{Eqn. 3-7}$$

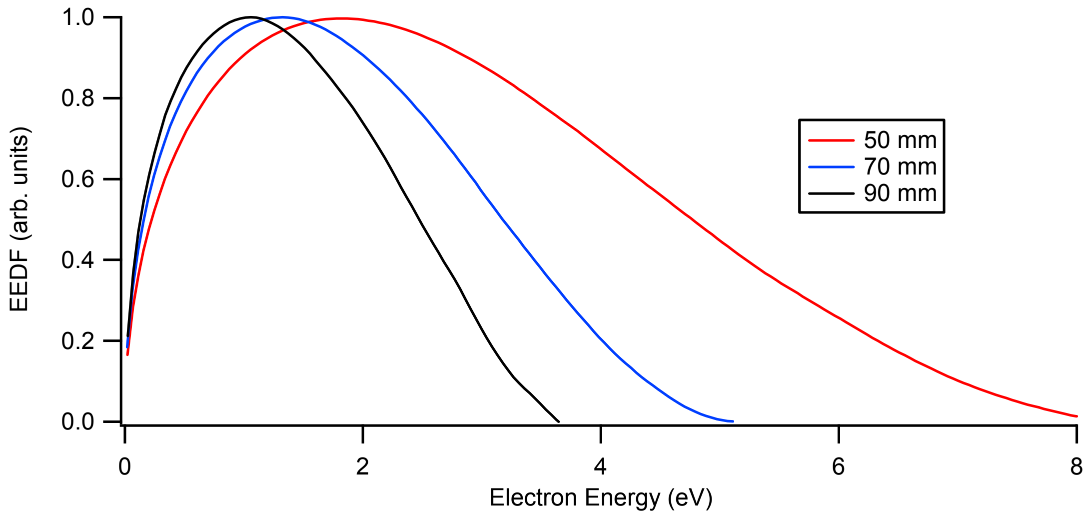

Figure 3-21: EEDF calculated at three distances downstream of the thruster along centerline. Note that each trace is normalized by its maximum value rather than normalized to unit area.

The distribution functions shown in Fig. 3-21 demonstrate the calculation technique and are in qualitative agreement with the electron temperature data presented previously with the EEDF being wider in the near-field, thus indicating a hotter plasma. Quantitatively, the electron temperatures calculated from the EEDF generally agree with those presented previously to within a factor of two. The high-energy tail exhibited by each trace is consistent with previously reported properties in the plume of a hollow cathode similar to the one used as an electron source for this thruster.[69] Beyond those traits, however, examination of the EEDF in the far-field plume provides little information that has not already been garnered from other, simpler diagnostic techniques.

Unlike the relatively benign far-field data, the second derivative of the probe traces taken in the very near-field show some rather unusual traits. Figure 3-22 shows the calculated second derivative at various radial locations at an axial distance of 20 mm downstream of the exit plane. Note that at this location, probe heating concerns limited the voltage sweep applied to the probe to 25 volts, which was below the plasma potential near the thruster centerline. This makes conversion of the second derivative profiles into EEDFs using Eqn. 2-4 very difficult, though information can still be gained by examining the profiles shown in Fig. 3-22.

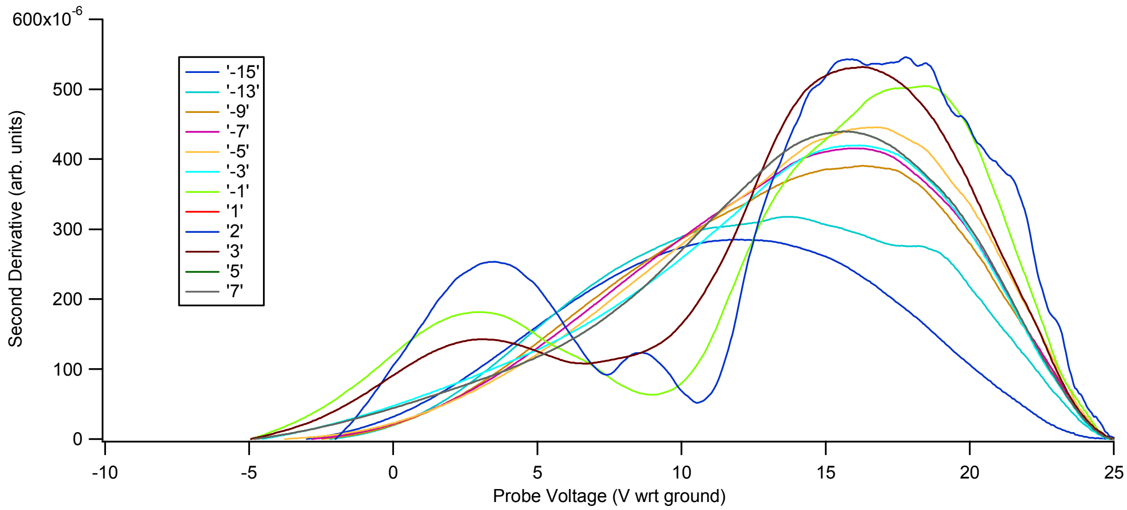

Figure 3-22: Second derivative of Langmuir probe traces taken in the near-field plume. Note the secondary peaks that occur in traces taken near the thruster centerline.

At locations far from the centerline, the second derivative shows a shape similar to the standard one depicted in Fig. 3-20. At locations within a few millimeters of the centerline, however, a secondary peak in the distribution can be seen at low probe voltages, which correspond to high electron energies. These secondary peaks are very pronounced in the curves labeled -1, 2, and 3 in Fig. 3-20. Care must be taken not to place too much emphasis on these results due to the multiple sources of error associated with the Langmuir probe, especially the perturbation caused by drawing current from the discharge. Taken in conjunction with the plasma potential profiles and the visual evidence, however, these traces support the notion that the plasma along the centerline of the thruster shows significantly different characteristics than the plasma elsewhere in the plume. Possible explanations for this difference will be discussed in Section 3.10.

3.8 Ion Energy Spectra

As an initial test of the ion energy analysis diagnostics, energy distributions measured with the RPA were compared to those measured with the ESA at identical locations. Figure 3-23 shows the measured distribution function for a single thruster at 0°, 15°, and 30° off centerline for each instrument. Notice the relatively good agreement between the two devices. For each of the three angular locations, the voltage at which the peak in the distribution function occurs agrees to within 8 volts. For example, on the thruster centerline the primary peak was measured at 220 volts by the RPA and at 228 volts by the ESA. All of the measurements presented below were recorded 0.5 meters downstream of the thruster along a radial arc.

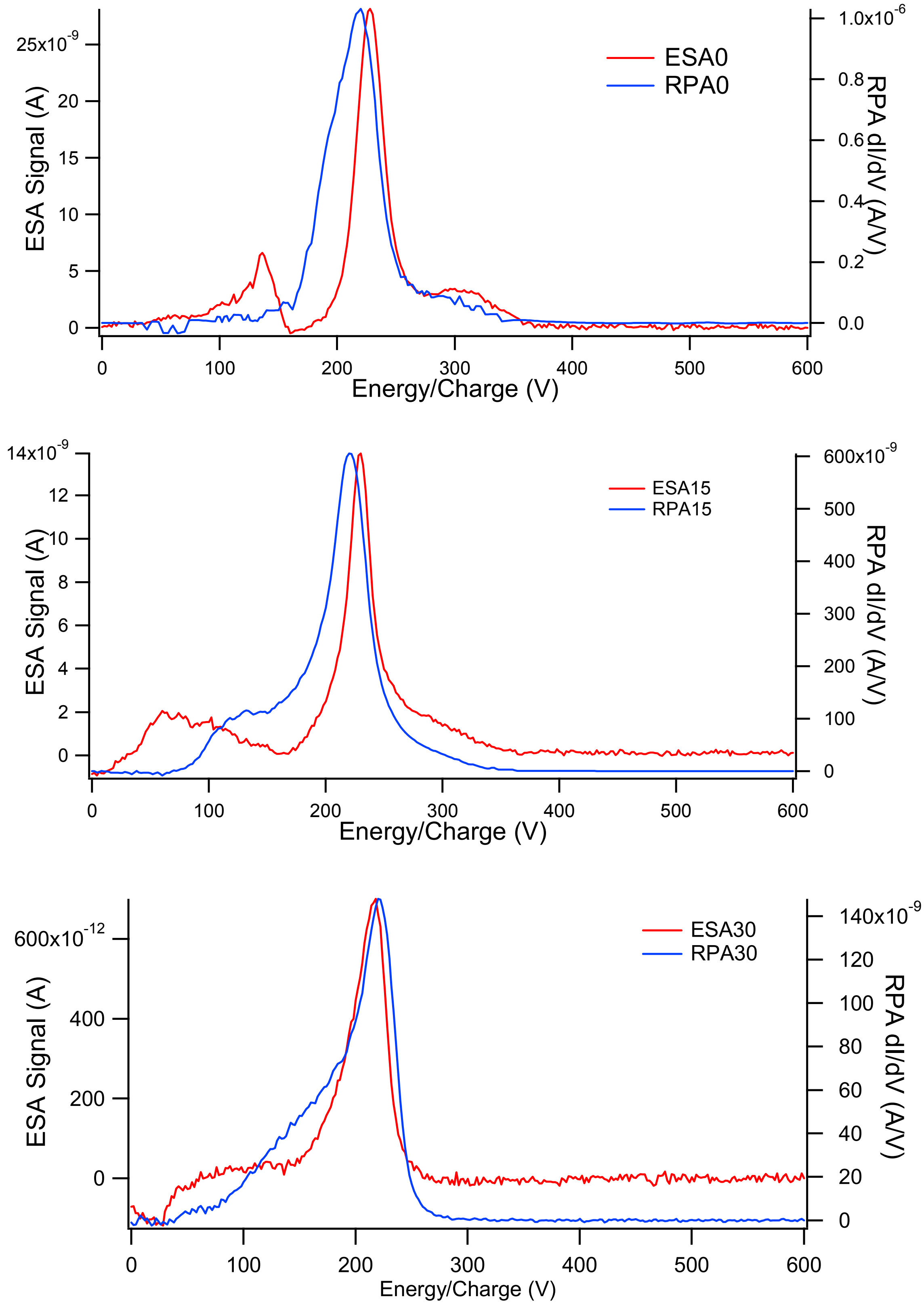

Figure 3-23: Comparison between ESA and RPA traces at three angles off the thruster centerline.

The most noticeable difference between the diagnostics demonstrated by Fig. 3-23 is the appearance of secondary peaks at voltages above and below the primary ion voltage, which are more pronounced in the ESA traces. Additionally, the primary peak in the distribution is consistently wider when measured with the RPA as opposed to the ESA. The shape of the distribution function is likely to be more accurate in the ESA traces since those data are not subject to the effects of numerical differentiation. The location of the primary peak in the distribution, however, is likely to be more accurately depicted by the RPA because slight misalignment of the grid components would not be expected to alter the performance of this device. Slight misalignment or improper spacing of the plates in the ESA, on the other hand, could cause a shift of several volts in the measured distributions.

Figures 3-24 and 3-25 summarize the ion energy distributions recorded by the ESA, while Figs. 3-26 through 3-28 depict similar data recorded by the RPA. Although traces were recorded for both positive and negative angles off centerline, only data for the positive angles are reported here due to the high degree of symmetry exhibited by the plume. The ESA traces show the peak ion energy to charge ratio to occur at approximately 228 volts for most of the angular spectrum, while the RPA shows the peak at 220 volts. The secondary structure occurring at energy to charge ratios below 150 volts can be attributed to elastically scattered primary ions.[53,70] The high-energy population shown at voltages in excess of the discharge voltage, particularly at low angles off centerline, is likely due to beam ions that have undergone charge decreasing collisions.[52,53] Data are not shown for the ESA at angles greater than 60° due to the prohibitively small signal to noise ratio in this regime caused by the small acceptance angle of the device. RPA data, however, show the plume to be composed primarily of low energy charge exchange products at angles greater than 70°.

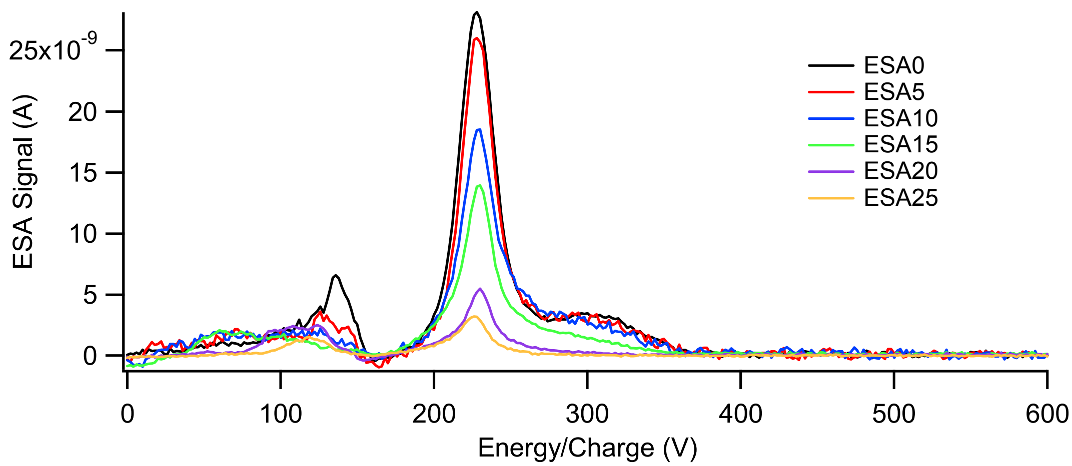

Figure 3-24: ESA traces at low angles off the thruster centerline. The peak energy to charge ratio occurs at approximately 228 volts.

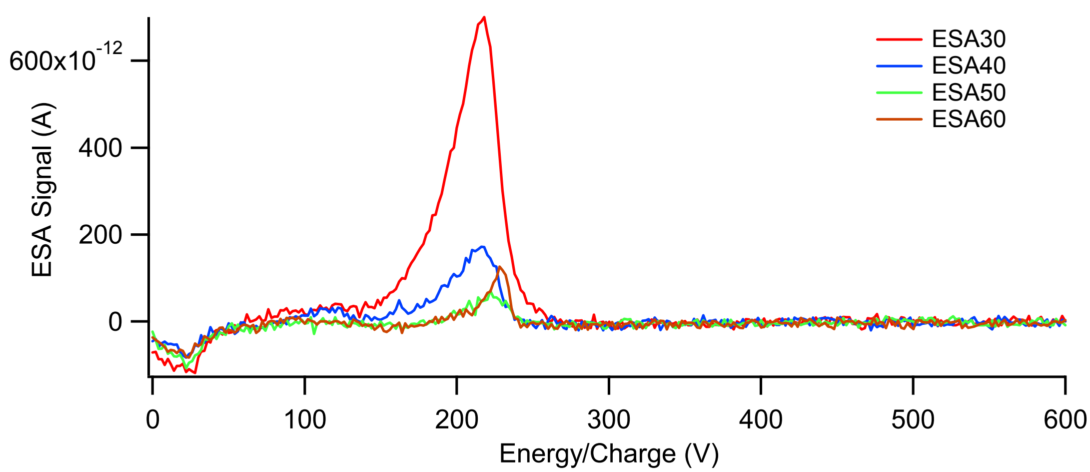

Figure 3-25: ESA traces at angles from 30 to 60 degrees off the thruster centerline.

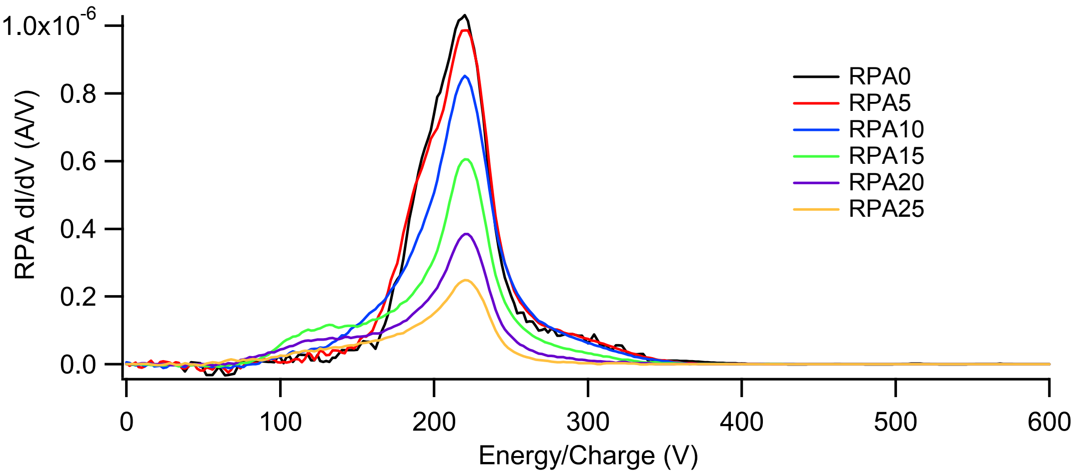

Figure 3-26: RPA traces taken at low angles off the thruster centerline.

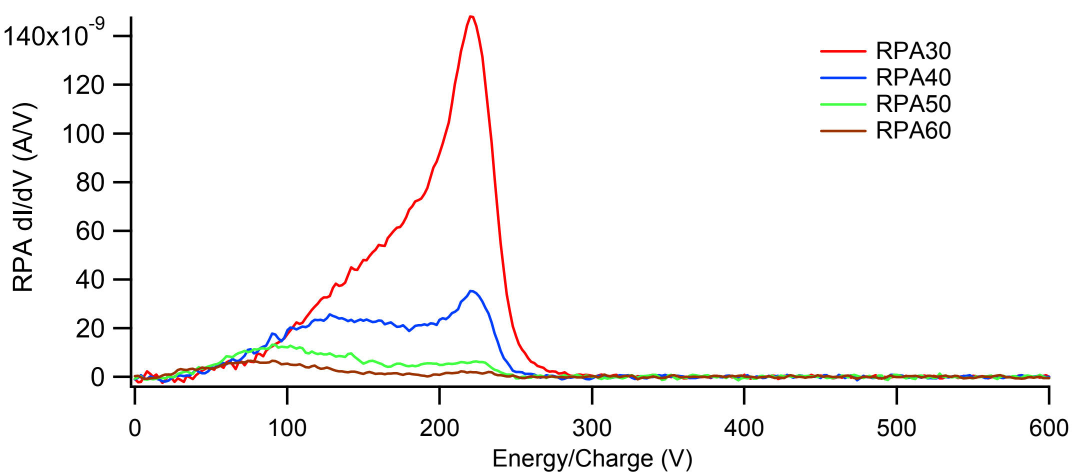

Figure 3-27: Energy per charge spectra recorded by the RPA at angles between 30 and 60 degrees. Note the low-energy, elastically scattered tail.

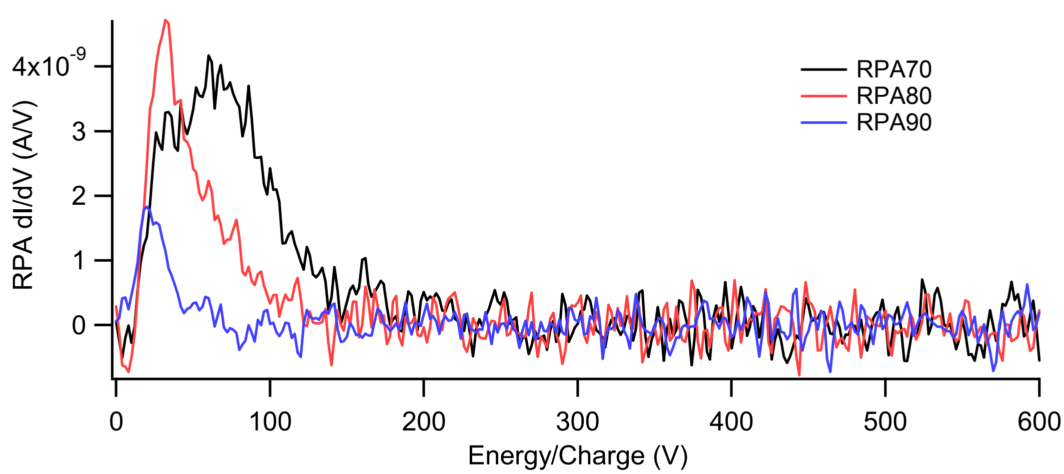

Figure 3-28: The high-angle energy spectra measured by the RPA. The spectra are dominated by low-energy CEX products.

3.9 Ion Species Fractions

The ion species fractions in the plasma plume were measured at a distance of 0.5 meters downstream of the thruster using the ExB probe described in Chapter 2. Measurements were taken along a radial arc at 5° intervals between the centerline and 30°, and at 10° intervals beyond that. Samples of the raw data are shown below in Figs. 3-29 through 3-32 for angles of 0, 15, 30, and 60 degrees off the thruster centerline, respectively. The resulting species fractions calculated according to the method described previously are plotted in Fig. 3-33 as a function of angle with respect to the thruster centerline. The species fractions shown in Fig. 3-33 are the average of three separate measurements and the displayed error bars depict the standard deviation at each location. Beyond 60°, the measured trace became extremely noisy and the signal was unusable.

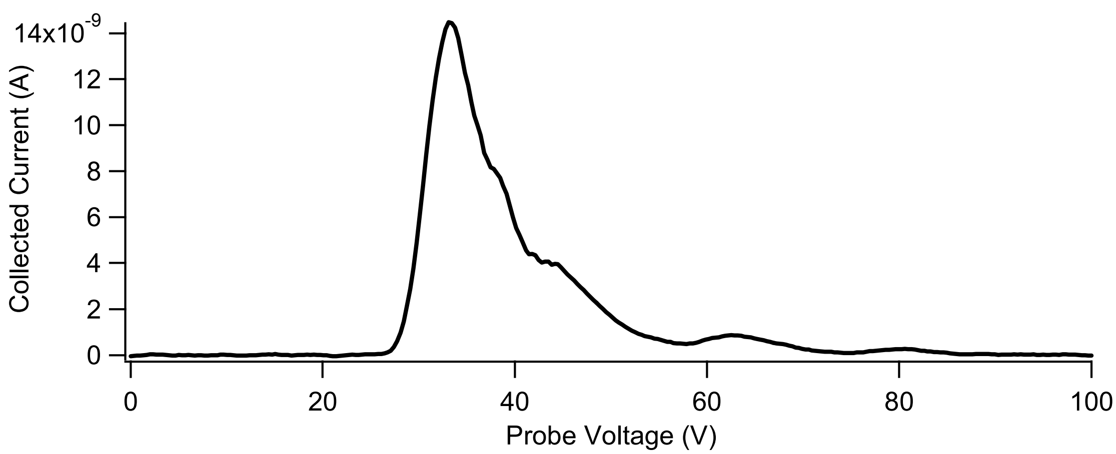

Figure 3-29: ExB probe data collected on centerline at a distance of 0.5 m downstream of the BHT-200.

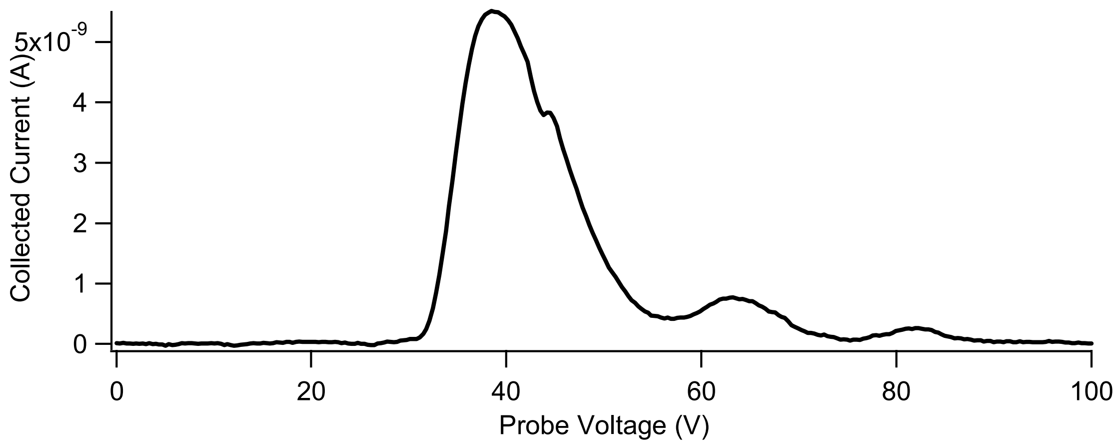

Figure 3-30: ExB probe data collected 15 degrees off centerline.

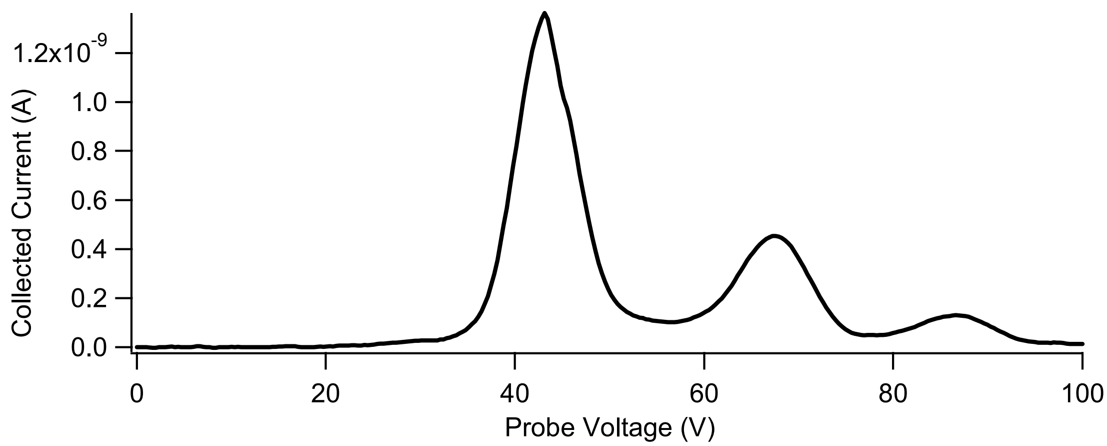

Figure 3-31: ExB probe data at 30 degrees off centerline.

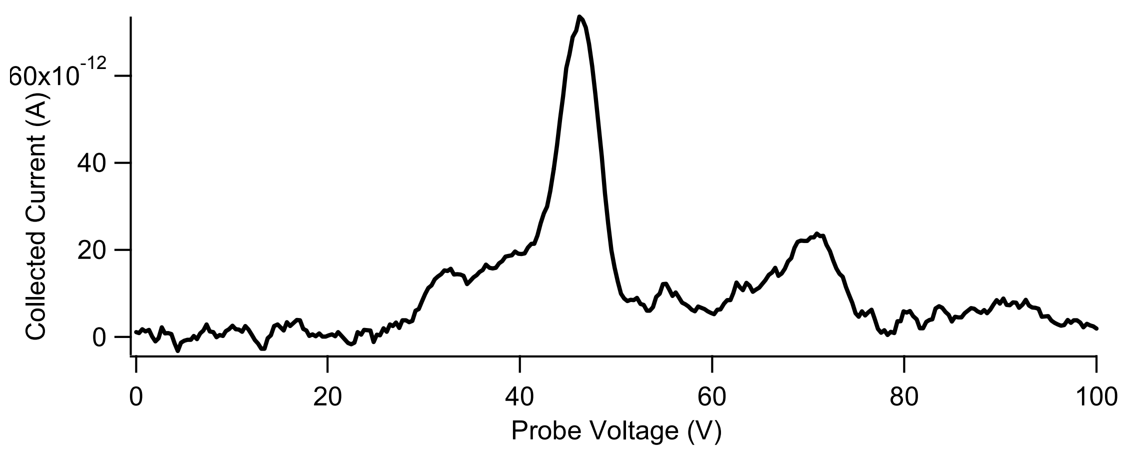

Figure 3-32: ExB probe data collected 60 degrees off centerline.

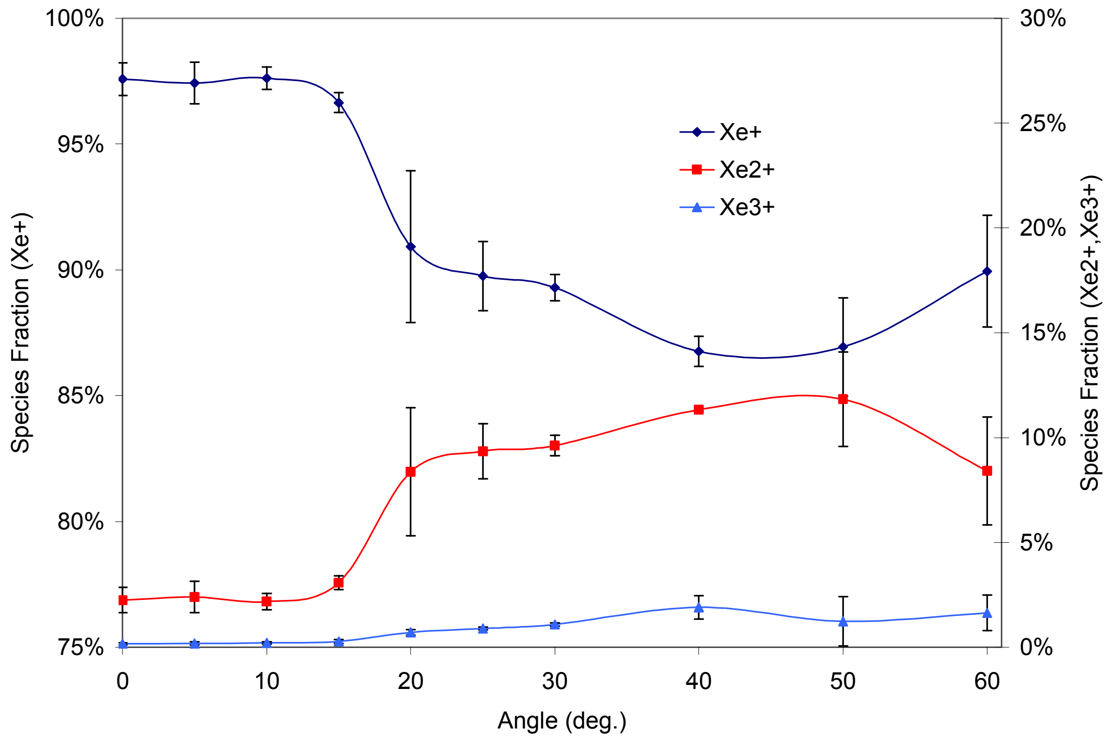

Figure 3-33: Species fractions measured 0.5 m downstream of the BHT-200 using the ExB probe.

As Fig. 3-33 shows, the fraction of singly-charged ions measured near the thruster centerline approaches 97%. Between 15° and 20°, this fraction shifts sharply lower and reaches a minimum of approximately 87% at 40° off centerline. Conversely, the percentage of Xe^{2+} ions is approximately 3% at angles less than 10° and rises sharply between 15° and 20° before reaching a maximum of almost 12% at 50°. The measured Xe^{3+} fraction is less than 2% over the entire angular range.

The measured fraction of singly-charged ions in this work is marginally higher than that reported by previous authors for larger Hall thrusters operating at somewhat higher discharge voltages.[47,52,56] These studies showed the fraction of Xe^{+} to generally fall in the range of 85-95% for thrusters operating at 300 volts. Recent measurements in the plume of an advanced Hall thruster have shown a strong correlation between the thruster discharge voltage and the fraction of multiply-charged ions observed in the plume.[57] The higher fraction of singly-charged ions ejected from the BHT-200 compared to other thrusters is therefore consistent with the lower voltage at which it operates.

The effect of discharge voltage on the fraction of multiply-charged ions can be explained by considering the electron dynamics in the thruster as well as the ionization potentials of xenon. As electrons exit the hollow cathode and diffuse toward the anode, they gain energy due to interactions with the electric field. Although this energy gain is tempered by elastic collisions with both heavy particles and the thruster walls, the electron temperature inside the discharge channel tends to increase as the electrons proceed upstream.[22] Since the source of the energy gain is the electric field, a thruster operating at a lower discharge voltage can be expected to exhibit a lower internal electron temperature than one operating at a higher voltage. The electron temperature is, in turn, related to the fraction of multiply-charged ions through consideration of the ionization potentials of xenon, which are 12.1, 21, and 32 eV for Xe^{+}, Xe^{2+}, and Xe^{3+}, respectively.[71] These potentials indicate that creation of a Xe^{2+} ion from a Xe neutral via electron bombardment requires the impacting electron to have almost twice the energy required to create a Xe^{+} ion. Since the electron temperature is a measure of the width of the Maxwellian electron energy distribution function, the lower electron temperature in a low voltage thruster implies a lower fraction of electrons with sufficient energy to create multiply-charged ions. The high fraction of singly-charged ions seen in the plume of the BHT-200 is thus an intuitive consequence of its low operating voltage.

The increase in the fraction of multiply-charged ions with increasing angle away from the thruster centerline shown in Fig. 3-33 has also been observed in studies of larger Hall thrusters.[56] An explanation for this phenomenon can be obtained by considering the internal plasma parameters measured by Haas along with the discussion of beam divergence given by Kim.[22,56] Since the plasma in the Hall thruster is largely collisionless, ions created in the discharge chamber will travel primarily in straight lines as they are accelerated by the imposed electric field. The angle at which ions can exit the device without striking a wall is therefore dependent on the location at which they are created, as described by Kim and sketched in Fig. 3-34.[56] Ions created further upstream are limited to a narrow band around the thruster centerline while ions created near the thruster exit plane can be directed to large divergence angles.

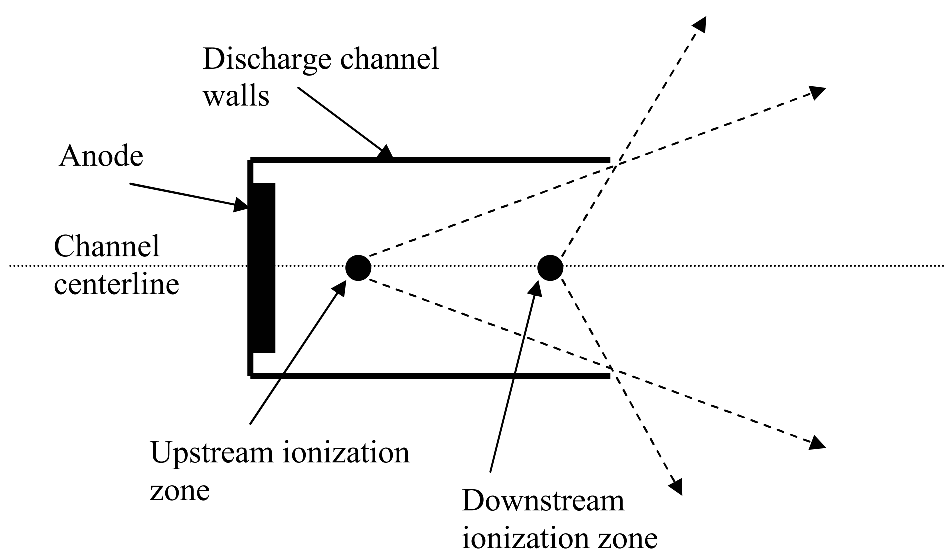

Figure 3-34: Sketch of the possible trajectories of ions created in different locations. Ions created near the exit plane can be directed to higher angles with respect to the centerline than ions created further upstream. (From the discussion in Ref. 56.)

Considering the discussion above, the structure seen in Fig. 3-33 appears to indicate that a larger fraction of the ions created at downstream locations are multiply-charged compared to those created upstream. The measurements obtained by Haas showed two distinct ionization regions inside the discharge chamber of the 5-kW class P5 Hall thruster.[22] The upstream ionization zone occurred in the region of maximum electron temperature. Since the electron temperature in the BHT-200 can be expected to be relatively low, the fraction of multiply-charged ions created in this region as a result of electron thermal motion can also be expected to be low, as discussed above. The second (downstream) ionization zone reported by Haas was attributed to the presence of the azimuthal electron Hall current.[22] The directed azimuthal velocity in this region could be expected to shift the thermal population to higher drift velocities, as sketched in Fig. 3-35, thus increasing the fraction of electrons with sufficient energy to produce multiply-charged ions.

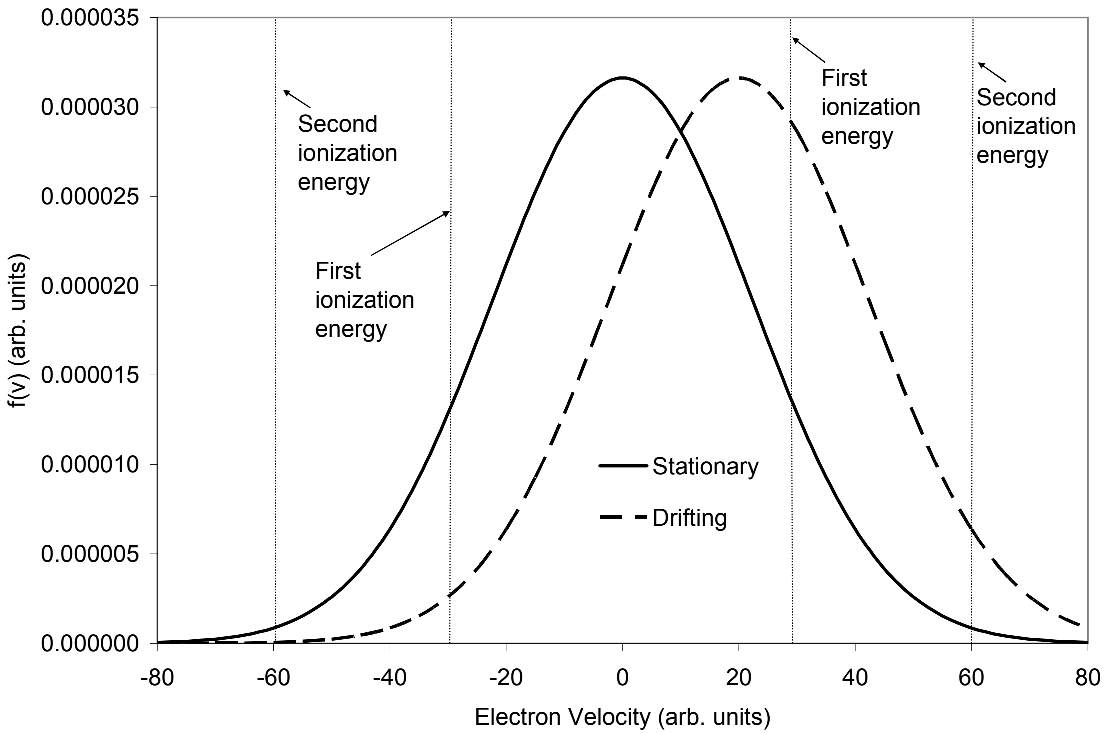

Figure 3-35: Sketch of a stationary Maxwellian electron velocity distribution and a drifting one. Note that the drifting Maxwellian results in a significantly higher fraction of electrons above the second ionization threshold.

From the discussion above and the plot shown in Fig. 3-35, it is clear that addition of a constant drift velocity, v_{drift}, to a thermal population causes an increase in the fraction of the total electron distribution occurring at energies above the second ionization potential. A point that is less obvious, but more important, is that the ratio of electrons with energies above the second ionization potential to those with energies above the first potential must increase in this case. To see this, consider Eqn. 3-8 below, which gives the ratio of electrons with speed greater than the velocity of the first ionization potential of xenon, κ_1, to those with speed greater than the second ionization velocity, κ_2. Taking the electron velocity distribution to be a drifting Maxwellian, as given by Eqn. 3-9, and introducing the error function defined by Eqn. 3-10 allows the ratio to be written in the more direct form of Eqn. 3-11. In the equations below, c depends only on the electron temperature and mass.

$$\Psi = \frac{\int_{-\infty}^{-\kappa_1} f_e(v)dv + \int_{\kappa_1}^{\infty} f_e(v)dv}{\int_{-\infty}^{-\kappa_2} f_e(v)dv + \int_{\kappa_2}^{\infty} f_e(v)dv} \qquad \textbf{Eqn. 3-8}$$

$$f_e(v) = \left(\frac{c}{\pi}\right)^{3/2} \exp\left[-c\left(v - v_{drift}\right)\right]^2 \qquad \textbf{Eqn. 3-9}$$

$$erf(x) \equiv \int_0^x \exp\left(-s^2\right)ds \qquad \textbf{Eqn. 3-10}$$

$$\Psi = \frac{2 - erf\left[\sqrt{c}\left(\kappa_1 + v_{drift}\right)\right] - erf\left[\sqrt{c}\left(\kappa_1 - v_{drift}\right)\right]}{2 - erf\left[\sqrt{c}\left(\kappa_2 + v_{drift}\right)\right] - erf\left[\sqrt{c}\left(\kappa_2 - v_{drift}\right)\right]} \qquad \textbf{Eqn. 3-11}$$

Examination of Eqn. 3-11 shows that Ψ decreases with increasing v_{drift} as long as the trivial condition $\kappa_2 > \kappa_1$ is satisfied. This means that addition of a constant drift velocity, such as that caused by the ExB drift in a Hall thruster, to a thermal electron distribution causes an increase in the ratio of electrons capable of producing multiply-charged ions to those only having at least enough energy to produce Xe^+. Assuming that the internal plasma structure of the BHT-200 is qualitatively similar to that of the P5 studied by Haas, this would explain the higher fraction of multiply-charged ions created at downstream locations in the thruster and the resulting populations of Xe^{2+} and Xe^{3+} shown at high angles in Fig. 3-33.

An additional phenomenon that may contribute to the increase in multiply charged ions at large angles with respect to centerline is “stepwise” or “multi-impact” ionization.[72] In this process, a particle becomes singly-ionized in the upstream ionization zone before undergoing additional collisions in the area of high Hall current density. These additional collisions may then increase the charge state of the ion. Since this process would be expected to create multiply-charged ions near the thruster exit plane, these particles would be capable of being directed to high divergence angles as explained above. Although the ExB probe is incapable of distinguishing multiply-charged ions created in this manner from those created directly from a xenon neutral, some numerical simulations suggest that stepwise ionization may play an important role in the Hall current region.[72]

3.10 Centerline Phenomena

As pointed out throughout this chapter, the properties measured along the centerline of the Hall thruster studied in this work show significantly different properties than the plasma elsewhere in the plume. The most notable difference is in the plasma potential, which was shown in Fig. 3-15 to rise sharply as the centerline is approached from the radial direction. The areas where anomalous plume properties have been measured coincide with the luminous core of the plume, which can be observed visually. In some larger thrusters, the structure along the centerline appears not only as a bright core, but as a cone structure with luminescent boundaries. This structure can be seen in

Fig. 3-36, which shows a picture of the Pratt & Whitney T-140, 3-kW class Hall thruster firing in the LVTF.

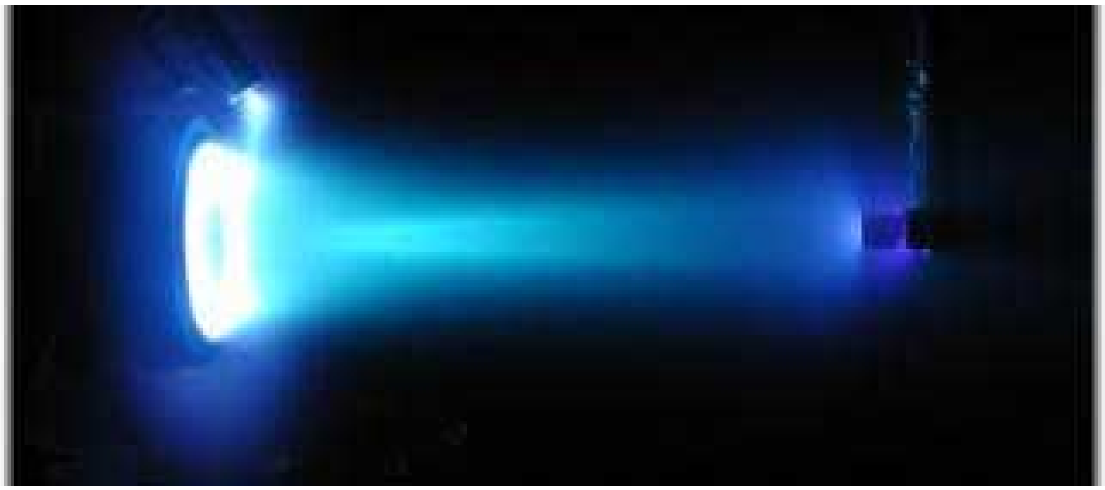

Figure 3-36: The Pratt & Whitney T-140 firing in the LVTF. Note the bright plasma cone seen along the centerline. Photo courtesy of the PEPL website.

One mechanism that has been suggested as a possible explanation for phenomena occurring along the centerline of a Hall thruster is the formation of collisionless shock waves.[5] The following discussion examines several instabilities that may occur in the plasma plume to determine whether the formation of collisionless shocks is feasible for the observed conditions. A low-order model is then presented to provide a qualitative estimate of the changes in plasma properties that could be expected across a shock. Finally, the issue of whether or not the presence of a shock is necessary to explain the observed plasma properties will be addressed.

3.10.1 Two-Stream Instabilities

In an annular thruster, such as the BHT-200-X3, a portion of the accelerated ion beam converges along the thruster centerline. This creates a situation where the ion beam from one part of the thruster passes through its mirror image created in a diametrically opposed location as sketched in Fig. 3-37. There are several instabilities that can be excited in a situation like this, but before discussing them it is useful to consider some of the key plasma parameters in the plume so that these estimates can be used to determine which instabilities are expected to dominate. Table 3-2 presents several important parameters for a plasma with density, n_e=5x10^{17} m^{-3}, and electron temperature, T_e=2 eV, which are approximate values taken from the presented triple probe data. The ion drift velocity, v_{drift}, was estimated by assuming the ions are accelerated through a potential drop of 200 V, which is consistent with the energy spectra presented in Section 3.8. The ion temperature, T_i, was assumed to be 1 eV, which is consistent with laser induced fluorescence (LIF) measurements obtained in the plume of a larger Hall thruster.[38, 73] Measurements of the magnetic field presented in Section 3.5 show the field strength to be approximately 80 gauss along the thruster centerline at an axial distance of 10 mm. By 20 mm downstream the field strength falls to roughly 30 gauss and to less than 10 gauss at a distance of 50 mm. A value of 30 gauss was used to estimate the parameters given in Table 3-2, which are intended only to show the scale of relevant parameters and are not necessarily quantitatively accurate. All quantities were calculated for xenon using approximate numerical formulas.[74]

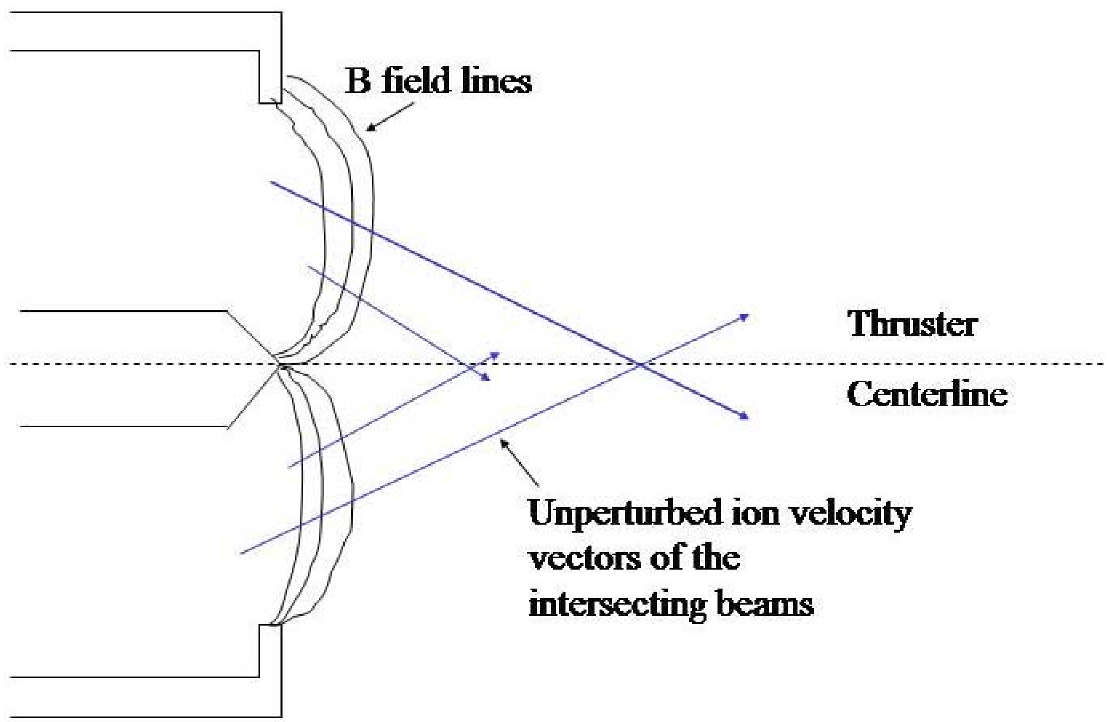

Figure 3-37: Sketch of intersecting ion beams crossing the thruster centerline.

Parameter	Approximate Value
Ion Drift Speed, v_{drift}, (m/s)	17,000
Ion Thermal Speed, v_i, (m/s)	850
Ion Acoustic Speed, C_s, (m/s)	1,500
Electron Thermal Speed, v_e, (m/s)	5.9×10^5
Alfven Speed, C_A, (m/s)	8,000
Beta, $\beta=2\mu_0 n_e k_b T_e/B^2$	0.04
Electron Larmor Radius, r_{Le}, (mm)	1.1
Electron Plasma Frequency, ω_p, (rad/s)	4.0×10^{10}
Electron Cyclotron Frequency, ω_c, (rad/s)	5.3×10^8
Electron Temperature, T_e, (eV)	2.0
Ion Temperature, T_i, (eV)	1.0

Table 3-2: Estimated plasma parameters in the near-field thruster plume.

In a situation where two unmagnetized ion components flow perpendicular to a magnetic field through a background of magnetized electrons there are at least six distinct instabilities that may exist.[75] These instabilities may be divided into two groups based on the frequency of the unstable waves. The higher-frequency "ion acoustic like instabilities" consist of the electron/ion acoustic (sometimes just called ion acoustic), the ion/ion acoustic (or ion/ion two-stream), and the electron cyclotron drift instabilities.[75] The "lower hybrid like instabilities" occur at lower frequencies and include the ion/ion lower hybrid instability and two electron/ion modified two-stream instabilities that can occur between the background electrons and each ion component.[75] Of these two groups, the lower hybrid like instabilities are less likely to occur in the Hall thruster plume for several reasons. First, these instabilities produce a magnetized electron response to the fluctuating fields.[75] Although the electrons are weakly magnetized by the static fields downstream of the Hall thruster, no evidence suggesting the existence of large scale fluctuating fields has been observed. Additionally, all three of the low-frequency instabilities occur at wavelengths that are large compared to the electron Larmor radius (Table 3-2).[75] This suggests that any effects due to this mode are likely to occur over length scales significantly larger than the structure seen in Fig. 3-15.

Of the high-frequency modes, the first to consider is the electron/ion acoustic instability that can occur in current carrying plasmas. This mode is not likely to be significant in the present situation since it has been shown to require $T_e/T_i >> 1$, which is inconsistent with the estimates reflected in Table 3-2.[76, 77] However, even in extreme cases where $T_e/T_i >>1$ (see discussion below), quasilinear theory shows that it generally only serves to flatten the slope of the electron velocity distribution function, df_e/dv, in a relatively narrow region of velocity space[78] and would not be expected to significantly alter macroscopic plasma parameters such as the electron temperature.

The electron cyclotron drift instability may play a crucial role along the centerline of a Hall thruster since it is the only high-frequency instability that persists for $T_e \approx T_i$.[75] This instability occurs as a result of coupling between a Doppler-shifted ion acoustic mode and an electron cyclotron mode[79] and can cause significant heating of the electron component.[80] Additionally, since the unstable waves involved in this instability typically have wavelengths much shorter than the electron gyroradius,[81] this mode is likely to be important in the present situation where the distance over which interactions appear to occur is on the order of the gyroradius.

The final, and perhaps most important, instability to consider is the ion/ion acoustic instability. Given the estimate of $T_e/T_i \approx 2$ reflected in Table I, this mode appears to be stable since it has been shown to require $T_e/T_i >> 1$ in order to grow.[82] This may not be the case, however, when one considers the significant margin of error contained in both the electron and ion temperatures used in the estimate of the temperature ratio. The electron temperature has an estimated uncertainty of 30%, while the ion temperature estimate of 1 eV is taken simply as a typical value from the measured range of 0.4 to 2.0 eV.[38, 73] Considering that numerical studies have shown the threshold value of the electron-to-ion temperature ratio to be approximately 3-4 for intersecting equidensity ion beams,[77] it is entirely possible that this criterion is met in the Hall thruster plume. Further, the electron cyclotron drift instability discussed above has been shown to be capable of causing electron heating over relatively short length scales. It is likely that this scenario could cause the electron-to-ion temperature ratio to increase to the threshold where the ion/ion mode becomes unstable. This phenomenon has been demonstrated by the computer simulations of Schriver and Ashour-Abdalla where initially cold electrons in the Earth's plasma sheet boundary layer are heated by electron/ion instabilities to the point where the ion/ion acoustic instability is excited.[83]

Assuming that the ion/ion acoustic instability is excited in the thruster plume, it can be expected to dominate the other modes discussed here since it has been shown to have the largest growth rate over a wide variety of parameters.[77] A final feature, which is relevant to the upcoming discussion, is the response of this instability to high flow speeds. As the ratio of the relative flow speed between the ion components to the ion thermal velocity is increased, the instability growth rate reaches a maximum and then returns to a stable condition for waves propagating parallel to the flow direction.[77, 84] As this happens, the direction of maximum wave growth shifts to successively steeper angles with respect to the flow.[85] This results in a condition where the instability propagates only at angles strongly oblique to the flow at high relative drift speeds.[77]

3.10.2 Collisionless Shocks

There are several reasons to suspect that collisionless shocks may occur in the plume of a Hall thruster. First, ion acoustic shocks have been proposed as an explanation for the well-defined boundaries of the bright core seen along the centerline of each thruster in Fig. 2-3.[5] Second, LIF measurements obtained by Smith *et al.* show a significant population of ions along the centerline of a Hall thruster having nearly zero radial velocity, but large axial velocity.[86] There is clearly no way for an ion originating in the annular discharge region of a Hall thruster to reach the centerline with zero radial velocity unless it is deflected somehow. Since there is no reason to expect collisions to systematically deflect a significant population into this region of velocity space, it is reasonable to hypothesize that the deflection mechanism may be a collisionless shock propagating obliquely to the flow direction. Finally, it has been well established, both analytically and experimentally, that the ion-ion two-stream instability discussed above can cause the dissipation necessary to form a collisionless shock.[87,88,89,90,91]

Unlike the rationale presented above suggesting the existence of collisionless shocks in the thruster plume, the data presented in Fig. 3-38 suggest that the heating exhibited in the plume may not be “shock-like” after all. Figure 3-38 shows the measured electron temperature as a function of the plasma density at three different axial locations downstream of the thruster. Also shown in Fig. 3-38 is a fit to the recorded data of the form given by Eqn. 3-12, which is derived from a simple plasma equation of state. In Eqn. 3-12, C is a constant and γ is the ratio of specific heats, which is also sometimes referred to as the adiabatic index. For the fit line presented in Fig. 3-38, γ is approximately 1.3. Since none of the data points depicted in this figure show drastic departures from the fit line, it appears that the rise in electron temperature is due to simple compression. On the other hand, the plasma potential measurements presented in Fig. 3-15, as well as the visual evidence, suggest a nearly discontinuous change in the plasma properties. Clearly the data presented in this work are insufficient to either prove or disprove the existence of collisionless shocks in the thruster plume. The following analysis seeks to determine whether or not the existence of such structures is consistent with the observed phenomena and, therefore, whether the hypothesis merits further study.

$$T_e = Cn_e^{\gamma-1} \quad \textbf{Eqn. 3-12}$$

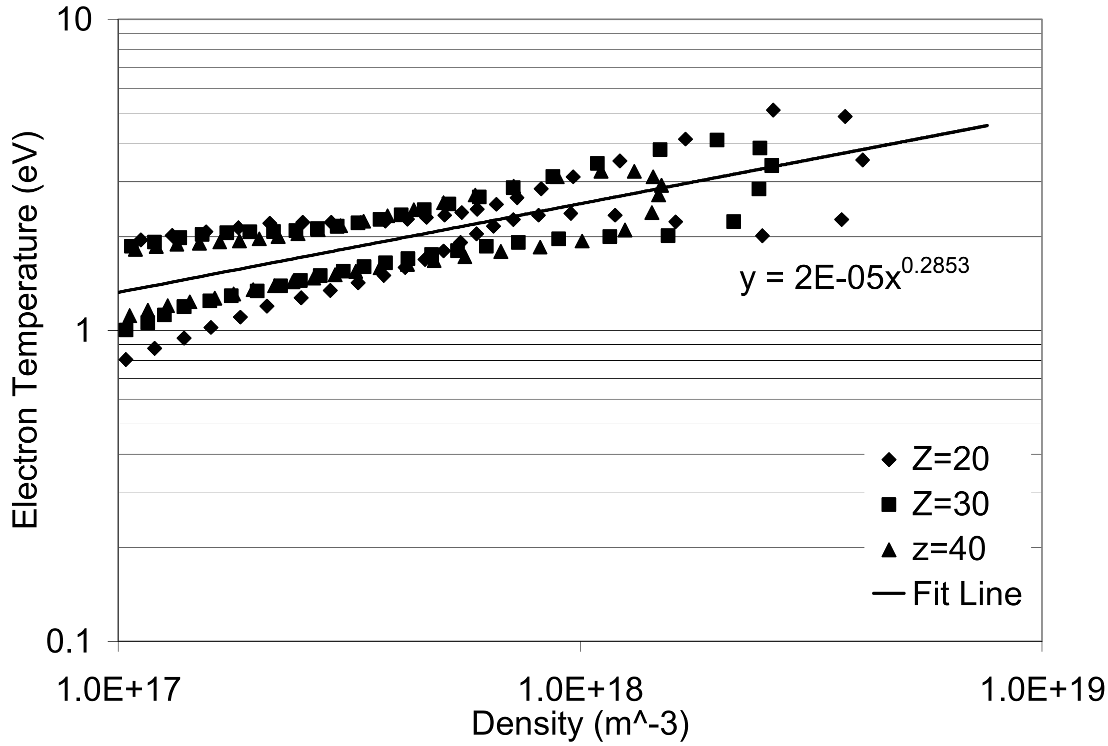

Figure 3-38: The electron temperature and plasma density in the very near-field plume. The two properties appear to be related by an adiabatic law.

Judging by the magnetic field profiles shown in Fig. 3-16 and the orientation of the boundaries of the bright core seen in Fig. 2-3, any shock present in the system is likely to propagate perpendicular to the magnetic field and thus be based on magnetosonic waves.[92] Although it may seem counterintuitive to consider the role of the weak magnetic field downstream of a Hall thruster, Tidman and Krall have shown that magnetosonic waves are dominant over ion acoustic waves in low-beta plasmas such as the one described by Table 3-2.[91] Further, since the magnetosonic shock degenerates into the ion acoustic shock when the magnetic field strength approaches zero,[92] it is possible to consider the former without losing information about the ion acoustic mode that occurs in this limit.

Across a magnetosonic shock, the magnetic field strength increases and an electric field exists that serves to decelerate the positively-charged ions.[93] Interactions with this electric field are the source of the electron heating observed across the discontinuity.[93,94,95] Rather than concentrate on the complexities of these physical mechanisms, however, it is sufficient for the purposes of this study to compare the results presented throughout this chapter to reported shock properties in an effort to determine if the existence of collisionless shocks in the thruster plume is consistent with the observed phenomena. To facilitate this effort, a simple model based solely on geometric arguments and observations of reported shocks is presented below. This method cannot be expected to produce quantitatively accurate results, because it neglects potentially important effects such as the thermal spread of the ion distribution and the change in magnetic field strength across the shock. It does, however, illustrate several properties of the proposed shock. In particular, this model explains how a distinct jump in electron temperature and plasma potential can occur with only a modest rise in plasma density. The geometry and nomenclature used for this simple model are given in Fig. 3-39. It should be understood that this model is only an attempt to provide low-order, qualitative estimates of the changes one could expect if the structures seen along the centerline of many Hall thrusters are due to the presence of collisionless shocks. It is not an attempt to capture the complicated physics that occur in a shock layer.

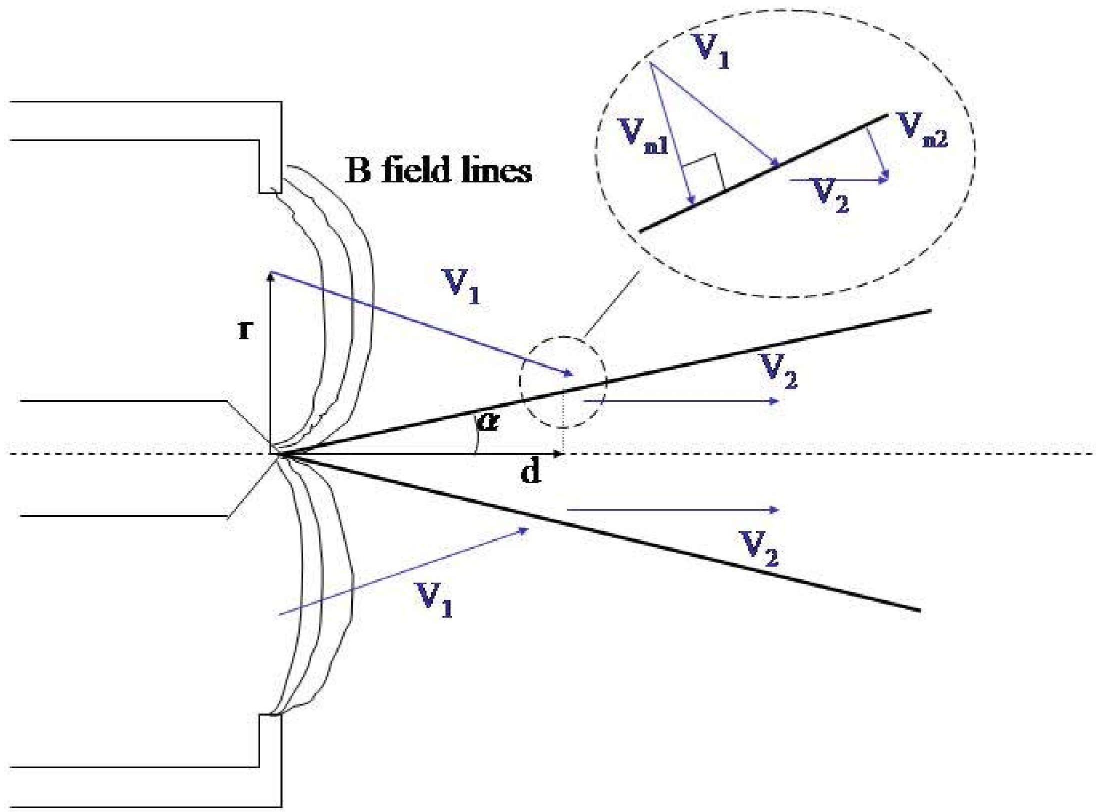

Figure 3-39: Geometry and nomenclature of a crude shock model.

The model illustrated in Fig. 3-39 gives a rough estimate of the changes in plasma properties as a function of the shock divergence angle, α, the radial location in the exit plane where a sample ion is created, r, and the downstream distance where that ion intersects the shock surface, d. The model depends on several limiting assumptions and geometric arguments, namely:

i.) The shock only affects the normal component of velocity such that, $v_{t1}=v_{t2}$, $v_{n1}>v_{n2}$.

ii.) The shock must turn the flow so that downstream of the discontinuity the flow is directed parallel to the thruster centerline.

iii.) Ions follow straight lines from the exit plane to the shock interface and are not subjected to collisions or external electric and magnetic fields.

iv.) At all points for which this model is applied, $r>d\sin(\alpha)$.

The assumptions listed above have several weaknesses. In particular, the assumption that the tangential velocity, v_t, is unchanged is only true for a purely perpendicular (with respect to the magnetic field) shock.[74] In fact, for oblique shocks, the change in tangential velocity can be related to the magnetic field deflection through the shock. Ignoring this change in the present model allows us to proceed without considering the details of the magnetic field and is equivalent to assuming that the shock geometry is such that the change in tangential velocity is small compared to the change in normal velocity. Additionally, assumption ii) overstates the change in plasma flow because a shock need only rearrange the velocity distribution such that the downstream distribution is stable. It does not necessarily turn all ions parallel to the centerline. Assumption iii) is not strictly accurate for a Hall thruster plume since it is widely acknowledged that a significant portion of the ion acceleration occurs downstream of the exit plane.[42] Assumption iii) restricts the model to cases where the change in energy associated with the magnetic field is small compared to the change in kinetic and thermal energy across the shock. The cumulative effect of these weaknesses is to limit the range of parameters over which the model gives reasonable results. Specifically, this simple model is only valid for d/r ≥ 3 such that the change in ion direction is not too large.

Using the assumptions mentioned above, it is possible to write the normal component of upstream and downstream ion velocity as given by Eqns. 3-13 and 3-14. These can then be used to calculate the change in number density and velocity across the shock as given by Eqn. 3-15. The electrostatic potential jump is, in general, dependent upon the frame in which it is measured.[93,95] For the relatively weak shocks considered here, however, the frame dependence can be ignored and the potential jump can be estimated as the change in ion kinetic energy as given by Eqn. 3-16.[96,97] The electron temperature jump across a collisionless shock is shown empirically to be 5-20% of the incident flow ram energy.[94,98] An estimate for the jump in electron temperature is given by Eqn. 3-17, where ζ is an empirical coefficient representing the fraction of dissipated ion kinetic energy that is converted to electron thermal energy.

$$\frac{v_{n1}}{v_1} = \frac{\cos(\alpha)}{\sqrt{\left(1 - \frac{d}{r}\tan(\alpha)\right)^2 + \left(\frac{d}{r}\right)^2}} \qquad \textbf{Eqn. 3-13}$$

$$\frac{v_{n2}}{v_1} = \sin(\alpha)\left[\frac{\frac{d}{r} + \frac{d}{r}\tan^2(\alpha) - \tan(\alpha)}{\sqrt{\left(1 - \frac{d}{r}\tan(\alpha)\right)^2 + \left(\frac{d}{r}\right)^2}}\right] \qquad \textbf{Eqn. 3-14}$$

$$\frac{n_2}{n_1} = \frac{v_{n1}}{v_{n2}} = \frac{\cot(\alpha)}{\frac{d}{r} + \frac{d}{r}\tan^2(\alpha) - \tan(\alpha)} \qquad \textbf{Eqn. 3-15}$$

$$\Delta\phi \cong \frac{m_i}{2e}\left(v_{n1}^2 - v_{n2}^2\right) \qquad \textbf{Eqn. 3-16}$$

$$\Delta\left(\frac{k_B T_e}{e}\right) \cong \frac{\zeta m_i}{2e}\left(v_{n1}^2 - v_{n2}^2\right) \qquad \textbf{Eqn. 3-17}$$

Considering the discussion above, an increase in plasma potential without a pronounced jump in plasma density above that expected from radial convergence can be explained as being related to the large mass of a xenon ion. A small change in ion velocity causes an equally small change in number density, but a relatively large change in kinetic energy due to the large ion mass. As Eqns. 3-15 through 3-17 demonstrate, the change in number density depends only on the velocity change across the discontinuity while the electron temperature and plasma potential changes also depend on the ion mass. Consequently, the change in plasma potential is quite noticeable because it is directly related to the kinetic energy lost by the ions rather than the density ratio across the shock, and therefore to relate the two quantities, it is necessary to assume an initial ion velocity. Figure 3-40 shows the predicted electron temperature change for various values of ζ as a function of the density jump across a shock with α=10° for 200 volt xenon ions using the simple model. The predicted change in plasma potential is also presented. As this figure shows, significant changes in electron temperature and plasma potential can occur across a shock even for a relatively modest change in plasma density. For example, if one uses the crude model discussed above and considers a shock divergence half angle of 10°, as observed by Hruby *et al.*,[5] and an initial ion kinetic energy of 200 volts, the plasma potential change of roughly 8 V shown in Fig. 3-15 corresponds to a density change of only about 30%.

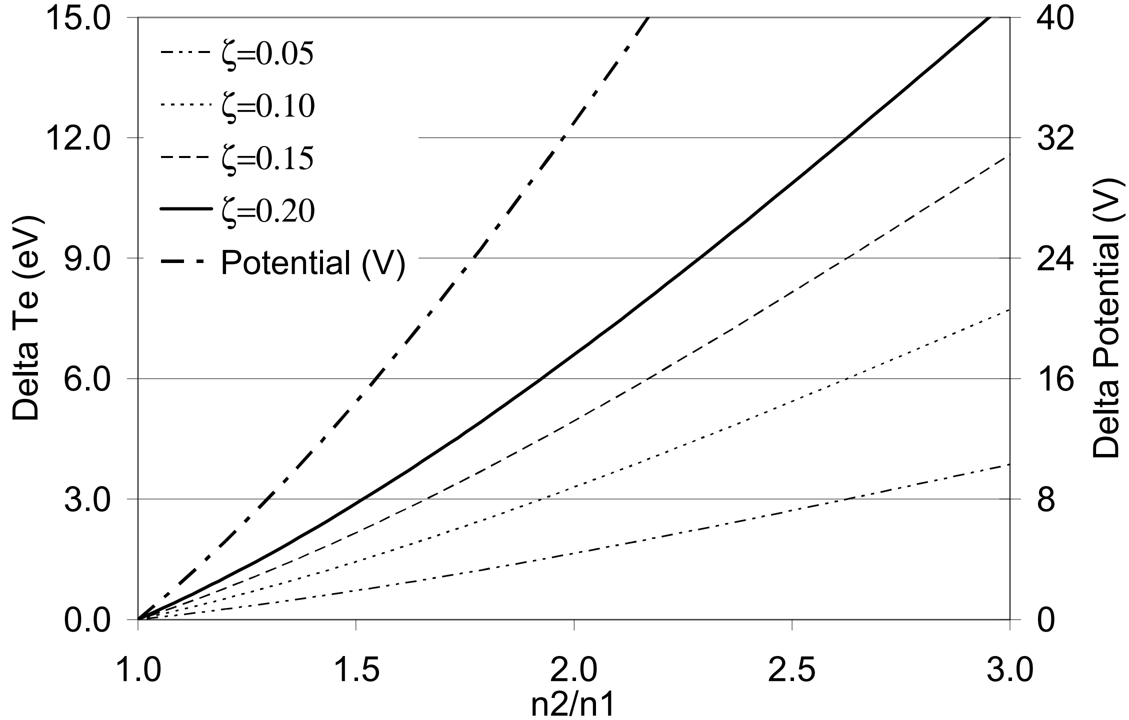

Figure 3-40: Estimated change in plasma potential and electron temperature as a function of electron temperature calculated using a simple model for a 10 degree shock angle and 200 volt xenon ions.

The discussion above shows that collisionless shocks are indeed a feasible explanation for the changes observed near the thruster centerline. The question now becomes whether or not the existence of a shock is a necessary condition to account for the observations. As noted previously, the correlation between the electron temperature and plasma density shown in Fig. 3-38 suggests that the plasma properties are governed by a simple adiabatic relation. The sharp change in plasma potential shown in Fig. 3-15, on the other hand, seems to support the shock hypothesis. This may not be the case, however, when one considers that the rise in plasma potential really only indicates a transfer of energy from the drifting ions to the potential field. It is entirely possible that this may occur without the presence of a shock. For example, the ion-ion two-stream instability may dissipate significant ion energy over a short distance to account for the observed potential rise without forming a shock layer. Due to the lack of direct evidence for the existence of a shock and the availability of alternative explanations, it must be concluded that the collisionless shock hypothesis is a feasible, but unnecessary, explanation for the observed phenomena.

4. CLUSTER CHARACTERIZATION – NOMINAL CONFIGURATION

Having thoroughly characterized the properties of a single BHT-200 Hall thruster in Chapter 3, it is now possible to examine the effects of clustering by operating multiple identical thrusters in close proximity to each other. This chapter presents measurements made downstream of a cluster of thrusters and compares the observed plasma plume properties to those measured downstream of a single thruster. These data are then used as verification of an analytical method for estimating the plasma properties downstream of a cluster based solely on knowledge of the plume structure of a single thruster. All of the measurements presented throughout this chapter were taken with the cluster in the nominal configuration described previously, i.e. each thruster was operated independently from the others using its own set of power supplies. Each thruster was coupled to its own floating hollow cathode.

4.1 Discharge Current Characteristics

To determine whether or not multi-thruster operation affects the basic operation of individual devices, the discharge currents of clustered thrusters were recording using the same oscilloscope and current probes referred to in Section 3.1. The natural discharge oscillations of TH 3&4 are shown in Fig. 4-1, while Fig. 4-2 depicts similar information for TH 2&3 running simultaneously. During each set of measurements, only the thrusters whose currents are shown were operating at the time. The first point to note from these figures is that the phases of the discharge current oscillations appear to be completely decoupled from each other. Additionally, Fig. 4-2 shows that the magnitude of the current oscillations can vary between two adjacent thrusters since the oscillations in thruster 2 are seen to be somewhat lower in amplitude than those of thruster 3. This slight variation has no discernible effect on the overall operation of the thrusters. All of the current traces in Figs. 4-1 and 4-2 exhibit characteristic frequencies near the 25 kHz (± 7 kHz) recorded with a single thruster in operation.

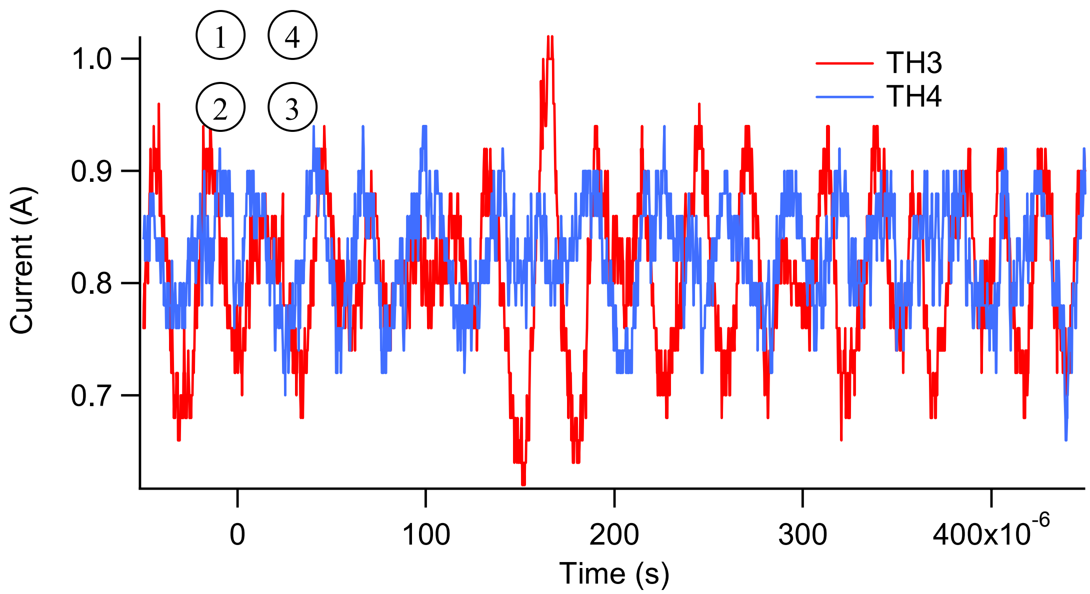

Figure 4-1: Natural discharge oscillations of TH 3&4 operating in the nominal configuration. The cartoon in the upper left-hand corner is a reminder of the thruster numbering convention.

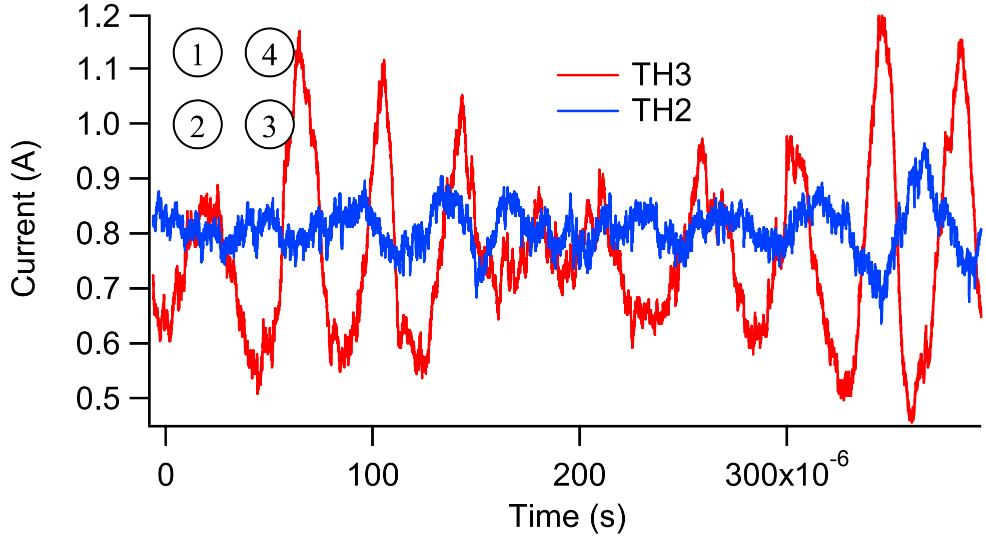

Figure 4-2: Natural discharge oscillations of thrusters 2 and 3.

To check for cross-talk between the engines, the current interrupt switch was used to disrupt the current to anode 3 while recording the response of both thrusters 2 and 3. Figure 4-3 displays the response of both thrusters to a disruption of approximately 10 microseconds. After the interruption, TH3 exhibits the same characteristics observed during single thruster operation with the current initially overshooting the nominal level before returning to its original state with low-level oscillations. The discharge current of TH2 appears to be unperturbed by the short duration interruption to TH3.

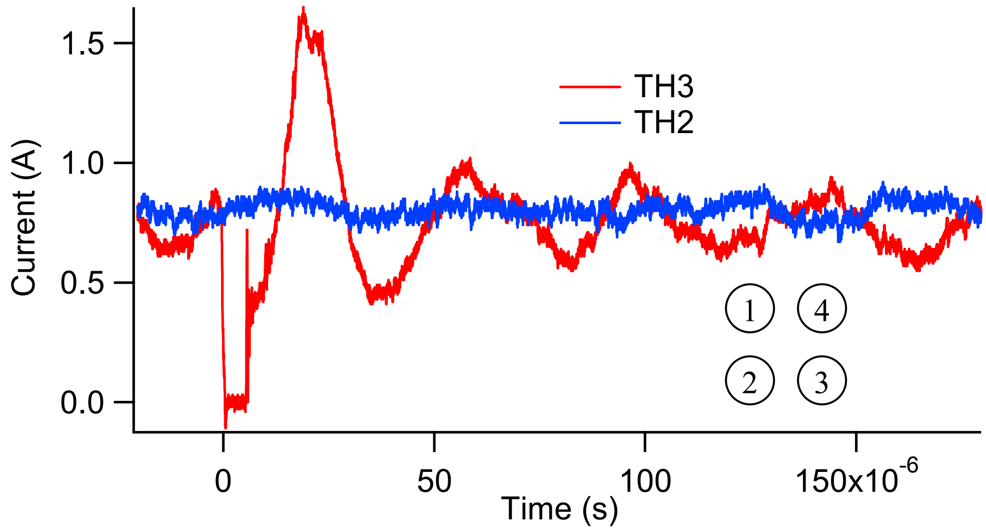

Figure 4-3: The response of TH 2& 3 to a 10 microsecond disruption to the discharge current of TH3. TH2 appears to be unaffected. The thruster naming convention is displayed in the lower right corner.

In an effort to induce cross-talk between the devices, the duration of the disruption to TH3 was increased to 100 microseconds for the current traces shown in Fig. 4-4. In this case, thruster 2 does seem to respond to the interruption of TH3's discharge current. When the current to thruster 3 is switched off thruster 2 does not show an appreciable response, but when the current to thruster 3 is switched back on TH2 responds by increasing its current. The spike in TH2's discharge current corresponds temporally to the "recovery overshoot" of thruster 3. Although only a single set of current traces are presented here, the structures shown in Fig. 4-4 are repeatable. When the current disruption duration is increased to more than about 150 microseconds, TH3's discharge is extinguished. For this reason, 100 microseconds is the longest interruption studied. Note that in Fig. 4-4 the discharge current of thruster 2 is plotted on a much smaller scale than that of thruster 3 for clarity.

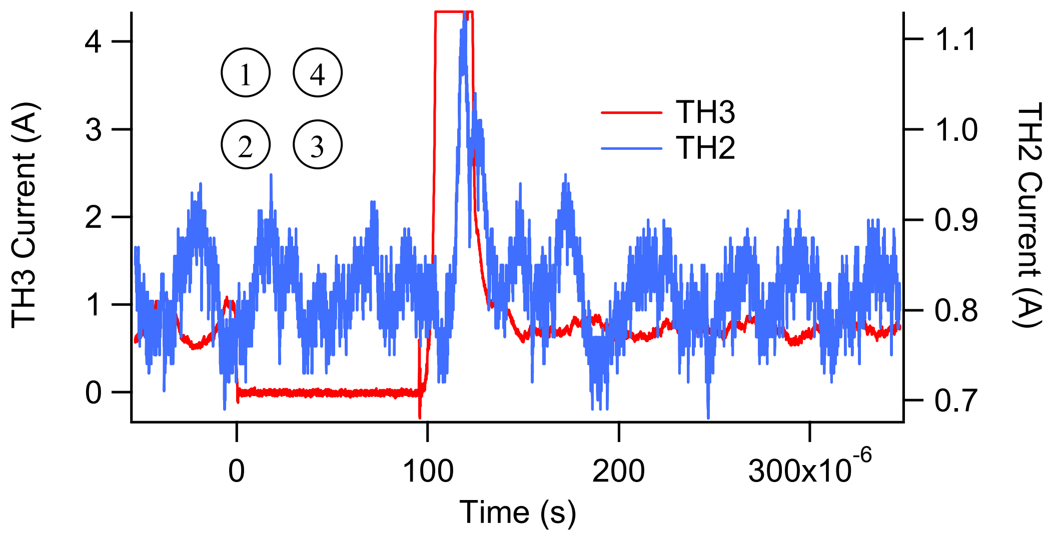

Figure 4-4: Response of engines 2 and 3 to a 100 microsecond current interruption to TH3. When the current to TH3 recovers, TH2 responds with a modest current spike.

Since thrusters 2 and 3 are electrically independent of each other, there are two apparent mechanisms that could account for the coupling seen in Fig. 4-4: magnetic induction through the thruster wiring and cross-talk through the plasma plume. That the response seen in Fig. 4-4 does not appear to be due to magnetic induction can be seen by considering the simple sketch shown in Fig. 4-5. Figure 4-5 shows a long conductor, such as the feed wire to thruster 3, next to the loop formed by the feed and return wires to thruster 2. When the current through thruster 3, I_3, increases as a function of time, the local magnetic field also increases according to the Biot-Savart law. The time-varying change in the magnetic flux through the loop formed by the wires to thruster 2 leads to an induced current in the circuit, I_{i2}, as stated in Eqn. 4-1. Since the induced current to circuit 2 is directly related to the time rate of change of I_3, one would expect to see perturbations to discharge current 2 during both the rise and fall of current 3 if the coupling depicted in Fig. 4-4 were due to magnetic induction in the thruster wiring. The fact that Fig. 4-4 shows only a single spike in the current to thruster 2 leads to the conclusion that the interaction seen in this plot is not likely to be caused by magnetic interference through the wiring.

$$\frac{dI_3}{dt} > 0 \Rightarrow \frac{dB}{dt} > 0 \Rightarrow I_{i2} < 0 \qquad \textbf{Eqn. 4-1}$$

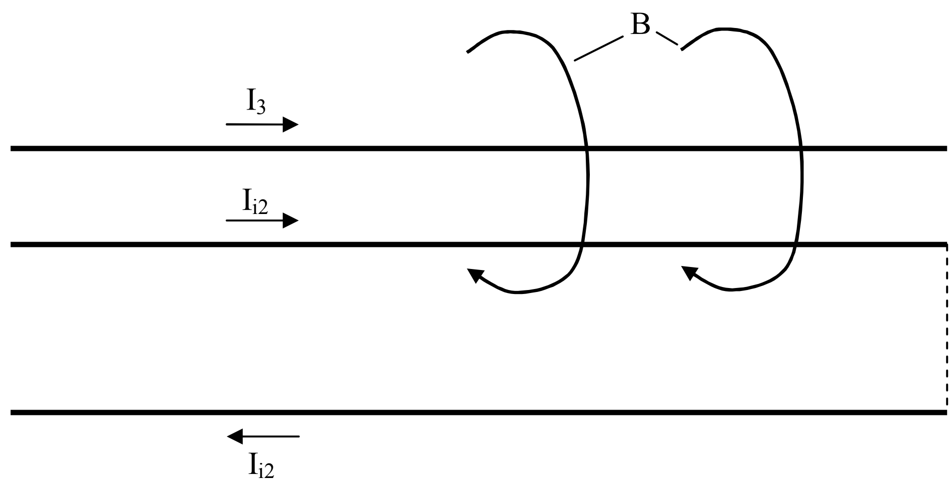

Figure 4-5: Mechanism of interaction between thruster discharge circuits. The interaction shown in Fig. 4-4 does not appear to be due to inductive coupling.

Having decided that the modest coupling between the thrusters shown in Fig. 4-4 is not likely to be caused by magnetic interference through the feed circuits, the most likely remaining explanation is cross-talk through the plasma plumes caused by changes in the resistivity of the plasma. Although the resistivity of a fully-ionized plasma is generally considered to be independent of density, this is not the case for a partially-ionized medium such as the one found in the plume of a Hall thruster.[78] In this case, the resistivity is inversely proportional to the number of charge carriers present. It follows that the increase in local plasma density resulting from the rapid ionization and efflux of propellant from thruster 3 immediately following the imposed current interruption should lead to a slight reduction in the resistivity of the plume. In response to the reduced resistivity, the discharge current of thruster 2 would be expected to increase slightly as seen in Fig. 4-4. This explanation is supported by the fact that interactions between the thrusters were only observed for very long disruptions of the discharge current, which led to transient current levels in thruster 3 in excess of five times the nominal value of 0.80 amps.

Although the discussion above indicates that it is possible to induce weak coupling between the thrusters of a cluster, the most important question for spacecraft designers is what implication, if any, this has for the design of power processing units (PPUs). Since interactions between the thrusters were only visible when one thruster was intentionally disrupted, and only then when the perturbation was near the most extreme that could be obtained by a current interruption, it is unlikely that any coupling between adjacent thrusters would be observed in space during normal thruster operation. Further, because the response induced in thruster 2 was of nearly the same magnitude and time scale as the fluctuations that occurred spontaneously in a single thruster, interactions between devices are not believed to impose any design constraints on PPUs intended for clustering. Any spacecraft electronics capable of dealing with the naturally occurring oscillations of a single Hall thruster are not apt to be adversely affected by the minimal degree of coupling observed between the devices in this work.

4.2 Magnetic Field Profiles

The magnetic field downstream of the cluster was recorded using the same Bell Model 7030 gaussmeter described in Chapter 3. Like the single thruster data, these measurements were obtained with the electromagnets energized, but with no plasma present. Figures 4-6 and 4-7 show the magnetic field profiles recorded in the XZ plane of thrusters 2 and 3 and in the YZ plane of thrusters 3 and 4, respectively. The differences in these plots are attributable to the different direction of magnet current flow between thrusters 2 and 4. Thrusters 2 and 3 were operated with the electromagnets in the nominal configuration while the magnet current flow was reversed in thruster 4. Reversing the polarity of electromagnets in alternate thrusters of a cluster has been suggested as a means of canceling the disturbance torques that typically result from the slight ExB drift of the beam ions.[28,29,99] Although the configurations displayed in Figs. 4-6 and 4-7 show different magnetic field shapes, reversing the magnet direction in TH4 had no apparent effect on the operation of the cluster or on the plasma properties in the plume. These data will be referred to later in this chapter to test the previously published theory that the plasma potential profiles downstream of a cluster can be predicted from measurements of the applied magnetic field.[65]

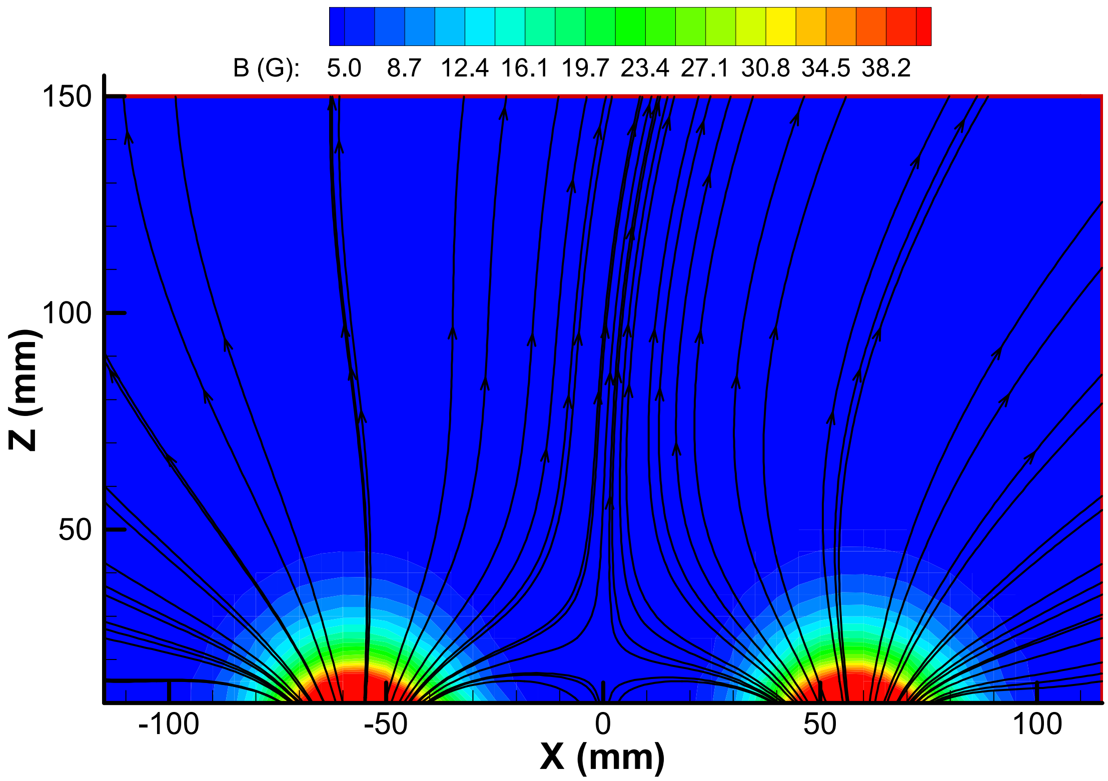

Figure 4-6: The magnetic field profiles measured in the XZ plane of thrusters 2 and 3. The colors represent magnetic field strength while the vectors show orientation.

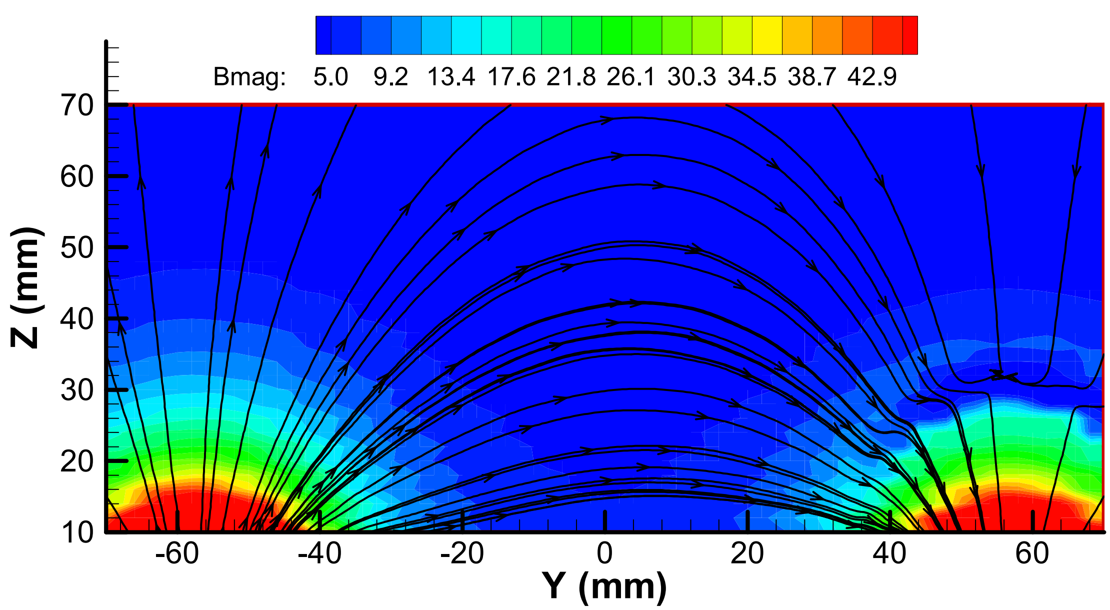

Figure 4-7: Magnetic field profiles in the YZ plane of thrusters 3 and 4. The direction of current flow to electromagnet 4 was reversed from nominal.

4.3 Plasma Density

The larger triple Langmuir probe was used to measure the plasma number density at 5 mm intervals in the cluster plume. Data were recorded in both the XZ plane of TH 2&3 and the YZ plane of TH 3&4. For both planes, measurements were obtained with each thruster operating alone and with two thrusters operating simultaneously. Due to the good agreement between the two data sets, only the data recorded in the YZ plane of TH 3&4 are reported here.

The plasma density profiles recorded downstream of thrusters 3 and 4 are shown in Fig. 4-8. As this plot shows, the maximum number density 50 mm downstream of the cluster exit plane is approximately 1×10^{18} m^{-3}, just as it is downstream of a single thruster. The density falls off rapidly in the downstream direction and by Z=250 mm the maximum plasma density has decreased by more than an order of magnitude to about 3×10^{16} m^{-3}. Figure 4-8 shows a well-defined jet structure downstream of each individual thruster. By about 250 mm downstream the plumes have merged to the point that the density is nearly constant across the width of the cluster and resembles the profile that would be expected downstream of a large monolithic thruster.

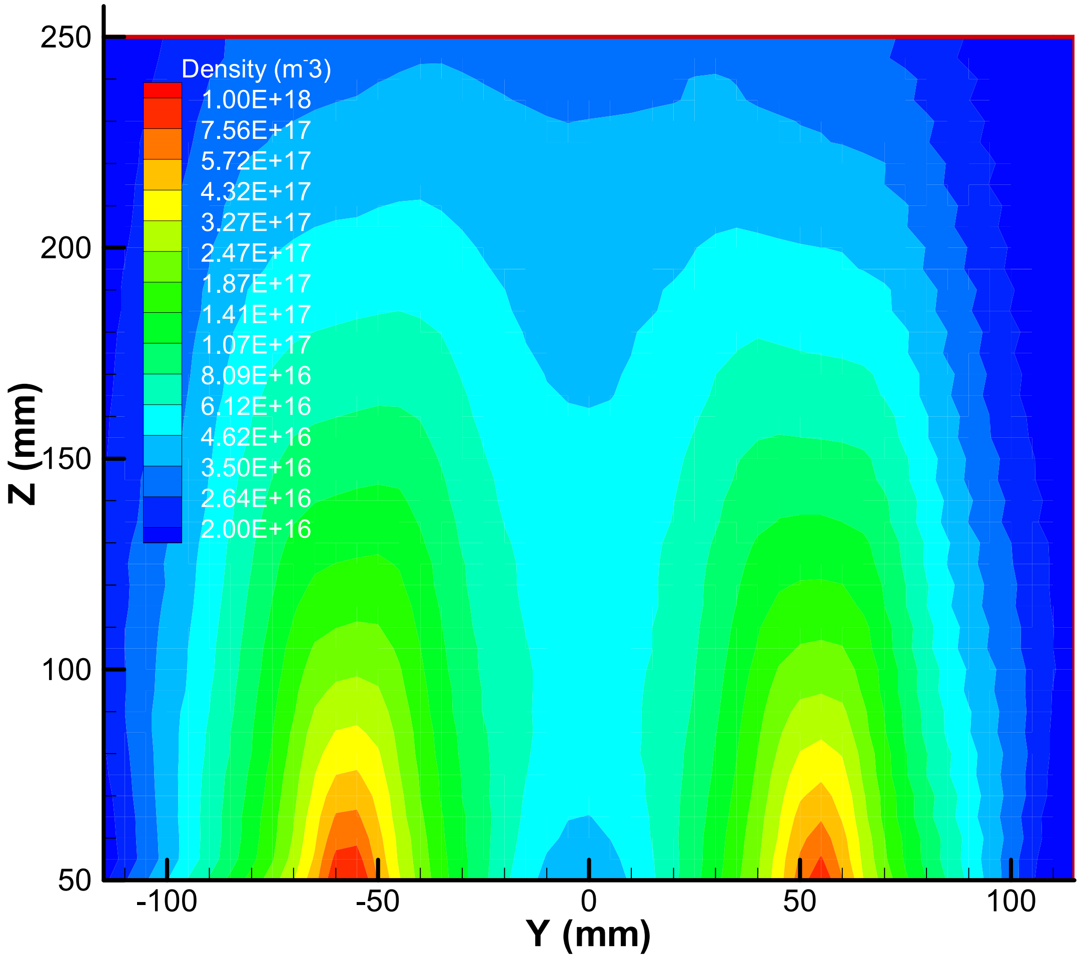

Figure 4-8: Plasma number density downstream of thrusters 2 and 3. Measurements were taken using the large triple probe at 5 mm intervals in each direction.

Figures 4-9 through 4-13 show plasma density profiles measured at axial locations ranging from 50 to 250 mm downstream of the cluster exit plane. The black lines in these graphs were calculated by simply summing the densities obtained with thrusters 3 and 4 running individually. The measurements taken with both thrusters operating simultaneously agree with the calculated values to within approximately 10%, which is well within the margin of error of the triple probe diagnostic. This implies that the density in a cluster plume can be predicted by summing the contributions of each thruster according to Eqn. 4-2, where the subscript j refers to each individual thruster. It should be noted that the values obtained using Eqn. 4-2 appear to slightly underpredict the measured values, particularly at locations far downstream of the cluster. The difference between measured and predicted values, however, is always much less than the uncertainty in the diagnostic and is not believed to be indicative of a flaw in the prediction method.

$$n = \sum_j n_j \qquad \textbf{Eqn. 4-2}$$

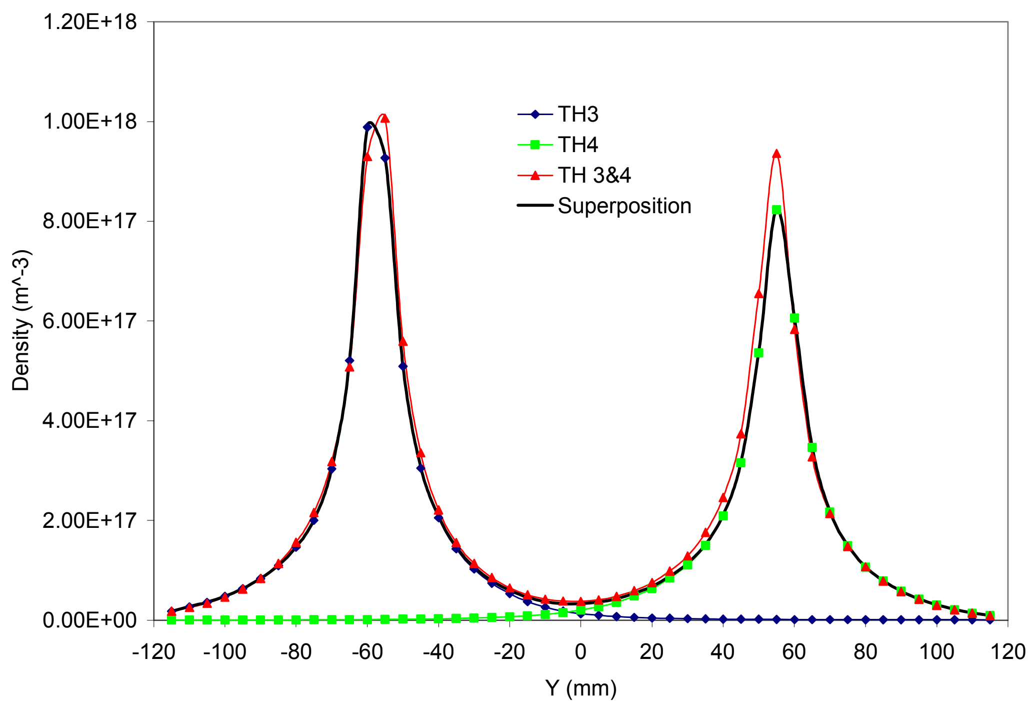

Figure 4-9: Plasma density recorded 50 mm downstream of TH 3&4 using the triple probe.

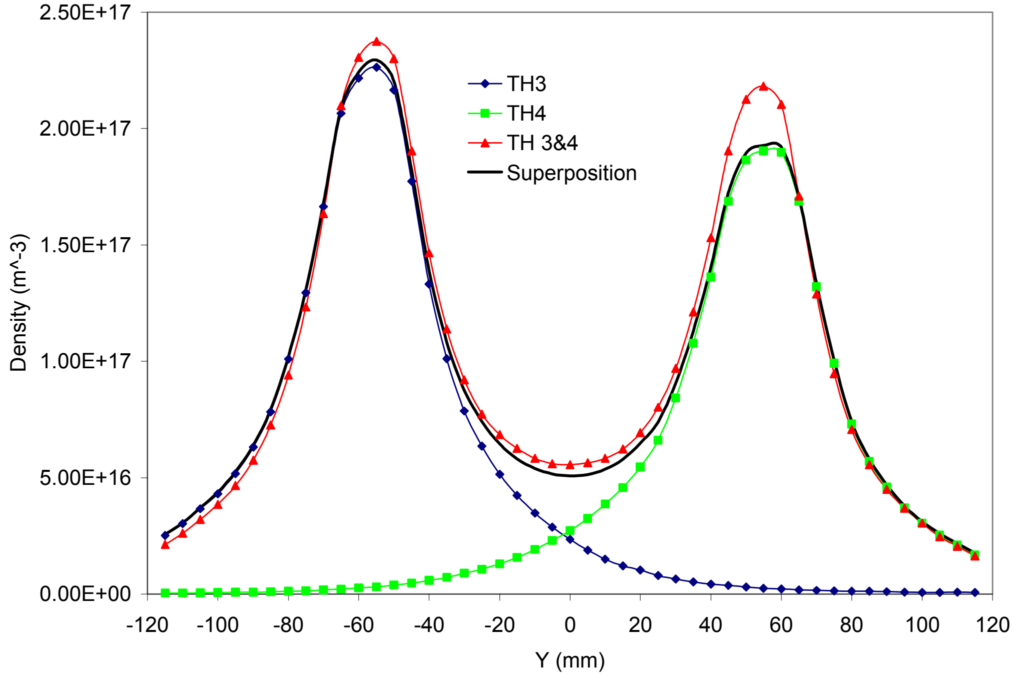

Figure 4-10: Plasma density 100 mm downstream of thrusters 3 and 4.

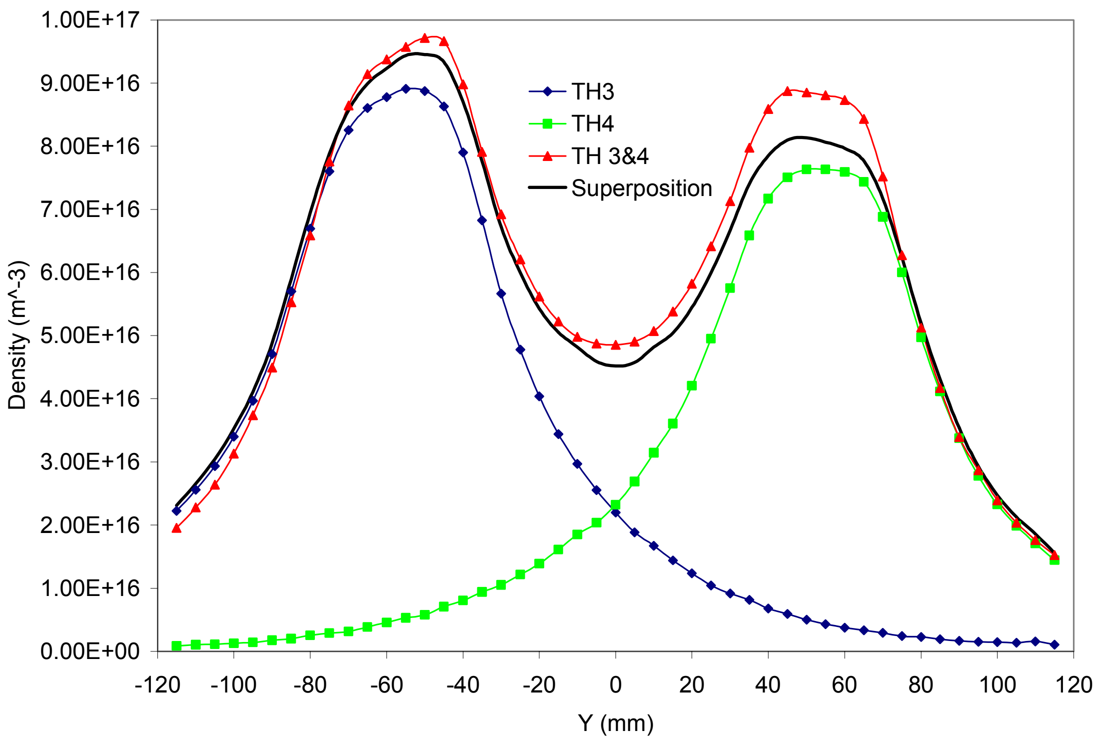

Figure 4-11: Plasma density 150 mm downstream of thrusters 3 and 4.

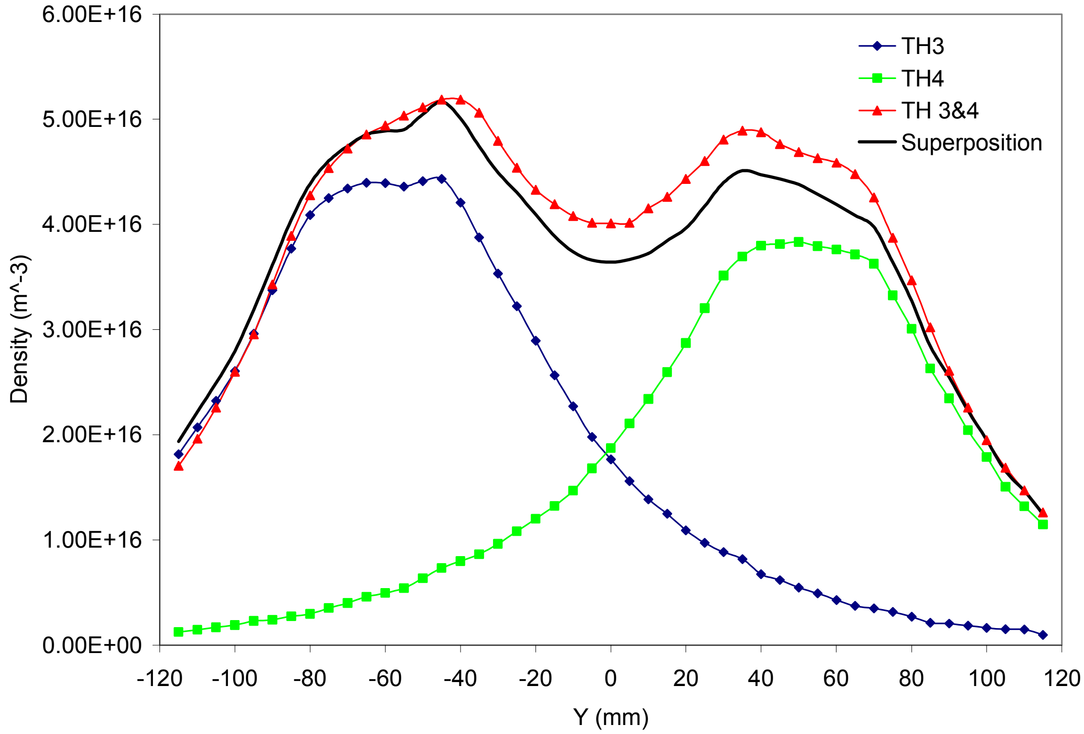

Figure 4-12: Plasma density 200 mm downstream of TH 3 & 4.

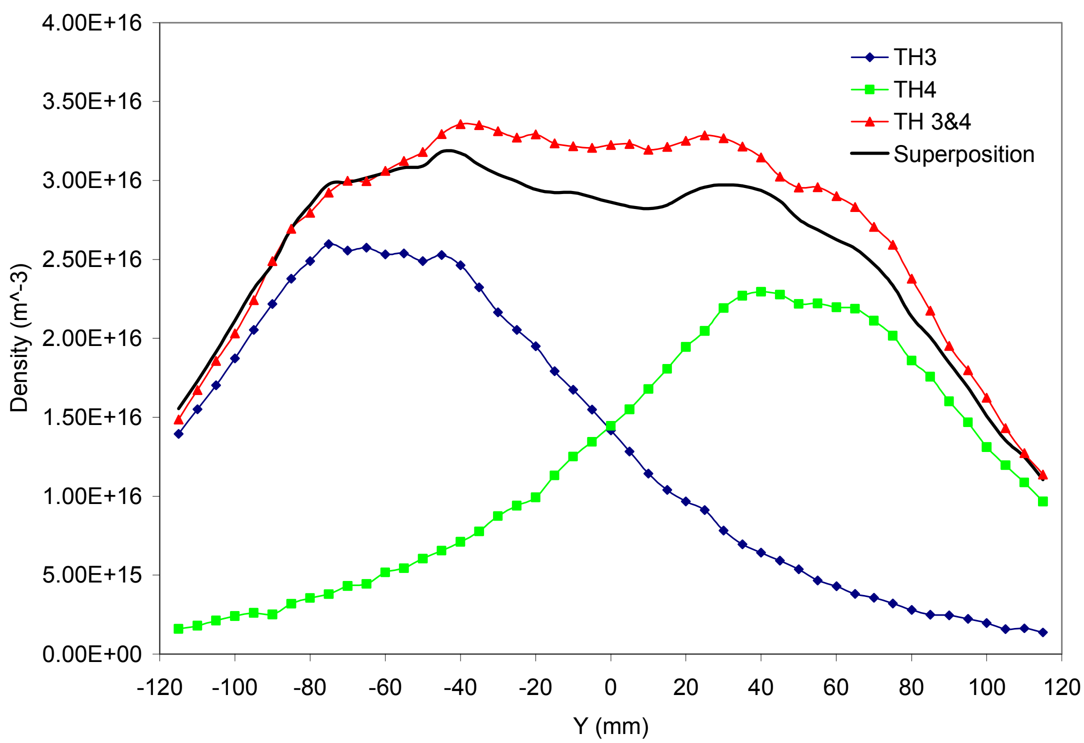

Figure 4-13: Plasma density recorded 250 mm downstream of thrusters 3 and 4. Note the agreement between the measured values and those obtained by linear superposition.

4.4 Electron Temperature

The electron temperature contours recorded downstream of TH 3&4 at 5 mm intervals using the triple probe are displayed in Fig. 4-14. The temperature varies between roughly 3 eV at Z=50 mm along the thruster centerlines to less than 1 eV near the boundaries of the sampled region. The data show slight discrepancies in the electron temperature measured in the near-field of each individual thruster. Measurements recorded downstream of thrusters 2 and 3 (not shown) indicate similar differences, thus the variations are not believed to be a result of the reversed magnetic field profiles mentioned previously. Rather, the discrepancies are probably due to tolerances in the manufacturing process or differences in the cumulative time of operation between the devices. The difference in the electron temperature in front of each thruster decreases as a function of downstream distance and by roughly Z=90 mm the difference between the two units becomes negligible.

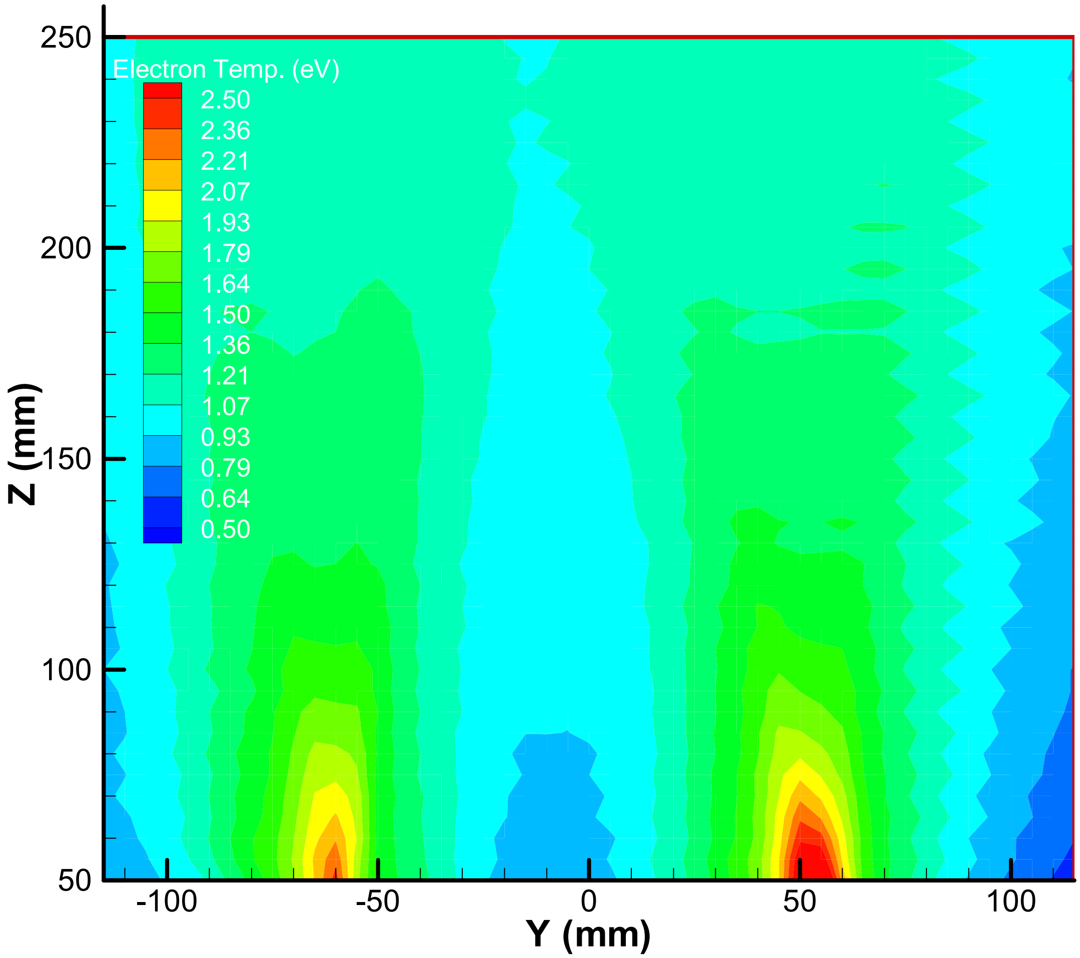

Figure 4-14: Electron temperature contours measured downstream of thrusters 3 and 4 using the triple probe. The slight asymmetry observed in the near-field disappears by about Z=90 mm.

Electron temperature profiles measured at axial locations ranging from 50 to 250 millimeters downstream of thrusters 3 and 4 are shown in Figs. 4-15 through 4-19, respectively. These plots show data recorded with each thruster running individually and with both thrusters running simultaneously in the nominal configuration. Three different methods have been examined for predicting the electron temperature in the cluster plume based on measurements downstream of a single thruster. The first method is to calculate a density weighted average of the contributions from each thruster according to Eqn. 4-3.

This simplistic method is based on conservation of energy and gives the electron temperature that would be expected if the electron populations from each thruster mixed together to create a single Maxwellian population. Clearly, this is an oversimplification of the true physics, which include some degree of energy transfer between the electrons and the heavy particles due to collisions and ionization. Nevertheless, values calculated using this method agree with the measured values to within about 0.2 eV, which is within the absolute uncertainty of the diagnostic for the temperatures present in the plume. The largest discrepancies between the measured and calculated values occur in areas between the thrusters, and the magnitude of the disagreement increases slightly as a function of axial distance. Predictions derived from Eqn. 4-3 are represented by the thick black lines in Figs. 4-15 through 4-19.

$$\frac{k_b T_e}{e} = \frac{\sum_j n_j \frac{k_b T_{ej}}{e}}{\sum_j n_j} \qquad \textbf{Eqn. 4-3}$$

The second method examined for predicting the electron temperature in the cluster plume uses the thermodynamic equation of state presented earlier as Eqn. 3-11. Assuming the constant in this expression remains truly constant throughout the plume, rather than a weak function of the plasma parameters, allows the electron temperature to be related to the density in the plume according to Eqn. 4-4. In Eqn. 4-4 the values $T_{e,0}$ and $n_{e,0}$ refer to reference values measured at some location in the plume. In the present case, the reference values ($n_{e,0} = 9.89 \times 10^{17}$ m^{-3} and $T_{e,0} = 2.56$) were taken from the measurements obtained 50 mm downstream along the centerline of thruster 3 when it was the only engine in operation. The densities used in Eqn. 4-4 are the ones calculated in the previous section by superimposing the densities measured with thrusters 3 and 4 running individually. The ratio of specific heats, γ, is taken to be 1.3, which was shown in Fig. 3-38 to give a good fit to the measured single thruster data. This empirically determined value of γ is interesting because it falls approximately halfway between the two values that one may reasonably expect *a priori*: γ=1 for isothermal electrons and γ=1.67 for adiabatic compression of a monotonic gas. That the observed value falls between these limits suggests that the expansion of the plume occurs too slowly for the electrons to remain strictly isothermal, but too quickly for the purely adiabatic value to hold. In other words, the time scale associated with the plume expansion appears to be on the order of the time required for perfectly adiabatic expansion. Electron temperatures calculated using Eqn. 4-4 are represented by the dashed lines in Figs. 4-15 through 4-19.

$$T_e = T_{e,0}\left(\frac{n_e}{n_{e,0}}\right)^{\gamma-1} \qquad \textbf{Eqn. 4-4}$$

As the figures below show, the electron temperatures predicted by Eqn. 4-4 are in fair agreement with the measured values. For the most part, the adiabatic relation and the method of weighted averages seem to be of roughly equal validity for predicting the electron temperature. Both methods lead to a slight underprediction of the measured values in the far-field, and the magnitude of the underprediction appears to increase with distance downstream of the exit plane. This underprediction can be greatly reduced by employing a variation to the adiabatic method of Eqn. 4-4. Specifically, improved results are obtained by allowing the reference values, $T_{e,0}$ and $n_{e,0}$, to vary with downstream distance. Doing this is equivalent to saying that the "constant" in Eqn. 3-11 is only truly invariant over a limited spatial area. This is consistent with the statement that the equation of state from which Eqn. 4-4 was derived includes an approximation regarding the smallness of the heat flow tensor in the plasma.[78] Inaccuracies in this approximation are believed to compound with increasing distance from the point where the plasma conditions are matched thus necessitating the use of sliding reference values in Eqn. 4-4.

The black dotted lines in Figs. 4-15 through 4-19 above were produced by using the values of density and electron temperature measured along the centerline of TH3 at each axial location as the reference values in Eqn. 4-4. It should be pointed out that this procedure does not significantly improve upon the absolute accuracy of the calculations, as evidenced by examination of Figs. 4-16 and 4-17. It does, however, reduce the systematic underprediction exhibited by the other two methods at large downstream distances and therefore can be used with confidence over a larger spatial range. The reference values used in implementation of Eqn. 4-4 at each axial location are summarized in Table 4-1, below.

Z (mm)	$n_{e,0}$ (m^{-3})	$T_{e,0}$ (eV)	Z (mm)	$n_{e,0}$ (m^{-3})	$T_{e,0}$ (eV)
50	9.89×10^{17}	2.56	55	8.30×10^{17}	2.38
60	6.92×10^{17}	2.23	65	5.79×10^{17}	2.10
70	4.95×10^{17}	1.97	75	4.23×10^{17}	1.87
80	3.68×10^{17}	1.78	85	3.19×10^{17}	1.70
90	2.81×10^{17}	1.64	95	2.48×10^{17}	1.57
100	2.22×10^{17}	1.52	105	1.97×10^{17}	1.48
110	1.78×10^{17}	1.44	115	1.58×10^{17}	1.40
120	1.46×10^{17}	1.36	125	1.30×10^{17}	1.32
130	1.21×10^{17}	1.29	135	1.09×10^{17}	1.29
140	1.01×10^{17}	1.24	145	9.33×10^{16}	1.23
150	8.91×10^{16}	1.19	155	7.91×10^{16}	1.21
160	7.57×10^{16}	1.16	165	6.76×10^{16}	1.19
170	6.46×10^{16}	1.14	175	5.90×10^{16}	1.16
180	5.66×10^{16}	1.12	185	5.16×10^{16}	1.14
190	4.96×10^{16}	1.10	195	4.55×10^{16}	1.11
200	4.39×10^{16}	1.07	205	4.05×10^{16}	1.09
210	3.92×10^{16}	1.05	215	3.60×10^{16}	1.07
220	3.59×10^{16}	1.01	225	3.17×10^{16}	1.07
230	3.10×10^{16}	1.03	235	2.84×10^{16}	1.06
240	2.78×10^{16}	1.03	245	2.57×10^{16}	1.05
250	2.53×10^{16}	1.01			

Table 4-1: The reference values of plasma density and electron temperature used to predict the dotted lines shown in Figs. 4-15 through 4-19. These values were taken from the plume of TH3 when it was operating alone.

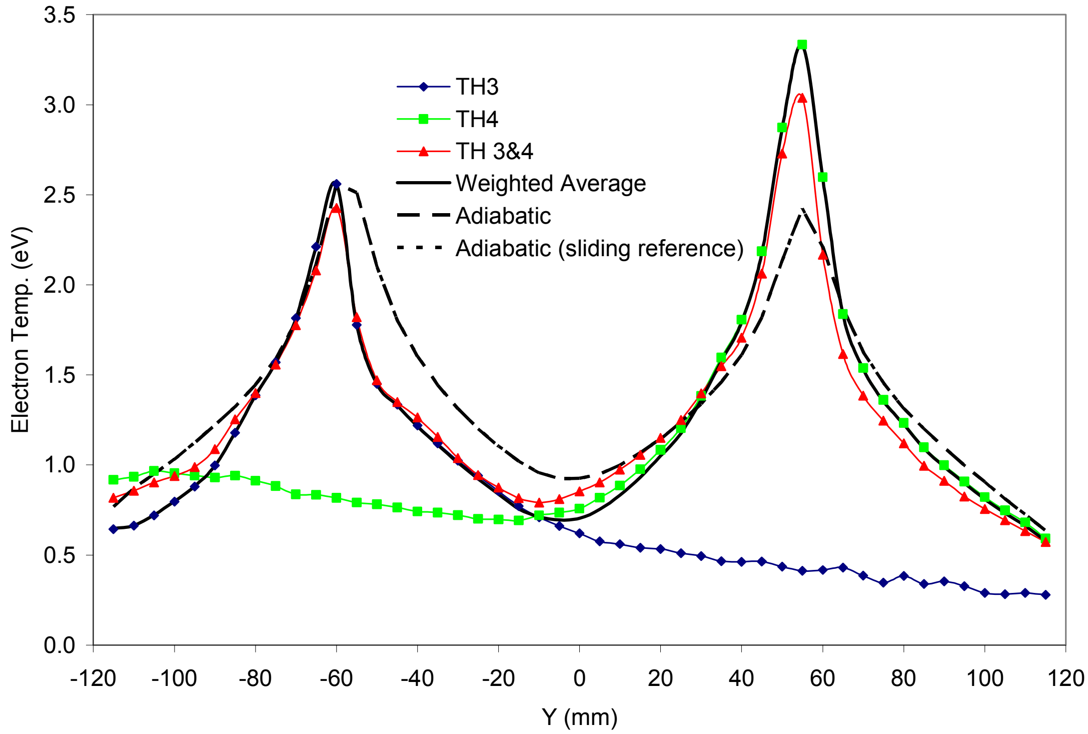

Figure 4-15: Electron temperatures measured 50 mm downstream of TH 3&4. The solid, dashed, and dotted black lines represent three different methods of predicting the electron temperature.

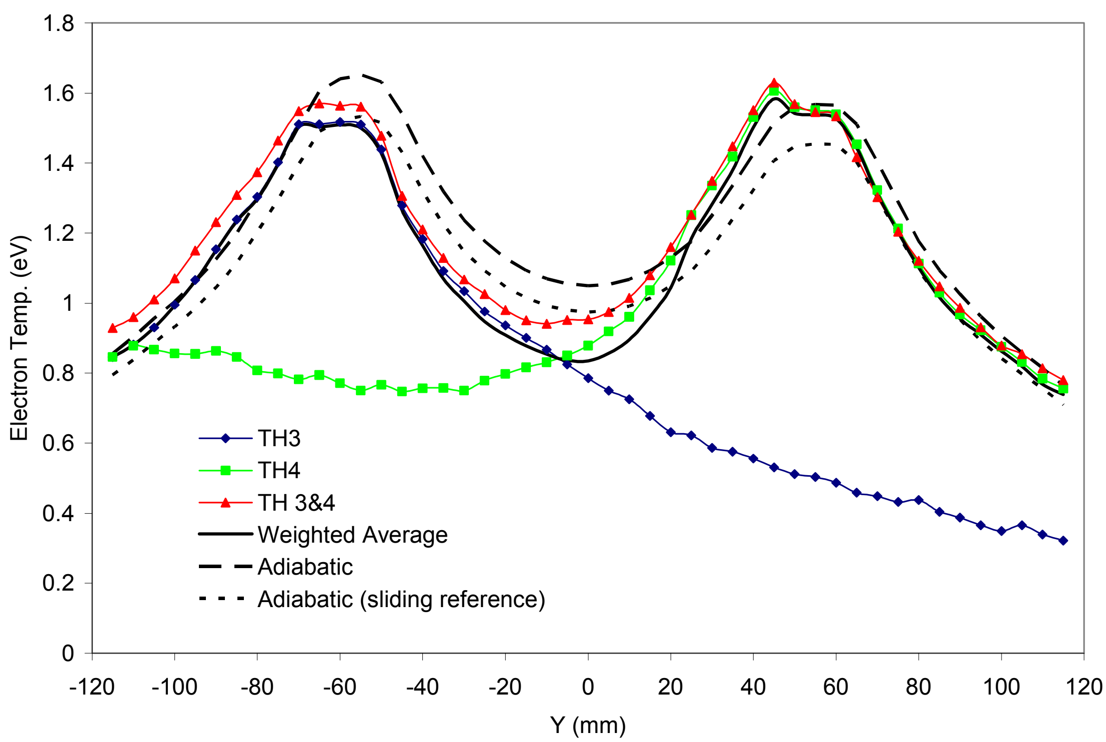

Figure 4-16: Electron temperatures 100 mm downstream of TH 3&4.

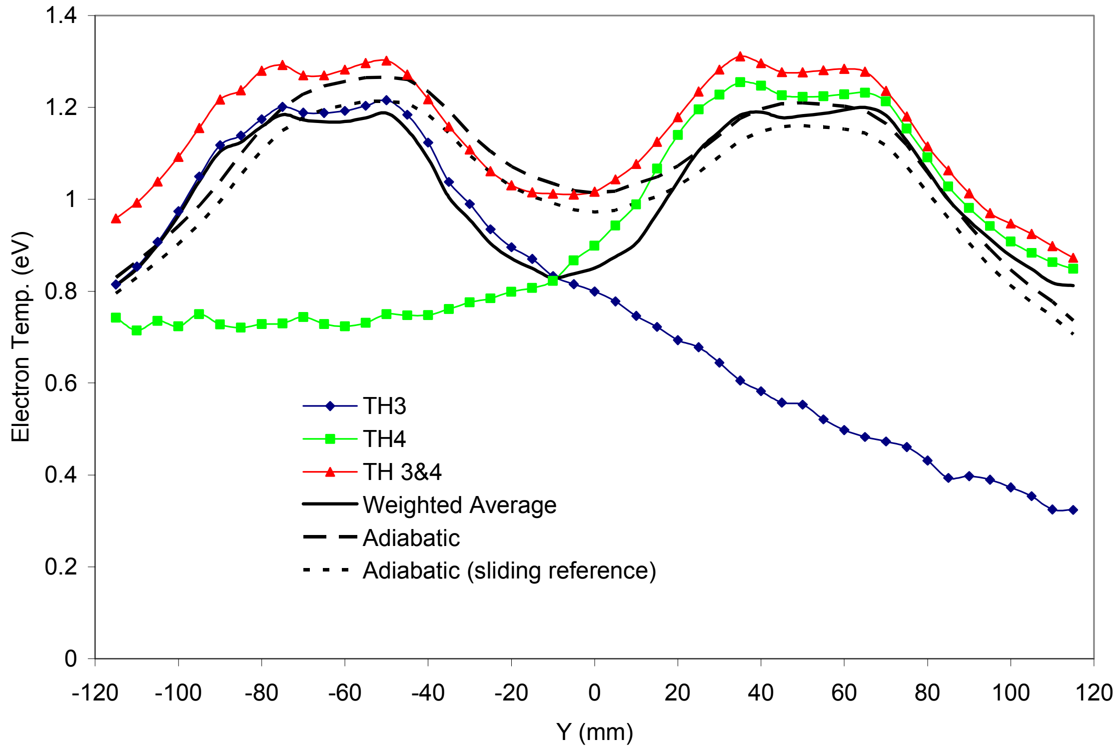

Figure 4-17: Measured and calculated electron temperatures 150 mm downstream of two operating Hall thrusters.

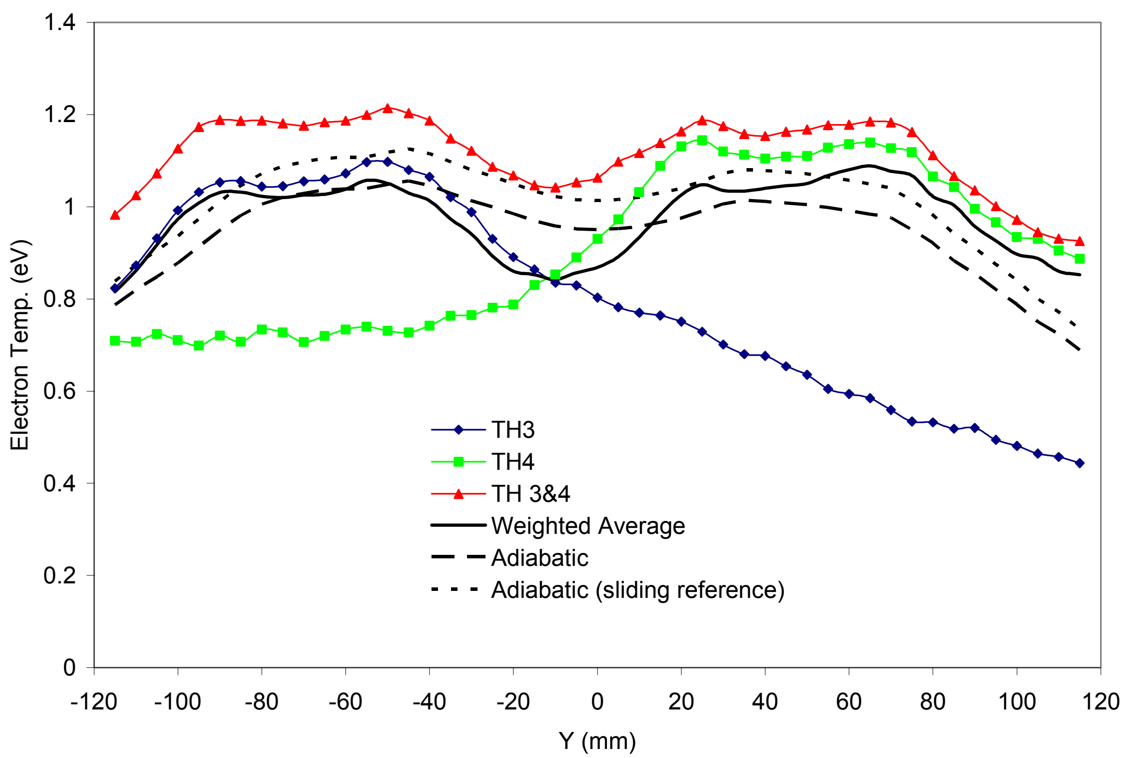

Figure 4-18: Electron temperature profiles 200 mm downstream of thrusters 3 & 4.

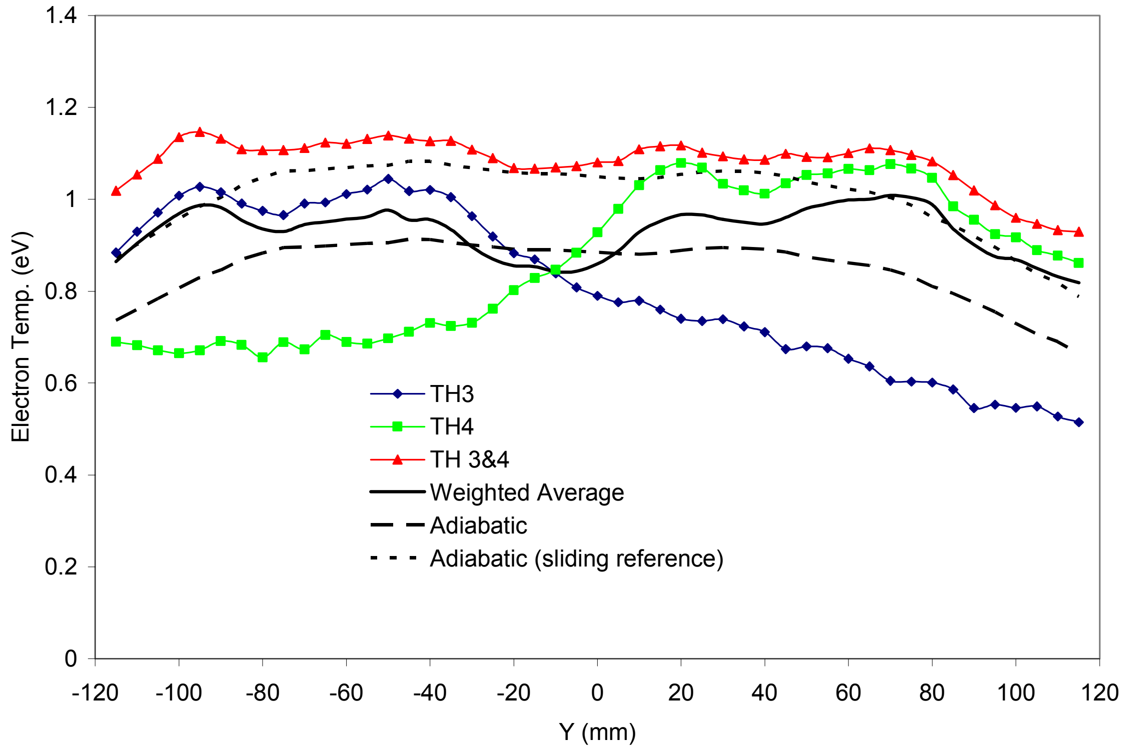

Figure 4-19: Measured and calculated electron temperature profiles 250 mm downstream of thrusters 3 and 4.

4.5 Plasma Potential

An emissive probe was used to measure the plasma potential at 5 mm intervals in the cluster plume. Results obtained with thrusters 3 and 4 operating simultaneously are shown in Fig. 4-20. As shown, the peak plasma potential is slightly higher than 20 volts with respect to ground near the centerline of each thruster at an axial distance of 50 mm from the exit plane. By 140 mm downstream, the peak potential falls to less than 10 volts. Moving radially away from the thrusters, the plasma potential is seen to fall to approximately 6 volts within about 50 mm of the centerline of each engine.

An interesting feature shown in Fig. 4-20 is the unique plasma potential profile in the area between the thrusters. Between approximately Y=-30 and Y=30 mm, the plasma potential increases with downstream distance indicating that there exists a region where the electric field vector is oriented in the upstream direction. This can be seen clearly in Fig. 4-21, which shows the plasma potential profiles at various axial locations. The reversed electric field could potentially cause ions produced in the area between the thrusters as a result of charge exchange collisions to be accelerated upstream toward the spacecraft on which the thrusters are mounted. Although this could hypothetically result in an increased erosion rate in some areas due to increased ion impingement, the effect will almost certainly be negligible in any practical situation since the impinging ions are unlikely to experience accelerating potentials greater than a few volts in the reverse direction.

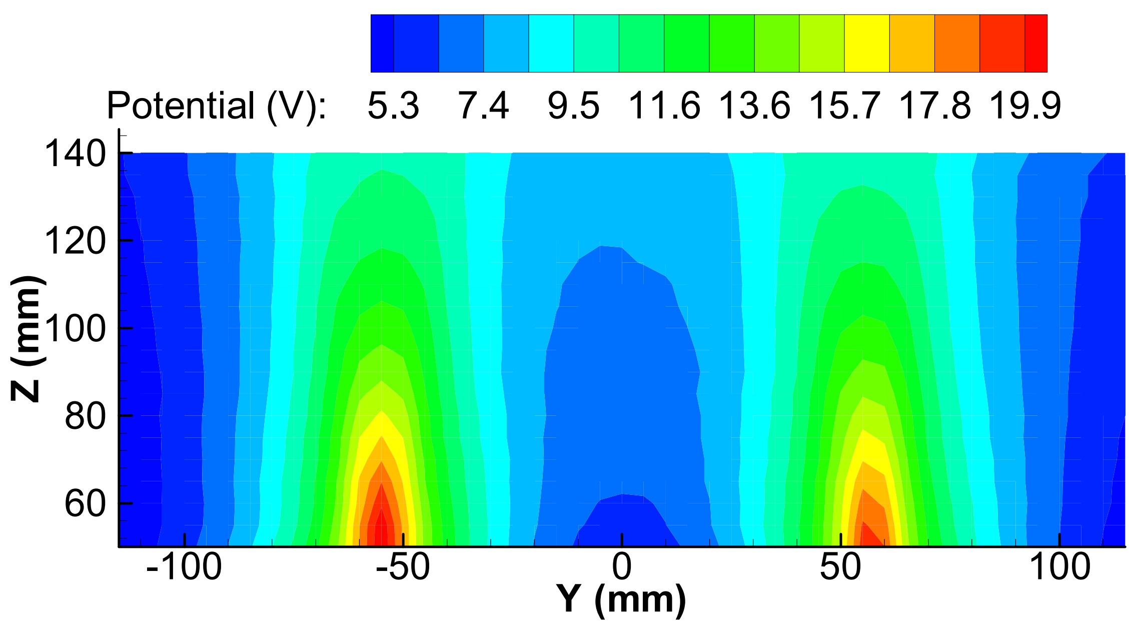

Figure 4-20: Plasma potential profiles downstream of thrusters 3 and 4. Data were obtained at 5 mm intervals in each direction using the emissive probe.

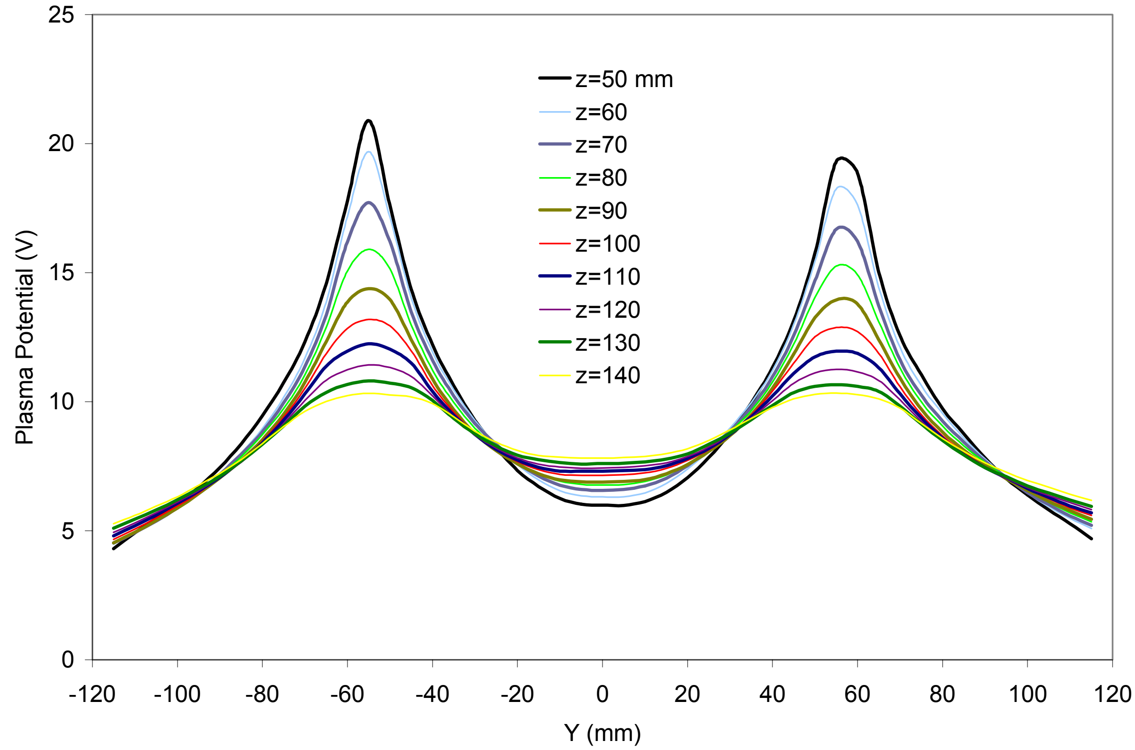

Figure 4-21: Plasma potential at various distances downstream of the cluster exit plane. Notice the increase in potential as a function of Z in areas between thrusters 3 and 4 (± 30mm). This indicates that the electric field is oriented upstream in these regions.

Figures 4-22 through 4-26 show plasma potential profiles recorded with thrusters 3 and 4 running individually and with them operating simultaneously. These profiles are presented at distances ranging from 60 to 140 mm downstream of the exit plane and will be used to examine several different techniques for predicting the potential in the cluster plume based on knowledge of a single thruster. For example, it has been suggested in the literature that the plasma potential could be predicted by simply integrating the magnetic field data.[65] This idea is contradicted by the data shown in Figs. 4-22 through 4-26. By inspection, it is clear that integration of the magnetic field along the lines of force shown in Figs. 4-6 and 4-7 does not reproduce the observed potential profiles.

A more conventional method for relating the magnetic field architecture to the plasma potential involves consideration of electron dynamics in a plasma. Along a magnetic field line, the motion of electrons is governed purely by electrostatic forces and can be described by the well known Boltzmann relation.[100] This leads naturally to the definition of a thermalized potential, ϕ_T, which is conserved along a line of force.[101] The thermalized potential is defined by Eqn. 4-5 where ϕ represents the plasma potential and $n_{e,0}$ is a reference density taken at some point along the field line. In the derivation of Eqn. 4-5, the electron temperature has been assumed constant along field lines.

$$\phi_T \equiv \phi - \frac{k_b T_e}{e} \ln\left(\frac{n_e}{n_{e,0}}\right) \qquad \textbf{Eqn. 4-5}$$

The concept of thermalized potential is useful in the design of Hall thrusters since it shows that the magnetic field lines can be approximated as equipotential lines in situations where the thermal energy of the electrons is negligible compared to the plasma potential. In other words, the thermalized potential is a useful tool for predicting plasma potential in situations where electrons are tightly bound to the magnetic field lines. This method, however, is less useful in the thruster plume since the correction term due to thermal effects and density gradients can be as large as the plasma potential. Comparing the plasma potential data of Fig. 4-20 to the magnetic field profiles shown in Figs. 4-6 and 4-7, it is clear that the lines of force do not correspond to equipotential contours. This is not surprising, since the magnetic field strength is generally less than 10 G and the electrons are only weakly magnetized throughout the areas where the plasma potential is presented. Further, since the different magnetic field shapes depicted in Figs. 4-6 and 4-7 result in virtually identical plasma parameters measured downstream of TH 2&3 and TH 3&4, respectively, it is clear that the magnetic field is not the dominant factor determining the evolution of the far-field plume structure.

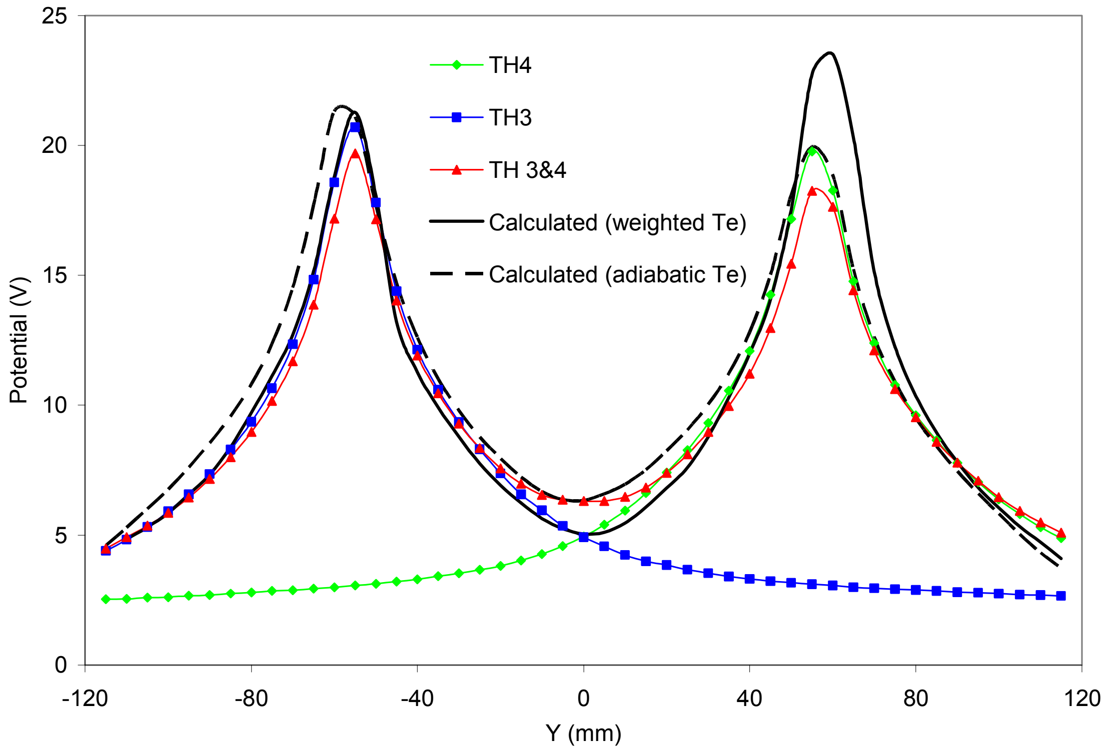

Figure 4-22: Measured and calculated values of plasma potential 60 mm downstream of TH 3&4.

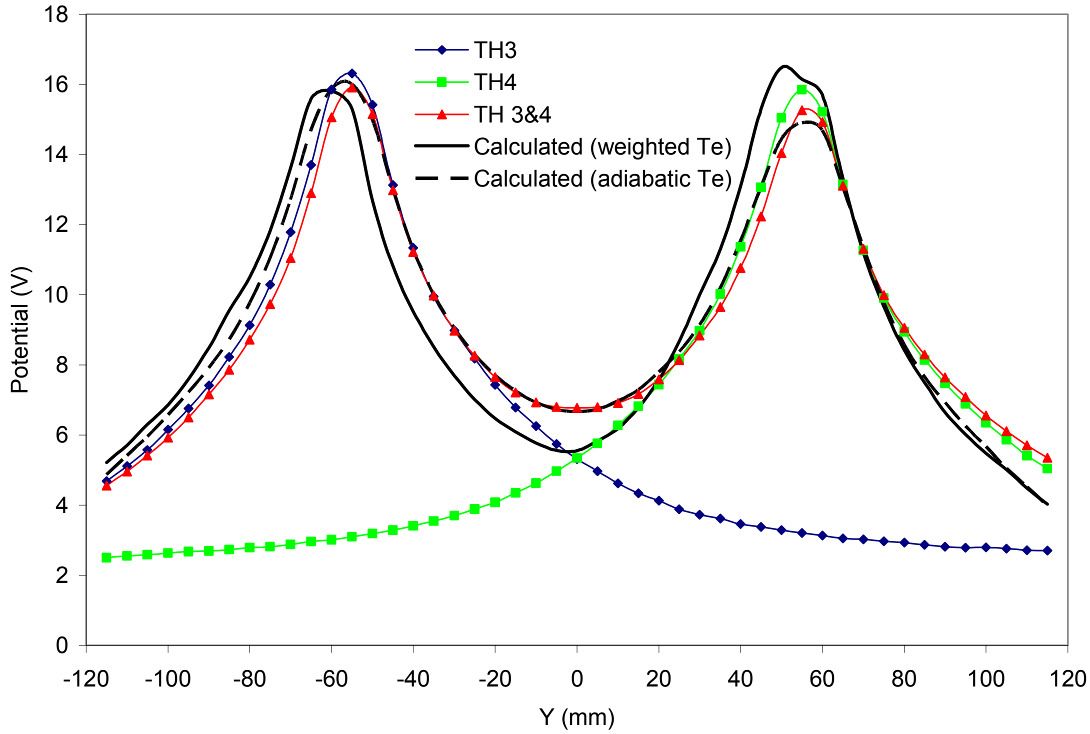

Figure 4-23: Measured and calculated values of plasma potential 80 mm downstream of TH 3&4.

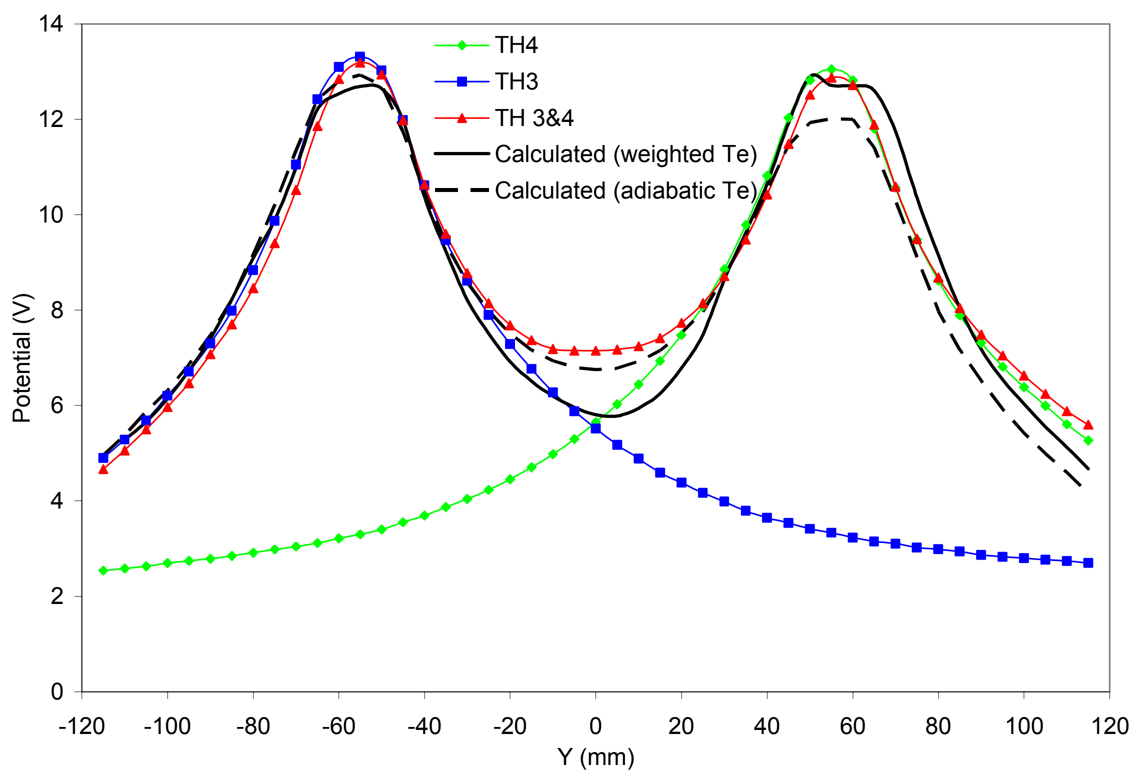

Figure 4-24: Measured and calculated values of plasma potential 100 mm downstream of TH 3&4.

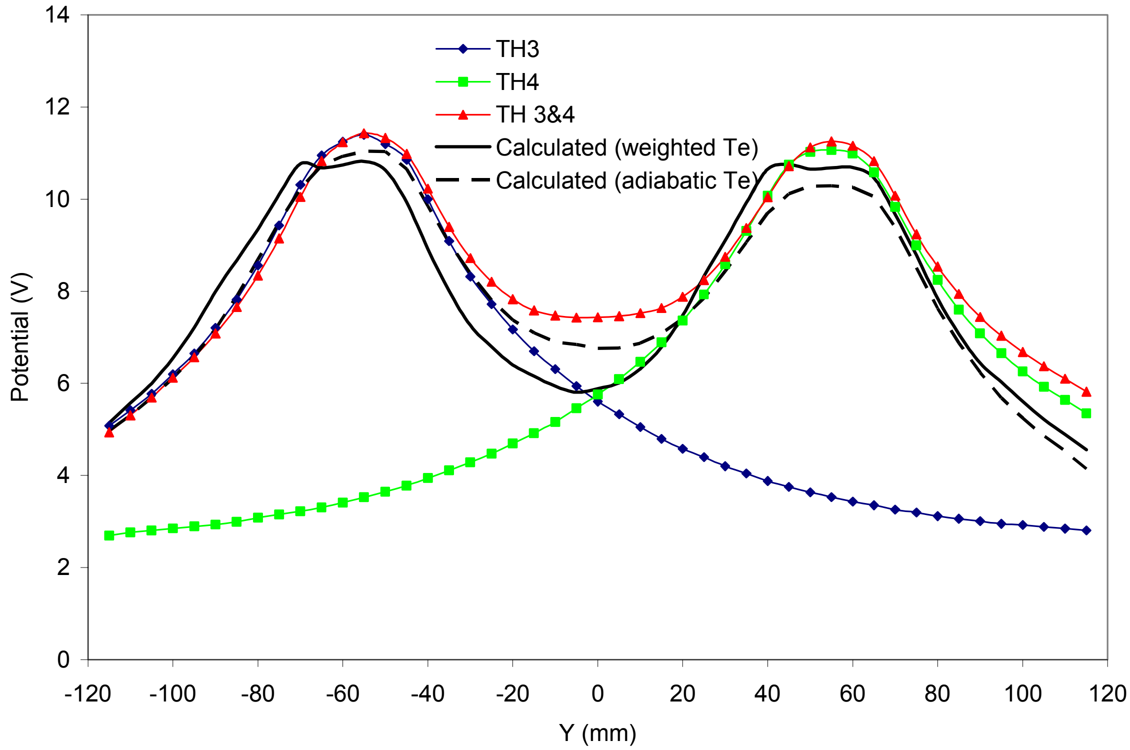

Figure 4-25: Measured and calculated values of plasma potential 120 mm downstream of TH 3&4.

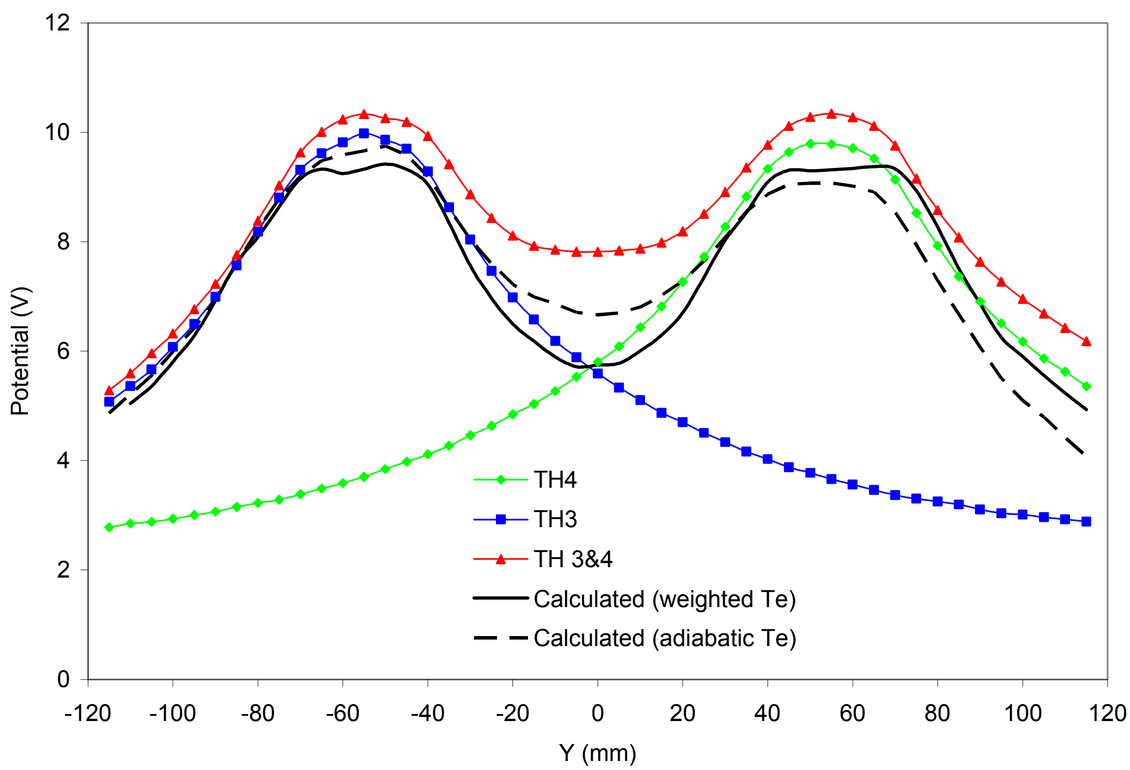

Figure 4-26: Measured and calculated values of plasma potential 140 mm downstream of TH 3&4.

In the far-field plume of a Hall thruster, thermal effects and density gradients are dominant over the effects of the magnetic field. This knowledge can be used to derive an analytical expression for the plasma potential starting with the generalized Ohm's law given by Eqn. 4-6.[17] Since the magnetic forces have been shown not to drive the potential field, terms involving B can be omitted from Eqn. 4-6. The resistive term can also be neglected since its magnitude is expected to be small except, perhaps, in the narrow regions along the centerline of each thruster discussed in Chapter 3. This leaves only electrostatic forces remaining and the electric field can be written as the negative gradient of the plasma potential. Invoking the ideal gas law and the chain rule of elementary calculus leads to Eqn. 4-7, which shows that the plasma potential evolution in the plume is explicitly related to the changes in electron temperature and plasma density. Examining the density and temperature measurements presented earlier in this chapter, it can easily be seen that the plasma density varies by more than two orders of magnitude in the plume while the electron temperature varies by only about a factor of three. For this reason, the second term on the right-hand side of Eqn. 4-7 can be neglected and the result integrated to arrive at Eqn. 4-8.

$$\vec{E} + \vec{v} \times \vec{B} = \eta \vec{j} + \frac{1}{e n_e}\left(\vec{j} \times \vec{B} - \nabla p_e\right) \qquad \textbf{Eqn. 4-6}$$

$$\nabla \phi = \frac{k_b T_e}{e} \frac{\nabla n_e}{n_e} + \nabla \frac{k_b T_e}{e} \qquad \textbf{Eqn. 4-7}$$

$$\phi = \frac{k_b T_e}{e} \ln\left(\frac{n_e}{n_{e,0}}\right) \qquad \textbf{Eqn. 4-8}$$

The barometric potential law given by Eqn. 4-8 is just the well known Boltzmann relation. Deriving it from the generalized Ohm's law, however, shows explicitly the terms that have been neglected and allows the assumptions in the derivation to be evaluated. For example, it is often pointed out that the Boltzmann relation is only mathematically exact for isothermal electrons. While this is certainly true, the discussion above shows that dropping the term involving temperature variations is a very reasonable approximation in the Hall thruster plume and the position dependent electron temperatures calculated in the previous section can be used with confidence. This method was used to calculate the black lines (solid and dashed) in Figs. 4-22 through 4-26 according to Eqn. 4-8, where the reference density, $n_{e,0}$, was taken to be $5x10^{13}$ m^{-3}. This value was chosen to provide a good fit to the TH3 centerline data at Z=100 mm. While the choice to match the data at 100 mm was arbitrary, a similar approach is expected to be valid in most practical cluster configurations since the data presented here show the plasma potential directly downstream of one thruster to be largely unaffected by the surrounding devices.

The two curves labeled "calculated" in each of Figs. 4-22 through 4-26 represent plasma potentials derived from two different sets of electron temperature data. The solid lines are based on electron temperatures obtained from the method of weighted averages while temperatures derived from the adiabatic relation were used to produce the dashed lines. As seen in the figures above, both sets of calculations agree quite well with the measured data. In general, the curves derived from the adiabatically calculated electron temperatures show slightly better agreement with the measurements, particularly in the areas between the thrusters. Over the region studied in this work, the predictions made using Eqn. 4-8 agree with the experimental data to within 2 volts, which is within the margin of error of the emissive probe.

The success of the plasma potential calculations discussed above shows that three of the most basic plume properties downstream of a cluster of Hall thrusters operating in the nominal configuration can be estimated analytically. First, the number density is obtained by linear superposition of the contributions due to individual thrusters. Then, the electron temperature is approximated using either the density weighted average of Eqn. 4-3 or the adiabatic relation of Eqn. 4-4. Finally, these values are used to estimate the plasma potential via Eqn. 4-8. Results obtained in this way appear to be accurate to within the experimental uncertainty of typical plasma diagnostics. Table 4-2 summarizes the methods used to predict plasma properties in the cluster plume.

Step	Quantity	Prediction Method
1	Plasma Density	Linear superposition of the contributions from individual thrusters
2	Electron Temperature	Adiabatic relation based on reference values measured in the plume of a single thruster
3	Plasma Potential	Boltzmann relation based on the plasma density and electron temperatures calculated in steps 1 & 2

Table 4-2: Prediction methods used to estimate the plasma properties downstream of a cluster based on knowledge of an individual thruster unit.

4.6 Ion Current Density

The nude Faraday probe was used to measure the ion current density downstream of the Hall thruster cluster in two different configurations. In the first configuration, measurements were recorded along a 0.5 meter radial arc centered halfway between TH 2&3. In the second configuration, the point of rotation was moved to the exit plane of TH3.

There are several geometric difficulties associated with interpretation of Faraday probe data taken downstream of a cluster. First, the spatial separation of the thrusters means that the probe cannot possibly be oriented perpendicular to the radial outflow from both devices at the same time. As illustrated in Fig. 4-27, this causes the projected area of the probe to differ from the physical area according to Eqn. 4-9. Fortunately, the geometry in the present situation is such that the maximum difference between the physical area and the projected area is less than 1% when the center of rotation is the midpoint between the two thrusters. When the data collection arc revolves around thruster 3, the maximum difference is less than 3%. The effect of the changing projected area is therefore neglected in the current measurements.

$$A_{proj} = A_p \cos(\theta_2) = A_p \frac{R - d\sin(\theta)}{\sqrt{R^2 + d^2 - 2Rd\sin(\theta)}} \qquad \textbf{Eqn. 4-9}$$

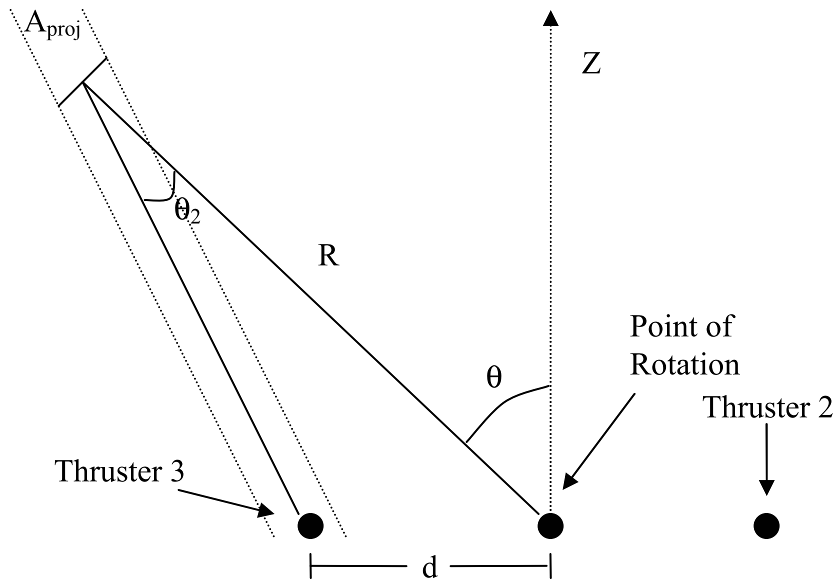

Figure 4-27: Geometry of the Faraday probe setup for one set of cluster measurements.

The second geometric complication involves integration of the measured profiles to estimate the total ion flux from the thrusters. Since the measurements in the cluster configuration did not focus on a single point source, integration of the profiles provides very little insight into the relevant physics. Insight can be gained, however, by examining the point by point contributions from individual thrusters to see if they superimpose. This is facilitated by Figs. 4-28 and 4-29 below which show measurements taken with the center of rotation between the thrusters and with it on TH3, respectively. Traces are presented for each thruster running individually and with both thrusters running simultaneously.

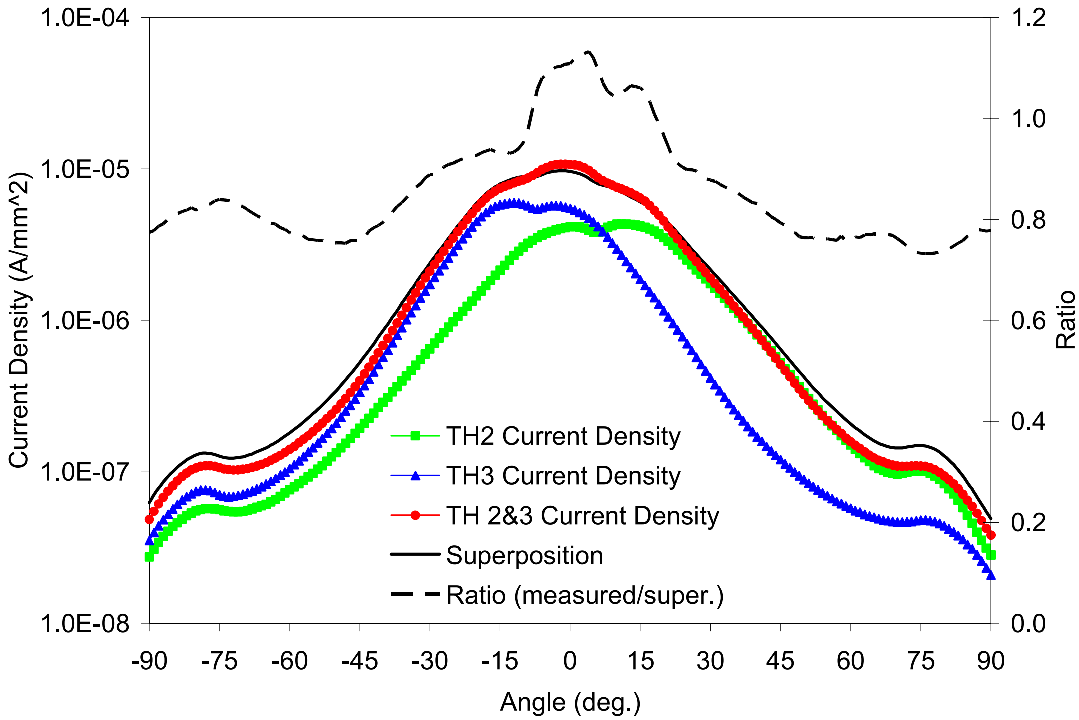

Figure 4-28: Faraday probe data taken in a 0.5 m arc centered around the midpoint between TH 2&3. Note the slight variation between the two-thruster data and the predictions from superposition.

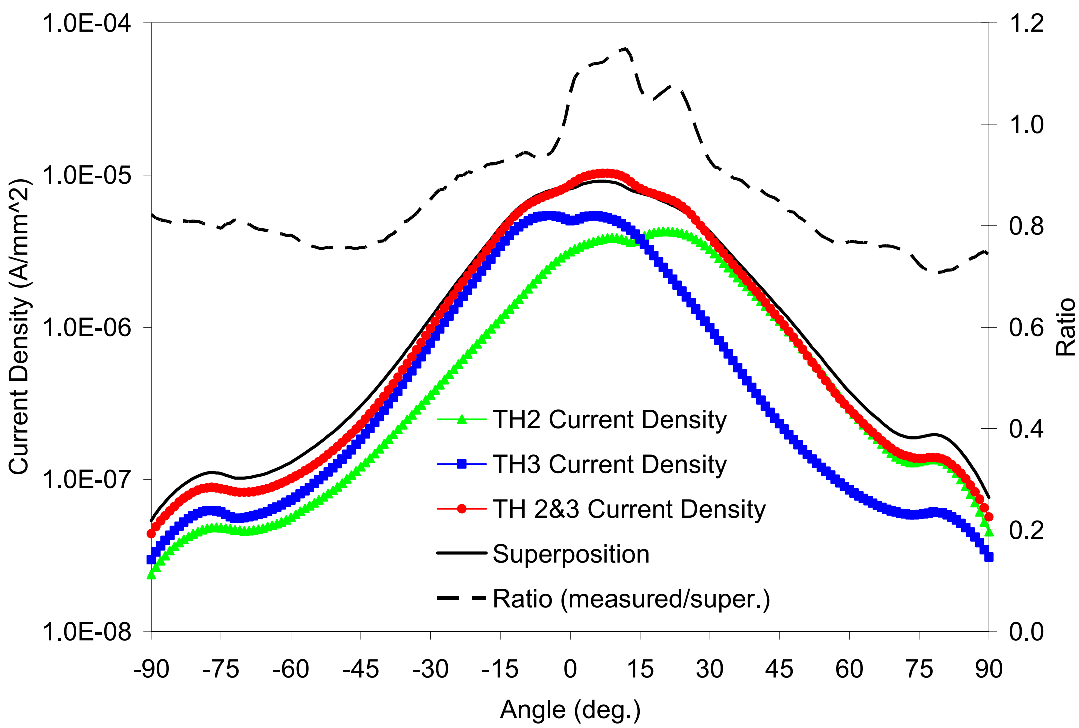

Figure 4-29: Ion current flux measured with the probe aligned to thruster 3. The dashed line gives the ratio of the measured current density to the one predicted by superposition.

As the figures above show, the ion flux measured near the cluster centerline was higher than the predictions of linear superposition by as much as 13%. On the other hand, at high angles off centerline the measured current flux fell short of predictions by more than 20%. This phenomenon is believed to be related to the plasma potential contours in the cluster plume, which are shown by the data presented in the last section to be fundamentally different than those found in the plume of a single thruster. When ions exit a single Hall thruster, they experience a continuous decline in plasma potential as they proceed away from the device. In other words, the electric field vector is everywhere directed away from the thruster. When multiple thrusters are operated together, however, a minimum in the plasma potential occurs in the region between the thrusters. This results in a situation where ions exiting one device and traveling toward the center of the cluster can be deflected downstream by the plasma potential "hill" created by adjacent thrusters, thus slightly reducing the effective beam divergence of the cluster plume.

To test the hypothesis that the plasma potential profiles are responsible for the slight narrowing of the ion beam noted in the cluster data, a simple particle tracking algorithm was developed. This algorithm works by taking the two-dimensional electric field vectors deduced from the plasma potential measurements presented earlier in this chapter and tracing the path of a test particle in these fields as a function of time. The test particle is specified in terms of an initial position, speed, and direction of travel. The resulting path of the ion in the measured electric field is then output as a series of data pairs representing the position of the test particle at successive time steps. The code used to implement this algorithm in the Igor data analysis package is given in Appendix B.

The particle tracking code was used to study the trajectories of several different test particles whose initial conditions are summarized in Table 4-3. The paths of these ions are shown graphically in Fig. 4-30 where the particle trajectories have been overlaid on the plasma potential profiles measured downstream of TH 3&4. The sample particles have been divided into two groups. The first two ions begin in the plume of thruster 4 and are depicted by black lines, while ions 3-5 begin in the plume of TH3 and are represented by yellow lines in Fig. 4-30. The test particles were given a range of initial velocities from 400 m/s, which is the approximate speed one would expect for a CEX ion created from a thermal neutral, to 17,000 m/s, which is the approximate speed of a singly-charged beam ion.

Figure 4-30 clearly shows that the path of a given ion depends strongly on the velocity with which it enters the potential well between adjacent thrusters. For instance, the low-energy ions labeled 1 and 3 in Fig. 4-30 are deflected downstream by the potential hills created by the adjacent thrusters. If only one thruster were operated, these ions would continue along their initial path and be detected at large angles with respect to the thruster centerline. Thus, the particle tracking algorithm shows that the increased current density at low angles shown in Figs. 4-28 and 4-29 can indeed be attributed to focusing of low-energy ions as a result of clustering. On the other hand, high-energy ions such as those labeled 2 and 4 are only weakly affected by clustering and show very slight deflections from the trajectories they would follow with just one thruster in operation. A final point to note about the ion paths shown in Fig. 4-30 is the trajectory of test particle 5. This particle shows that very slow CEX ions reaching the area between the thrusters can be reflected back upstream toward the cluster by the weak reversed electric fields in this region as hypothesized previously in Section 4.5.

Particle Number	Y_0 (mm)	Z_0 (mm)	Initial Speed (m/s)	Initial Angle of Travel (deg.)
1	45	60	400	160
2	45	60	4,000	160
3	-45	50	1,000	45
4	-45	50	17,000	45
5	-45	50	400	45

Table 4-3: Initial conditions for five test ions whose trajectories were tracked to study the effects of clustering on beam divergence.

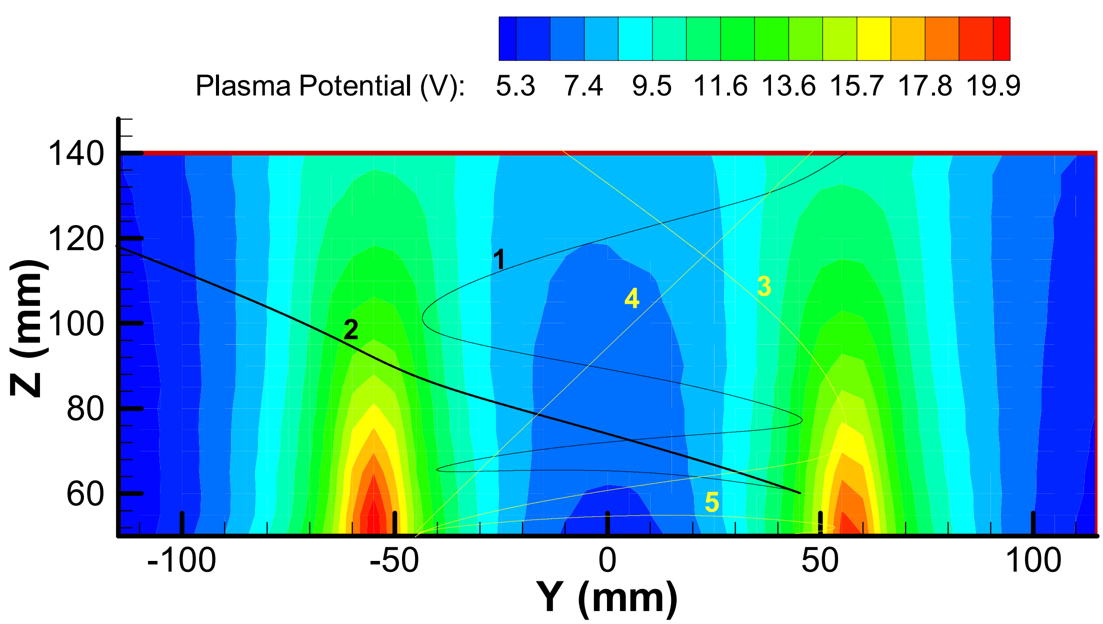

Figure 4-30: The trajectories of various test particles in the cluster potential field. Note how low-energy ions are preferentially deflected downstream.

4.7 Ion Energy Spectra

Both the RPA and the ESA were used to study the ion energy per charge distributions downstream of the Hall thruster cluster. Unlike the data recorded downstream of a single thruster, the energy per charge measurements obtained with the instruments aligned to the center of the cluster and all four thrusters in operation show marked differences between the two diagnostics. These differences are believed to be caused primarily by the different acceptance angles of the RPA and ESA. The ESA entrance slit provides an ion acceptance angle of approximately 4° in one direction and 0.5° in the other direction, while the cylindrical RPA has an acceptance cone half angle of approximately 25°. This discrepancy is not important for the case of a single thruster because both diagnostics are able to image the entire width of the thruster at a downstream distance of 0.5 m. At this distance, the ESA images a cross section only about 70 mm wide. In the cluster configuration, this results in the ESA imaging the space between the thrusters rather than the thrusters themselves. The RPA, on the other hand, has a wide enough viewing angle to accept ions originating from any of the four thrusters. For this reason, data obtained with the RPA are believed to be of greater utility for studying the effects of clustering, though ESA data are also included in this section for completeness.

Figures 4-31 and 4-32 summarize the cluster data collected with the parallel plate energy analyzer. At angular positions less than 10° with respect to the cluster centerline, the peak in the distribution occurs at energy to charge ratios near the 250 volt discharge voltage. Between 10° and 20° the peak shifts down to approximately 134 volts, which is near the voltage of the elastically scattered ions measured in the plume of a single thruster. The 134 volt peak can be observed out to 80° off the cluster axis before the signal is lost between 80° and 90°. It should be noted that the signal level recorded by the ESA in this configuration is approximately a factor of 25 lower than that measured for a single thruster. This is consistent with the previous statement that the instrument is unable to image ions traveling directly from any of the individual thrusters.

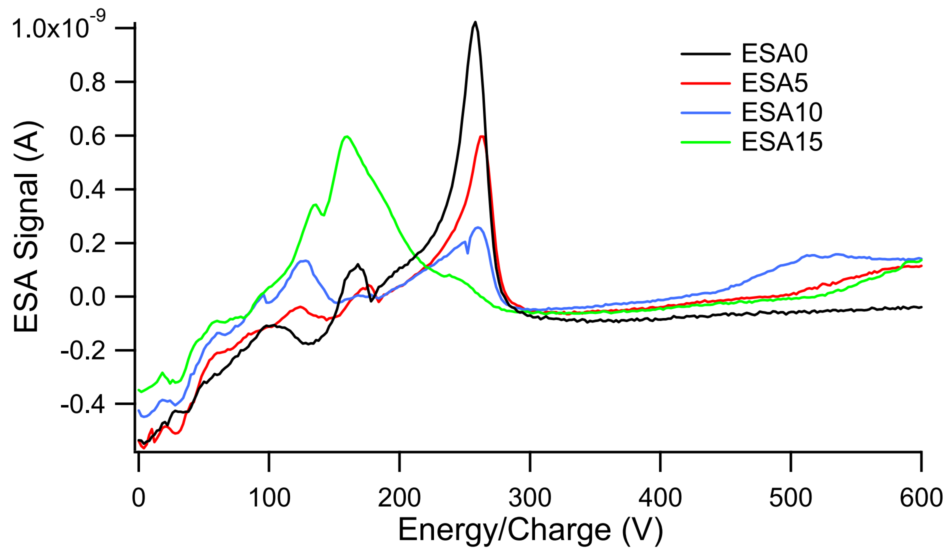

Figure 4-31: ESA data recorded at low angles off the cluster centerline.

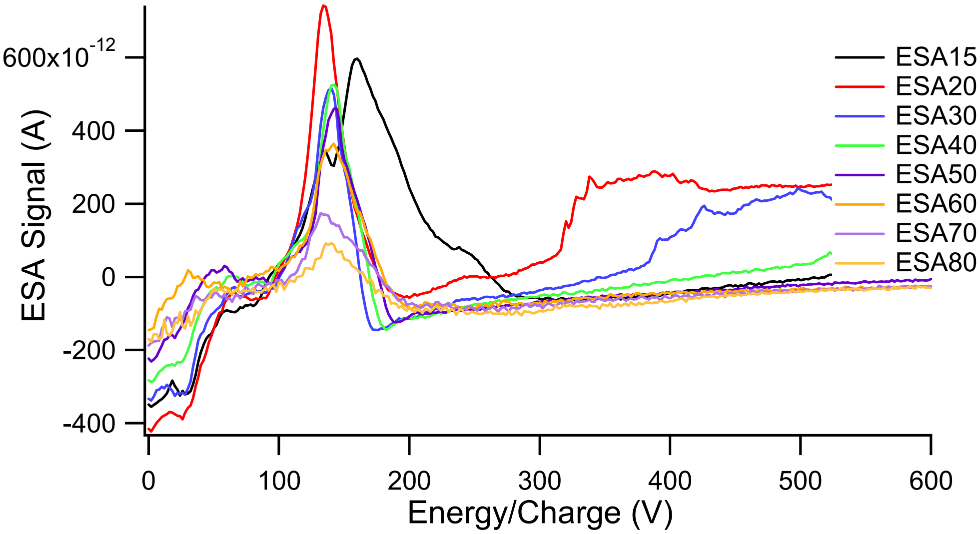

Figure 4-32: ESA data recorded in the cluster plume. Note the constancy of the main peak at 134 volts at angles from 20 to 80 degrees off the cluster axis.

The RPA data presented in Figs. 4-33 through 4-35 show several unusual characteristics, particularly along the cluster centerline where the spectrum shows three distinct, repeatable peaks at 224, 116, and 74 volts. Just 5° off centerline, the spectrum changes to a double-peaked structure with equally abundant populations occurring at 122 and 222 volts. As the angle off centerline is increased, the two peaks merge together to form a single peak near 206 volts with a low energy tail as shown in Fig. 4-34. The three phenomena that come to mind as potentially contributing to this behavior are: geometric effects caused by sampling ions from discrete thrusters that are not perfectly aligned to the RPA, preferential ion focusing due to the plasma potential structure described previously, and collisional effects. Each of these possibilities will be considered individually in the following subsections.

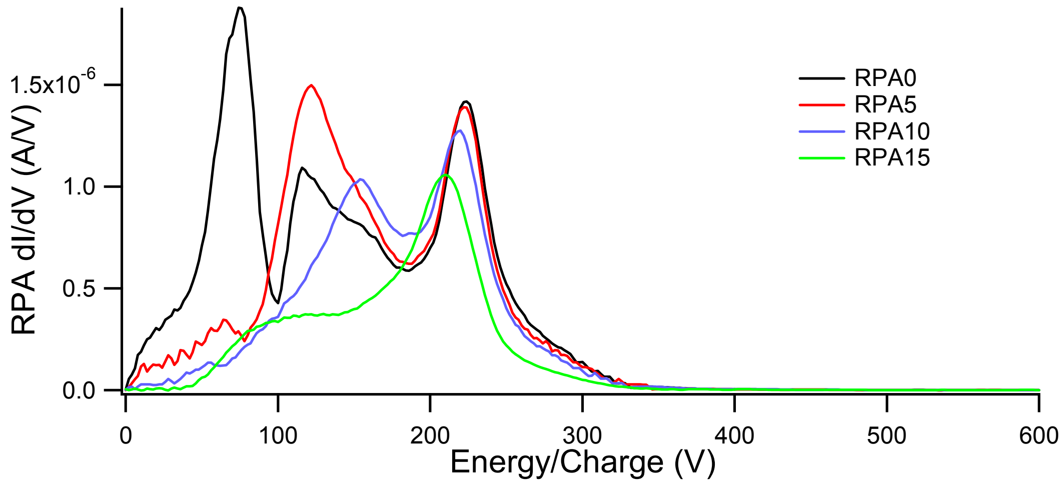

Figure 4-33: RPA data at angles from 0 to 15 degrees off the cluster centerline. Note the multi-peak structure at low angles.

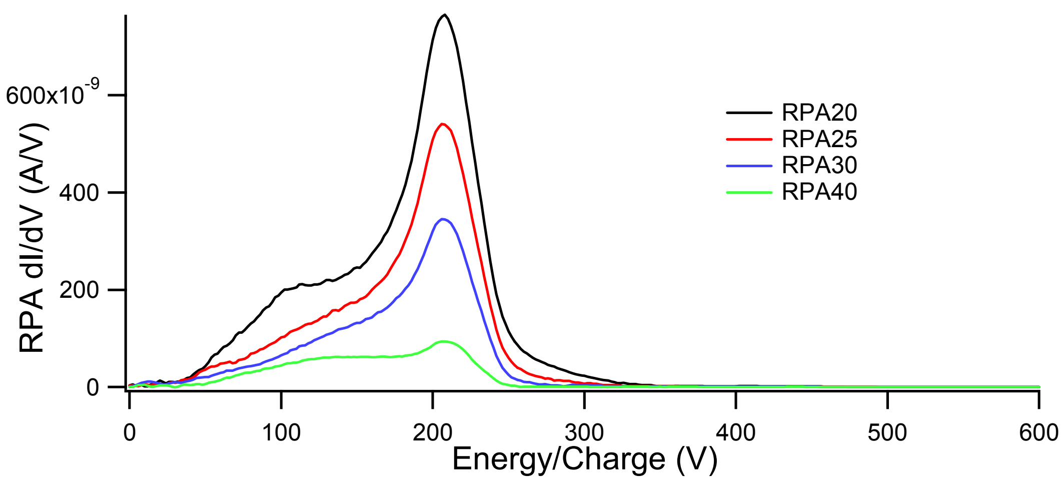

Figure 4-34: RPA data at angles from 20 to 40 degrees off the cluster axis.

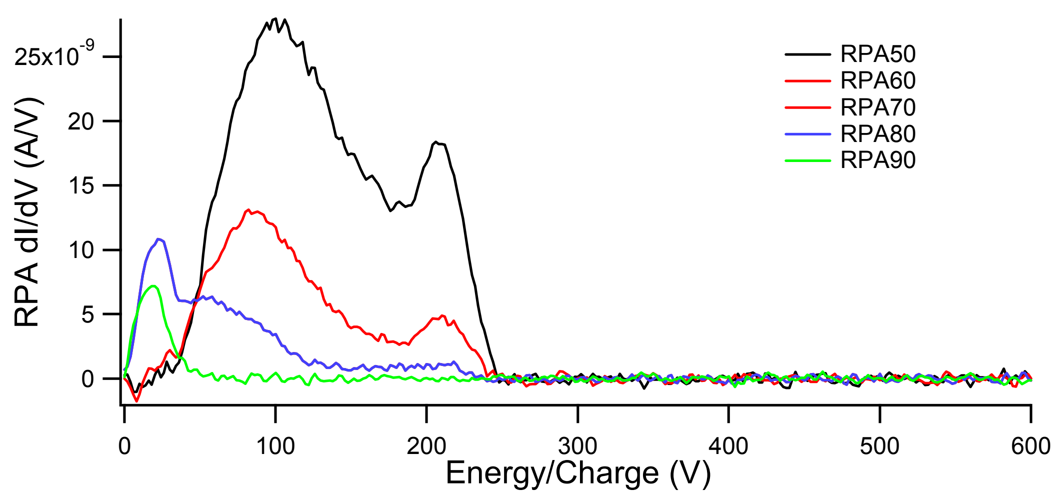

Figure 4-35: Ion energy per charge structure at angles greater than 50 degrees with respect to the cluster centerline.

4.7.1 Geometric Effects

When measuring the ion energy spectra downstream of a cluster of thrusters, there are two geometric effects that should be considered. First, the RPA is focused on the center of the cluster rather than any of the individual thrusters, and the finite spacing of the engines dictates that ions reaching the inlet of the instrument are not those traveling in the direction given by the angle of the RPA with respect to the cluster centerline. For example, when the RPA is aligned with the cluster centerline as sketched in Fig. 4-36 below, only ions traveling at an angle of about 9° with respect to the centerline of any individual thruster are collected. As the cluster is rotated about its vertical axis, two thrusters move closer to the RPA while two move farther away. The result is that the angle between the thrust vector and the path of collected ions differs between thrusters. This variation is shown in Fig. 4-37 for the geometry of the present study.

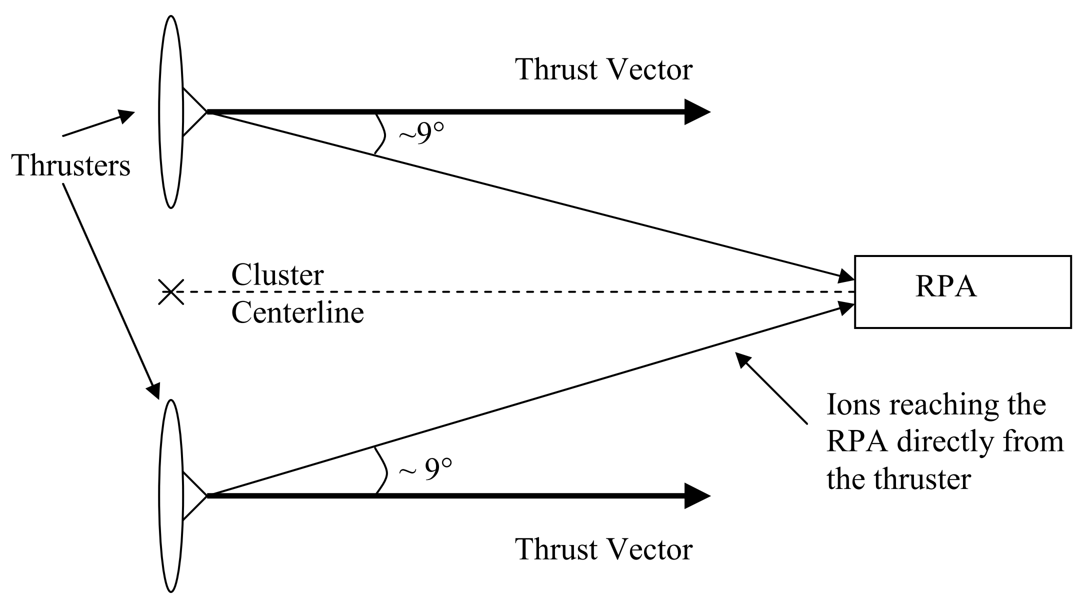

Figure 4-36: A sketch showing the angle between the thruster centerlines and the angle of collected ions when the RPA is aligned to the center of the cluster.

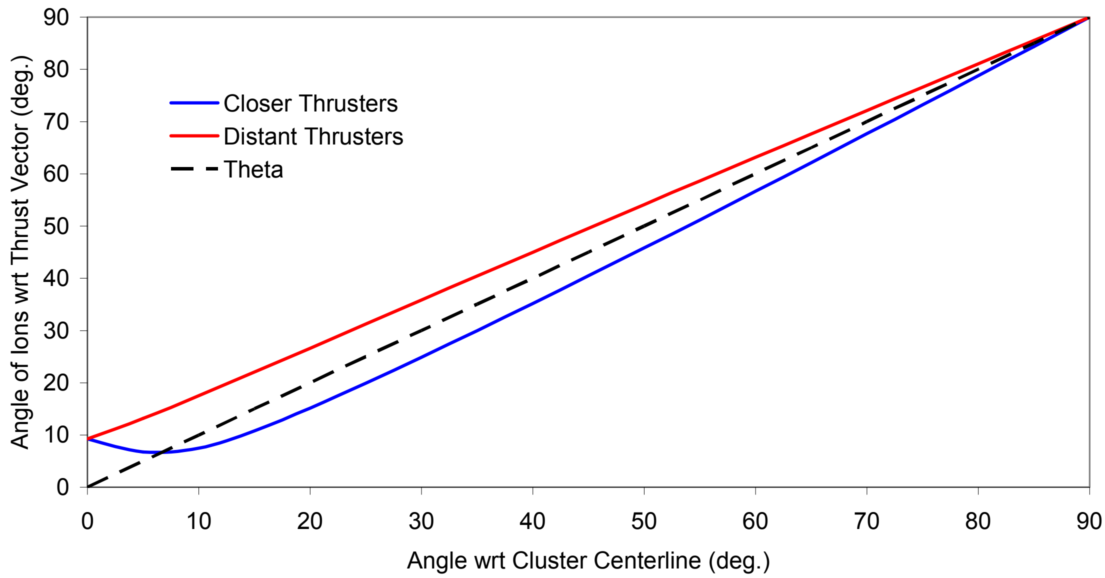

Figure 4-37: Variation of the angle between the thrust vector and path of collected ions as a function of angle from the cluster centerline. Note that this angle is different depending on which thruster an ion originates from.

The second geometric effect to consider when interpreting energy spectra collected downstream of a cluster relates to the fact that ions traveling from the exit of one thruster to the inlet of the RPA cannot be directed exactly parallel to the axis of the instrument. Rather, ions enter the RPA at a slight angle and therefore only the axially directed component of velocity is measured. Fortunately, the geometry of the measurements presented here is such that the inlet angle never exceeds 10° and therefore the possible error in velocity is less than 3%. Considering this and the relatively minor variations in ion angle shown in Fig. 4-37 leads to the conclusion that geometric effects alone cannot be responsible for the multi-peak structure shown in Fig. 4-33. It is interesting to note, however, that this structure disappears at angles greater than about 10° from the cluster centerline, which corresponds to the angle where the thrust vectors from the closer thrusters pass in front of the RPA entrance. In other words, the multi-peak structure appears to be confined to the region between the thrusters.

4.7.2 Electrostatic Focusing Effects

The second possible contributing factor to the low-energy structure involves ion focusing as a result of clustering. This is the same phenomenon shown previously to reduce the beam divergence downstream of a cluster by deflecting the low-energy ions that would otherwise have reached the wings of the plume. The mechanism by which this could also affect the ion energy spectra is illustrated in Fig. 4-38 below, where the dashed lines represent contours of constant plasma potential and the heavy arrows represent the paths of sample ions. To understand this figure, consider two ions, A and B, exiting a thruster and traveling in an identical direction toward the center of the cluster, but with different initial kinetic energies. In this situation, the slower moving ion, B, would be deflected by a given potential rise to a greater extent than its high-energy counterpart, ion A, as depicted in Fig. 4-38. Considering this, a detector swept through the plume would detect ion A at a higher angle off centerline, while ion B with its lower energy would be deflected further downstream and detected at a relatively low angle. At first glance, this phenomenon appears to be capable of accounting for the secondary structure shown in Fig. 4-33, in which the low energy population shifts to higher voltages with increasing angle off centerline. A crude estimate of the magnitude of the deflection that can be caused by the observed plasma potentials can be obtained by considering an ion traveling with kinetic energy of 150 eV, for example. If a step change in velocity equal to that caused by a 20 volt potential is applied perpendicular to the original direction of travel, the ion will be deflected by approximately 20°. This seems to indicate that the ion focusing mechanism may be capable of causing significant deflections to ions with kinetic energies of interest and therefore warrants further examination.

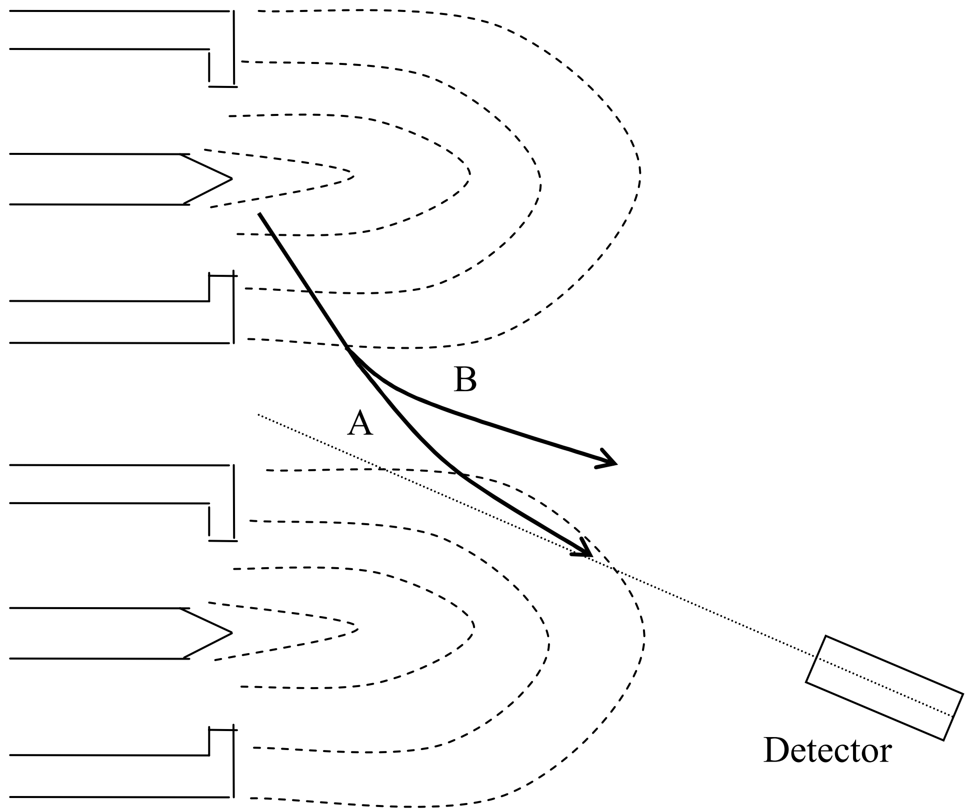

Figure 4-38: A sketch showing the proposed ion focusing resulting from the plasma potential structure in the cluster plume.

To determine whether the relatively modest plasma potentials in the cluster plume really are capable of causing the level of deflections necessary to cause the structures shown at low angles in Fig. 4-33, the particle tracking algorithm discussed previously was employed. Test particles represented by the initial conditions given in Table 4-4 were tracked in the two-dimensional potential field measured downstream of thrusters 3 and 4. The initial conditions were chosen to represent singly-charged ions originating at thruster 4 and traveling at a 45° angle toward the plume of thruster 3 with energies of 150, 100, and 50 eV. As Fig. 4-39 shows, the ions of different energies are indeed deflected to slightly different angles, but the magnitudes of the deflections are almost imperceptible for the kinetic energies of interest. It must therefore be concluded that electrostatic ion focusing alone cannot be responsible for the behavior of the structures shown in Fig. 4-33 at energy per charge ratios below the main peak in the distribution.

Color of Trace in Fig. 4-39	X_0 (mm)	Y_0 (mm)	Ion Kinetic Energy (eV)	Initial Speed (m/s)	Initial Direction of Travel (deg.)
Red	7	50	150	14,770	-135
Black	7	50	100	12,060	-135
Blue	7	50	50	8,528	-135

Table 4-4: Initial condition of test particles used to examine the energy dispersion hypothesized to occur in the cluster potential field.

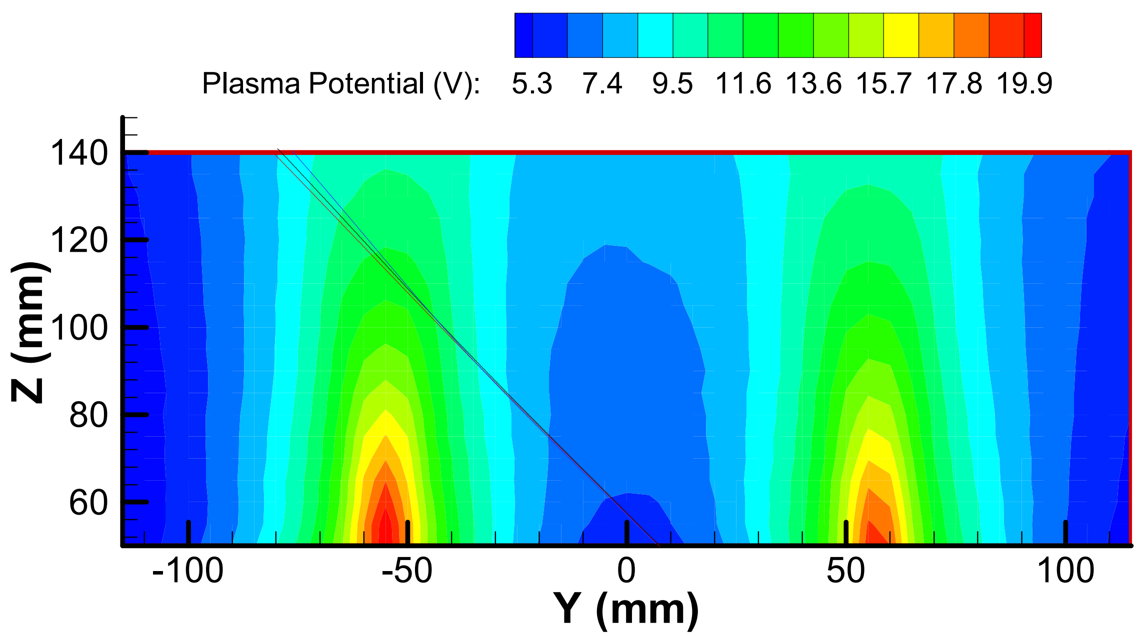

Figure 4-39: Trajectories of ions with various energies in the potential field of thrusters 3 and 4. For kinetic energies of interest, the measured potentials have very little effect.

4.7.3 Collisional Effects

Collisions within a plasma can be divided into two main types: elastic and inelastic. In an elastic collision, the colliding particles retain their original identities and both the momentum and total kinetic energy of the colliding pair is conserved. In an inelastic collision, on the other hand, a portion of the initial kinetic energy is dissipated through a secondary process such as ionization or excitation. Previous authors have shown all inelastic processes in the thruster plume to be negligible except for charge exchange collisions, which can have a significant effect on the observed energy per charge spectra.[47,52] The interactions likely to have a significant effect on the plume structure are therefore limited to CEX collisions and elastic collisions between heavy particles (ions and neutrals).

As explained by King, the peaks at 116 and 74 volts along the cluster centerline could hypothetically be caused by ions exiting a thruster at a beam velocity, V_b, of 224 volts before undergoing CEX collisions that result in populations with energy to charge ratios of approximately $V_b/2$ and $V_b/3$, respectively.[52] The reactions capable of creating these products, however, are summarized in Table 4-5 and inevitably involve multiply-charged ions.[47] The relatively low fraction of multiply-charged ions inferred from the ExB probe data taken downstream of a single thruster casts doubt on the possibility that CEX collisions could account for the structures seen in Fig. 4-33. Further, most of the reactions shown in Table 4-5 also produce ions at energy to charge ratios other than $V_b/2$ and $V_b/3$. None of these complementary products were detected by the RPA. Finally, charge exchange collisions tend to generate signatures in the energy per charge spectra at discrete multiples of the main peak in the distribution.[102] The fact that the ratio between the peak voltages changes as a function of angle in Fig. 4-33 seems to indicate that, if the multi-peak structure is due to collisions, the dominant interactions are likely elastic rather than charge exchange. It should be mentioned, however, that the significance of charge exchange collisions cannot be totally dismissed since their signatures may be masked by three-dimensional effects.

Reactants	Detectable Products	Electrons Transferred
Xe^{2+}, Xe^{+}	Xe^{+} at $2V_b$ and Xe^{2+} at $V_b/2$	1
Xe^{2+}, Xe^{+}	Xe^{3+} at $V_b/3$	2
Xe^{3+}, Xe^{+}	Xe^{2+} at $3V_b/2$ and Xe^{2+} at $V_b/2$	1
Xe^{3+}, Xe^{+}	Xe^{+} at $3V_b$ and Xe^{3+} at $V_b/3$	2
Xe^{3+}, Xe^{2+}	Xe^{+} at $3V_b$ and Xe^{4+} at $V_b/2$	2
Xe^{4+}, Xe^{+}	Xe^{3+} at $4V_b/3$ and Xe^{2+} at $V_b/2$	1
Xe^{4+}, Xe^{+}	Xe^{2+} at $2V_b$ and Xe^{3+} at $V_b/3$	2
Xe^{4+}, Xe^{2+}	Xe^{2+} at $2V_b$ and Xe^{4+} at $V_b/2$	2
Xe^{4+}, Xe^{3+}	Xe^{+} at $4V_b$ and Xe^{6+} at $V_b/2$	3

Table 4-5: Charge exchange reactions capable of producing ions with energy per charge ratios of $V_b/2$ and $V_b/3$. Most reactions create complementary products that are not shown in the collected RPA data. (Adapted from Ref. 47)

Elastic scattering has been shown to play an important role in the evolution of the ion energy spectra downstream of a Hall thruster by broadening the main distribution.[47,52] Additionally, numerical simulations incorporating recently calculated differential cross sections for collisions between xenon ions and neutrals have shown elastic scattering to be responsible for secondary peaks in the ion energy spectra at voltages below the main peak in the distribution, but above the peaks caused by low-energy CEX ions.[70,103] The voltage at which these secondary peaks occur is strongly related to the scattering angle, which in turn is related to the angle with respect to the thruster centerline.[70] The RPA data shown in Figs. 4-34 and 4-35 show secondary peaks that shift to lower voltage and increase in relative magnitude (compared to the height of the main peak) with increasing angle from the cluster centerline. These structures are visible at angles greater than about

20° and are in very good qualitative agreement with the reported trends for elastic scattering.[53,70]

Since the energy spectra in a large area of the plume have been shown to be consistent with the predominance of elastic collisions, and because several other mechanisms have been eliminated as possibilities, it seems reasonable to hypothesize that elastic scattering may be responsible for the multi-peak structure observed at angles below about 10° in Fig. 4-33. In this region, there are three possible “target populations” with which an ion from any of the individual thrusters could collide: background neutrals, fast ions from other thrusters, and low-energy CEX ions residing in the area between the thrusters. The neutral density in this region is not likely to be significantly higher than that in the near field of a single thruster since the background pressure in the chamber did not increase dramatically, so it may be that the observed effects are related to the increased ion density between the engines. Because of the ion focusing mechanism explained in Section 4.6, low-energy CEX ions can be expected to have a relatively long residence time in the area between the thrusters as they are reflected back and forth between the potential hills before escaping downstream. The low effective axial velocity of these ions implies that only a small fraction of beam ions would need to undergo charge exchange collisions to account for a significant population of slow target ions near the cluster centerline. It should be pointed out, however, that the mechanism by which ion-ion collisions could cause the distinct peaks shown in Fig. 4-33 is unclear and is suggested as an interesting topic for further study.

As a final check on the statement that elastic collisions are likely to be more important than charge exchange collisions in the cluster plume, it is instructive to refer to the estimated collision mean free paths given in Table 4-4. These values were calculated according to Eqn. 4-9 using the cross sections and other parameters given in Eqns. 4-10 through 4-14.[74,103,104] All cross sections are given in units of m^2. In estimating the mean free paths, the following plasma parameters were used: $n_i = 5x10^{16}$ m^{-3}, $n_n = 1.2x10^{17}$ m^{-3} (from $3.6x10^{-6}$ Torr background pressure), $T_i = 1$ eV, $T_e = 2$ eV, $T_n = 300$ K, and $v_i =$ 17,000 m/s. As Table 4-6 shows, the mean free path for ion-ion elastic collisions is somewhat shorter than the mean free path for any of the other collision types. Elastic scattering between ions therefore represents an interesting candidate for further study despite the fact that it generally causes significant momentum transfer only as a result of multiple small-angle scattering collisions rather than a single large-angle event. The mean free paths reflected in Table 4-6 are in good agreement with previously published estimates made under similar conditions.[102]

$$\lambda_c = \frac{1}{\sqrt{2}\sigma n_{target}} \qquad \textbf{Eqn. 4-9}$$

$$\sigma_{EL}(Xe, Xe) \approx \frac{2.12\times10^{-18}}{v_{rel}^{0.24}} \qquad \textbf{Eqn. 4-10}$$

$$\sigma_{EL}(Xe, Xe^+) \approx \frac{6.42\times10^{-16}}{v_{rel}} \qquad \textbf{Eqn. 4-11}$$

$$\sigma_{CEX}(Xe, Xe^+) \approx [-23.30\log_{10}(v_{rel})+142.21]\times8.423\times10^{-21} \qquad \textbf{Eqn. 4-12}$$

$$\nu_{ii} \approx 4.80\times10^{-14}\,\frac{q^4 n_i \ln\Lambda}{\left(m_i / m_p\right)^{1/2} T_i^{3/2}}$$ **Eqn. 4-13**

$$\sigma_{ii} = \frac{\nu_{ii}}{n_i v_i}$$ **Eqn. 4-14**

Collision Type	Approximate Mean Free Path (m)
Xe-Xe elastic	11.4
Xe-Xe^+ elastic	162.0
Xe^+-Xe^+ elastic	4.4
Xe-Xe^+ charge exchange	16.6

Table 4-6: Estimated mean free paths for various collision types in the cluster plume. Elastic scattering between ions appears to be significant despite the fact that it originates from multiple small-angle scattering events.

4.7.4 Offset Cluster Configuration

To further explore the effects of clustering on the ion energy per charge profiles, measurements were obtained in one final configuration where the cluster was shifted on the rotary table so that the axis of rotation was perpendicular to the centerlines of thrusters 3 and 4. In this "offset cluster" arrangement, the ESA and RPA were aligned to the center of thruster 3. The acceptance angle of the ESA is such that it can only measure ions traveling directly from thruster 3 while the RPA is capable of imaging the entire cluster.

Some of the ESA data taken in the offset cluster configuration are partially unreliable due to a slight malfunction in the operation of the instrument. The data collection method was as follows. First, measurements were taken with only thruster 3 operating. These data showed the main peak in the distribution to occur at an energy to charge ratio between 225 and 230 volts, which is in very good agreement with the single thruster data presented in Chapter 3. The other thrusters were then turned on and ESA traces were taken at successive time steps as the thrusters were allowed to reach steady state operating conditions. Careful examination of the resulting traces showed the location of the main peak in the distribution to shift to successively higher values before stabilizing at a level of approximately 260 volts. This behavior is believed to be due to a shift in the effective spectrometer constant resulting from thermal expansion of the ESA components in response to the increased heat load resulting from cluster operation. The 260 volt (with respect to ground) indicated peak in the ion energy spectra is clearly nonphysical since the discharge potential is only 250 volts (from anode to cathode). The locations of the primary and secondary peaks depicted in Figs. 4-40 through 4-42 below are therefore incorrect. However, because the change in the spectrometer constant represents a systematic rather than random source of error, useful information can still be gained from examination of the ESA data.

One particularly interesting feature is the predominance of the low-energy peak shown at angles above about 40° in Figs. 4-41 and 4-42. While this population is observable at low angles in the single thruster traces, its magnitude is much less than that of the main peak at angles between 30° and 50°. In the offset cluster data, the low-energy structure dominates the spectra at angles greater than 40° and appears to indicate a significant increase in elastic scattering as a result of clustering.

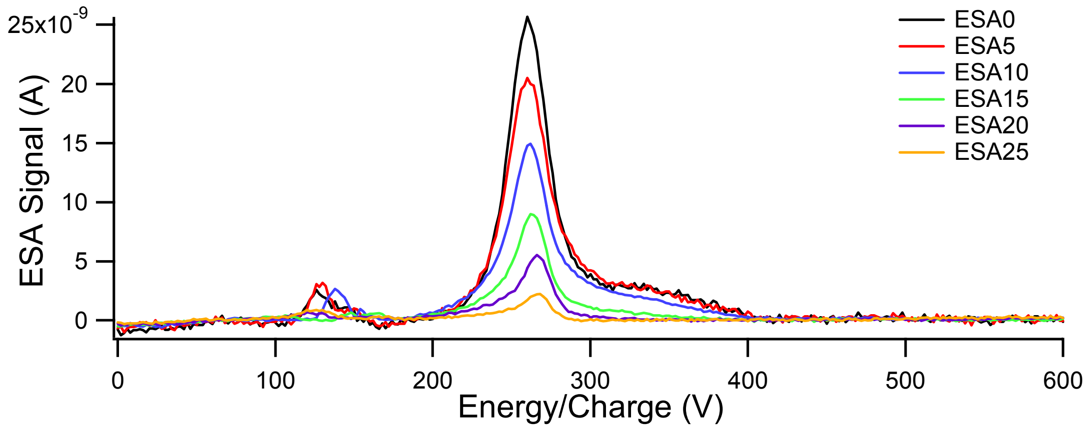

Figure 4-40: ESA data obtained at low angles in the offset cluster configuration. Due to a shift in the spectrometer constant, the apparent locations of the peaks are incorrect, but the shapes of the profiles are valid.

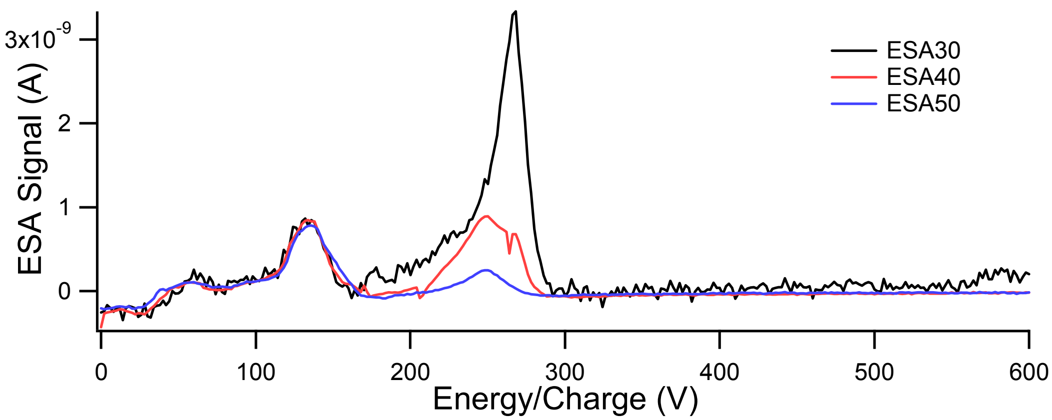

Figure 4-41: ESA data taken from 30 to 50 degrees off the centerline of thruster 3 in the offset cluster configuration. Note the magnitude of the secondary peaks.

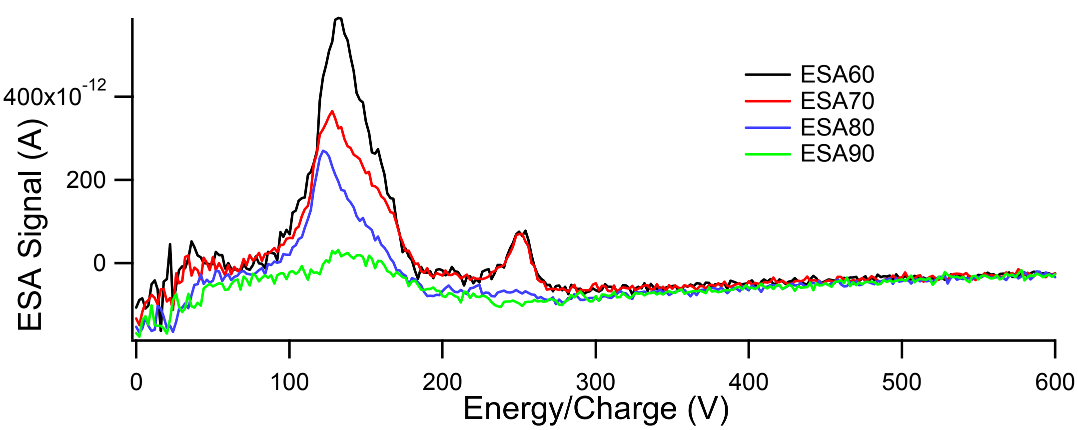

Figure 4-42: Large-angle ESA traces taken in the offset cluster configuration.

Figures 4-43 through 4-45 below show RPA data obtained in the offset cluster configuration. The low angle traces show a primary peak at 226 volts and a wide secondary structure occurring between 100 and 170 volts. The absence of this structure in the single thruster data indicates that it is an effect of clustering multiple thrusters. Since the spacing of the thrusters is such that this feature cannot be explained as a geometric effect, it appears to indicate an increase in elastic scattering due to clustering. The relatively small magnitude of the corresponding low energy structure in the ESA data presented in Figs. 4-40 through 4-42 indicates that most of the ions forming this feature originate at locations outside the ESA's field of view, i.e. in the area between the thrusters.

Similar to the trend shown in the ordinary cluster configuration, the primary peak in the offset cluster RPA data gradually shifts to lower voltages at angles greater than 10° off centerline. This differs significantly from the single thruster case in which the primary peak remained detectable near 220 volts out to an angle of 50°. As shown in Figs. 4-44 and 4-45, the peak shifts down to approximately 200 volts above 20°, and the low-energy ions begin to dominate the spectrum at angles greater than about 60°.

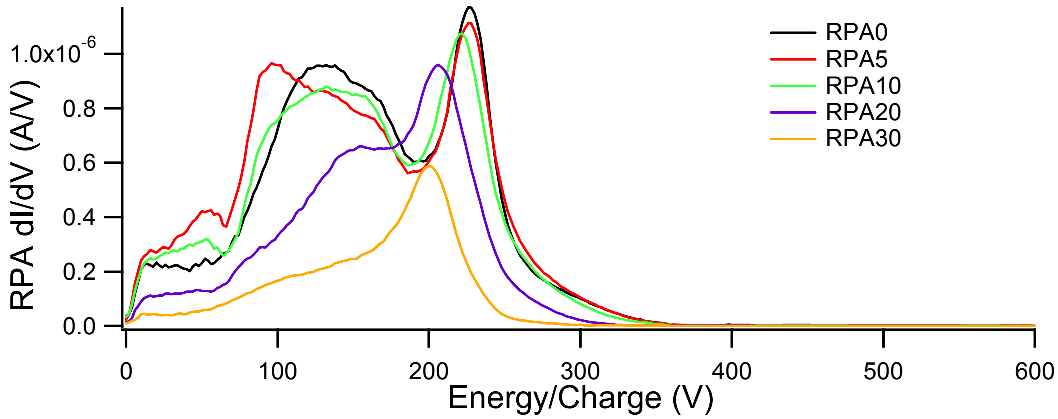

Figure 4-43: RPA data collected at low angles in the offset cluster configuration. The low-energy structure appears to be due to elastically scattered ions originating from the area between the thrusters.

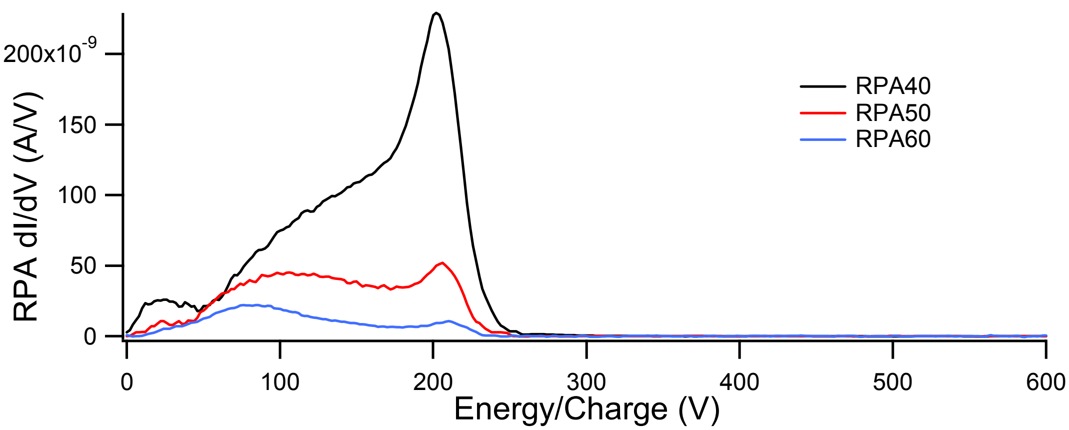

Figure 4-44: Energy per charge spectra measured by the RPA at angles between 40 and 60 degrees in the offset cluster configuration.

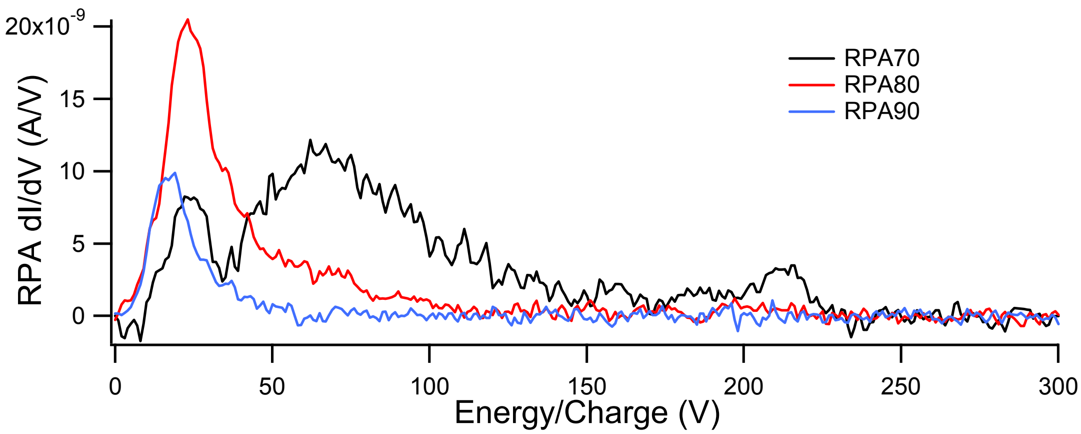

Figure 4-45: Large angle RPA data taken in the offset cluster configuration.

4.8 Ion Species Fractions

Measurements were taken with the ExB probe aligned to the center of the Hall thruster cluster over a range of angles spanning 0° to 50° before the signal was lost at approximately 60° with respect to the cluster centerline. In order to allow the probe to image ions originating from all four thrusters, the measurements were taken at an axial distance of 1 meter rather than the 0.5 meter distance of most of the other measurements presented in this chapter. Sample ExB traces recorded at angles of 0°, 20° and 40° off the cluster centerline are shown in Figs. 4-46 through 4-48, respectively. The species fractions inferred from these measurements according to the method presented in Chapter 2 are plotted in Fig. 4-49. Like the single thruster data, the fractions shown in Fig. 4-49 are the average of three traces and the error bars represent the standard deviation at each location.

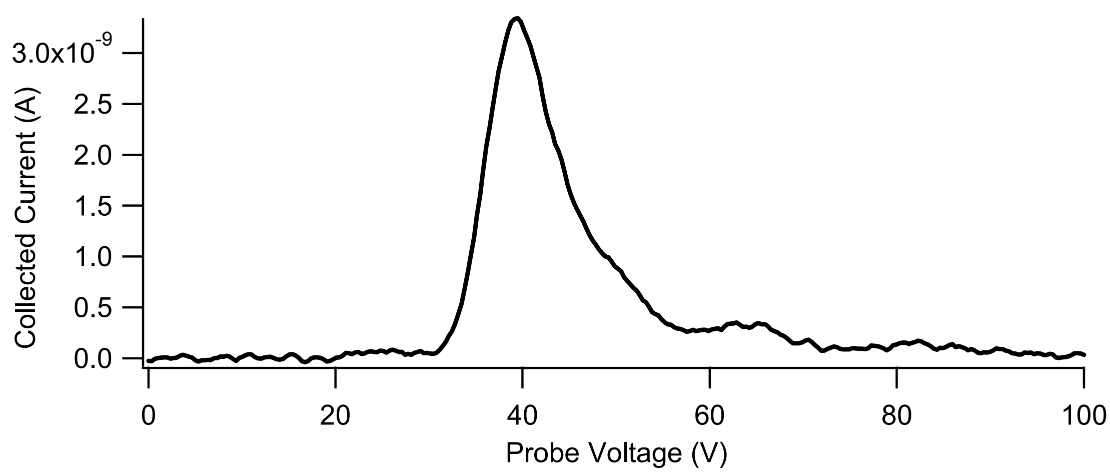

Figure 4-46: Sample ExB probe data taken 1 meter downstream of the cluster on centerline.

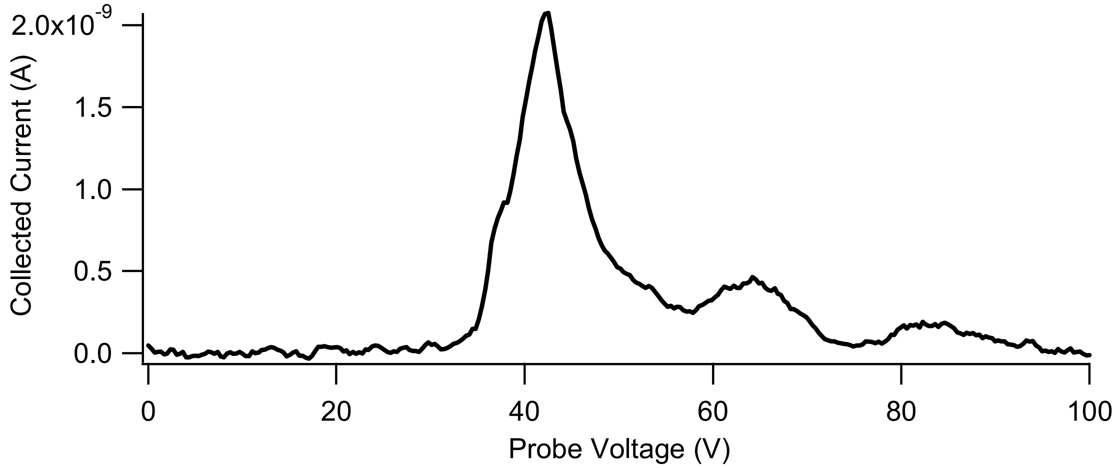

Figure 4-47: ExB probe data taken 20 degrees off the cluster centerline with all 4 thrusters operating.

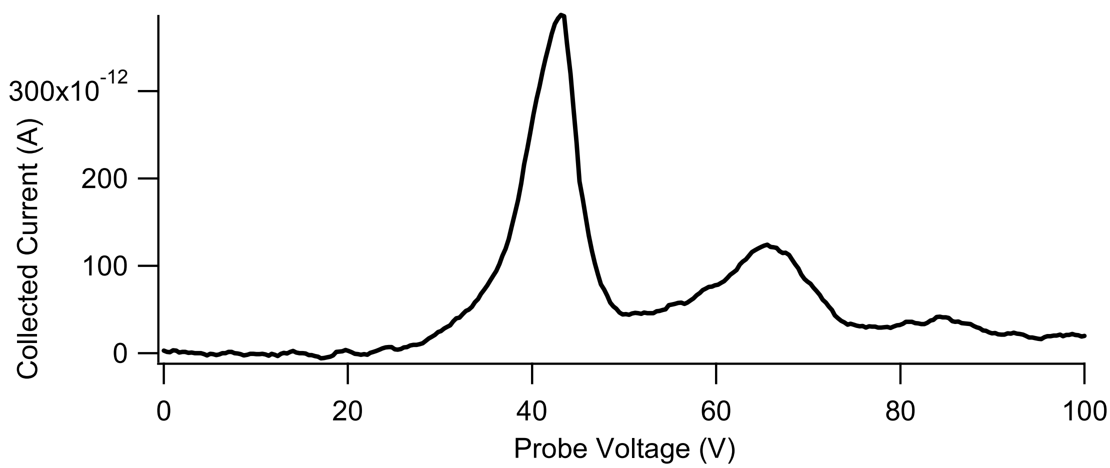

Figure 4-48: ExB data taken 40 degrees off the cluster centerline at a distance of 1 meter.

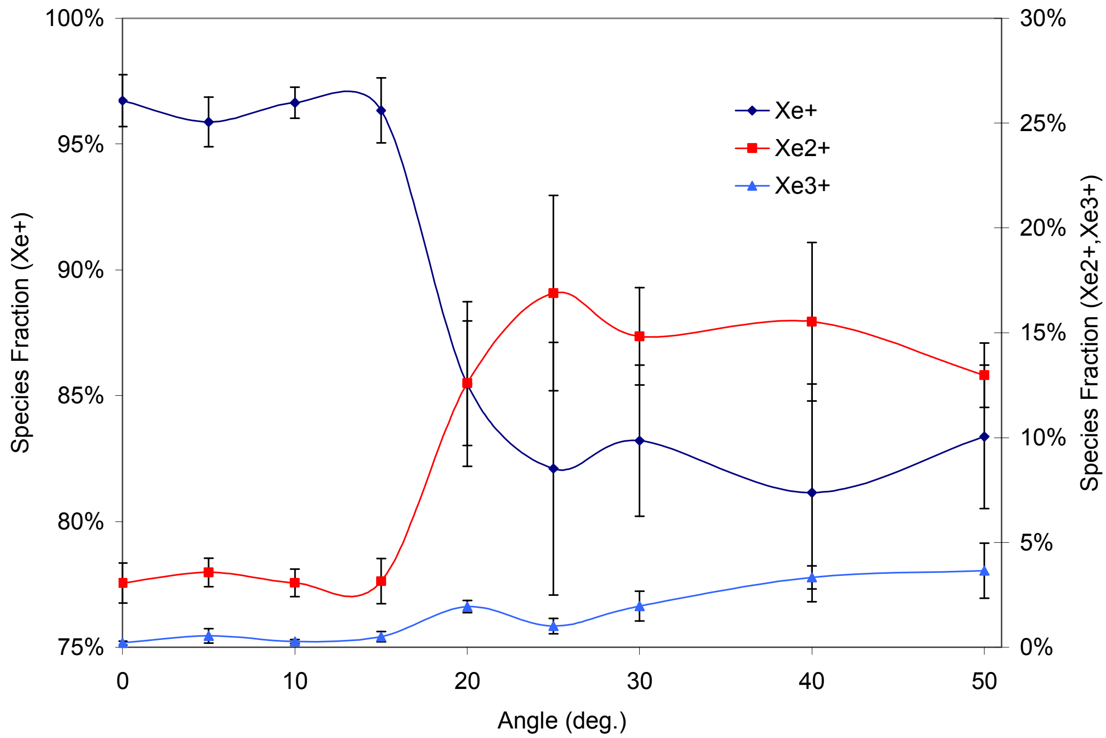

Figure 4-49: Apparent species fractions calculated from ExB probe traces in the cluster plume. Recall that this instrument cannot detect changes in species that occur downstream of the ion acceleration region.

The species fractions depicted in Fig. 4-49 show a structure very much like the one recorded downstream of a single thruster. The fraction of singly-charged ions is approximately 97% near the cluster centerline and falls sharply to slightly less than 85% at angles above 15°. The fraction of Xe^{2+} is less than 5% at low angles and climbs to about 15% between 15° and 20°. These numbers agree with the single thruster data to within the standard deviation of the measurements. It must be reiterated, however, that the ExB probe is purely a velocity filter (see the discussion in Chapter 2). This means that the instrument is unable to detect changes in charge state that occur downstream of the thruster acceleration region because the "charge states" are inferred based on the assumption that all ions are created at approximately the same location in the thruster discharge chamber and experience the same accelerating potential. The fact that the cluster measurements agree with the single thruster data really only indicates that clustering does not affect the ion production and acceleration mechanisms within any of the individual thrusters. The data depicted in Fig. 4-49 should not be interpreted as giving detailed information about charge exchange processes that occur in the plume.

5. CLUSTER CHARACTERIZATION – ALTERNATIVE CONFIGURATIONS

Although the nominal cluster configuration discussed in the last chapter may be preferred in many cases due to its favorable combination of modularity and scalability, there are some situations in which alternative cluster arrangements may prove advantageous. For example, it may be beneficial in some situations to operate a cluster of thrusters in parallel so that the entire assembly may be powered from a single, large PPU rather than several smaller ones. In other situations, performance benefits may be achieved by operating multiple thrusters from a single cathode. Since propellant injected through the hollow cathode is not accelerated through the engine, it provides no thrust and therefore reduces the overall specific impulse of the system. Clearly, operating multiple thrusters from a single cathode (without increasing the cathode mass flow rate) would mitigate the effects of this loss mechanism compared to operating each thruster with its own cathode. This chapter examines some of the technical issues related to each of these alternative configurations.

5.1 Experimental Configurations

Several different experimental configurations were tested to explore the various modes of cluster operation discussed above. In the first arrangement, both thrusters 2 and 3 were operated from a single discharge power supply, as sketched in Fig. 5-1. The main goal of operating the thrusters in parallel was to examine the possibility of cathode current sharing between the devices through the plasma plume. The electromagnet, keeper, and cathode heater circuits remained separate between the thrusters.

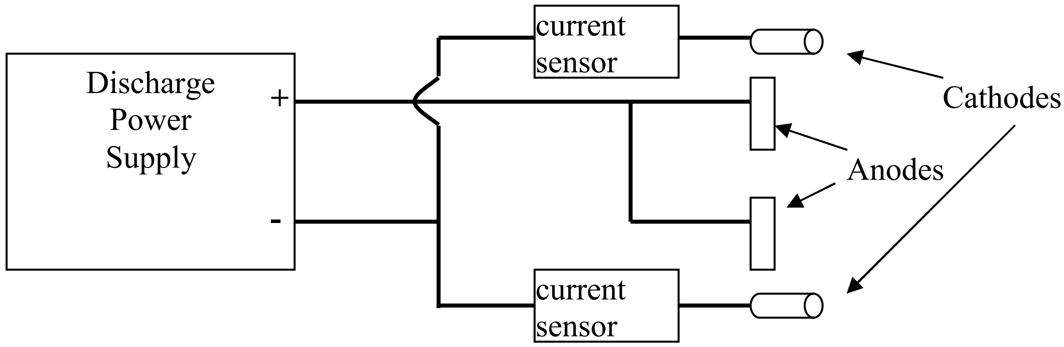

Figure 5-1: Two thrusters operated in parallel to examine current sharing.

In the second experimental configuration, two thrusters were operated from a single hollow cathode to examine the effects of cathode number and placement on plume properties. This was accomplished with two separate cathode arrangements. In one case, two thrusters were operated from cathode 3. Measurements were conducted at AFRL with thrusters 3 and 4 operating from cathode 3, while the shared cathode tests at PEPL used thrusters 2 and 3 simply because of the different probe positioning systems used in these facilities. In both facilities, the xenon flow rate through the cathode remained constant at 1 sccm. The second neutralizer tested in this "shared cathode" configuration was a 6.35-mm (¼") Model HCN-252 hollow cathode available from Ion Tech, Inc. It was placed at the center of the cluster and operated with a constant 5 sccm xenon flow rate. Since it is unlikely that the different cathode designs have any significant effect on the operation of the engines, comparing data obtained with the Ion Tech cathode to measurements made using the shared Busek cathode allows the effect of cathode location to be examined. The discharge circuit used during the shared cathode measurements is sketched in Fig. 5-2.

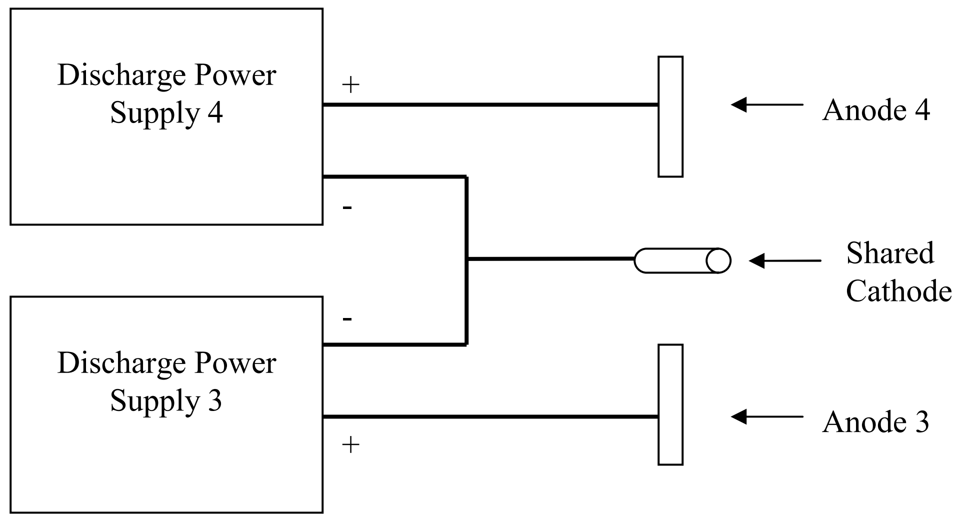

Figure 5-2: Discharge circuit for shared cathode experiments.

5.2 Discharge Current Characteristics

Discharge current characteristics recorded with two thrusters operating in parallel are shown in Fig. 5-3. As shown, the current flowing through each anode is approximately 0.80 amps and is nearly constant between the thrusters. This is not surprising since the anode current is controlled primarily by the propellant mass flow rate through each engine. The cathode current traces, on the other hand, show distinct differences between the two units with cathode 3 supplying nearly all of the current necessary to operate both engines. This dominance is probably due to minor variations between the cathodes resulting in one having a slightly lower affinity for electron emission. This creates a higher effective resistance for current flowing through that cathode and electrons, choosing the path of least resistance, flow preferentially through cathode 3. In Fig. 5-3, the constant 0.50 amp keeper current flowing through each cathode has been subtracted from the displayed traces. The high current levels recorded during the first few minutes of operation were due to the cathode heaters, which were turned off after the system reached steady-state operation.

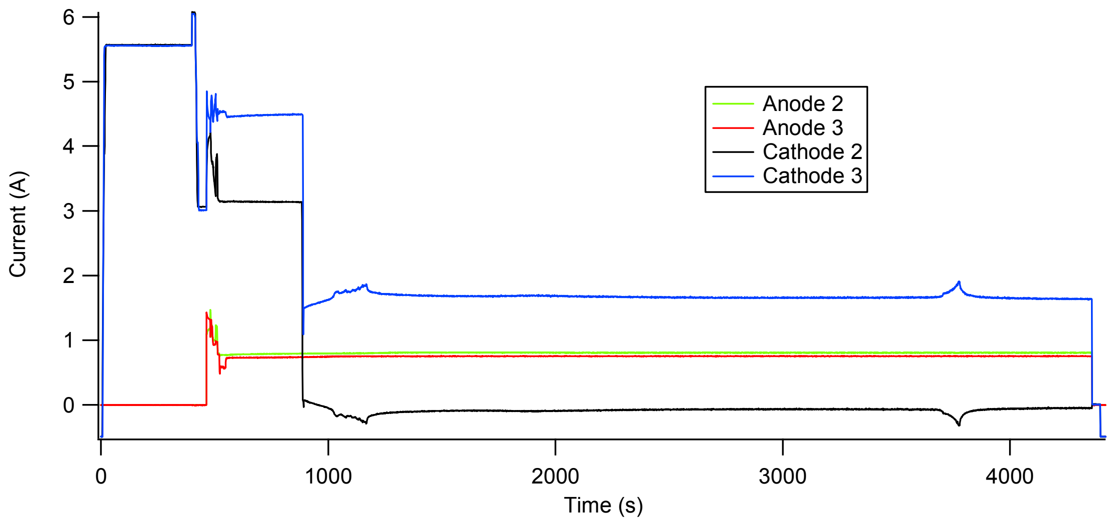

Figure 5-3: Anode and cathode currents recorded with two thrusters operating in parallel. Note that one cathode supplies almost the entire electron current.

The dominance of one cathode shown in Fig. 5-3 has several potentially important implications for cluster design. First, it implies that each cathode in a cluster of thrusters designed for parallel operation should be capable of supplying sufficient current to neutralize the entire cluster since it is doubtful that manufacturing tolerances could be reduced enough to prevent one cathode from dominating the discharge. Drawing sufficient charge from a single cathode is not particularly difficult for a low-power cluster with a total current throughput of only a few amps, but for the very high-power systems in which clusters will likely be implemented, emission of the entire cluster current from a single hollow cathode may prove to be impractical. In this case, the PPU would need to be modified to ensure that the current flowing through each cathode remained at an acceptable level. The added complexity associated with the current balancing circuitry could potentially negate any performance and mass advantages associated with using a single, large PPU instead of several smaller ones.

Turning our attention to the case where two thrusters were operated with individual power supplies and a single, shared cathode, it was found that no especially interesting or surprising phenomena occurred when both thrusters were operated simultaneously. Running a single thruster from a distant cathode, on the other hand, caused significant changes in operating conditions. The discharge current and cathode potential data displayed in Fig. 5-4 were obtained with both TH2 and TH3 coupled to cathode 3 in the LVTF. As shown, when TH2 was operated alone with cathode 3, the discharge current was slightly higher than normal and the level of current oscillations was also higher than observed in the nominal configuration. This is consistent with previously published measurements that showed the electromagnetic noise radiated from a larger Hall thruster to increase as the distance between the engine and cathode was increased.[105] When TH3 was ignited, the discharge current and magnitude of oscillations in TH2 decreased to near nominal levels. At the same time, the cathode potential increased (moved closer to ground) by about 2.5 volts, thus bringing it to near the nominal level. When TH3 was then shut off without changing any settings to TH2, the discharge current and cathode potential returned to their original, anomalous values. This behavior is explained further in Section 5.7.

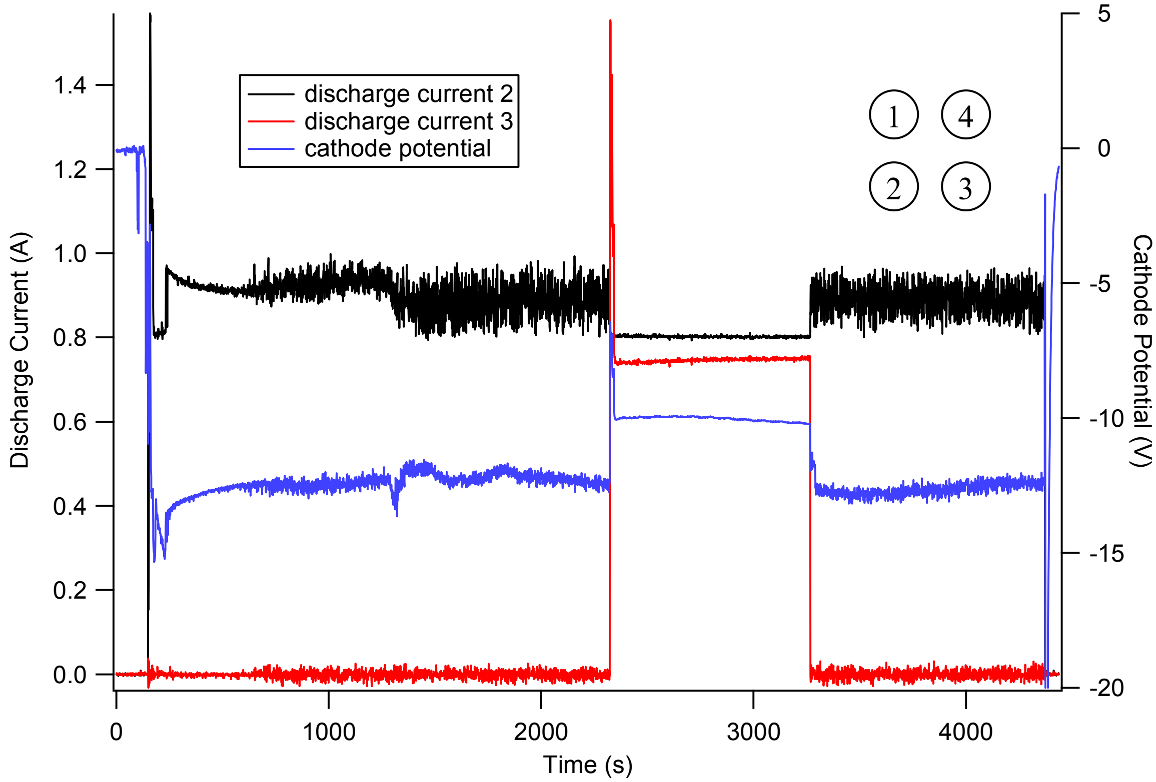

Figure 5-4: Discharge currents and cathode floating potential for operation with TH 2&3 coupled to cathode 3. The sketch in the upper right shows the relative thruster positions.

To examine the coupling between two thrusters sharing a single cathode, the current interrupt switch was used to perturb one thruster while both were operated from the central Ion Tech cathode in Chamber 6. Figures 5-5 through 5-7 show the response of TH2 and TH3 to interruptions of discharge current 3 lasting 10, 60, and 100 microseconds, respectively. As Fig. 5-5 shows, a short current disruption of 10 microseconds caused only a modest overshoot in the discharge current of TH3 and no apparent reaction in TH2. When the disruption duration was increased to 60 microseconds, however, the current flowing through TH3 increased transiently to more than 7 amps after the circuit was closed. This led to a distinct perturbation to the discharge current of TH2. When the current interruption duration was increased to 100 microseconds, the overshoot in the current through TH3 increased to more than 10 amps. The perturbation in TH2 remained very similar in character and magnitude to the one observed after the 60 microsecond disruption. In both cases, the perturbation was slightly larger than the one observed in the nominal configuration, but not large enough to imply any particular complications in the basic operation of a cluster using a single, shared cathode. The more interesting aspects of running a cluster in this mode are illuminated in the following sections regarding the plasma plume properties.

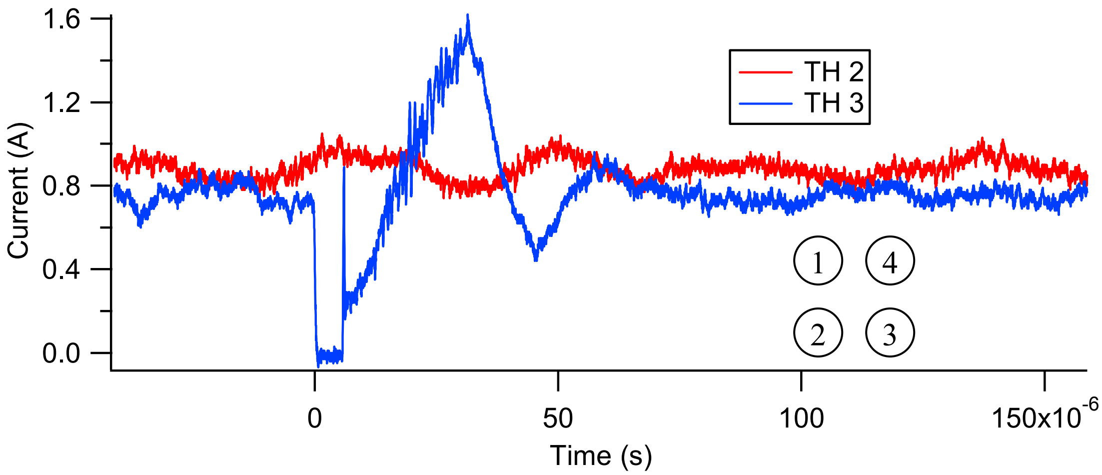

Figure 5-5: Response of TH 2&3 to a 10 microsecond disruption of the current to TH3.

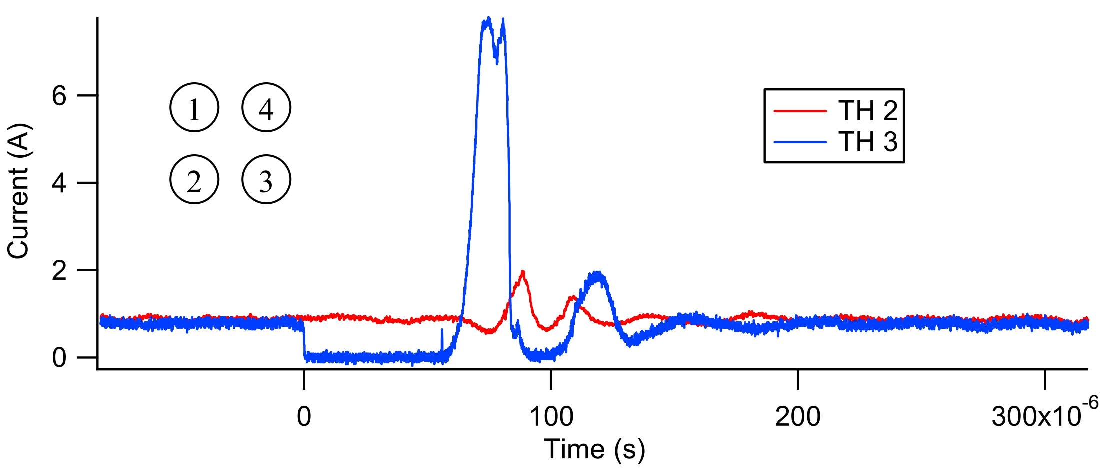

Figure 5-6: Response of TH 2&3 to a 60 microsecond current disruption. Note the apparent coupling between the devices.

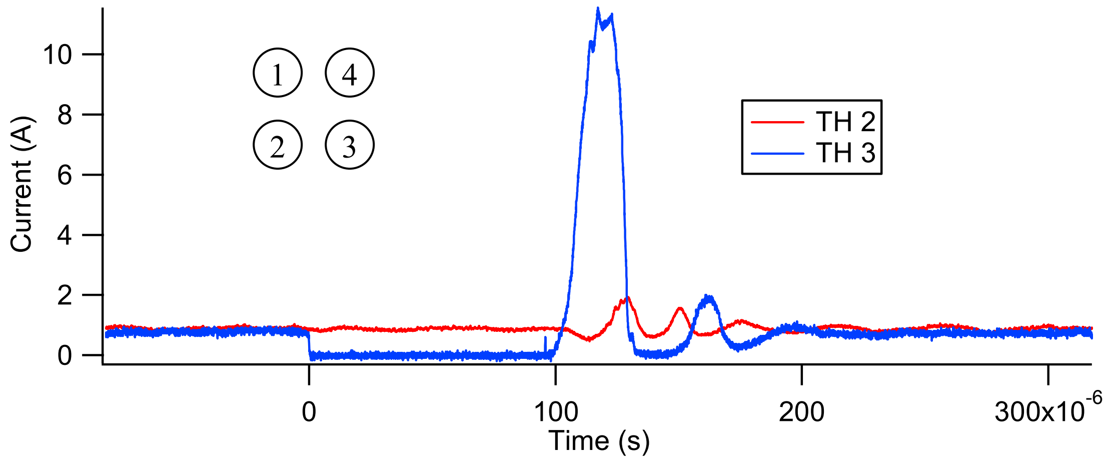

Figure 5-7: Response of TH 2&3 to a 100 microsecond current interruption.

5.3 Plasma Density

The large triple probe was used to measure the plasma density in the plume for both shared cathode configurations: the shared Ion Tech cathode and the shared cathode 3. Measurements were obtained in Chamber 6 with thrusters 3 and 4 operating individually and simultaneously. Figures 5-8 through 5-12 show the profiles recorded at five different axial locations in the plume. Although these plots each contain a large amount of data, the colors and symbols have been chosen to enhance clarity. As the legend shows, all of the blue traces were obtained with the thrusters sharing the Ion Tech cathode located at the center of the cluster. The data recorded with cathode 3 shared are depicted in red. Measurements made with thruster 3 operating alone are represented by diamonds, thruster 4 by circles, and both thrusters operating together by triangles. The thick black line in each figure depicts the density profile measured with each thruster operating in conjunction with its own Busek cathode, i.e. in the nominal configuration studied in Chapter 4.

The plasma density measurements shown below reveal several interesting features related to shared cathode operation. First, the density downstream of a cluster operating with a single neutralizer cannot be predicted by simply summing the contributions from each individual thruster. This is particularly evident from examination of the data taken with cathode 3 shared. In this situation, thruster 3 shows no unusual plume characteristics when operating alone, which is to be expected since it is coupled to its own cathode. When thruster 4 is operated on this same cathode, however, the plume appears very diffuse and the peak density is more than a factor of 10 lower than the one measured with the engine coupled to its own cathode. Most surprising is that the density downstream of thruster 4 increases to near the nominal profile (within about 25%) when TH 3&4 are operated simultaneously. Clearly, operating both thrusters together changes the basic operation of thruster 4, thus eliminating the possibility of predicting the cluster plume via superposition. Incidentally, the data presented here confirm the previous statement that it is the location of the hollow cathode and not the specific design of the electron emitter that causes changes in the plume properties. This is obvious since the profile downstream of thruster 4 differs greatly from that of thruster 3 when each is operated individually with cathode 3. Increasing the distance between the thruster and the neutralizer seems to dramatically decrease the plasma density in the plume.

Examination of the data taken with the thrusters coupled to the central Ion Tech cathode shows similar trends to those discussed above. Since this cathode is significantly farther away from the anode of each thruster than the cathodes of the nominal configuration, the lower density observed in the plume with each thruster running individually is consistent with the observations reported above. When both thrusters are operated together, the peak density downstream of each engine increases significantly compared to the level measured during individual operation. The plasma density with both thrusters operating from the central cathode, however, falls short of the ones measured with cathode 3 shared as well as those measured in the nominal configuration.

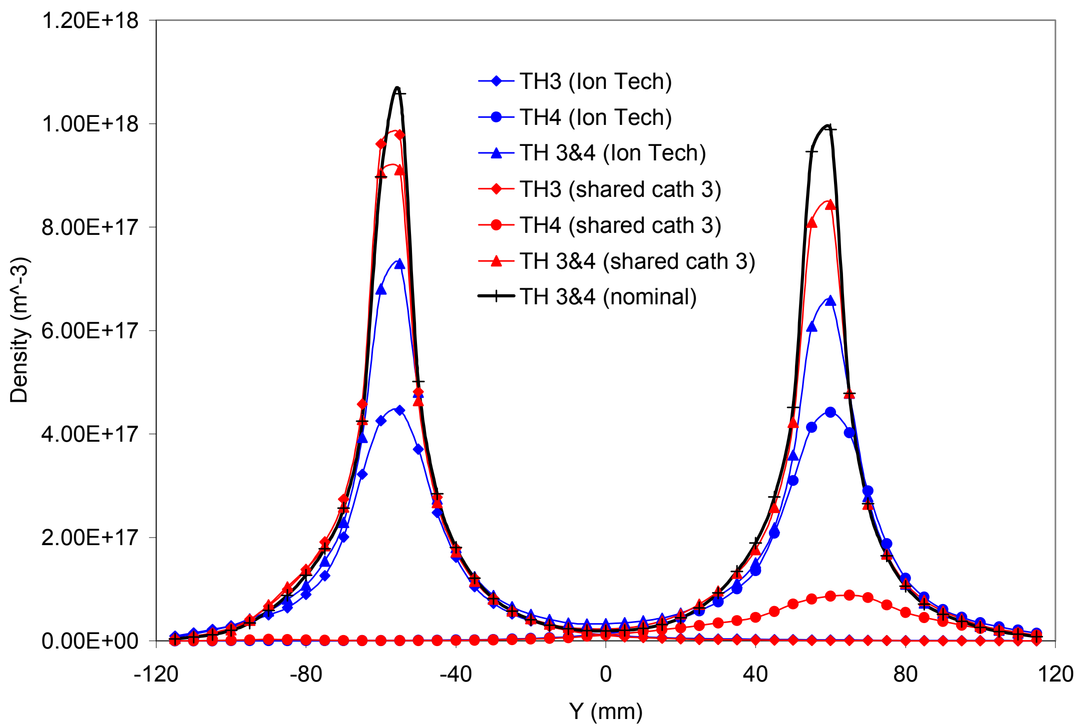

Figure 5-8: Plasma density measured 50 mm downstream of thrusters 3 and 4 for two different shared cathode configurations.

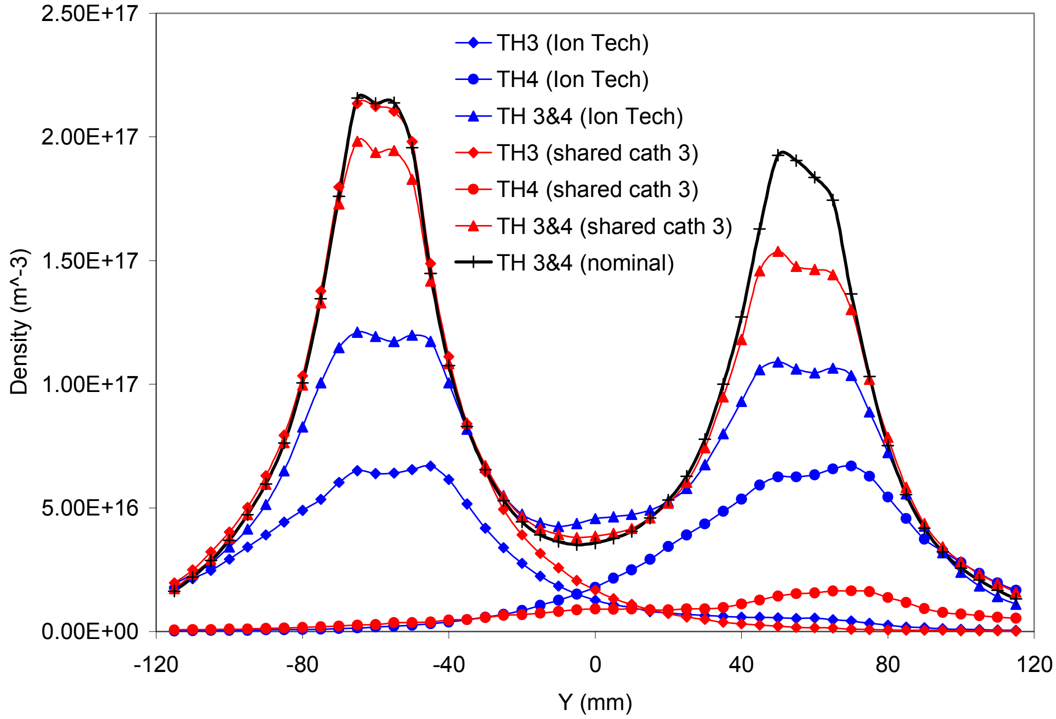

Figure 5-9: Plasma density measured with the triple probe at Z=100 in the shared cathode configuration. Note that the density downstream of a given thruster increases when an adjacent engine is operated.

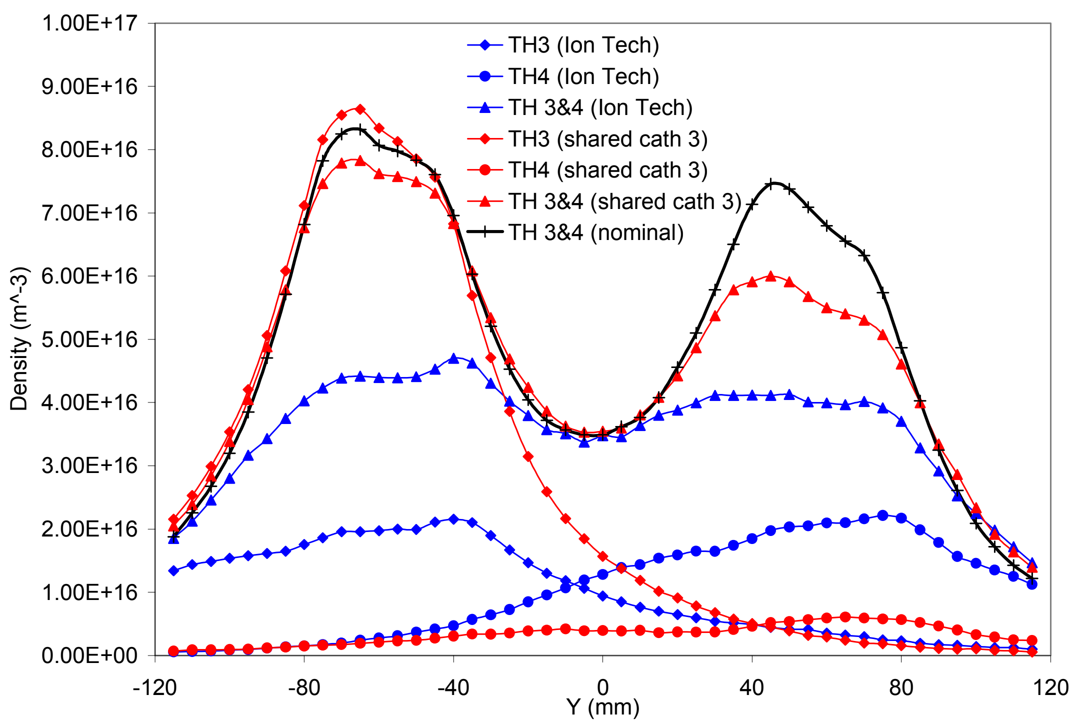

Figure 5-10: Density data taken in the shared cathode configuration at Z=150 mm.

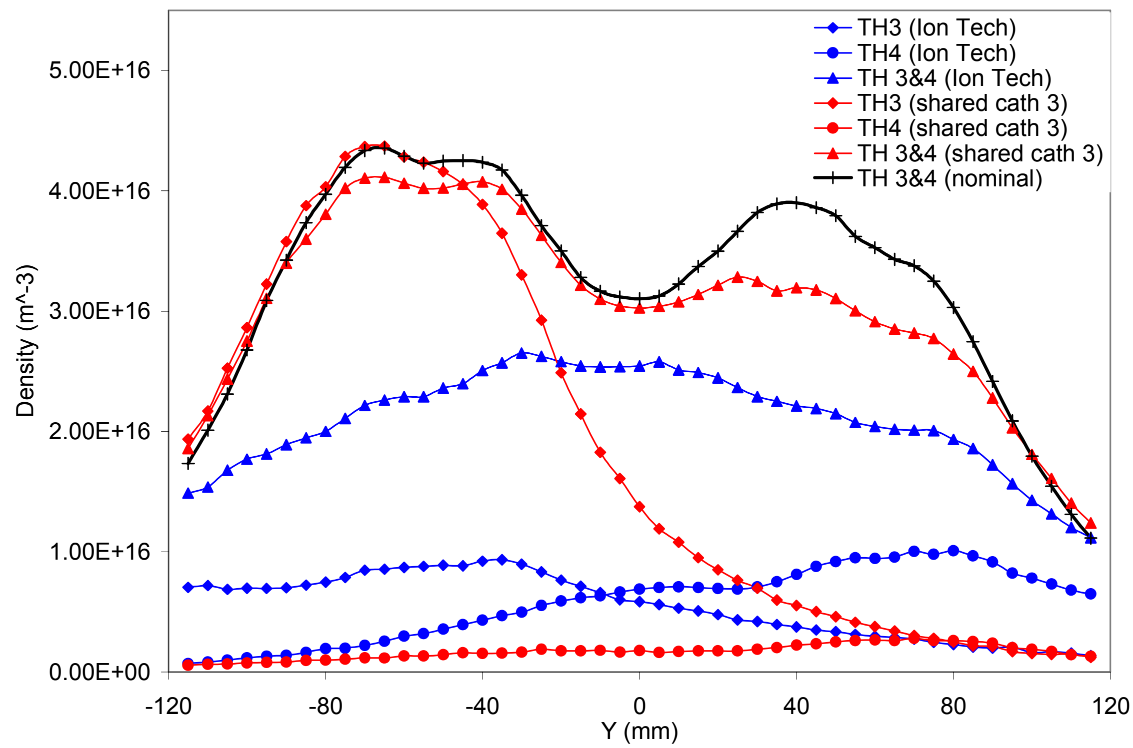

Figure 5-11: Density profiles at Z=200 with TH 3&4 sharing a cathode.

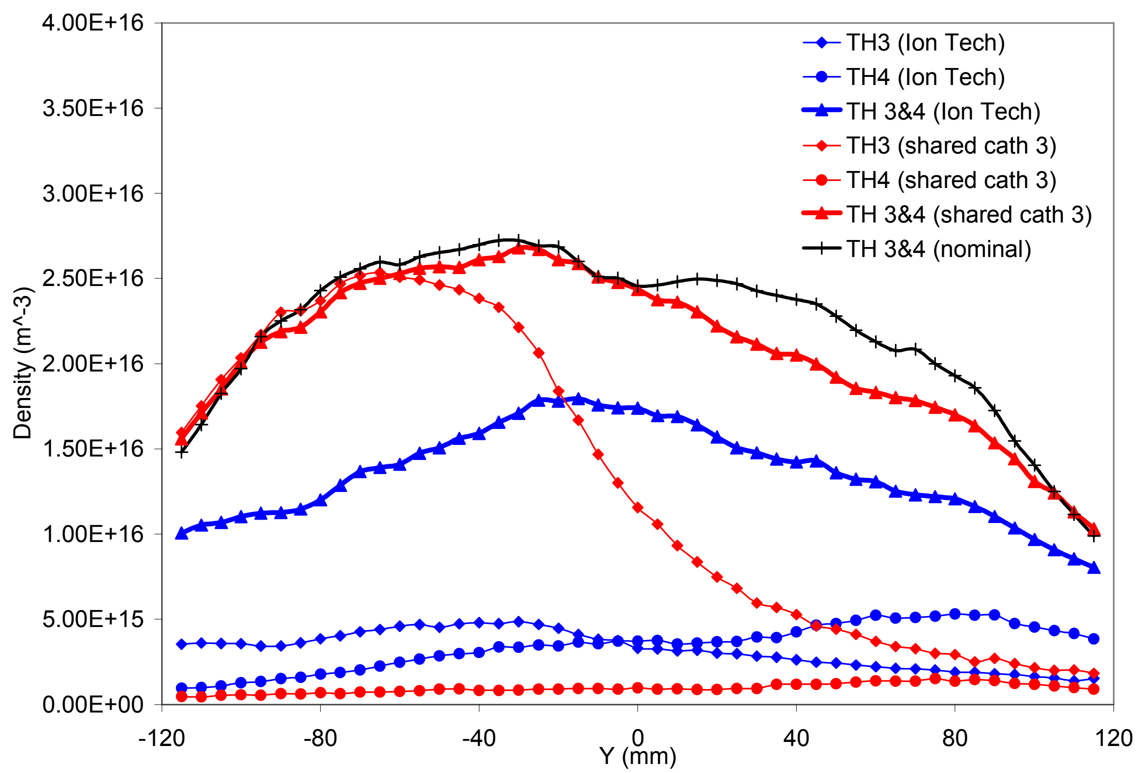

Figure 5-12: Plasma density 250 mm downstream for two different shared cathode configurations.

While the figures above show clearly that the location of the cathode has a significant effect on the properties in the plasma plume, they do not explain why this is the case. To provide a data base for studying possible causes, several additional sets of measurements were obtained at PEPL with thrusters 2 and 3 coupled to cathode 3. The configurations tested were: TH2 running alone, TH2 running and propellant flowing through TH3 (without a discharge), TH2 running with propellant flowing through TH3 and electromagnet 3 energized, and thrusters 2 and 3 operating simultaneously. Testing with propellant flowing through thruster 3 allows the effect of collisions to be evaluated (qualitatively, at least) by increasing the local neutral density in the region between cathode 3 and thruster 2.

The plasma density profiles recorded at three different locations downstream of thrusters 2 and 3 at PEPL are shown in Figs. 5-13 through 5-15 below. As shown in these plots, operating thruster 2 alone with cathode 3 resulted in a very diffuse plume with a low plasma density in agreement with the behavior discussed above. The addition of flow through thruster 3, and the concomitant increase in local pressure, caused the density in the plume to increase by about a factor of two, although it remained far below the levels exhibited during normal operation. Energizing the electromagnet of thruster 3 had no discernible effect. Finally, igniting thruster 3 caused the plasma density downstream of both thrusters to increase dramatically to levels consistent with those reported in Chapter 4.

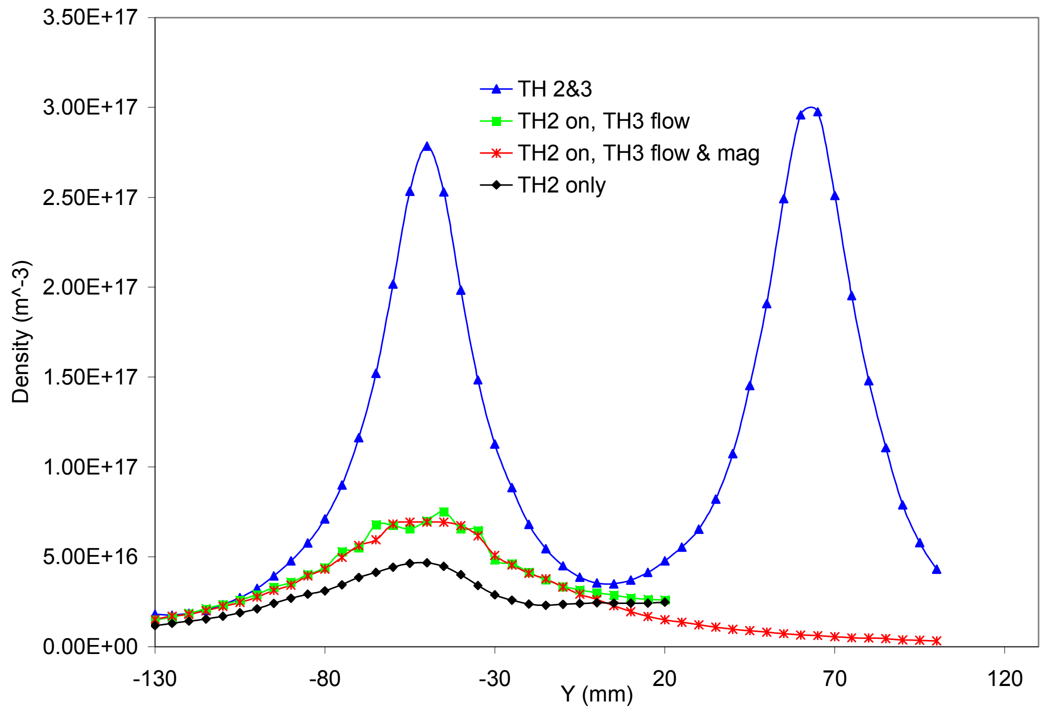

Figure 5-13: Plasma density recorded 70 mm downstream of TH 2&3 with cathode 3 shared. Note the effect of adding the flow through thruster 3.

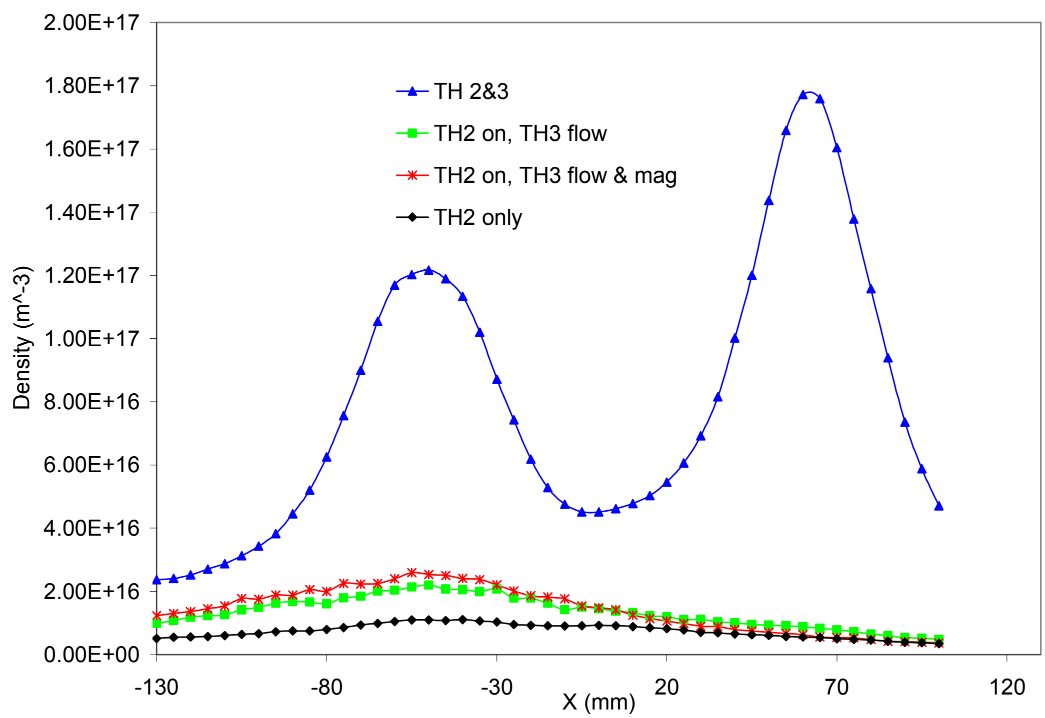

Figure 5-14: Plasma density measured 120 mm downstream of TH 2&3 at PEPL. Both thrusters were coupled to cathode 3.

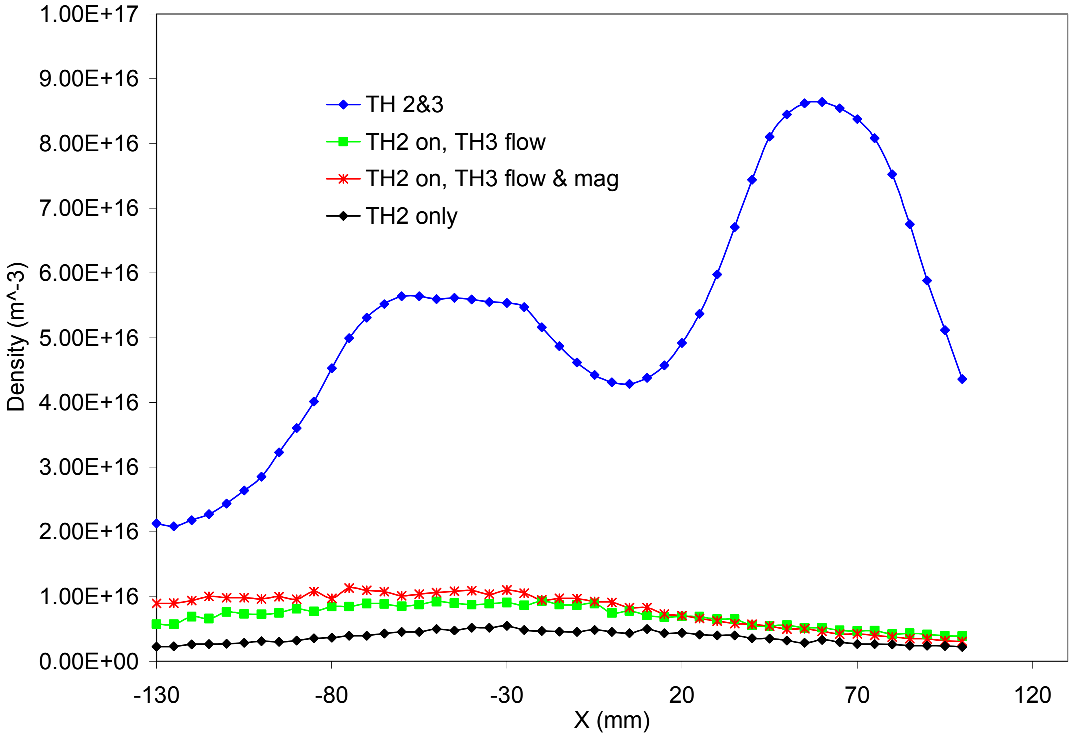

Figure 5-15: Plasma density at Z=170 mm with thrusters 2 and 3 operating from a shared cathode.

5.4 Electron Temperature

The same triple probe used to obtain the density measurements presented in the previous section also gave the local electron temperature. Figures 5-16 through 5-20 show the electron temperatures measured in Chamber 6 at AFRL for the two different shared cathode experiments. As shown, the electron temperature downstream of a thruster tended to increase when it was operated with a distant cathode. For example, when TH4 was operated in conjunction with cathode 3, Fig. 5-16 shows that the temperature peaked at over 10 eV compared to approximately 3 eV during normal operation. Coupling to the Ion Tech cathode caused similar behavior and the peak electron temperature with one engine running rose to approximately 6 eV. As expected, the peak electron temperature decreased with increasing downstream distance. Regardless of which cathode was used, running multiple thrusters tended to reduce the electron temperature in the plume, bringing it closer to the normal level. Operating both thrusters with cathode 3 caused the electron temperature to fall to almost exactly the nominal values, while it remained somewhat above normal during operation of the Ion Tech cathode.

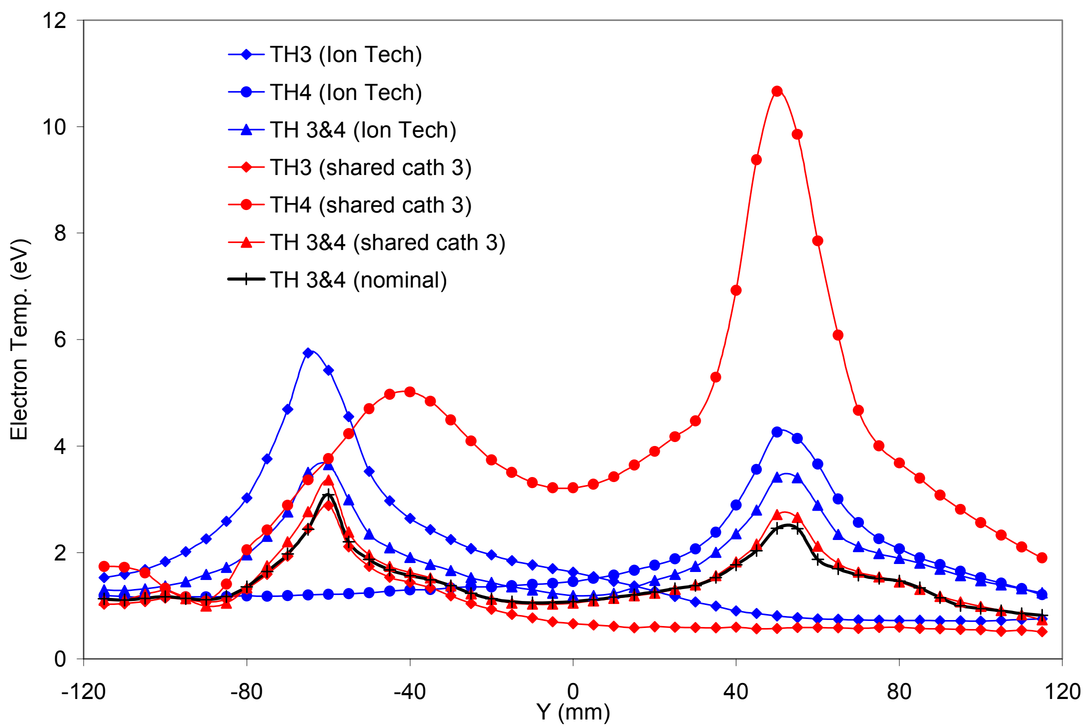

Figure 5-16: Electron temperature 50 mm downstream of thrusters 3 and 4 during shared cathode operation.

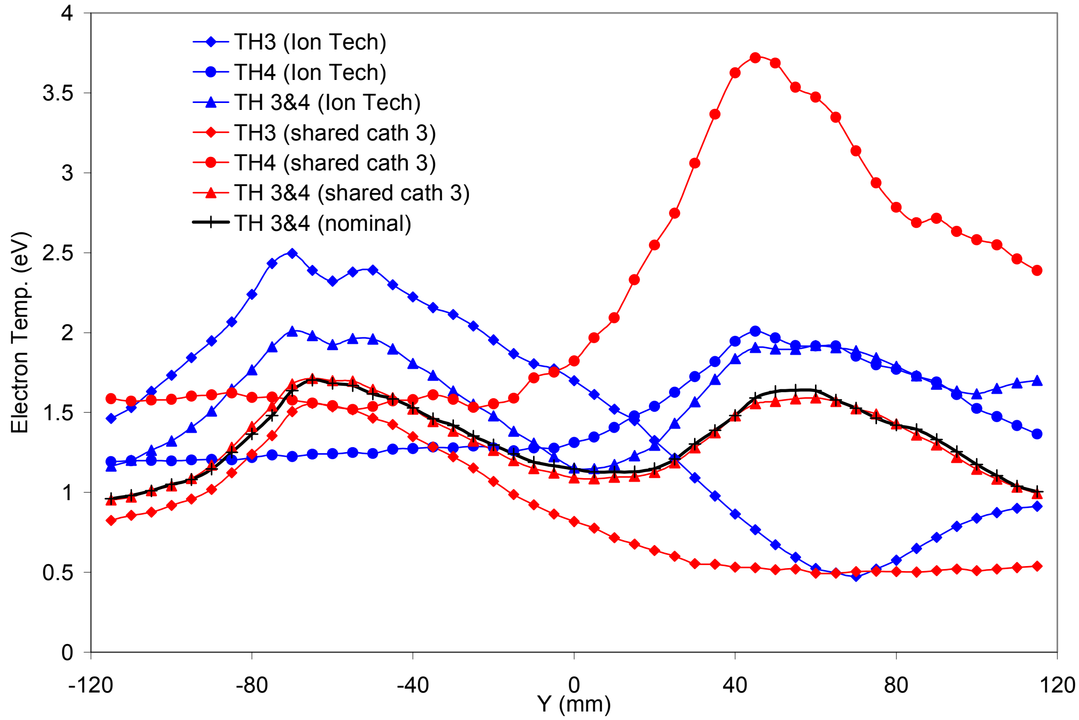

Figure 5-17: Electron temperature profiles downstream of TH 3&4 at Z=100 mm.

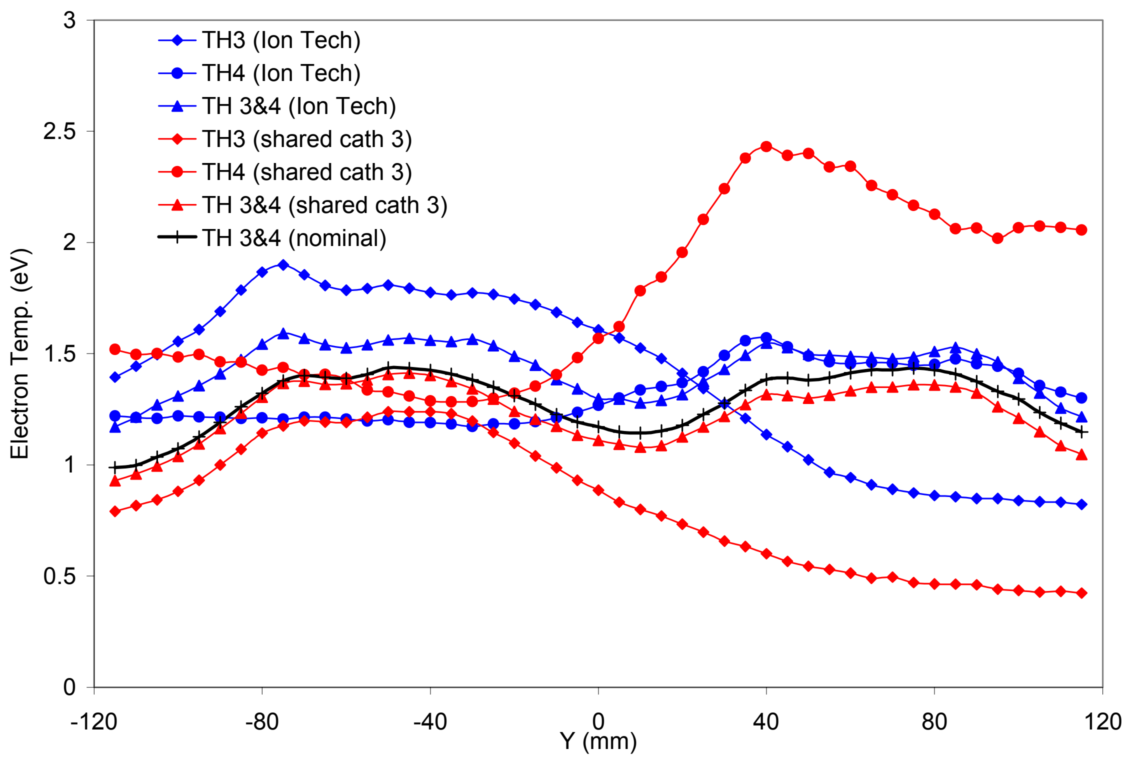

Figure 5-18: Electron temperature at Z=150 mm downstream of TH 3&4.

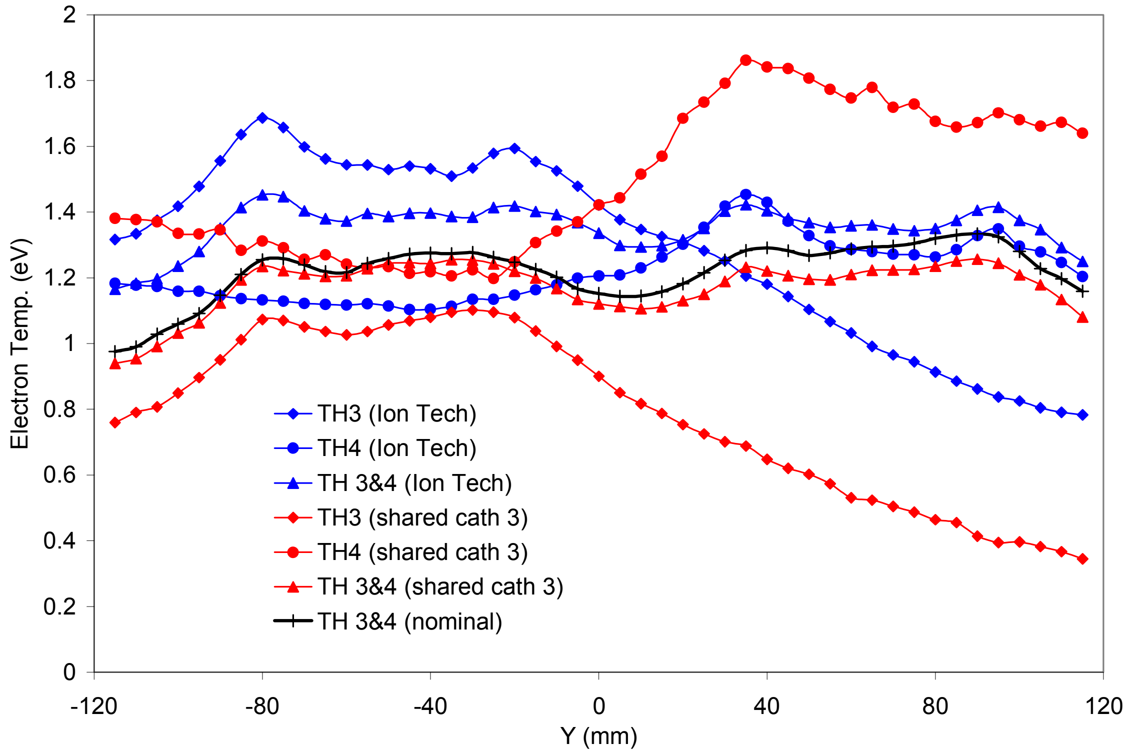

Figure 5-19: Measurements of electron temperature obtained using a triple probe at Z=200 mm.

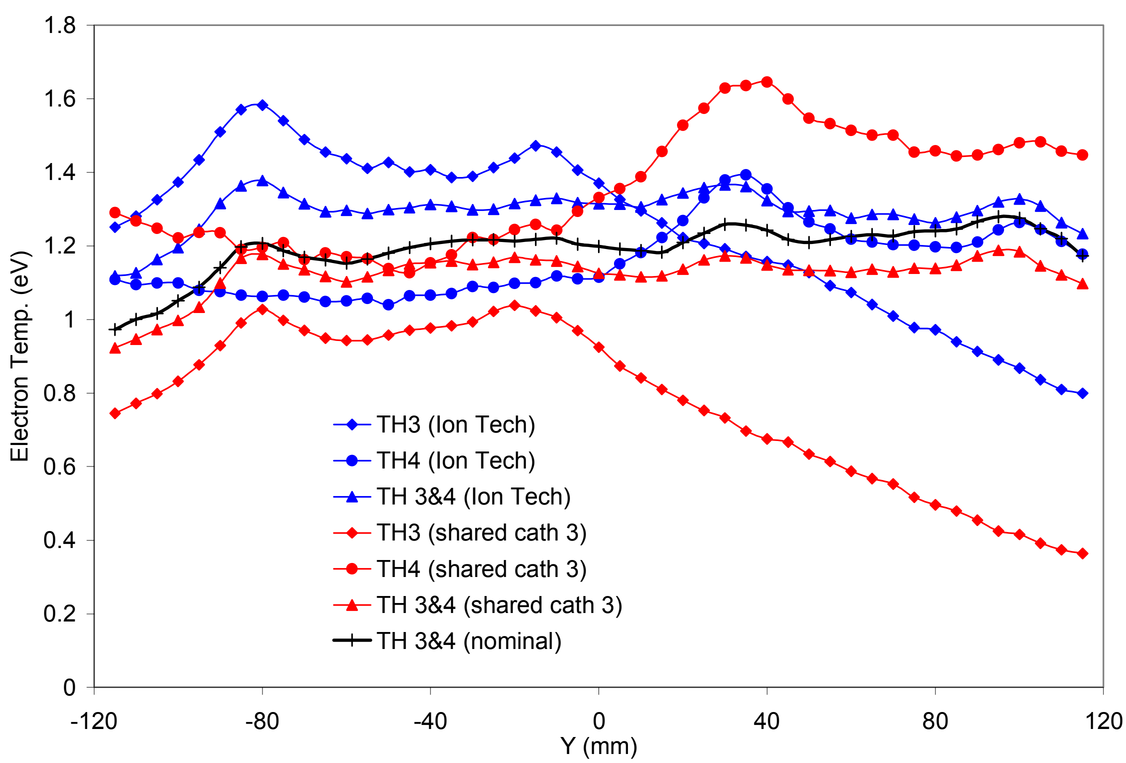

Figure 5-20: Far-field (Z=250 mm) measurements of electron temperature for shared cathode operation.

Electron temperatures measured at three axial locations in the LVTF with thrusters 2 and 3 sharing a single Busek cathode are shown in Figs. 5-21 through 5-23. As expected, operating thruster 2 with the distant cathode 3 caused the electron temperature in the plume to rise well above the values measured in the nominal configuration. In this mode, the temperature along the centerline of TH2 was approximately 6.5 eV at Z=70 mm and fell to less than 2.5 eV by 170 mm downstream of the exit plane. When an 8.5 sccm propellant flow was initiated through thruster 3, the electron temperature downstream of TH2 fell to about 3.5 eV at 70 mm and 1.5 eV by 170 mm downstream. This is similar to the behavior of the plasma density, which also showed significant changes when the average neutral density between the thruster and cathode was increased. Energizing the electromagnet of thruster 3 had very little effect on the temperature in the plume. When thruster 3 was operated in conjunction with thruster 2, the electron temperature fell to nominal levels and exhibited a high degree of symmetry between the plumes of the two engines, despite the fact that the hollow cathode was much closer to TH3 than it was to TH2. It can therefore be said that increasing the local pressure and running multiple thrusters both tend to decrease the electron temperature in the plume for clusters operated with a single cathode. The cause of this behavior will be discussed later in this chapter.

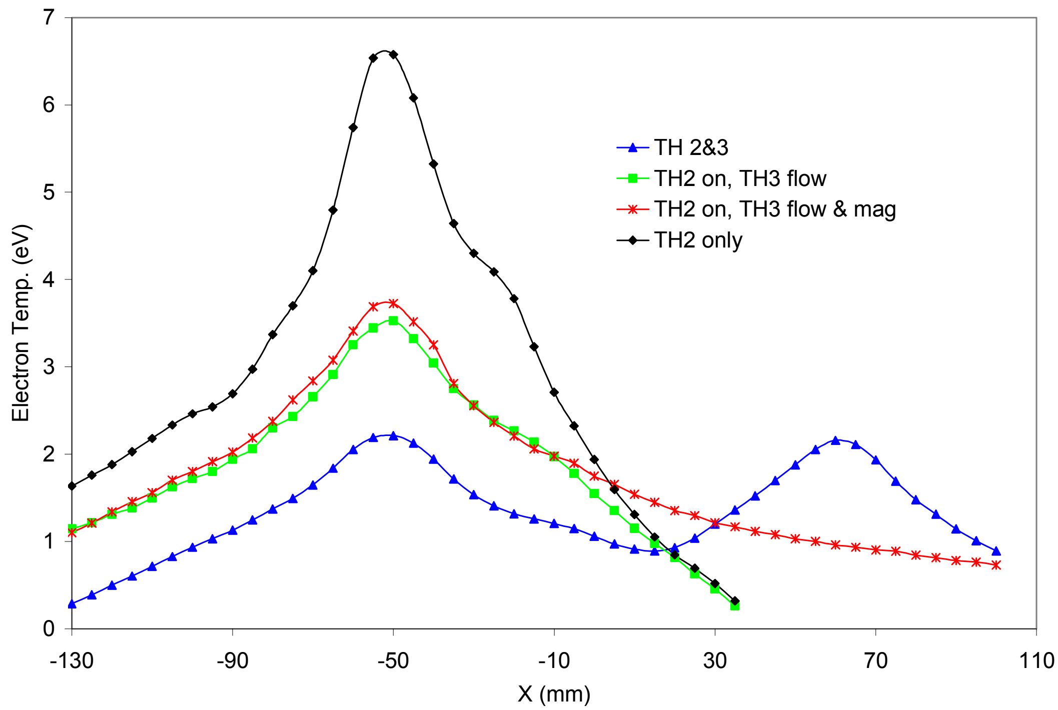

Figure 5-21: Electron temperature profiles 70 mm downstream of thrusters 2 and 3 under various configurations. Note how increasing the local neutral density and operating multiple thrusters both tend to decrease the temperature in the plume.

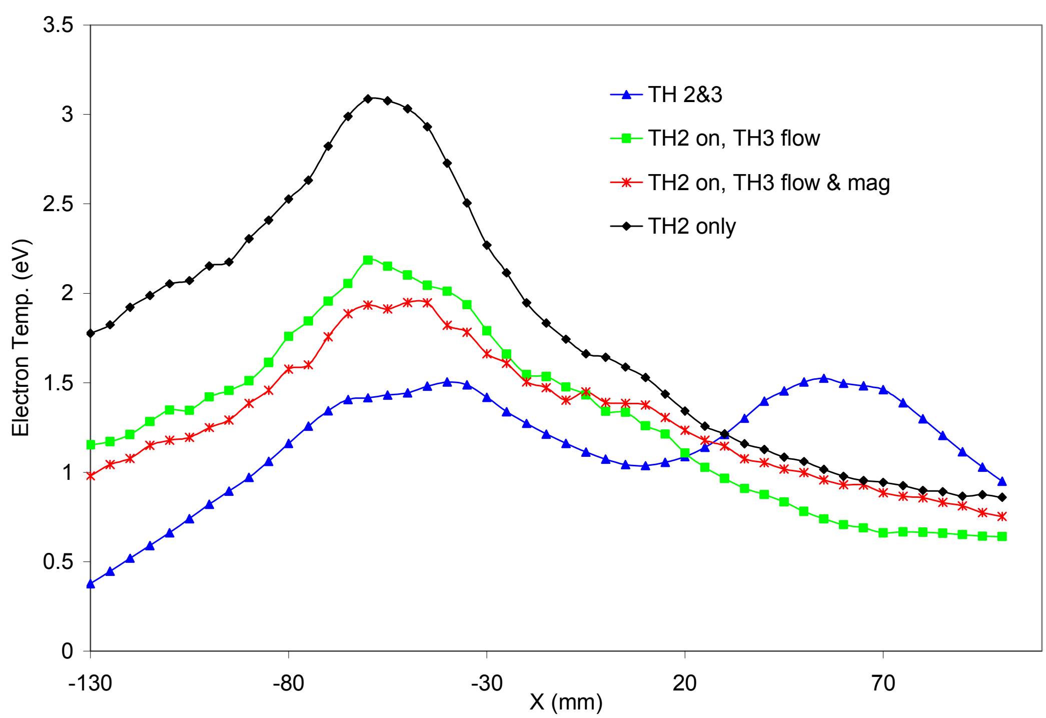

Figure 5-22: Profiles of electron temperature measured 120 mm downstream of TH 2&3 during operation with cathode 3 shared by the devices.

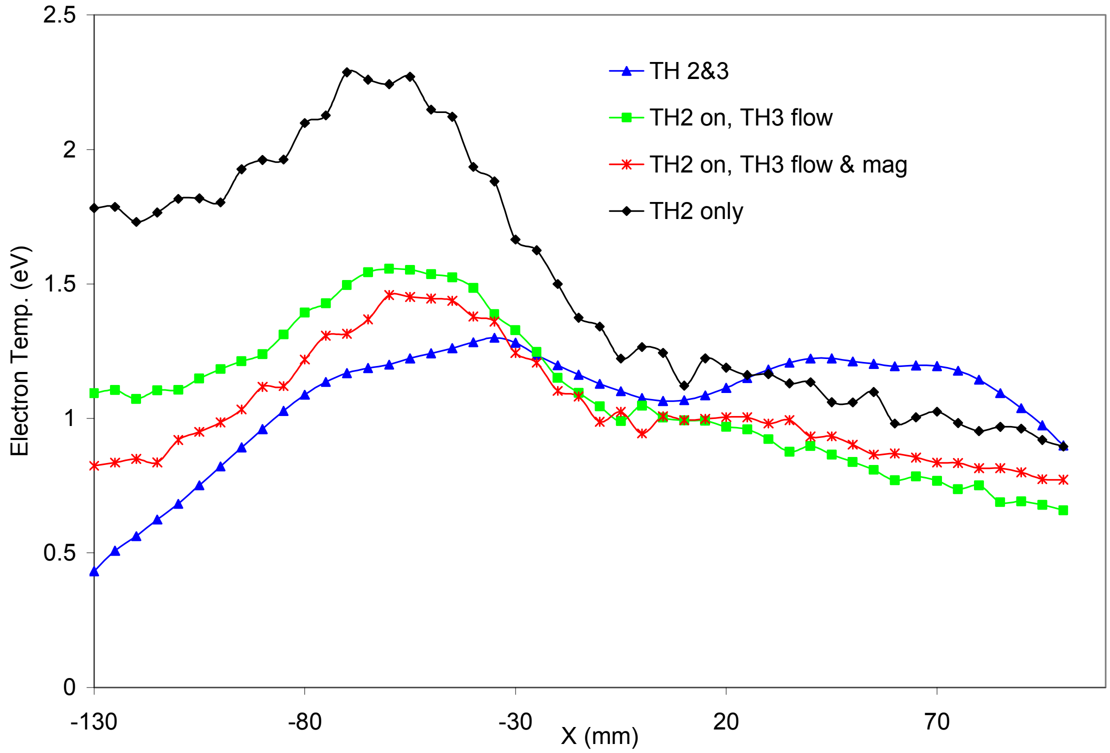

Figure 5-23: Electron temperature profiles 170 mm downstream of thrusters 2 and 3.

5.5 Plasma Potential

Like the plasma density and electron temperature, the plasma potential profiles in the plume also exhibited major changes from the nominal values when the cluster was operated with a single, shared cathode. Figures 5-24 through 5-26 show potentials measured downstream of TH 3&4 for several different configurations. As shown, operating a single thruster from the 3.2-mm (¼") Ion Tech cathode located at the center of the cluster caused the peak potential at Z=50 mm to increase to more than 50 volts compared to a normal value of just over 20 volts at this location. Operating both thrusters together with this cathode caused the peak plasma potential to fall to about 35 volts at this location. Similar to the behavior observed in the profiles of number density and electron temperature, coupling two thrusters to a single Busek cathode located in close proximity to one of the devices resulted in plasma potentials nearly identical to the ones recorded with each thruster operating independently. As expected, all of the potentials decreased with increasing axial distance. The relative positions of the curves, however, remained consistent, with the two-thruster, shared central cathode potentials falling between the nominal values and those measured with a single thruster operating from the central cathode.

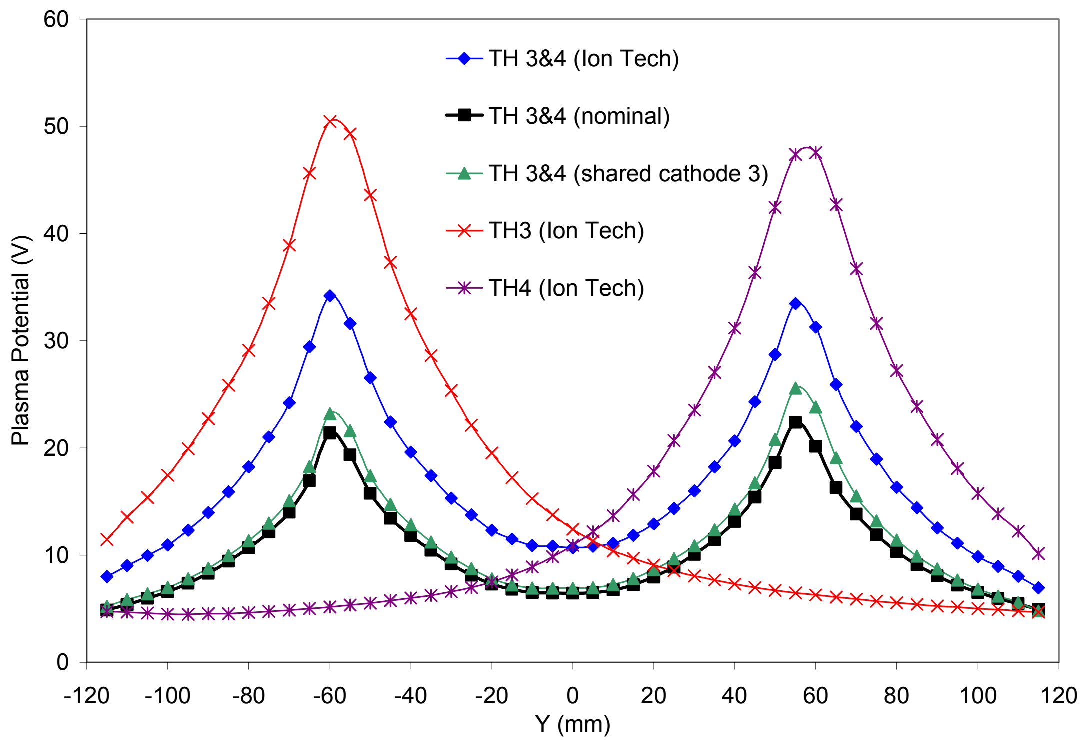

Figure 5-24: Plasma potential profiles measured 50 mm downstream of thrusters 3 and 4 in various experimental configurations. These data were recorded in Chamber 6 at AFRL.

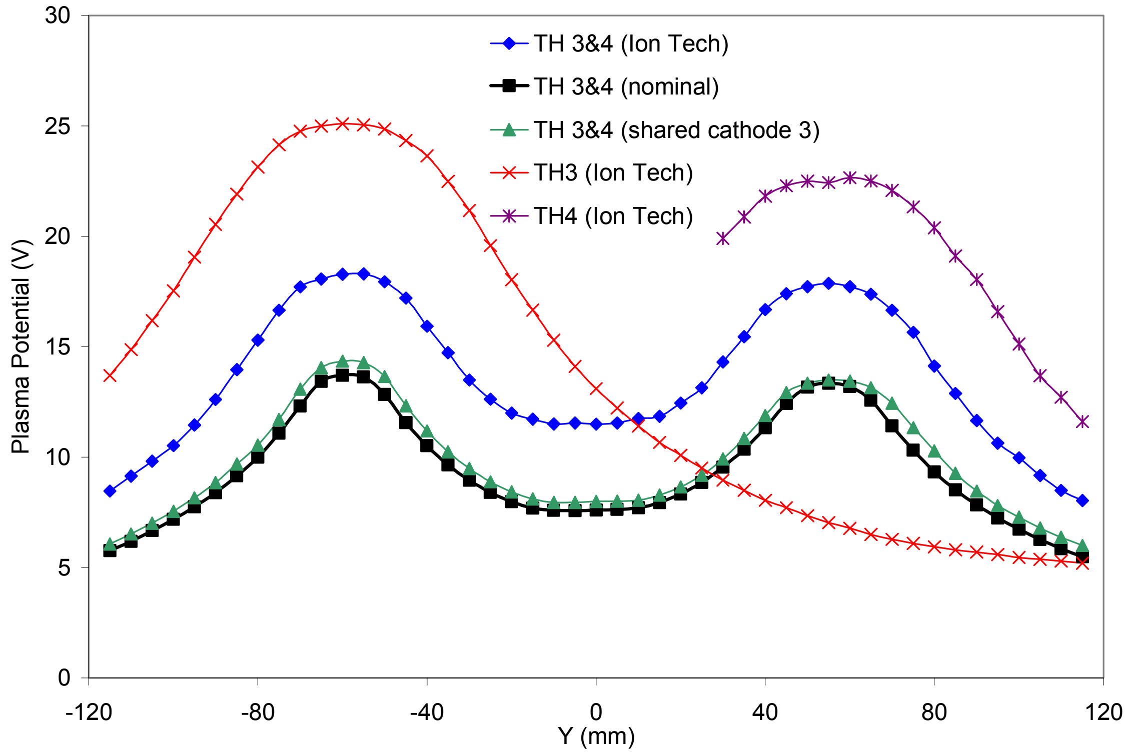

Figure 5-25: Plasma potential profiles downstream of TH 3&4 at Z=100 mm.

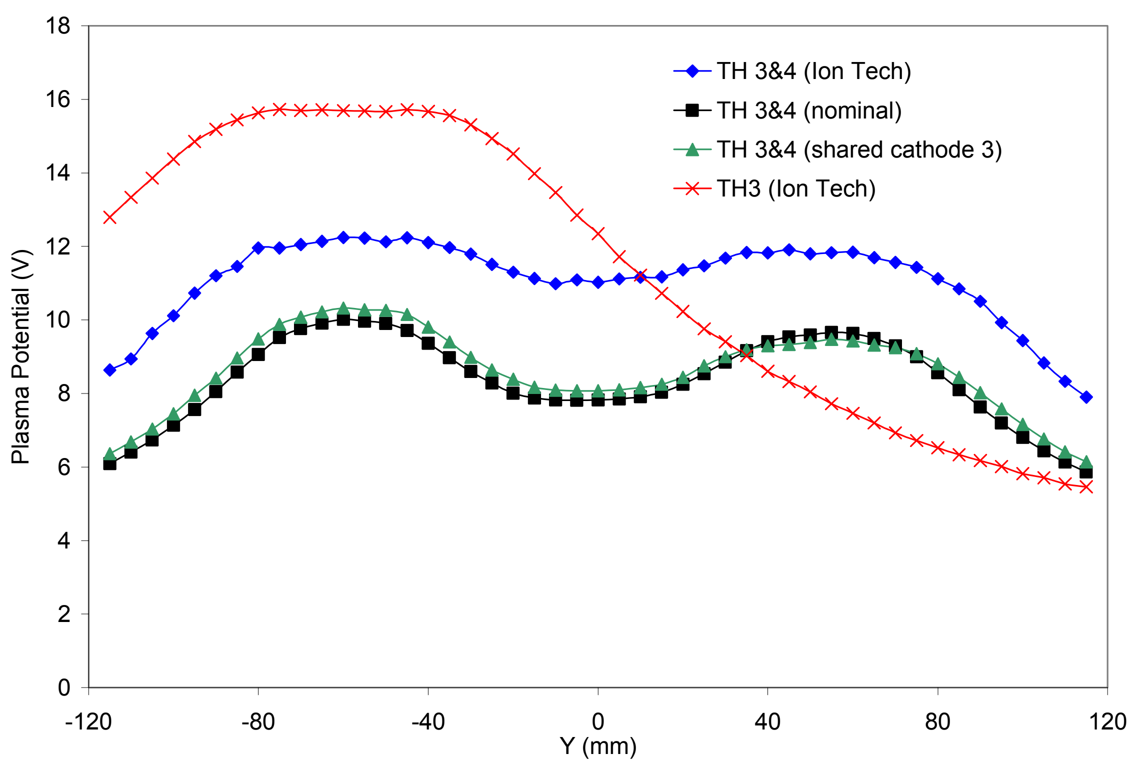

Figure 5-26: Profiles of plasma potential 150 mm downstream of TH 3&4. Note the effect of cathode location on the magnitude of the potential.

To examine the effects of neutral density and magnetic fields on the plasma potential profiles, additional experiments were performed at PEPL. Like the triple probe measurements, these data were recorded downstream of TH 2&3 with both devices tied to cathode 3. The resulting data are presented in Figs. 5-27 through 5-29 below. The curves labeled “TH2 plus TH3 flow” represent data obtained with thruster 2 running and 8.5 sccm of xenon flowing through thruster 3, while the flow through thruster 3 was increased to 17 sccm for the curves labeled “TH2 plus TH3 double flow.”

As shown in Figs. 5-27 through 5-29, the plasma potential downstream of TH2 was much higher at a given axial location when operated with cathode 3 than it was in the nominal configuration presented in Chapters 3 and 4. Since the boundary conditions of the potential field were set by the applied discharge voltage, these measurements depict a “pushing out” of the plasma potential such that a larger fraction of the potential drop occurred outside of the discharge channel. The stronger electric fields outside of the engine should have a detrimental effect on thruster performance because they can be expected to lead to increased beam divergence. The plots below show that increasing the neutral density, and therefore the particle pressure, between the anode and the cathode reduced the potential in the plume somewhat. Doubling the flow through thruster 3 caused a further reduction in the plasma potential, although the difference between the “flow” and “double flow” curves decreased as a function of distance. By about 170 mm downstream, the two curves became nearly indistinguishable from each other. Finally, compared to the data measured with 8.5 sccm flowing through TH3, energizing electromagnet 3 appeared to cause slight decreases in the plasma potential directly downstream of TH2 and increases in the potential directly downstream of the cathode. The magnitude of the change caused by the magnetic field, however, was relatively small and no definitive conclusions about this effect can be drawn from the collected data (see Section 5.7). As expected, operating both thrusters together caused the potential in the plume to fall to almost exactly the values measured in the nominal configuration. This behavior is explained in Section 5.7.

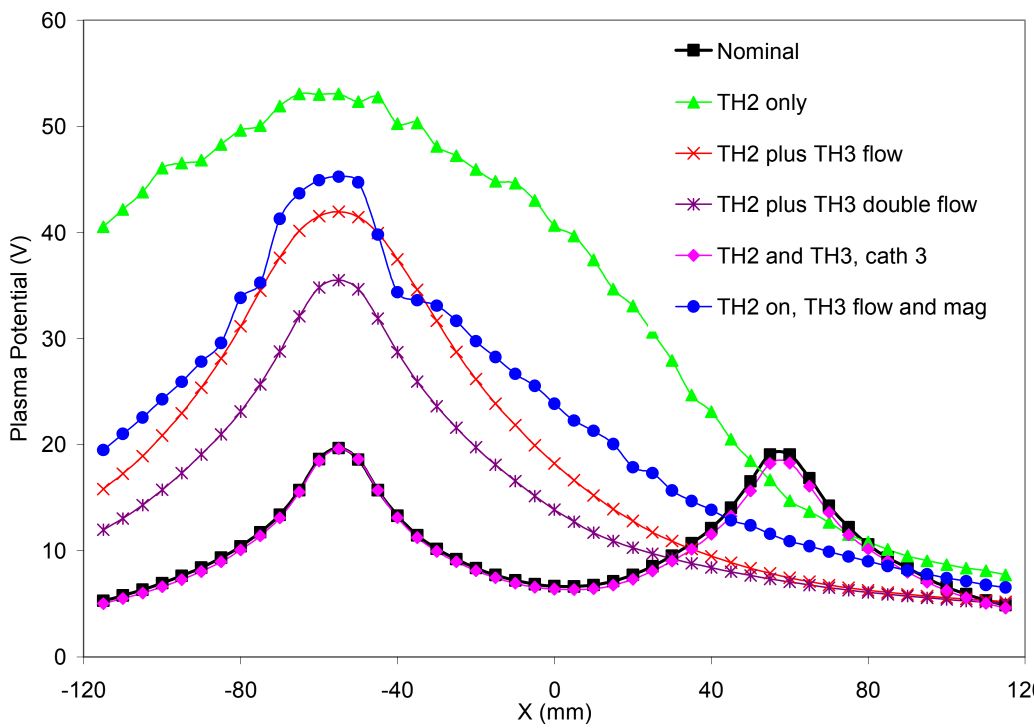

Figure 5-27: Plasma potential 70 mm downstream of TH 2&3. Increasing the local neutral pressure reduces the potential.

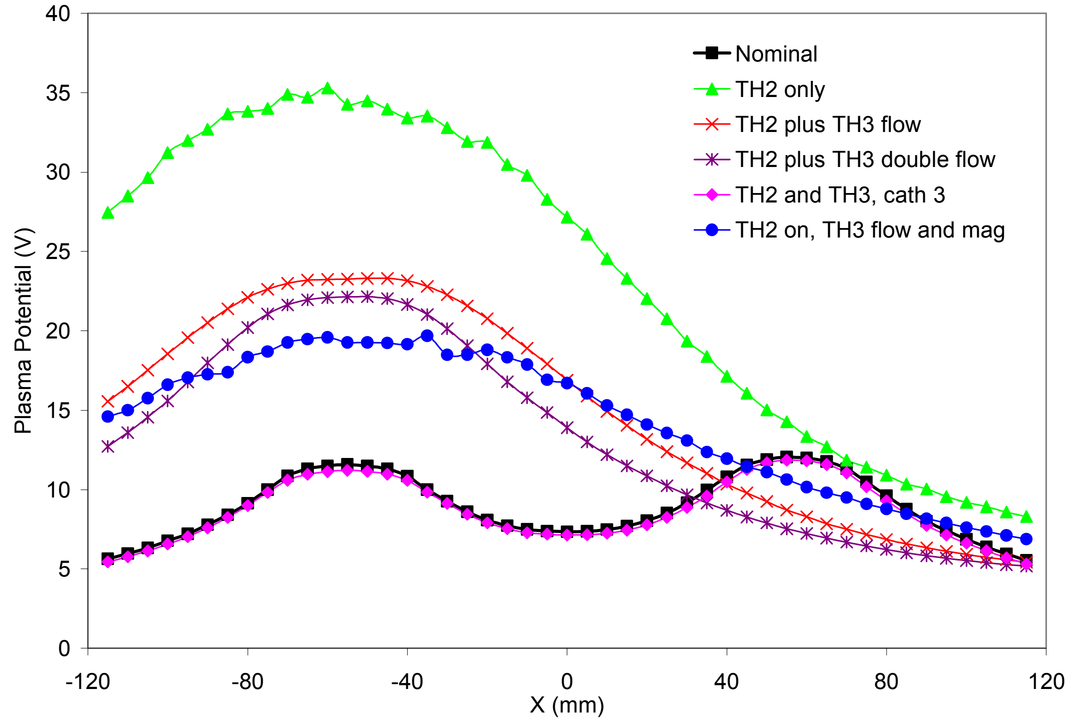

Figure 5-28: Measurements of the plasma potential 120 mm downstream of thrusters 2 and 3 taken using a floating emissive probe.

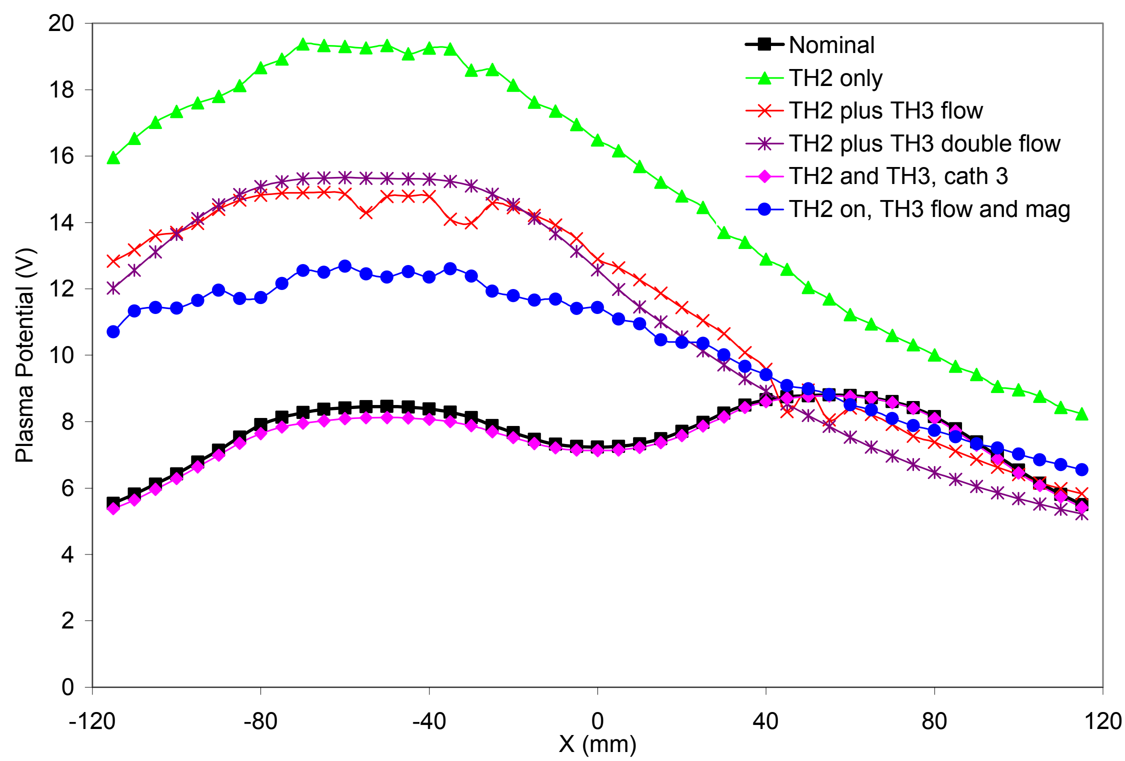

Figure 5-29: The plasma potential profiles obtained at Z=170 mm with cathode 3 shared between TH 2&3.

5.6 Ion Current Density

The final diagnostic used to study the effects of shared cathode operation was the nude Faraday probe. Figure 5-30 shows the ion current density profiles measured along a radial arc 500 mm downstream of the cluster. The center of rotation was the midpoint between thrusters 2 and 3. Results are shown for the engines running with the central Ion Tech cathode as well as in the nominal configuration. As shown, the profiles recorded with a single thruster operating in conjunction with the Ion Tech cathode (symbols) were much wider and more diffuse than the nominal ones (solid lines). This indicates a larger beam divergence when the thruster was operated from a distant cathode. The same trend continued with two engines running. Compared to the nominal values, the ion current densities measured during operation with the Ion Tech cathode and shown in Fig. 5-30 were significantly lower at low angles with respect to centerline and higher at high angles.

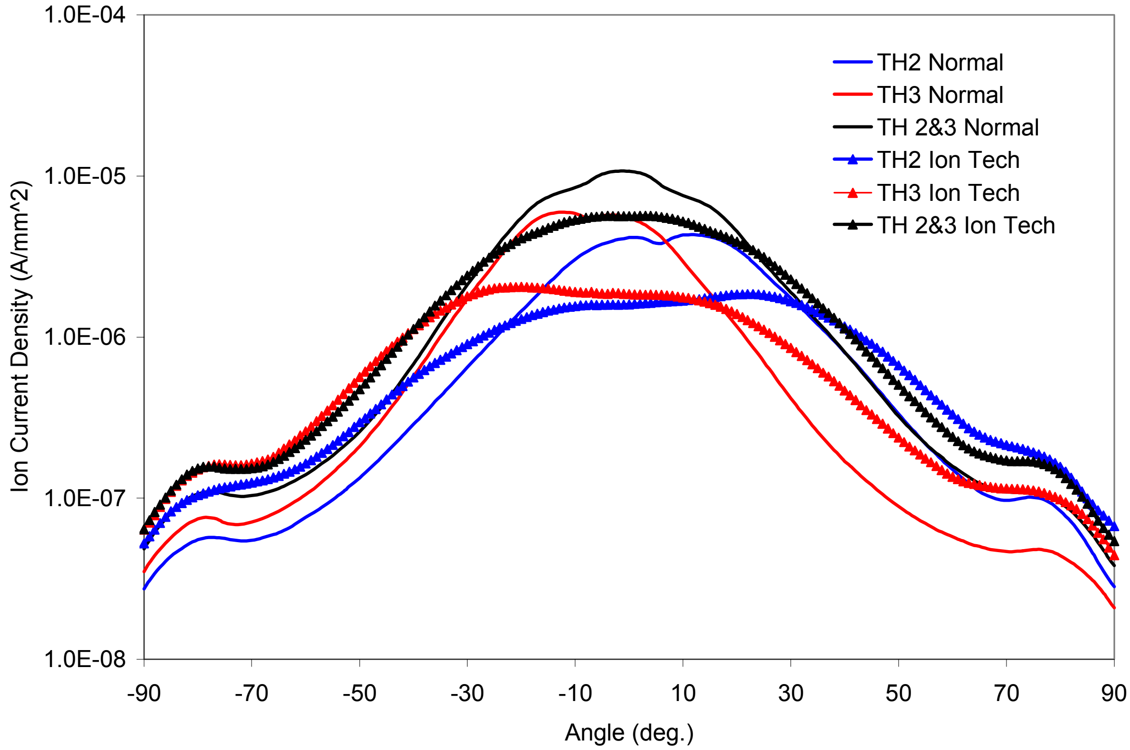

Figure 5-30: Ion beam profiles for nominal and shared cathode operation. Note that when the thrusters are operated from the central cathode, the beam becomes much wider and more diffuse.

The last important point to note from the Faraday probe data is shown in Fig. 5-31, which depicts the beam profiles measured in the shared central cathode configuration along with the prediction from linear superposition. Despite the major differences observed between this mode and normal operation, the measured beam profile during multi-thruster operation is still significantly narrower than predicted. This is consistent with the observations made in Chapter 4 regarding the effects of clustering on beam profiles with each thruster operating from its own cathode. This suggests that a prudent method to follow when integrating a cluster onto a spacecraft, regardless of cathode number and placement, would be to design the surfaces to survive the sputtering resulting from linear superposition of the ion flux from each individual device. Since this profile indicates a “worst case scenario” in terms of beam divergence, this design methodology would inherently incorporate a certain margin of safety.

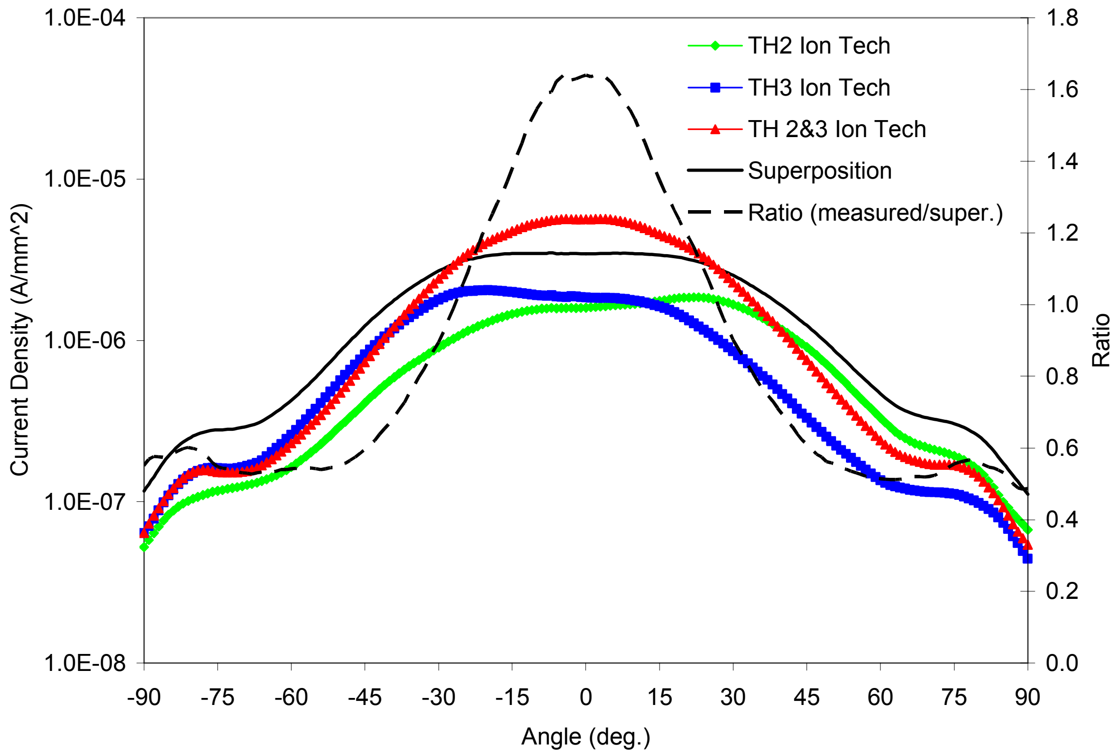

Figure 5-31: Ion beam profiles downstream of thrusters 2 and 3 when operated from the cathode in the center of the cluster. Note that the measured profile is narrower than the one predicted by linear superposition. The dashed line gives the ratio of the measured current density to the one calculated according to linear superposition.

5.7 Analysis of Cathode Phenomena

The data presented in the previous sections indicate that the plasma plume properties and basic operating characteristics of a Hall thruster are both influenced by the coupling between the anode and cathode. The most important parameters controlling this process are likely to be the distance between the electrodes and the properties of the medium in the inter-electrode gap. To provide a framework for discussing how these parameters affect the basic operation of the cluster, it is useful to consider the equivalent circuit diagram shown in Fig. 5-32. This is not meant to imply that the actual transport through the plasma plume is as simple as a purely resistive circuit, but it is useful as a qualitative illustration of where the main voltage drops occur in the plume. In this figure, location P is an arbitrary point in the plume where the plasma potential is measured. The other points are self-explanatory.

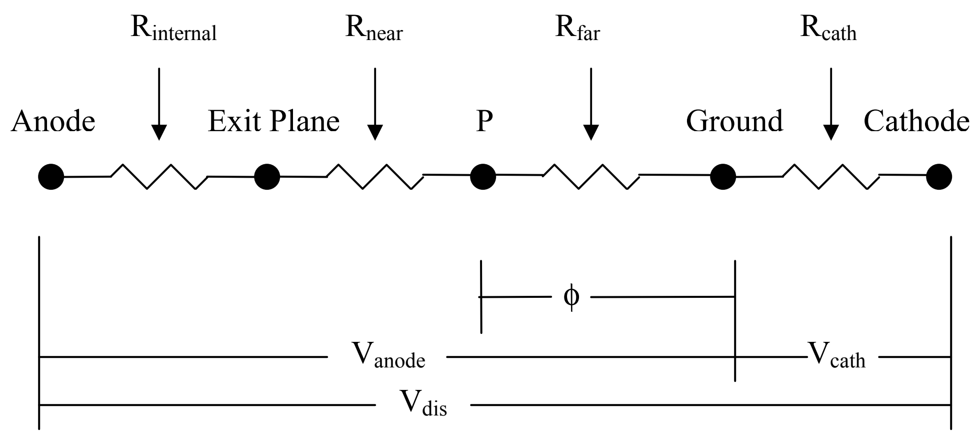

Figure 5-32: Simple equivalent circuit diagram for discussion of electron transport in the plume.

Since the discharge voltage, V_{dis}, was set by the power supply and the cathode potential, V_{cath}, was observed to be nearly constant (to within a few volts) over the operating conditions of interest, the anode voltage, V_{anode}, can also be considered constant to a first approximation. Referring to Fig. 5-32, the plasma potential can be written as Eqn. 5-1. This shows that the increase in plasma potential observed throughout the plume when a thruster was operated from a distant cathode is indicative of an increase in the effective "resistance" between the cathode and that point in the plume. From the data presented above, it can be concluded empirically that the resistance to electron transport is increased by increasing the distance between the thruster and neutralizer, while it is decreased by increasing the local neutral and plasma densities between the electrodes.

$$\phi = \frac{R_{far}}{R_{far} + R_{near} + R_{internal}} V_{anode} \qquad \textbf{Eqn. 5-1}$$

The effect of cathode position and plume properties on the electron transport can be understood by first realizing that the main impediment to electron flow is the magnetic field. Even for the relatively low magnetic field strengths found in the far-field plume (less than 5 gauss), the electron Larmor radius is on the order of several millimeters for temperatures of a few electron volts. To cross the field lines and travel to the anode, the electrons therefore require elastic collisions with other particles. Considering this, it is easy to see that increasing the neutral density or ion density in the cathode region enhances the electron transport by increasing the target population for collisions. Moving the cathode farther away from the thruster, on the other hand, increases the resistance to electron flow by forcing the emitted particles to cross more field lines.

The qualitative description of cathode coupling effects given above can be improved upon by considering the factors influencing electron migration across a magnetic field. Based on the derivation given by Chen, the electron current across the magnetic field can be expressed by Eqn. 5-2.[17] In this expression, ν, μ, and D represent the total electron collision frequency, electron mobility, and diffusion coefficient, respectively. The subscript $\perp$ is a reminder that it is primarily the quantities perpendicular to the magnetic field that influence the cathode coupling process. As a first approximation, the last term in this expression involving the ExB and diamagnetic drifts can be neglected. It is also helpful to ignore the term involving the density gradient. This will be shown later to have very little effect on our understanding of the processes of interest. With these approximations, Eqn. 5-2 can be simplified and written as Eqn. 5-3.

$$\overrightarrow{j_{e\perp}} = -n_e e v_{e\perp} = e\left[-n_e \mu_\perp \vec{E} - D_\perp \nabla n_e + n_e \frac{\overrightarrow{V_{ExB}} + \overrightarrow{V_D}}{1 + \left(\nu / \omega_c \right)^2} \right] \qquad \textbf{Eqn. 5-2}$$

$$\overrightarrow{j_{e\perp}} \approx -n_e e \mu_\perp \vec{E} \qquad \textbf{Eqn. 5-3}$$

Based on the properties presented earlier, it appears that the electron current to the thruster can be considered nearly constant regardless of the processes occurring in the plume. This can be deduced by first noting that the discharge current measured with thruster 2 coupled to cathode 3 was only slightly higher than the one measured in the nominal configuration (see, for example, Figs. 5-4 and 3-1). Second, referring to Fig. 5-30, it can be seen that although the shape of the beam profile was changed during operation from a distant cathode, the total ion current exiting the thruster was comparable to the one measured during nominal operation. Since the total discharge current is the sum of both the ion and electron currents, these observations show that the electron current can be considered constant, at least to the level of accuracy needed to deduce the expected trends from Eqn. 5-3.

Considering the necessary electron current to the thruster to be a constant, understanding the cathode coupling then really boils down to understanding the factors that affect electron mobility. The electron mobility perpendicular to a magnetic field can be expressed by the classical relation given by Eqn. 5-4.[17] Even for relatively low magnetic field strengths, the electron cyclotron frequency is much larger than the collision frequency for the densities of interest in the Hall thruster plume. This allows the expression for electron mobility to be simplified by eliminating the collision term in the denominator and replacing the cyclotron frequency with the definition given by Eqn. 5-5. Combining this result with Eqn. 5-3 and approximating the electric field to be characterized by the voltage between the cathode and a point in the plume divided by the distance, L, to that point, leads to Eqn. 5-6.

$$\mu_{\perp} = \frac{\nu e / m_e}{\nu^2 + \omega_c^2} \qquad \textbf{Eqn. 5-4}$$

$$\omega_c \equiv \frac{eB}{m_e} \qquad \textbf{Eqn. 5-5}$$

$$n_e \frac{m_e \nu}{B^2} \frac{\left(\phi + \left|V_{cath}\right|\right)}{L} \approx const. \qquad \textbf{Eqn. 5-6}$$

The derivation leading to Eqn. 5-6, although simplistic, provides a theoretical basis for understanding the behavior observed throughout this chapter as the cluster operating conditions were varied. For example, when TH2 was operated from cathode 3, L was increased compared to the nominal configuration and the plasma potential, ϕ, increased in response. When flow was added through TH3, the total electron collision frequency, ν, was increased in the vicinity of the cathode and the plasma potential in the plume decreased as predicted by Eqn. 5-6. Although this expression is based on far too many simple approximations to be of much use quantitatively, it does explain the trends in plasma potential that can be expected when the cathode position and plume properties near the cathode are varied. The behavior of the electron temperature can, in turn, be understood by referring to the previous statement that interaction with the electric field is the main source of energy causing heating of the electrons as they flow toward the anode. It follows trivially that anything causing an elevation of the plasma potential in the plume should have a similar effect on the electron temperature, as seen in Figs. 5-21 through 5-23.

One aspect of the observed data that does not, at first glance, appear to be consistent with the trends expected based on Eqn. 5-6 is the behavior of the plume properties when the electromagnet of TH3 was turned on. According to the arguments presented above, activating TH3's electromagnet while TH2 was running would be expected to cause a drastic increase in the plasma potential throughout the plume. The small magnitude of the change in plasma potential measured by the emissive probe in this configuration is believed to be a result of the location of the cathode with respect to TH 2&3. Referring to Fig. 2-2, it can be seen that electrons exiting cathode 3 do not need to cross directly in front of TH3 in order to reach TH2, i.e. electrons can flow nearly sideways to TH2 rather than flowing upward to cross the magnetic field lines directly downstream of TH3. Thus, energizing the electromagnet of TH3 does not necessarily cause a significant increase in the number of magnetic field lines that electrons from cathode 3 must cross en route to TH2. Further, since electrons are free to flow parallel to lines of force, it is conceivable that activating TH3's magnet could cause electrons to follow a slightly different path to TH2 without significantly changing the overall impedance through the plasma. This explanation is consistent with the behavior shown in Figs. 5-28 and 5-29 where activating the magnet caused a modest increase in the plasma potential directly downstream of TH3, which was not operating, and a similar decrease downstream of TH2.

Incidentally, the scaling shown in Eqn. 5-6 relates back to the justification for omitting the diffusion term from the electron transport equation (Eqn. 5-2). It has been shown that the diffusion coefficient perpendicular to B scales in a way that is very similar to the scaling of the electron mobility, i.e. it is proportional to the collision frequency and inversely proportional to the square of the perpendicular magnetic field.[17] Thus, the omission of diffusion due to density gradients in the above analysis does not seriously detract from our qualitative understanding of the factors affecting the cathode coupling process.

The changes in plasma properties observed downstream of TH2 as a function of the flow rate through TH3, and whether or not this thruster was operating, can be further illuminated by considering the collision phenomena in the plume. Since it can easily be shown that collisions with like particles do not contribute to electron transport across a magnetic field,[17] the elastic collision types that influence the cathode coupling process are electron-ion and electron-neutral collisions. The characteristic frequencies of these collisions are given by Eqns. 5-7 and 5-8 while estimates of the Coulomb logarithm and electron-neutral cross section are given by Eqns. 5-9 and 5-10.[106]

$$\nu_{ei} = 2.9\times10^{-12} n_e \ln(\Lambda)\left(\frac{k_b T_e}{e}\right)^{-3/2}$$ **Eqn. 5-7**

$$\nu_{en} = \sigma_{en} n_n \sqrt{\frac{k_b T_e}{m_e}}$$ **Eqn. 5-8**

$$\ln(\Lambda) \cong 23 - \frac{1}{2}\ln\left(\frac{10^{-6} n}{\left(k_b T_e/e\right)^3}\right)$$ **Eqn. 5-9**

$$\sigma_{en} \approx 6.6\times10^{-19}\left\{\frac{k_b T_e/4e - 0.1}{1+\left(k_b T_e/4e\right)^{1.6}}\right\}$$ **Eqn. 5-10**

Looking first at collisions between electrons and neutrals, Eqn. 5-8 gives an estimated collision frequency of about 6x10^{3} s^{-1} for 2 eV electrons and a neutral density of 5.2x10^{16} m^{-3}. This density is based on the background population that would cause the measured pressure of 1.1x10^{-6} Torr when just one thruster was running in the LVTF. When flow was added through thruster 3, the local neutral density was artificially increased and can be approximated at the exit plane according to Eqn. 5-11, which assumes that neutrals exit the device at the thermal speed. For a mass flow rate of 0.84 mg/s and a neutral temperature of 350 K, the estimated neutral density at the exit plane is about 3.2x10^{19} m^{-3}. Taking the characteristic density to be about half of this value (to account for the rapid decrease caused by radial expansion), the electron-neutral collision frequency predicted by Eqn. 5-8 becomes 1.8x10^{6} s^{-1}. The differences in plume properties between operation of TH2 with cathode 3 and operation with flow through thruster 3 are thus the result of increasing the electron collision frequency by more than two orders of magnitude.

$$n_n = \frac{\dot{m}}{m_i A_{exit} \sqrt{\frac{8 k_b T_n}{\pi m_i}}} \qquad \textbf{Eqn. 5-11}$$

The electron-ion collision frequency is estimated by assuming a characteristic plasma density in the region between cathode 3 and thruster 2. When both TH2 and TH3 are operated together, the previously presented data show 5×10^{17} m^{-3} to be a reasonable estimate. According to Eqn. 5-7, this leads to an electron-ion collision frequency of approximately 5×10^{6} s^{-1}. This is a very interesting result because it is only about a factor of 3 higher than the estimate of the electron-neutral collision frequency given above, yet operation of thruster 3 (with cathode 3 shared) caused the plume properties to return to approximately the nominal values while just adding flow through thruster 3 caused much smaller changes. This implies that operating multiple thrusters enhances electron transport from the cathode in more ways than by simply increasing the electron collision rate and electron mobility.

The enhancement of electron transport when multiple thrusters are running is believed to be partially due to a "virtual cathode" effect where the plume of one thruster acts as an electron source for another. In other words, when one thruster is operated from a distant cathode, all of the electrons reaching the anode must originate at the cathode.

When a second thruster is operated in the area between the first thruster and the cathode, the plume electrons from the intermediate device serve as a second source of electrons for the other thruster. Although Kirchoff's laws dictate that all of the electron current must still flow through the hollow cathode, the electrons themselves do not have to travel nearly as far. To visualize this, consider the analogous situation in which an electrical wire is connected to an AC voltage source. In this case, electron current can propagate over large distances at nearly the speed of light, despite the fact that individual electrons move only a short distance in the conductor.

Having examined several of the factors that influence cathode coupling in the Hall thruster plume, it is natural to ask what implications this process has for design and operation of a cluster. Comparing the measurements presented in Chapter 4 to those presented in this chapter, it is clear that designing a cluster intended for shared cathode operation presents several complications that are not present in the nominal configuration. First, the basic operational characteristics of each thruster using a shared cathode depend on whether or not adjacent thrusters are running. This means that there are likely to be cases where a cluster will perform well when all of the thrusters are running, but operation of a single thruster may result in poor performance due to an inability to efficiently couple the cathode to the plume. This could result in problems for missions that require variable power propulsion systems since operation of a single thruster, such as for station keeping maneuvers, may not be possible. Additionally, a system that requires all of the thrusters to be operational to achieve peak performance of any individual engine is inherently vulnerable to single point failures, or at least disproportionate reductions in performance for failure of certain engines. For example, consider the case discussed throughout this chapter where both thrusters 2 and 3 were coupled to cathode 3. Failure of thruster 2 in this configuration would be expected to result in a 50% reduction in thrust with little or no effect on system efficiency or specific impulse because thruster 3 would still be capable of operating normally. Failure of thruster 3, on the other hand, would result in drastic reductions in system performance because thruster 2 would be incapable of proper operation without thruster 3 running. Obviously, operating multiple devices from a single cathode presents an especially difficult fault tolerance analysis for mission planners and, perhaps, particularly demanding reliability requirements for thruster manufacturers.

In addition to limitations on operational flexibility and fault tolerance, a cluster using a shared cathode presents difficulties for predicting the basic properties of the plume. As shown clearly by the data presented in Sections 5.3 through 5.5, the prediction methods used with success in the nominal configuration do not work when the basic operational characteristics of each thruster depend on the number of engines operating. This means that a cluster using a shared cathode would need to be ground tested in every conceivable operating mode before it could be used in flight. This may be practical for low-power clusters, but for systems operating at hundreds of kilowatts it is not clear that the entire system could be tested at reasonable background pressures in existing vacuum facilities. Further, the need to test each operating mode individually with the shared cathode partially negates the advantages in development cost and system scalability that were cited as justification for considering a cluster rather than a single, monolithic thruster. For these reasons, the nominal mode discussed in Chapter 4 is likely to be the preferred cluster configuration except, perhaps, in rare situations where the performance benefits associated with shared cathode operation are sufficiently compelling so as to overshadow the difficulties discussed above.

5.8 Facility Effects

A final issue that relates to ground testing of all high-power electric propulsion systems, including clusters of Hall thrusters, is the effect of the facility background pressure on performance and plume characteristics. There are two main sources of error related to operating at elevated background pressure: entrainment of background gases into the thruster and increases in the collision rate in the plume. Background gas that is ingested into the thruster often results in an overestimate of the device's performance because it can be ionized and accelerated to produce thrust even though the propellant is not accounted for in calculations of specific impulse. In other words, the entrained gas acts as "free xenon," which would not be available in space. An estimate of the ingested mass flux due to free molecular flow is given by Eqn. 5-12.[107]

$$\dot{m}_{in} = \frac{1}{4} m_i n_n \overline{v_n} A_{exit} = p_B \sqrt{\frac{m_i}{2\pi k_b T_n}} A_{exit} \qquad \textbf{Eqn. 5-12}$$

For all of the measurements presented in this dissertation, the effect of background gas ingestion was determined to be negligible because the maximum pressure in Chamber 6 was 2.3×10^{-5} Torr. At this pressure, the ratio of ingested background gas to propellant mass flow was estimated to be 0.5%, which is well within the margin of error of virtually all measurements of Hall thruster performance. As clusters of larger thrusters are tested, however, it is clear that both the pressure in the vacuum chamber and the thruster area will increase, thus resulting in an increase in the ingested mass flux. This effect can be quantified in several ways. First, we note that many Hall thruster designs are scaled such that the propellant flux density is nearly constant regardless of the power at which the device is intended to operate. This criterion dictates that the thruster exit area must scale linearly with the propellant mass flow rate. Combining this information with Eqn. 5-12 allows the ratio of ingested mass flux to propellant mass flow rate to be written as Eqn. 5-13, where factors that remain constant regardless of pressure have been incorporated into the proportionality constant. The linear dependence of the entrained mass fraction on the background pressure has prompted Randolph *et al.* to suggest a maximum background pressure of 5×10^{-5} Torr for obtaining reliable Hall thruster performance measurements.[107]

$$\frac{\dot{m}_{in}}{\dot{m}} \propto p_B \qquad \textbf{Eqn. 5-13}$$

The analysis of gas ingestion can be taken one step further by noting that the pressure in a vacuum chamber with a constant pumping speed is directly proportional to the mass flow rate into the chamber.[108] This means that the ingested flux for thrusters operating in a given chamber should scale as the square of the propellant mass flow rate. The mass flow rate to the thruster, in turn, scales approximately linearly with the discharge current for thrusters with similar propellant utilization efficiencies. For thrusters operating at a similar voltage (specific impulse), it follows that the thruster power is proportional to the discharge current and, therefore, to the propellant mass flow rate. Under these assumptions, the ratio of ingested mass to injected mass can be written as Eqn. 5-14, which shows that the issue of background gas entrainment during ground testing becomes significantly more problematic as thrusters increase in power. This illustrates why it is so important to be able to predict the plume properties of a cluster based on knowledge of a single thruster since testing of an entire high-power cluster may result in unacceptable perturbations due to facility effects.

$$\frac{\dot{m}_{in}}{\dot{m}} \propto \dot{m} \propto I_D \propto P_{in} \qquad \textbf{Eqn. 5-14}$$

The second commonly noted way in which the facility pressure adversely affects measurements is by artificially increasing the collision rate in the plume. The mean free paths for various types of collisions were calculated using the cross section estimates given in Section 4.7.3 and are shown in Fig. 5-32 as a function of background pressure. In order for measurements of ion current density profiles and energy spectra to be valid, collisions with background neutrals should be rare compared to collisions with products emitted from the thruster. Since the latter would occur in space, they should be considered characteristic of the device. To provide a low-level estimate of the mean free path for collisions with un-ionized propellant gas, the neutral density at the exit plane of the BHT-200 was estimated according to Eqn. 5-11 where the total propellant mass flow was replaced by the fraction of that flow that escapes the thruster without being ionized. Assuming a propellant utilization efficiency of 95%,[109] the neutral density at the exit plane is approximately 1.5×10^{18} m^{-3}. Using this value, the characteristic mean free path for CEX collisions with the un-ionized propellant is estimated to be about 1.3 meters as shown in Fig. 5-33. Assuming that the mean free path of collisions with background neutrals should be a factor of three longer for these interactions to be considered negligible, the background pressure should be below about 1×10^{-5} Torr for measurements that are significantly influenced by collisions. This is in good agreement with estimates made by other authors, which state that the pressure should be below 1.3×10^{-5} Torr for plume measurements.[107] It should be noted, however, that both of these estimates are somewhat arbitrary since the effects of collisions differ depending on the type of measurement being made. For example, collisional effects are clearly visible in the ion current density data of Fig. 3-18 despite the fact that the measurements were taken at pressures well below 1×10^{-5} Torr. The pressure criterion should therefore be considered a guideline rather than a strict condition on the acceptability of plume measurements.

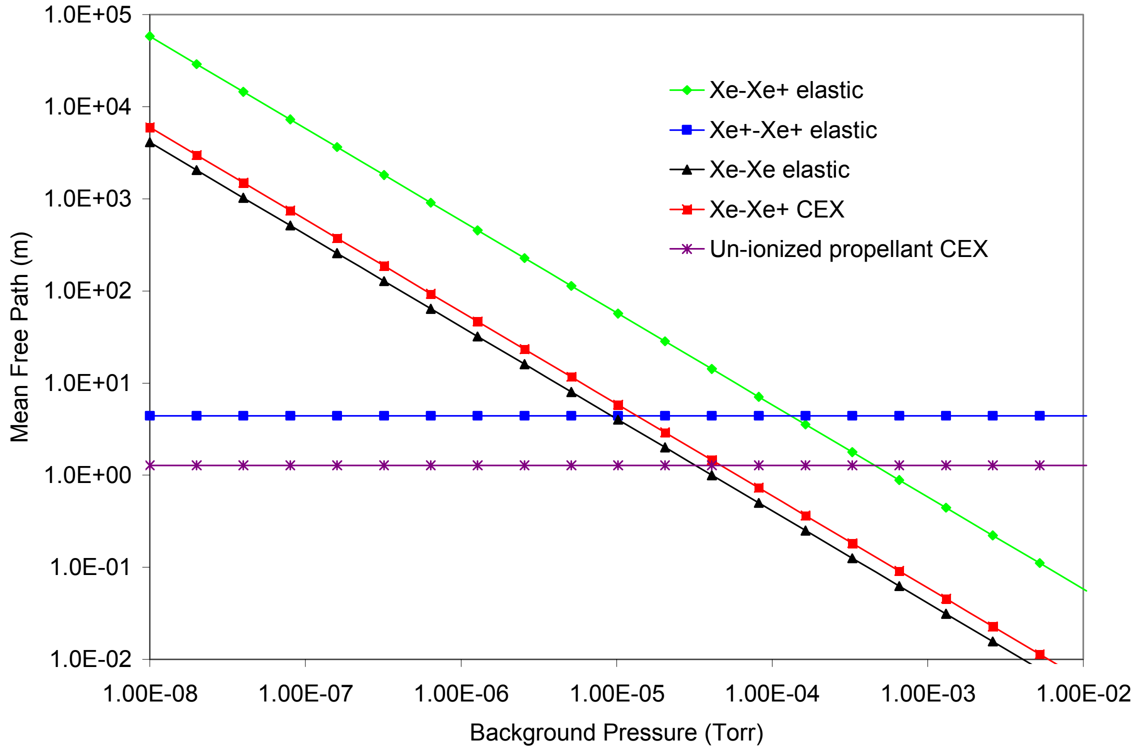

Figure 5-33: Mean free path estimates for various types of collisions as a function of background pressure assuming a neutral temperature of 300 Kelvin, 200 volt ions, and 95% propellant utilization efficiency (for estimation of the un-ionized particle flux from the thruster).

A third way in which the facility background pressure may affect ground testing of thruster clusters was revealed in the previous section, which discussed cathode coupling to the thruster plume. The plasma density, electron temperature, and especially the plasma potential measurements presented throughout this chapter showed that a thruster coupled to a distant cathode can be significantly affected by raising the local electron-neutral collision frequency. It is therefore possible that a high-power thruster operating with a cathode at a non-optimum location in a vacuum chamber at elevated pressure would perform better than the same thruster-cathode pair at the reduced pressures found in space. Based on the density of 1.6×10^{-19} m^{-3} used as an estimate to characterize the conditions that existed when flow was running through thruster 3, a similar electron-neutral collision frequency could be expected if the pressure in the vacuum chamber were allowed to rise to approximately 5×10^{-4} Torr. While this pressure is well above the level that would normally be considered acceptable for Hall thruster testing, it is yet another example of the difficulties associated with qualifying a cluster of thrusters using a shared cathode.

6. CONCLUSIONS

This dissertation contains a large body of plasmadynamic data obtained in an effort to facilitate the design of Hall thruster clusters for high-power electric propulsion applications. Like most research projects, this work has answered many questions while raising several others. This chapter will summarize the results presented throughout this thesis and suggest future avenues for targeted exploration into issues related to multi-thruster operation.

6.1 Single Thruster Properties

A single Busek BHT-200 Hall thruster was characterized using a wide variety of plasma diagnostics. In general, the plume properties of this device were found to be similar to the characteristics reported in the literature for larger engines. Some of the most interesting plume features were observed near the thruster centerline where the plasma density, electron temperature, and plasma potential were all shown to increase over a relatively narrow region of the plume. Efforts were made to assess a hypothesis presented by other authors, who claimed that the appearance of collisionless shocks could account for the structure observed visually near the center of the plume.[5] A survey of well-known plasma instabilities showed that the ion-ion acoustic mode, which is capable of leading to collisionless shocks, may be unstable for the conditions found along the centerline of a Hall thruster. The lack of direct evidence for a discontinuity, though, dictates that the existence of a collisionless shock must be considered a feasible possibility, rather than a necessary condition to account for the observed plasma properties.

Two additional interesting features observed during the characterization of a single thruster involved the evolution of plasma potential and ion species fractions in the plume. Specifically, the plasma potential near the centerline of the thruster was shown to change more rapidly than can be explained by purely ambipolar expansion. This is consistent with recently completed computer simulations that show a method incorporating the effects of current flow on the plasma potential to be in better agreement with measurements than previous methods, which ignored current flow.[110] The species fraction measurements obtained using an ExB probe showed the fraction of multiply-charged ions to increase dramatically at angles greater than about 15° with respect to the thruster centerline. This appears to indicate that ions created farther downstream in the discharge channel are more likely to become multiply-charged compared to those created in the upstream regions.

6.2 Hall Thruster Cluster Properties

The same diagnostics used to study a single Hall thruster were applied to the characterization of four engines running in close proximity to each other with each operating from its own discharge power supply and hollow cathode. It was found that, with the cluster operating in this condition, the plasma density in the plume can be predicted to a high level of accuracy by simple superposition of the contributions from each individual thruster. The electron temperature can then be approximated as a weighted average of the contribution from each thruster or calculated to a higher degree of accuracy by invoking a simple adiabatic relation. The calculated plasma density and electron temperature can then be used to predict the plasma potential using a barometric potential law. Predictions made in this way agree with the measured values to within the margin of error of typical plasma diagnostics.

Measurements of ion current density downstream of two thrusters operating simultaneously showed the beam divergence to be slightly smaller than predicted based on linear superposition of the ion flux from the thrusters operating individually. This is believed to be due to an "ion focusing" effect where the plasma potential hills created by adjacent thrusters cause low-energy ions to be preferentially deflected downstream rather than proceeding to the wings of the plume. A particle tracking algorithm supports this hypothesis by showing that slow CEX ions can indeed be deflected by the weak electric fields in the cluster plume while faster beam ions proceed nearly unaffected. This same particle tracking code shows that CEX ions created in the region between thrusters can be accelerated upstream by the reversed electric fields resulting from the convergence of the individual thruster plumes. This phenomenon, however, is not expected to create significant problems for spacecraft utilizing Hall thruster clusters because the magnitude of the accelerating potential is unlikely to exceed a few volts in the upstream direction.

Ion energy spectra measured in the cluster plume showed a multi-peak structure that was both distinct and unexpected. Both geometric effects and preferential focusing due to the unique plasma potential profiles caused by clustering have been eliminated as possible explanations for this structure. The most likely remaining mechanisms that may account for the presence of multiple peaks in the energy per charge spectra are collisional effects, although the signatures do not appear to be consistent with structures caused by charge exchange collisions. This implies that elastic collisions may play an important role in determining the ion energy distribution downstream of a cluster and estimates of the ion-ion elastic collision mean free path show it to be somewhat shorter than those of other collision types under the conditions considered. The mechanism by which these interactions could produce the observed structures, however, remains unclear. Outside of the region between the thrusters, the ion energy spectra appear qualitatively similar to measurements taken downstream of a single thruster with appendages on the main peak caused by elastic and charge exchange collisions. A secondary peak at energies below the main peak in the distribution is attributable to beam ions that have undergone elastic collisions with slow moving heavy particles. In general, the large fraction of ions at energies below the main peak in the distribution seems to indicate an increase in elastic scattering as a result of clustering.

6.3 Alternative Cluster Configurations

Although the nominal cluster configuration discussed above was the main topic of this study, several other arrangements were investigated as well. In particular, operation of two thrusters in parallel using a single discharge power supply resulted in one of the cathodes emitting significantly more current than the other. The demonstrated affinity for cathode current sharing implies that, if multiple thrusters are to be operated in parallel, each cathode should be capable of supplying the entire cluster current without sustaining damage. If this proves to be impractical, the discharge power circuit would need to be modified to ensure balancing of the current flowing through each neutralizer.

Experiments performed with multiple engines operating from a single cathode showed several important characteristics. First, the discharge current characteristics with one thruster operating from a distant cathode showed a higher than normal level of oscillations. When a second thruster operating from the same cathode was ignited, the discharge current of the first engine returned to the nominal condition. Second, the basic plume properties downstream of each thruster changed significantly depending on how many engines were in operation. This led to the result that the electron number density, electron temperature, and plasma potential in the plume could not be predicted using the methods that were successful in the nominal configuration. This behavior is related to the fact that the properties downstream of a single thruster were altered when the distance between the anode and cathode was changed. Specifically, operating one thruster from a distant cathode caused the plasma potential and electron temperature in the plume to rise while the plasma density fell dramatically. The return of these properties to normal levels when an adjacent engine was operated is believed to have been caused by two effects: enhanced electron mobility due to increased particle collision rates and a virtual cathode effect where the plume of an intermediate thruster can supply electrons to a distant one.

As explained in Chapter 5, the inability to predict the plasma parameters downstream of a cluster operating with a shared cathode based on the properties of a single thruster is an important discovery for a number of reasons. First, it implies that there may be situations where an entire cluster operating from a shared cathode will work well, but operation of a single thruster will result in degraded performance. This indicates that the shared cathode configuration is not the best approach to missions that require various numbers of operational engines for different phases of the flight, i.e. the LEO-GEO transfer discussed in Chapter 1. Second, and perhaps more important, one of the reasons cited for studying multi-thruster operation was to establish the ability to deploy high-power clusters without the need to perform expensive ground-based testing of the entire system. This is only possible if the performance and plume properties of the cluster can be accurately predicted based on knowledge of a single unit. Any operating mode, such as the shared cathode configuration, that undermines this ability also negates one of the major advantages of the clustered approach to high-power EP systems. For these reasons, a cluster in which each thruster operates with its own neutralizer and discharge power supply is likely to be the configuration that offers the lowest development risk and most predictable plume properties.

6.4 Suggestions for Future Work

Although this dissertation has addressed many fundamental issues related to operating multiple Hall thrusters in close proximity to each other, it is by no means a comprehensive answer to all clustering questions. Some of the key areas that still need to be addressed, as well as suggested approaches for doing so, are discussed below.

6.4.1 Multiple Peaks in Energy Spectra

One of the issues raised in this work that remains partially unexplained is the behavior of the multi-peak structure in the energy per charge spectrum recorded in the area between the thrusters. Although several possibilities have been eliminated, the cause of this feature remains unclear. A detailed theoretical analysis of collision physics, as well as cluster simulations that incorporate the effects of elastic scattering, are suggested as a potentially fruitful approach to understanding this phenomenon. These theoretical studies should be used in conjunction with further measurements of the energy per charge spectrum. An instrument capable of measuring the ion voltage traces as a function of the direction from which the particles approach the measurement point would be particularly useful for this purpose.

6.4.2 Local Species Fraction Measurements

As noted previously, the ExB probe used in this work to measure ion species fractions is incapable of detecting changes that occur downstream of the ion acceleration zone. Measurements of the ion charge states using a truly local instrument such as a time-of-flight mass spectrometer would comprise a useful addition to this research. Comparing these measurements with the ExB probe data presented in this dissertation would provide additional information regarding charge exchange phenomena that may occur in the plume as a result of operating multiple engines. Insight into the collisional processes occurring as a result of clustering may relate back to understanding the multiple peaks in the energy spectrum discussed above.

6.4.3 Thrust Measurements

Although previously published research showed that clustering had no effect on the thrust produced by individual engines,[31] this result needs to be confirmed. Further, thrust measurements in the alternative configurations discussed in Chapter 5 would be useful to determine whether the changes in plume properties resulting from operating with a distant cathode reflect a degradation of thruster performance, as suspected. These measurements can best be accomplished using a cluster of larger thrusters than the ones studied throughout this dissertation. Modifying a thrust stand to accommodate the propellant feed lines and electrical wires needed to operate four thrusters would be difficult to accomplish without inducing frictional errors and hysteresis effects comprising a significant fraction of the low thrust level produced by the 200-watt thrusters. These errors can be mitigated by using a higher-power cluster of two or three engines.

6.4.4 Larger Thrusters

A final suggestion that comes to mind for further studies into clustering is to conduct a thorough plume study on a cluster of higher-power thrusters, in addition to using the larger array for the performance measurements mentioned above. First, this should be done to verify the universality of the methods developed in this dissertation for using measurements downstream of a single thruster to predict the plume properties of a cluster operating in the nominal configuration. Second, the shared cathode cluster configuration should be explored further using larger thrusters. As Hall thrusters increase in power, the ratio of the discharge chamber diameter to the diameter of the entire device tends to increase. In other words, the plasma source approaches (as a fraction of the total device size) the edge of the engine because the dimensions of the magnetic circuit do not necessarily increase as rapidly as the diameter of the discharge as power is increased. This may allow multiple thrusters to be placed closer together such that the relative distance, in terms of thruster diameters, between adjacent engines can be reduced compared to the arrangement studied in the work presented here. The proximity of the engines to a neutralizer placed at the center of the cluster could potentially improve cathode coupling during single thruster operation. This, in turn, would make operating a cluster of larger thrusters from a single, shared cathode much more practical than it appears to be based on the measurements presented in this dissertation.

APPENDICES

Appendix A: LINEAR GRIDLESS ION THRUSTER

Although not directly related to clustering, an interesting exercise in the study of electric propulsion has been the design of a new type of thruster. The Linear Gridless Ion Thruster[§], or LGIT, is a two-stage, linear electric propulsion device developed at the University of Michigan. It is intended to combine the strengths of gridded ion engines with the gridless acceleration mechanism of conventional Hall thrusters. The LGIT is designed for operation at approximately 2 kilowatts of power and has many unique features compared to currently operational plasma thrusters. This appendix will present the motivation and design methodology leading to the development of this device, while also discussing its current status and suggesting improvements to the design.

A.1 Motivation and Design Goals

In a conventional Hall thruster, electrons from a single hollow cathode must ionize and accelerate the injected propellant while maintaining quasineutrality of the beam. Using a single source of electrons affords very little control over the ionization process because it is strongly coupled to the acceleration process. A result of this coupling is that, until recently, typical single-stage Hall thrusters have had a relatively small operating range over which efficient operation could be maintained. While acceptable efficiency (>50%) has been achieved at specific impulses near 1600 seconds, operation below this value often results in rapid declines in thruster performance.[111]

[§] United States Patent Number: 6640535

Further, operation at the high discharge voltages necessary to attain high specific impulses (greater than 3000 seconds, for example) has historically resulted in declines in total efficiency due to declines in ionization efficiency, although recent advances in magnetic field architecture have been successful in mitigating this deficiency.[24]

One approach that has been used in an effort to gain greater control over the ionization process is to create two-stage thrusters by introducing an intermediate electrode into the discharge chamber. The intermediate electrode then serves as the cathode for the first (ionization) stage and as the anode in the second (acceleration) stage. Figure A-1 shows a schematic of a typical two-stage thruster.[18] In some cases, a non-emitting intermediate electrode was used in an attempt to essentially separate the ionization and acceleration zones by controlling the voltage drop in each of the stages.[112] In other cases, an emitting intermediate electrode was used as an electron source for the ionization stage.[113] These approaches have shown some promise in increasing total thruster efficiency,[114] which is related to the acceleration efficiency given by Eqn. A-1, where I represents current, V stands for voltage, and the subscripts ‘a’ and ‘d’ denote the acceleration and discharge stages, respectively.[112] As Eqn. A-1 implies, a two-stage thruster’s efficiency is maximized by minimizing the power consumed by the ionization, or discharge, process. In practice, this is accomplished by operating the ionization stage at the lowest voltage for which the necessary discharge can be maintained.

$$\eta_a = \frac{1}{1 + {I_d V_d}/{I_a V_a}} \qquad \textbf{Eqn. A-1}$$

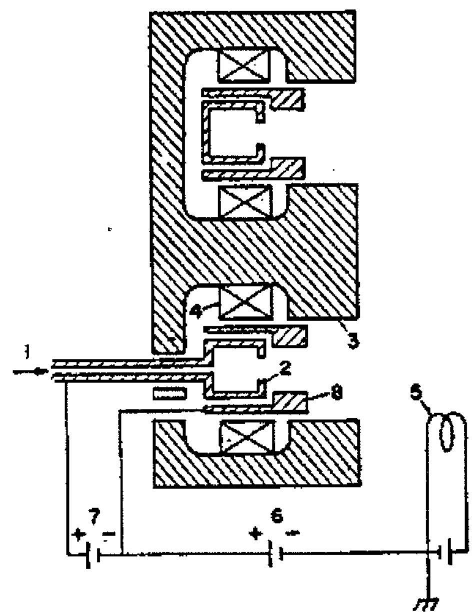

Figure A-1: A typical two-stage Hall thruster showing 1) propellant feed, 2) anode, 3) magnetic circuit, 4) magnet winding, 5) cathode, 6) acceleration stage potential, 7) ionization stage potential, 8) intermediate electrode. (from Ref. 18)

The LGIT seeks to improve upon the overall efficiency and throttling range of conventional Hall thrusters by effectively decoupling the ionization and acceleration processes. This is accomplished by using an ionization stage similar to those used in gridded ion engines such as NASA's NSTAR, which uses a ring-cusp magnetic field to enhance ionization. The LGIT ionization stage consists of a hollow cathode surrounded by a rectangular chamber, which serves as the anode. By utilizing two distinct electron sources for the first and second stages, it should be possible to optimize the ionization and acceleration processes nearly independently of each other, thus increasing overall efficiency.

Ions created in the ionization stage are accelerated through the discharge channel by an electric field, which is created by electrons from the downstream cathode streaming toward the anode through a magnetic field, just as in a conventional Hall thruster. Using this type of acceleration mechanism is advantageous because it eliminates the need for biased grids, the erosion of which constitutes a major potential failure mode of conventional ion thrusters. Additionally, because the accelerated plasma maintains quasineutrality, space charge limitations are avoided. This allows the LGIT to achieve a much higher thrust density and smaller size than a similarly powered gridded thruster.

As the previous discussion implies, it is convenient to think of the LGIT as a combination of the ionization stage from a gridded ion thruster combined with the acceleration region of a Hall thruster. The two-stage nature of the LGIT is shown schematically in Fig. A-2. It should be noted that some of the features shown in this sketch, such as the size and shape of some components, are exaggerated for clarity.

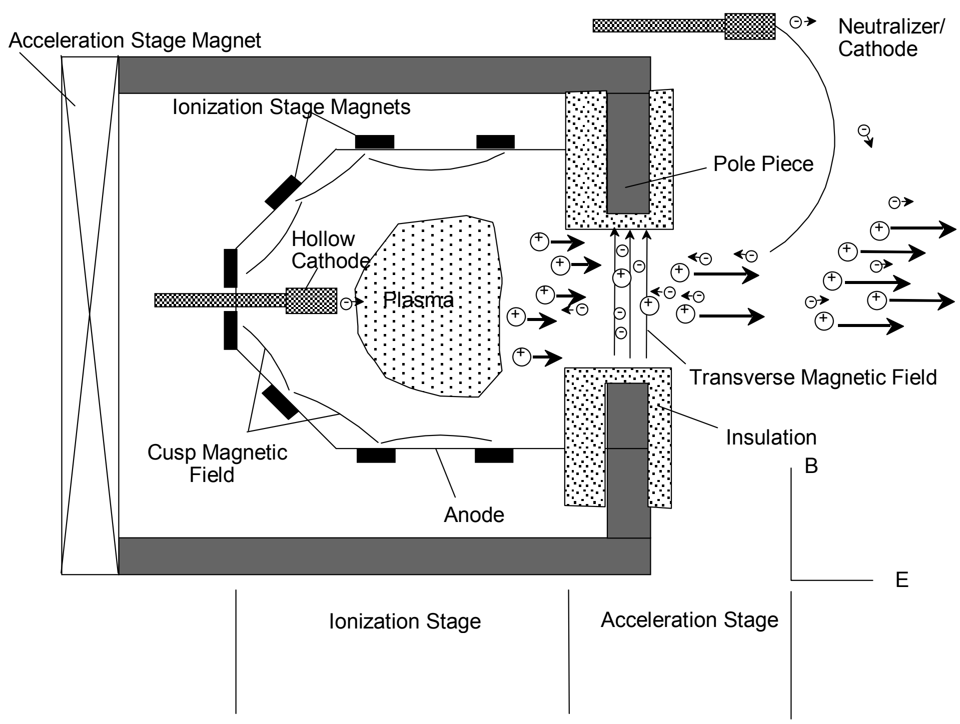

Figure A-2: A functional schematic of the Linear Gridless Ion Thruster.

In addition to its two-stage nature, one of the most striking features of the Linear Gridless Ion Thruster is its unusual shape. Unlike conventional Hall thrusters that use an annular geometry to facilitate closure of the electron drift current, the LGIT has a linear discharge chamber as shown in Fig. A-3. This geometry was chosen to simplify the design of the magnetic circuit for both the ionization and acceleration stages. Additionally, the linear geometry lends itself to easy spacecraft integration, clustering of multiple thrusters, and possibly to the use of thrust vectoring by varying the magnetic field shape in the acceleration region.

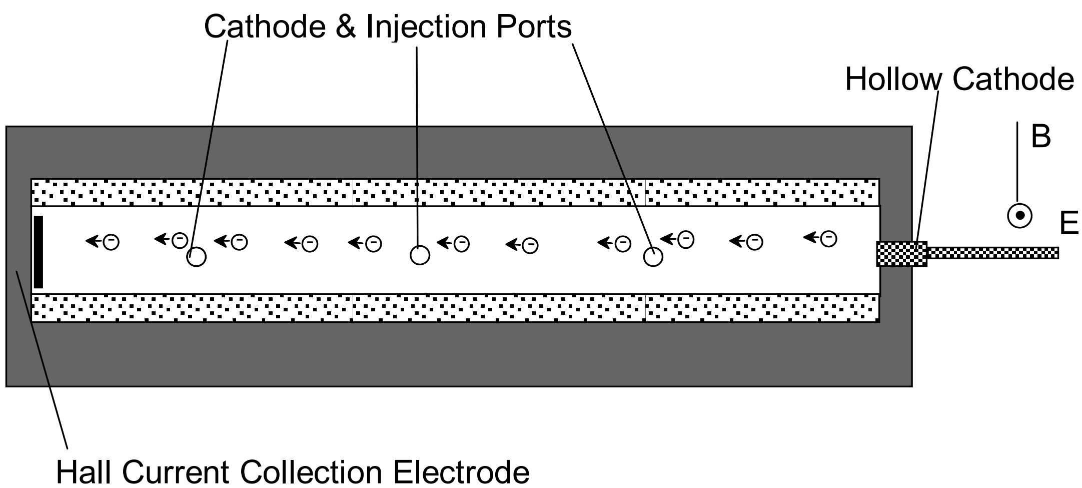

Figure A-3: Front view of the linear acceleration stage.

A direct consequence of the linear shape of the acceleration stage is that the Hall current flows across the face of the thruster and is not closed. Researchers at Stanford University have proven that closure of the electron drift current is not necessary for maintaining a discharge by successfully operating a single-stage, linear Hall thruster.[15] To avoid excessive erosion of the ceramic acceleration stage, an optional tantalum electrode can be used in the LGIT to collect the Hall current. There are several options for handling the collected current such as allowing the electrode to float, grounding it, or connecting it to a cathode such that the collected current may be re-emitted.

A.2 Design Methodology

A.2.1 Scaling

The LGIT is designed for operation at approximately 2 kilowatts. The acceleration stage has been sized to handle a 3 amp discharge at 500 volts with an expected ionization stage power of 500 watts. This assumes ionization costs of approximately 150 watts per amp of discharge current. The overall scaling was accomplished using a combination of empirical scaling laws[47] and by comparison to an existing coaxial thruster.[111] The acceleration channel height and width were determined by scaling from the USAF/University of Michigan P5 thruster and maintaining a constant current density and aspect ratio. In effect, this dictates that the exit area of the thruster should be proportional to the desired power level for devices operating at comparable voltages. This scaling method was chosen partly to keep the heat transfer to the thruster walls manageable. The result is an acceleration channel that is 198 mm wide and 22 mm high for the chosen power level.

Empirical scaling laws[47] suggest a discharge channel depth of 18 mm, however the method used to arrive at this estimate is for a stationary plasma thruster (SPT) and hence it assumes that ionization, as well as acceleration, must occur in this depth. Since the plasma in the LGIT is produced in the ionization stage, it was determined that the acceleration stage could be shortened to reduce the loss of ions by recombination at the walls. The actual depth of the acceleration zone was chosen to be 15 mm by optimizing the magnetic field in this region as discussed in the next section. The completed acceleration stage thus measures 198 x 22 x 15 mm and is constructed of a ceramic composed of 50% boron nitride and 50% silicon dioxide.

The height and width of the ionization chamber were chosen so that the two stages of the thruster mate smoothly with each other. The rear of the chamber must also be sufficiently large to accommodate a standard NASA 6.4-mm diameter hollow cathode. These considerations led to an ionization stage that is 16 mm high in the back and 22 mm high in the front. The width is 198 mm.

The length of the ionization stage was determined by ensuring that a neutral xenon atom injected at the rear has a high probability of being ionized before escaping into the acceleration zone due to thermal motion. This was accomplished by comparing the characteristic ionization time of an injected xenon atom, τ_{ion}, to the thermal escape time, τ_{esc}. The escape time is given by Eqn. A-2 and is a function of the length of the chamber (L_{ch}), the temperature of the neutral gas, and the mass of a xenon atom. Equation A-3 gives the characteristic ionization time, which can be expressed in terms of the neutral density, the electron temperature, and the ionization cross section (σ_i). In applying Eqn. A-3, the temperature dependent ionization cross section, given in m^2 by Eqn. A-4, has been used.[115]

$$\tau_{esc} \cong \frac{L}{\sqrt{\frac{8k_bT_n}{\pi m_i}}}$$ **Eqn. A-2**

$$\tau_{ion} \cong \frac{1}{n_n\sigma_i\sqrt{\frac{8k_bT_e}{\pi m_e}}}$$ **Eqn. A-3**

$$\sigma_i \approx 1.73\times10^{-21}\frac{k_bT_e}{e} - 2.095\times10^{-20}$$ **Eqn. A-4**

Combining Eqns. A-2 through A-4 and examining a range of expected electron and neutral temperatures led to the selection of a 50 mm long ionization stage. The anode, which is the outer shell of the ionization stage, was constructed of 316 stainless steel. Figure A-4 shows a solid model of the ionization stage and ceramic acceleration stage without any of the surrounding components. The blue stripes on the anode represent the placement of the permanent magnets discussed in the next section.

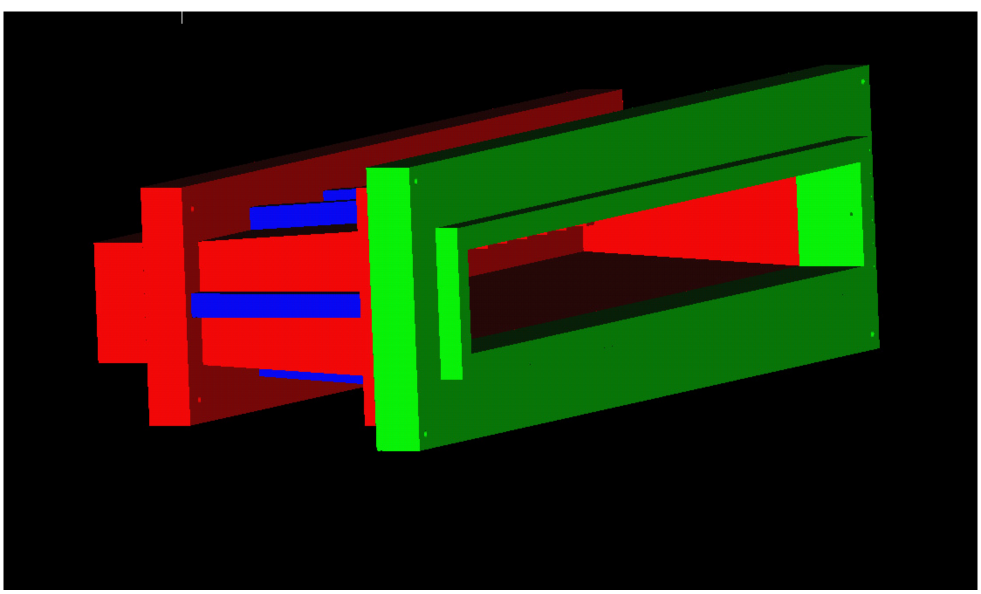

Figure A-4: A solid model showing the ionization and acceleration stages without the surrounding components.

A.2.2 Magnetic Circuit Design

The magnetic field in the LGIT, as in virtually all electrostatic thrusters, is one of the most critical design considerations. As Fig. A-2 implies, there are two very different magnetic field topologies in the two stages of this device. The first stage features cusped fields designed to enhance ionization by increasing the effective path length between the cathode and the anode walls. The acceleration stage uses transverse magnetic fields to impede the flow of electrons toward the anode.

The magnetic fields in the acceleration stage of the LGIT have the same function as those in a conventional Hall thruster and are applied to ensure that electrons are magnetized and ions are not. The magnetic field strength required was estimated by comparison with the P5 thruster. The goal of the scaling was to keep constant the ratio of the electron gyroradius to the characteristic thruster dimensions. This was accomplished by considering the strategy used previously where the thruster exit area, and hence the square of the characteristic length scale, was kept proportional to the design power level. Since the electron Larmor radius is inversely proportional to the magnetic field strength, it follows that Eqn. A-5 should be satisfied for thrusters operating at a similar discharge voltage. Considering that the peak magnetic field in the 5-kW class P5 is approximately 250 gauss, Eqn. A-5 suggests that the acceleration stage magnetic circuit of the LGIT should be able to provide a peak field of at least 450-500 gauss.

$$P_{in}B^2 \approx const. \qquad \textbf{Eqn. A-5}$$

The ionization stage magnetic fields are provided by samarium-cobalt permanent magnets in a cusped configuration to enhance ionization. Both ring-cusp and line-cusp arrangements were considered with a predisposition toward the ring-cusp option since it has been shown to reduce ionization costs by as much as 20% compared to line-cusp arrangements.[116] Unfortunately, it was determined that the ring-cusp design would interfere with the magnetic field in the acceleration region. As sketched in Fig. A-5, a ring-cusp arrangement would have placed magnets having the same orientation next to each other on one edge of the ionization/acceleration interface while placing magnets of opposite orientations next to each other on the other edge. This would have made it impossible to create a symmetric discharge. A line-cusp configuration, on the other hand, allows the permanent magnets to be arranged in such a way that the magnetic fields are symmetric across both midplanes of the thruster. For this reason, a line-cusp arrangement with the long axis of the magnets running parallel to the flow direction was chosen.

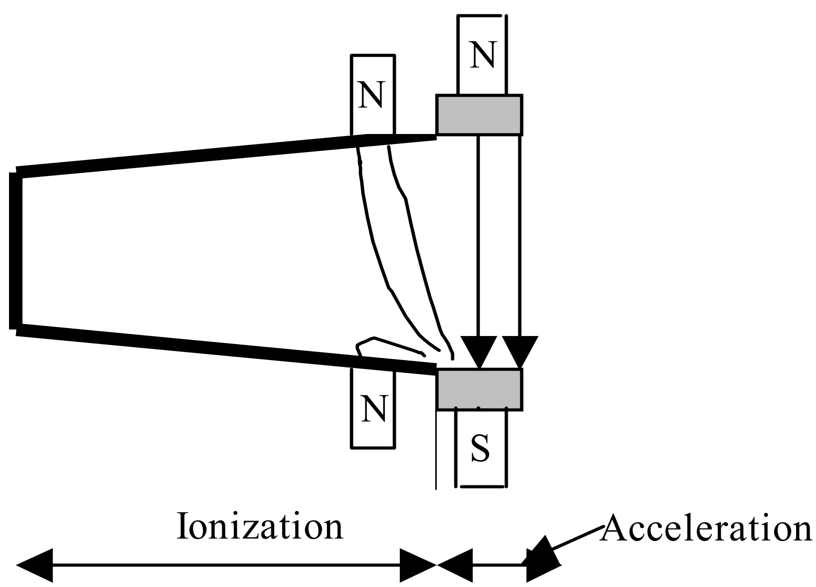

Figure A-5: A simplified sketch showing the unacceptable asymmetric magnetic fields that would have been produced by a ring-cusp arrangement.

After determining the overall magnetic configuration, the 3D magnetostatic simulation tool MagNet 6.1 was used to size the pole pieces, and to optimize the number and size of permanent magnets used. The main goal of the design was to find an arrangement that would create a weak field in the middle of the first stage to enhance ionization and a strong field near the walls to reduce the loss of primary electrons. This was achieved using 40 mm long samarium-cobalt magnets with a 5 mm x 5 mm cross section. After an iterative process, a configuration was chosen in which the magnets were arranged with 5 on both the top and bottom of the anode and one on each side for a total of 12 magnets. Figure A-6 shows the resulting magnetic cusps predicted by the MagNet software. The cross section shown was taken from approximately halfway down the length of the ionization chamber in a direction perpendicular to the flow velocity.

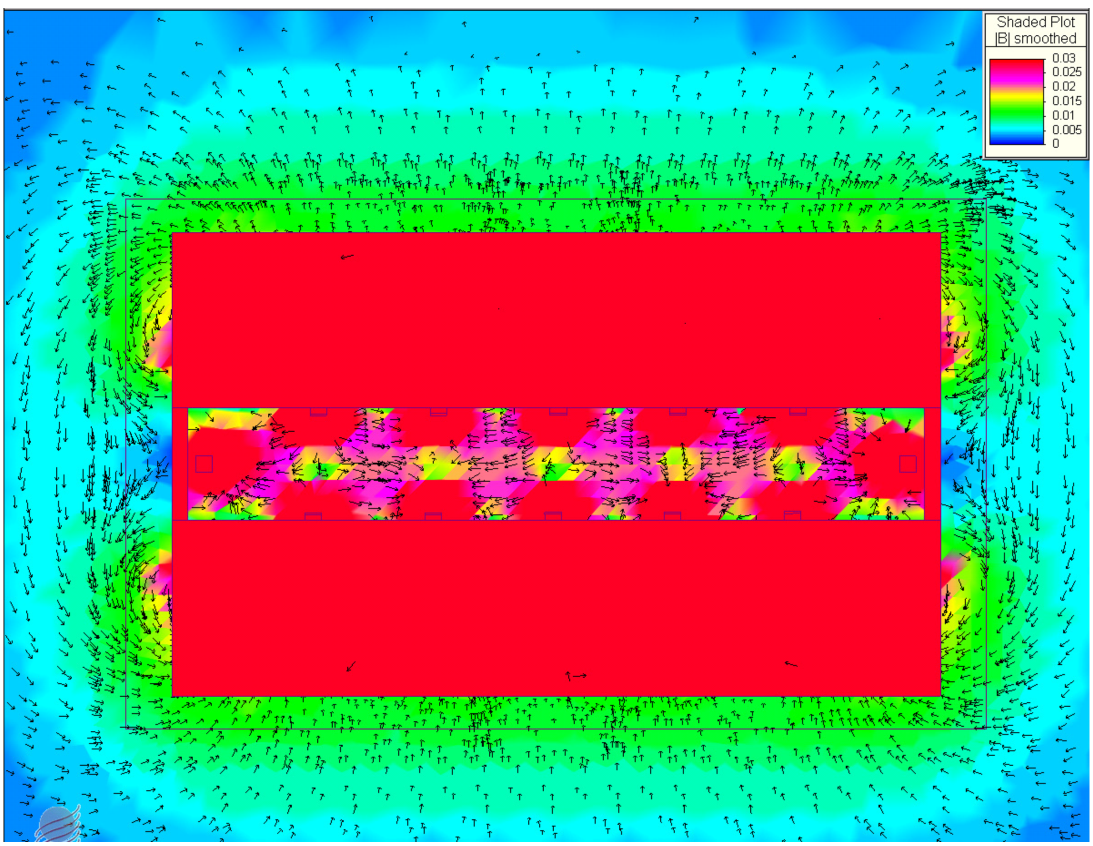

Figure A-6: Magnetic cusps predicted by Magnet 6.1 near the midplane of the LGIT first stage.

An electromagnet circuit constructed of cold-rolled steel provides the transverse magnetic fields in the acceleration region. This circuit was designed to be capable of producing a peak magnetic field strength of at least 750 gauss, which is well above the maximum expected operating value of 500 gauss. The circuit consists of 8 solid cores connecting 3/8" thick front and back pole pieces. A magnetic screen surrounds the anode to prevent the fields created in the acceleration stage from interfering with the magnetic cusps of the ionization stage. A solid model of the magnetic circuit, including the rectangular screen, is shown in Fig. A-7.

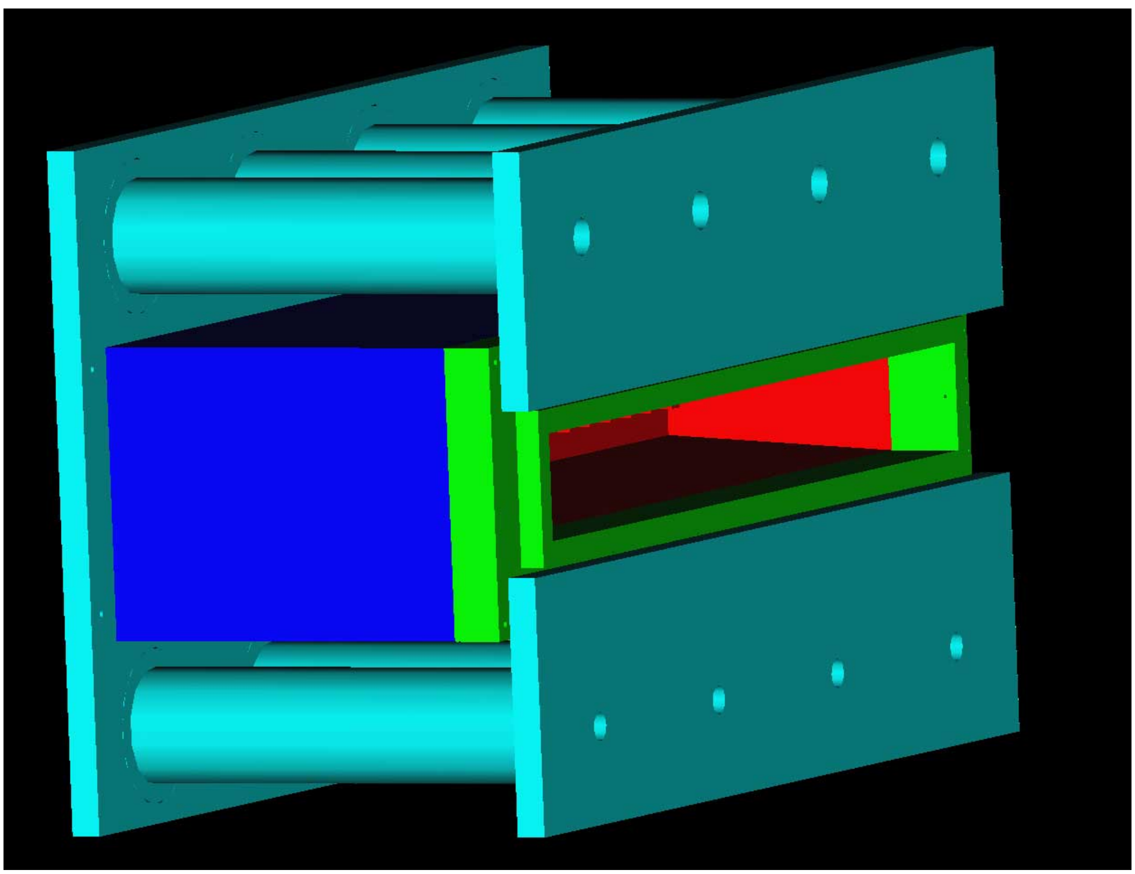

Figure A-7: A solid model showing the main components of the Linear Gridless Ion Thruster.

Recent work has suggested that the shape of the magnetic field in the acceleration zone may affect the loss of ions to the channel walls.[22] There is reason to believe that symmetric, "cupped" magnetic field lines having high strength near the walls and a lower strength near the center of the channel would tend to keep the bulk of the plasma away from the channel walls, thus reducing ion losses due to recombination.[22,24] In a linear thruster such as the LGIT, symmetric field lines are easy to achieve. As Fig. A-8 shows, the field lines in the LGIT run nearly perpendicular to the flow direction at the exit plane with cups developing upstream. Figure A-8 shows a side view of the thruster. The multiple field lines shown at each axial location represent 5 different streamtraces taken at evenly spaced points across the long dimension (width) of the thruster. It is interesting to note that the lines of force are nearly uniform across the face of the thruster near the exit plane while further upstream the nonuniform field lines are evidence of interaction between the ionization and acceleration stage fields.

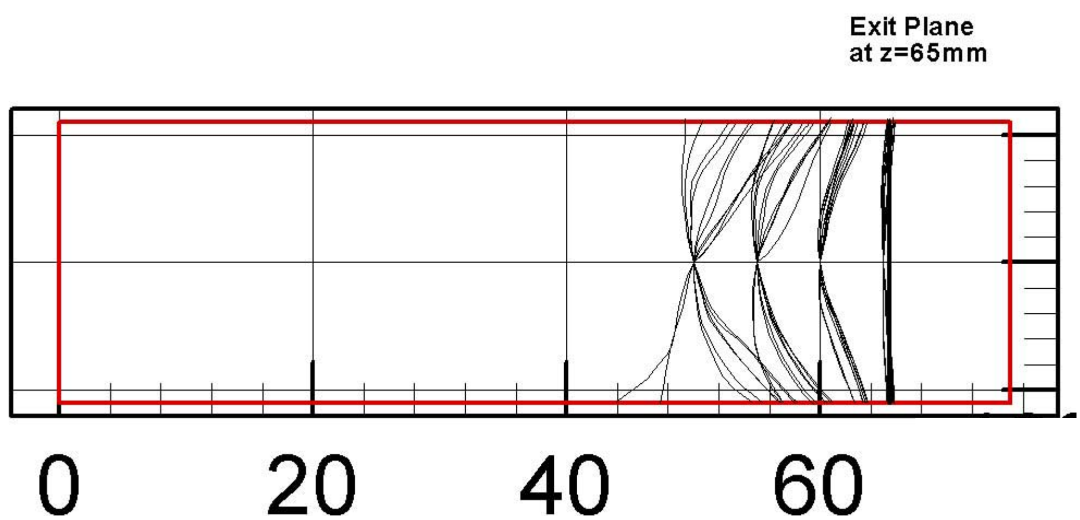

Figure A-8: Simulation results showing the magnetic field profiles in the acceleration zone.

It has been well established that the optimum magnetic field in a conventional Hall thruster consists of a low field strength in the upstream portion of the channel increasing to a peak near the thruster exit plane.[117] As Fig. A-9 shows, this was achieved in the LGIT by careful placement of the front pole pieces. Note the nearly uniform field strength in the center of the ionization zone and the sharp increase near the exit plane. The completed thruster is shown in Fig. A-10.

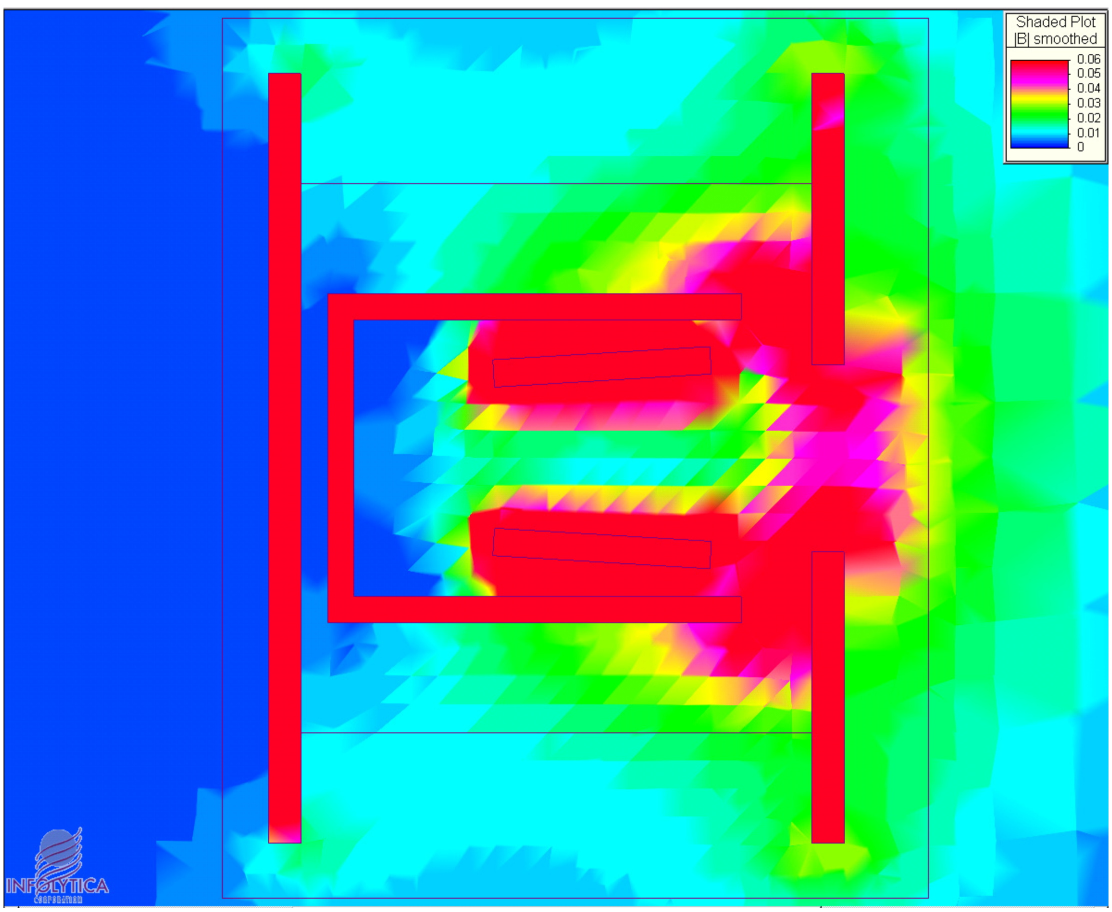

Figure A-9: Contour plot showing the magnetic field strength in the LGIT. The direction of flow is from left to right.

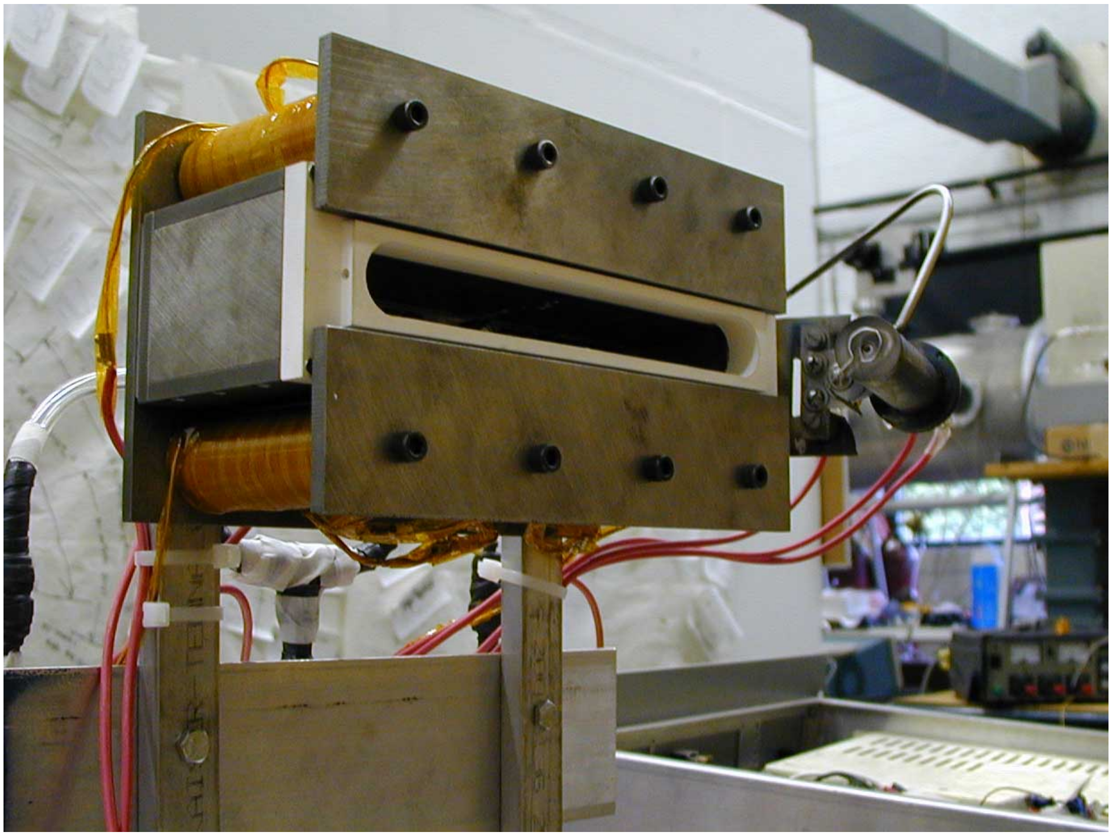

Figure A-10: The completed Linear Gridless Ion Thruster (LGIT).

A.3 Development Status

The LGIT has demonstrated stable operation in both one- and two-stage mode. Some of the throttling points at which the thruster has been operated are presented in Table A-1. During the testing reflected here, the discharge stage power supply was operated in constant current mode while the acceleration stage voltage was set. Unfortunately, reliable thrust measurements have not yet been obtained. One thing that can be seen from the data presented in Table A-1 is that the acceleration stage current is somewhat higher than one would expect for the given propellant mass flow rates. For example, if the 15.0 sccm anode flow and 5.0 sccm discharge cathode flow were all singly ionized, this would account for an ion current of about 1.45 amps. The measured current in this configuration was almost twice that (2.7 A), which appears to indicate that a significant fraction of the current is carried by electrons. Although this inference cannot be completely verified based on the limited data available, if correct, the high electron current can be expected to detract from the performance of the device and reduce the overall electrical efficiency.

Anode Flow Rate (sccm)	Discharge Cathode Flow (sccm)	Discharge Voltage (V)	Discharge Current (A)	Acceleration Voltage (V)	Acceleration Stage Current (A)
10.0	5.0	24.0	5.0	300	1.5
10.0	5.0	24.0	1.0	300	2.0
15.0	5.0	23.0	3.0	300	2.7
25.0	5.0	22.0	5.0	300	4.9

Table A-1: A sample of the parameters for which the LGIT has exhibited stable operation.

A final observation regarding initial tests of the LGIT involves the behavior during single-stage operation. In this mode, the discharge stage cathode was disconnected from the power supply and allowed to float. When the acceleration voltage was set to 300 volts, the discharge cathode floated at only about 50 volts above ground. Since the floating potential generally tracks the plasma potential (to a multiplicative factor of the electron temperature), this implies that a significant portion of the potential drop occurs far upstream in the discharge chamber. Optimally, the potential drop in the discharge chamber would be just large enough to ionize the propellant and the bulk of the acceleration would occur downstream near the exit plane. Strong electric fields in the upstream region are likely to lead to large wall losses and a low total efficiency.

A.4 Suggestions for Improvement

The testing of the LGIT that has occurred to date has been very preliminary in nature and has been intended mainly to demonstrate stable operation of this device, which is dramatically different than conventional Hall thruster designs. This was accomplished, although some of the observed characteristics suggest that the device may not be performing as well as hoped due to an elevated electron current fraction and non-optimal location of the potential drop.

One suggested modification that may improve the performance of the LGIT is the addition of an intermediate grid between the ionization and acceleration stages. This may seem counterintuitive since the term “gridless” is part of the device’s name, but what this really refers to is the quasineutral acceleration mechanism, which would not be sacrificed by this alteration. A grid between the stages biased at the discharge (first stage) cathode potential would facilitate axial ion diffusion into the acceleration zone by creating weak electric fields in the ionization stage. Although it may seem that addition of a negatively biased (with respect to the anode) grid would cause ions from the discharge chamber to be collected and lost, this does not appear to represent a serious problem in conventional ion thrusters where leakage of the electric field through the openings of the intermediate grid preferentially direct ions through the grid rather than into it. If this same process holds in the LGIT, addition of an intermediate grid would not be likely to result in a detrimental increase in ion losses from the discharge chamber. Further, in this configuration the acceleration voltage would be applied between the intermediate electrode and the downstream cathode, rather than between the anode and cathode. This would force the entire acceleration potential drop to occur in the downstream stage regardless of the processes occurring upstream. It is hypothesized that this may enhance the performance of the LGIT compared to the original design, although this remains to be confirmed.

Appendix B: PARTICLE TRACKING ALGORITHM

The code listed below implements a particle tracking algorithm in the data analysis program Igor. The program first reads in a spreadsheet containing position locations and measured plasma potential data. Currently, the spreadsheet must also contain the local electric fields at each grid location, but the procedure could easily be modified to calculate the electric fields directly from the input potential data.

The tracking algorithm starts with a particle at a given initial position, velocity, and direction of travel. The procedure then steps through time and updates the particle position and velocity at each time step. The change in velocity is obtained by finding the grid point closest to the particle's current position and using the electrostatic force at that location to calculate the step change in particle velocity assuming constant acceleration over the time step. The algorithm stops when the particle exits the specified spatial range and the particle trajectory is output as a set of X,Y pairs indicating the ion's position at successive times. To work correctly, the time step must be chosen so that the distance a particle moves in that increment is small compared to the spacing of the points at which the plasma potential was measured. The code used to implement this algorithm is given below. Comment lines are in red font.

```
#pragma rtGlobals=1		// Use modern global access method.

Function trajectory2(x0, y0, theta0, vel0)
variable x0, y0, theta0, vel0

wave xwave, ywave, pot_wave, Ex_wave, Ey_wave, pos_x, pos_y, vel_x, vel_y
variable theta, delta_t, j, vel_mag, done, next_x, next_y, dist, min_dist
variable len, found_next_x, found_next_y, delta, found, index, e_charge, mi, Ex, Ey, i

e_charge=1.6e-19
mi=2.2e-25
delta_t=1e-8
KillWaves pos_x, pos_y
// xwave ... Ey_wave are input locations, plasma potential, and E field
// pos_x, pos_y are particle position variables
// delta_t is time step
LoadWave/N/J

duplicate/o wave0 xwave
duplicate/o wave1 ywave
duplicate/o wave2 pot_wave
duplicate/o wave3 Ex_wave
duplicate/o wave4 Ey_wave
duplicate/o xwave vel_x
duplicate/o xwave vel_y

make/o/n=20000 pos_x
make/o/n=20000 pos_y

killwaves wave0, wave1, wave2, wave3, wave4

len=numpnts(xwave)
printf "length=" + num2str(len) + "\r"
j=0
pos_x[j]=x0
pos_y[j]=y0
vel_mag=vel0
vel_x[j]=vel_mag*cos(theta0*3.14159/180)
vel_y[j]=vel_mag*sin(theta0*3.14159/180)

done=0

do

	min_dist=50
	i=0
```

```
	do
		dist=sqrt((xwave[i]-pos_x[j])^2+(ywave[i]-pos_y[j])^2)
		if (dist<min_dist)
			index=i
			min_dist=dist
		endif
		i=i+1
	while (i<len)
	Ex=Ex_wave[index]
	Ey=Ey_wave[index]
	printf "Position is: " + num2str(pos_x[j]) + ", " + num2str(pos_y[j]) + "\r"
	printf "Closest grid point: " + num2str(xwave[index]) + ", " +
num2str(ywave[index]) + "\r"
	j=j+1
	vel_x[j]=vel_x[j-1]+e_charge*Ex*delta_t/mi
	vel_y[j]=vel_y[j-1]+e_charge*Ey*delta_t/mi
	pos_x[j]=pos_x[j-1]+vel_x[j-1]*1000*delta_t  // velocities in m/s, distance in mm
	pos_y[j]=pos_y[j-1]+vel_y[j-1]*1000*delta_t


	// Quit when ion exits range where plasma potential was measured
	if (pos_x[j]>115 || pos_y[j]>140)
		done=1
	elseif (pos_x[j]<-115 || pos_y[j]<50 || j>19999)
		done=1
	endif

while (done==0)
duplicate/o/R=[0,j] pos_x temp_x
duplicate/o/R=[0,j] pos_y temp_y
Save/J/M="\r\n" temp_x, temp_y
end
```

REFERENCES

[1] Stuhlinger, E., *Ion Propulsion For Space Flight*, McGraw-Hill Book Company, New York, NY, 1964.

[2] Dunning, J., "NASA's Electric Propulsion Program: Technology Investments for the New Millenium," AIAA-2001-3224, 37th AIAA / ASME / SAE / ASEE Joint Propulsion Conference, Salt Lake City, UT, July 2001.

[3] Boden, D.G., "Introduction to Astrodynamics," in *Space Mission Analysis and Design,* edited by Larson, W.J. and Wertz, J.R., Microcosm Inc. and Kluwer Academic Publishers, United States of America, 1992.

[4] Sackheim, R.L. and Wolf, R.S., "Space Propulsion Systems," in *Space Mission Analysis and Design*, edited by Larson, W.J. and Wertz, J.R., Microcosm Inc. and Kluwer Academic Publishers, United States of America, 1992.

[5] Hruby, V., Monheiser, J., Pote, B., Rostler, P., Kolencik, J., and Freeman, C., "Development of Low-Power Hall Thrusters," AIAA-99-3534, 30th Plasmadynamics and Lasers Conference, Norfolk, VA, June 1999.

[6] Martinez-Sanchez, M. and Pollard, J.E., "Spacecraft Electric Propulsion – An Overview," *Journal of Propulsion and Power*, Vol. 14, No. 5, Sept.-Oct. 1998, pp. 688-699.

[7] Sutton, G.P., *Rocket Propulsion Elements*, John Wiley & Sons, Inc., New York, NY, 1992.

[8] Britt, E.J. and McVey, J.B., "Electric Propulsion Activities in U.S. Industries," AIAA-2002-3559, 38th AIAA / ASME / SAE / ASEE Joint Propulsion Conference, Indianapolis, IN, July 2002.

[9] Auweter-Kurtz, M., Golz, T., Habiger, H., Hammer, F., Kurtz, H., Riehle, M., and Sleziona, C., "High-Power Hydrogen Arcjet Thrusters," *Journal of Propulsion and Power*, Vol. 14, No. 5, 1998, pp. 764-773.

[10] Cassady, R.J., "Overview of Major U.S. Industrial Programs in Electric Propulsion," AIAA-2001-3226, 37th AIAA / ASME / SAE / ASEE Joint Propulsion Conference, Salt Lake City, UT, July 2001.

[11] Reichbach, J.G., Sedwick, R.J., and Martinez-Sanchez, M., "Micropropulsion System Selection for Precision Formation Flying Satellites." AIAA-2001-3646, 37th AIAA / ASME / SAE / ASEE Joint Propulsion Conference, Salt Lake City, UT, July 2001.

[12] Lapointe, M.R. and Mikellides, P.G., "High Power MPD Thruster Development at the NASA Glenn Research Center," AIAA-2001-3499, 37th AIAA / ASME / SAE / ASEE Joint Propulsion Conference, Salt Lake City, UT, July 2001.

[13] Wilbur, P.J. Rawlin, V.K., and Beattie, J.R., "Ion Thruster Development Trends and Status in the United States," *Journal of Propulsion and Power*, Vol. 14, No. 5, Sep.-Oct. 1998, pp. 708-715.

[14] Polk, J.E., Kakuda, R.Y., Anderson, J.R., Brophy, J.R., Rawlin, V.K., Patterson, M.J., Sovey, J., Hamley, J., "Validation of the NSTAR Ion Propulsion System on the Deep Space One Mission: Overview and Initial Results," AIAA-99-2274, 35th AIAA / ASME / SAE / ASEE Joint Propulsion Conference, Los Angeles, CA, June 1999.

[15] Schmidt, D.P, Meezan, N.B., Hargus Jr., W.A., Cappelli, M.A., "A low-power, linear-geometry Hall plasma source with an open electron-drift," *Plasma Sources Science and Technology*, Vol. 9, 2000, pp. 68-76.

[16] Beal, B.E., and Gallimore, A.D., "Development of the Linear Gridless Ion Thruster," AIAA-2001-3649, 37th AIAA / ASME / SAE / ASEE Joint Propulsion Conference, Salt Lake City, UT, July 2001.

[17] Chen, F.F., *Introduction to Plasma Physics and Controlled Fusion Volume 1: Plasma Physics*, Plenum Press, New York, NY, 1984.

[18] Kauffman, H.R., "Technology of Closed-Drift Thrusters," *AIAA Journal*, Vol. 23, No.1, 1985, pp. 78-87.

[19] Zhurin, V.V., Kaufman, H.R., and Robinson, R.S., "Physics of closed drift thrusters," *Plasma Sources Science and Technology*, Vol. 8, 1999, pp. R1-R20.

[20] Yashnov, Y.M., Koester, J.K., McVey, J.B., and Britt, E.J., "Fundamental Design of Highly Effective Hall Thrusters," IEPC-99-099, 26th International Electric Propulsion Conference, Kitakyushu, Japan, Oct. 1999.

[21] Choueiri, E.Y., "Fundamental difference between the two Hall thruster variants," *Physics of Plasmas*, Vol. 8, No. 11, Nov. 2001, pp. 5025-5033.

[22] Haas, J.M., *Low-Perturbation Interrogation of the Internal and Near-Field Plasma Structure of a Hall Thruster Using a High-Speed Probe Positioning System*, Ph.D Dissertation, University of Michigan Department of Aerospace Engineering, University Microfilms International, 2001.

[23] Gulczinski III, F.S. and Spores, R.A., "Analysis of Hall-effect Thrusters and Ion Engines for Orbit Transfer Missions," AIAA-96-2973, 32nd AIAA / ASME / SAE / ASEE Joint Propulsion Conference, Orlando, FL, July 1996.

[24] Hofer, R.R. and Gallimore, A.D., "The Role of Magnetic Field Topography in Improving the Performance of High-Voltage Hall Thrusters," AIAA-2002-4111, 38th AIAA / ASME / SAE / ASEE Joint Propulsion Conference, Indianapolis, IN, July 2002.

[25] Jacobson, D.T. and Manzella, D.H., "50 kW Class Krypton Hall Thruster Performance," AIAA-2003-4550, 39th AIAA / ASME / SAE / ASEE Joint Propulsion Conference, Huntsville, AL, July 2003.

[26] Williams, L.A., Engel, M., and Dolgopolov, A., "Commercial Satellite and Launch Vehicle Buying Trends," AIAA-2002-980, 20th AIAA International Communications Satellite Conference and Exhibit, Montreal, Quebec, May 2002.

[27] NASA Project Prometheus website: http://spacescience.nasa.gov/missions/prometheus.htm.

[28] Spanjers, G.G., Birkan, M., and Lawrence, T.J., "The USAF Electric Propulsion Research Program," AIAA-2000-3146, 36th 39th AIAA / ASME / SAE / ASEE Joint Propulsion Conference, Huntsville, AL, July 2000.

[29] Spores, R.A., Spanjers, G.G., Birkan, M., Lawrence, T.J., "Overview of the USAF Electric Propulsion Research Program," AIAA-2001-3225, 37th AIAA / ASME / SAE / ASEE Joint Propulsion Conference, Salt Lake City, UT, July 2001.

[30] Dunning, J.W., Benson, S., Oleson, S., "NASA's Electric Propulsion Program," IEPC-01-002, 27th International Electric Propulsion Conference, Pasadena, CA, Oct. 2001.

[31] Zakharenkov, L.E., Semenkin, A.V., Rusakov A.V., Urchenko, N.A., Tverdokhlebov, S.O., Garkusha, V.I., Lebedev, U.V., Podkolsin, S.N., Fife, J.M., "Study of Multi Thruster Assembly Operation," IEPC-2003-0311, 28th International Electric Propulsion Conference, Toulouse, France, March 2003.

[32] Tverdokhlebov, S.O., Semenkin, A.V., Baranov, V.I., Zakharenkov, L.E., Solodukhin, A.E., "Consideration of Cluster Design Approach for High Power Hall Propulsion," AIAA-2003-0494, 41st Aerospace Sciences Meeting and Exhibit, Reno, NV, Jan. 2003.

[33] Schott, L., "Electrical Probes," in *Plasma Diagnostics*, edited by W. Lochte-Holtgreven, American Institute of Physics, Woodbury, NY, 1995.

[34] Chen, S.L., and Sekiguchi, T., "Instantaneous Direct-Display System of Plasma Parameters by Means of a Triple Probe," *Journal of Applied Physics*, Vol. 36, No. 8, 1965, pp. 2363-2375.

[35] Fernandez Palop, J.I., Ballesteros, J., Colomer, V., and Hernandez, M.A., "A new smoothing method for obtaining the electron energy distribution function in plasmas by the numerical differentiation of the I-V probe characteristic," *Review of Scientific Instruments*, Vol. 66, No. 9, 1995, pp. 4625-4636.

[36] Tilley, D.L., Kelly, A.J., and Jahn, R.G., "The Application of the Triple Probe Method to MPD Thruster Plumes," AIAA-90-2667, 21st International Electric Propulsion Conference, Orlando, FL, July 1990.

[37] Peterson, E.W. and Talbot, L., "Collisionless Electrostatic Single-Probe and Double-Probe Measurements," *AIAA Journal*, Vol. 8, No. 12, 1970, pp. 2215-2219.

[38] Williams Jr., G.J., Smith, T.B., Gulczinski III, F.S., Beal, B.E., Gallimore, A.D., and Drake, R.P., "Laser Induced Fluorescence Measurement of Ion Velocities in the Plume of a Hall Effect Thruster," AIAA-99-2424, 35th AIAA/ASME/SAE/ASEE Joint Propulsion Conference, Los Angeles, CA, June 1999.

39 Hutchinson, I.H., *Principles of Plasma Diagnostics*, Cambridge University Press, Cambridge, UK, 2002.

40 Beal, B.E., Gallimore, A.D., and Hargus Jr., W.A., "The Effects of Clustering Multiple Hall Thrusters on Plasma Plume Properties," AIAA-2003-5155, 39th AIAA/ASME/SAE/ASEE Joint Propulsion Conference, Huntsville, AL, July 2003.

41 Beal, B.E., Gallimore, A.D., and Hargus Jr., W.A., "Anomolous plasma properties in the plume of a low-power Hall thruster," submitted to *Physics of Plasmas*, May, 2003.

42 Haas, J.M. and Gallimore, A.D., "Internal Plasma Potential Profiles in a Laboratory Model Hall Thruster," *Physics of Plasmas*, Vol. 8, No.2, 2001, pp. 652-660.

43 Kemp, R.F. and Sellen Jr., J.M., "Plasma Potential Measurements by Electron Emissive Probe," *Review of Scientific Instruments*, Vol. 37, No. 4, 1966, pp. 455-461.

44 Ye, M.Y. and Takamura, S., "Effect of space-charge limited emission on measurements of plasma potential using emissive probes," *Physics of Plasmas*, Vol. 7, No. 8, 2000, pp. 3457-3463.

45 Hofer, R.R., Walker, M.L.R., Gallimore, A.D., "A Comparison of Nude and Collimated Faraday Probes For Use With Hall Thrusters," IEPC-01-020, 27th International Electric Propulsion Conference, Pasadena, CA, Oct. 2001.

46 Manzella, D.H. and Sankovic, J.M., "Hall Thruster Ion Beam Characterization," AIAA-95-2927, 31st AIAA/ASME/SAE/ASEE Joint Propulsion Conference, San Diego, CA, July 1995.

47 Gulczinski III, F.S., *Examination of the Structure and Evolution of Ion Energy Properties of a 5kW Class Laboratory Hall Effect Thruster at Various Operational Conditions*, Ph.D Dissertation, University of Michigan Department of Aerospace Engineering, University Microfilms International, 1999.

48 Kaminsky, M., *Atomic and Ionic Impact Phenomena on Metal Surfaces*, Springer-Verlag, New York, NY, 1965.

49 Haas, J.M., Air Force Research Laboratory, Personal Communication, Jan. 2003.

50 Hofer, R.R., Haas, J.M., and Gallimore, A.D., "Development of a 45-Degree Parallel-Plate Electrostatic Energy Analyzer for Hall Thruster Plume Studies: Preliminary Data," IEPC-99-113, 26th International Electric Propulsion Conference, Kitakyushu, Japan, Oct. 1999.

51 Pollard, J.E., "Plume Angular, Energy, and Mass Spectral Measurements with the T5 Ion Engine," AIAA-95-2920, 31st AIAA/ASME/SAE/ASEE Joint Propulsion Conference, San Diego, CA, July 1995.

52 King, L.B., *Transport Property and Mass Spectral Measurements in the Plasma Exhaust Plume of a Hall-Effect Space Propulsion System*, Ph.D Dissertation, University of Michigan Department of Aerospace Engineering, University Microfilms International, 1998.

[53] Pollard, J.E., Diamant, K.D., Khayms, V., Werthman, L., King, D.Q., and de Grys, K., "Ion Flux, Energy, and Charge-State Measurements for the BPT-4000 Hall Thruster," AIAA-2001-3351, 37th AIAA/ASME/SAE/ASEE Joint Propulsion Conference, Salt Lake City, UT, July 2001.

[54] Brown, S.C., *Basic Data of Plasma Physics*, John Wiley & Sons, Inc., New York, NY, 1959.

[55] Hofer, R.R., Haas, J.M., and Gallimore, A.D., "Ion Voltage Diagnostics in the Plume of a High-Specific Impulse Hall Thruster," AIAA-2003-4556, 39th AIAA/ASME/SAE/ASEE Joint Propulsion Conference, Huntsville, AL, July 2003.

[56] Kim, S.W., *Experimental Investigations of Plasma Parameters and Species-Dependent Ion Energy Distribution in the Plasma Exhaust Plume of a Hall Thruster*, Ph.D Dissertation, University of Michigan Department of Aerospace Engineering, University Microfilms International, 1999.

[57] Hofer, R.R. and Gallimore, A.D., "Ion Species Fractions in the Far-Field Plume of a High-Specific Impulse Hall Thruster," AIAA-2003-5001, 39th AIAA/ASME/SAE/ASEE Joint Propulsion Conference, Huntsville, AL, July 2003.

[58] Hagstrum, H.D., "Auger Ejection of Electrons from Tungsten by Noble Gas Ions," *Physical Review*, Vol. 96, No. 2, 1954, pp. 325-335.

[59] Prioul, M., Bouchoule, A., Roche, S., Magne, L., Pagnon, D., Touzeau, M., and Lasgorceix, P., "Insights on Physics of Hall Thrusters through Fast Current Interruptions and Discharge Transients," IEPC-01-059, 27th International Electric Propulsion Conference, Pasadena, CA, Oct. 2001.

[60] Hargus Jr., W.A., "Near Exit Plane Velocity Field of a 200 W Hall Thruster," AIAA-2003-5154, 39th AIAA/ASME/SAE/ASEE Joint Propulsion Conference, Huntsville, AL, July 2003.

[61] Hargus Jr., W.A. and Pote, B., "Examination of a Hall Thruster Start Transient," AIAA-2002-3956, 38th AIAA/ASME/SAE/ASEE Joint Propulsion Conference, Indianapolis, IN, July 2002.

[62] Choueiri, E.Y., "Plasma oscillations in Hall thrusters," *Physics of Plasmas*, Vol. 8, No. 4, 2001, pp. 1411-1426.

[63] Vial, V., Lazurenko, A., Bouchoule, A., and Prioul, M., "Physical Insights on SPT Thrusters Through Ultra-Fast Externally Driven Current Interruptions," IEPC-03-0220, 28th International Electric Propulsion Conference, Toulouse, France, March 2003.

[64] Peterson, P.Y., Gallimore, A.D., and Haas, J.M., "An experimental investigation of the internal magnetic field topography of an operating Hall thruster," *Physics of Plasmas*, Vol. 9, No. 10, 2002, pp. 4354-4362.

[65] Hargus Jr., W.A. and Reed, G., "The Air Force Clustered Hall Thruster Program," AIAA-2002-3678, 38th AIAA/ASME/SAE/ASEE Joint Propulsion Conference, Indianapolis, IN, July 2002.

[66] Kim, V., "Main Physical Features and Processes Determining the Performance of Stationary Plasma Thrusters," *Journal of Propulsion and Power*, Vol. 14, No. 5, 1998, pp. 736-743.

[67] Hofer, R.R. and Gallimore, A.D., “Recent Results from Internal and Very-Near-Field Plasma Diagnostics of a High Specific Impulse Hall Thruster,” IEPC-2003-0037, 28^{th} International Electric Propulsion Conference, Toulouse, France, March 2003.

[68] Haas, J.M., Hofer, R.R., and Gallimore, A.D., “Hall Thruster Discharge Chamber Characterization Using a High-Speed Axially Reciprocating Electrostatic Probe,” AIAA-99-2426, 35^{th} AIAA/ASME/SAE/ASEE Joint Propulsion Conference, Los Angeles, CA, June 1999.

[69] Domonkos, M.T., *Evaluation of Low-Current Orificed Hollow Cathodes*, Ph.D Dissertation, University of Michigan Department of Aerospace Engineering, University Microfilms International, 1999.

[70] Katz, I., Jongeward, G., Davis, V., Mandell, M., Mikellides, I., Dressler, R., Boyd, I., Kannenberg, K., Pollard, J., and King, D., “A Hall Effect Thruster Plume Model Including Large-Angle Elastic Scattering,” AIAA-2001-3355, 37^{th} AIAA/ASME/SAE/ASEE Joint Propulsion Conference, Salt Lake City, UT, July 2001.

[71] Engel, A., *Ionized Gases*, Oxford University Press, London, England, 1955.

[72] Boyd, I.D., University of Michigan, Personal Communication, Dec. 2003.

[73] Williams, G.J., Smith, T.B., Gulczinski, F.S., and Gallimore, A.D., “Correlating Laser Induced Fluorescence and Molecular Beam Mass Spectrometry Ion Energy Distributions,” *Journal of Propulsion and Power*, Vol. 18, No. 2, 2002, pp. 489-491.

[74] Huba, J.D., *NRL Plasma Formulary*, Naval Research Laboratory, Washington, DC, 1998.

[75] Gary, S.P., Tokar, R.L., and Winske, D., “Ion/Ion and Electron/Ion Cross-Field Instabilities Near the Lower Hybrid Frequency,” *Journal of Geophysical Research*, Vol. 92, No. A9, 1987, pp. 10,029-10,038.

[76] Fried, B.D. and Gould, R.W., “Longitudinal Ion Oscillations in a Hot Plasma,” *Physics of Fluids*, Vol. 4, No. 1, 1961, pp. 139-147.

[77] Gary, S.P. and Omidi, N., “The ion-ion acoustic instability,” *Journal of Plasma Physics*, Vol. 37, No. 1, 1987, pp. 45-61.

[78] Goldston, R.J. and Rutherford, P.H., *Introduction to Plasma Physics*, Institute of Physics Publishing, Philadelphia, PA, 1997.

[79] Wong, H.V., “Electrostatic Electron-Ion Streaming Instability,” *Physics of Fluids*, Vol. 13, No. 3, 1970, pp. 757-760.

[80] Forslund, D.W., Morse, R.L., and Nielson, C.W., “Electron Cyclotron Drift Instability,” *Physical Review Letters*, Vol. 25, No. 18, 1970, pp. 1266-1270.

[81] Zhou, Y.M., Li, Y.Y., and Wu, C.S., “Stabilizing Effects of a Magnetic Field Gradient in a Perpendicular Shock Wave on Electron-Cyclotron-Drift Instability,” *Physics of Fluids*, Vol. 27, No. 8, 1984, pp. 2049-2054.

[82] Stringer, T.E., "Electrostatic Instabilities in Current-Carrying and Counterstreaming Plasmas," *Plasma Physics*, Vol. 6, 1964, pp. 267-279.

[83] Schriver, D. and Ashour-Abdalla, M., "Cold Plasma Heating in the Plasma Sheet Boundary Layer: Theory and Simulations," *Journal of Geophysical Research*, Vol. 95, No. A4, 1990, pp. 3987-4005.

[84] Fried, B.D. and Wong, A.Y., "Stability Limits for Longitudinal Waves in Ion Beam-Plasma Interaction," *Physics of Fluids*, Vol. 9, No. 6, 1966, pp. 1084-1089.

[85] Forslund, D.W. and Shonk, C.R., "Numerical Simulation of Electrostatic Counterstreaming Instabilities in Ion Beams," *Physical Review Letters*, Vol. 25, No. 5, 1970, pp. 281-284.

[86] Smith, T.B., Herman, D.A., Gallimore, A.D., and Drake, R.P., "Deconvolution of Axial Velocity Distribuitions from Hall Thruster LIF Spectra," IEPC-2001-0019, 27th International Electric Propulsion Conference, Pasadena, CA, Oct. 2001.

[87] McKee, C.F., "Simulation of Counterstreaming Plasmas with Application to Collisionless Electrostatic Shocks," *Physical Review Letters*, Vol. 24, No. 18, 1970, pp. 990-994.

[88] Taylor, R.J., Baker, D.R., Ikezi, H., "Observation of Collisionless Electrostatic Shocks," *Physical Review Letters*, Vol. 24, No. 5, 1970, pp. 206-209.

[89] Forslund, D.W. and Shonk, C.R., "Formation and Structure of Electrostatic Collisionless Shocks," *Physical Review Letters*, Vol. 25, No. 25, 1970, pp. 1699-1702.

[90] Eselevich, V.G. and Fainshtein, V.G., "Turbulent Electrostatic Shock Wave in an Interaction of Oppositely Directed Low-Density Plasma Streams," *Soviet Journal of Plasma Physics*, Vol. 10, No. 3, 1984, pp. 313-318.

[91] Tidman, D.A. and Krall, N.A., *Shock Waves in Collisionless Plasmas*, John Wiley & Sons, New York, NY, 1971.

[92] Krall, N.A., "What Do We Really Know About Collisionless Shocks?" *Advances in Space Research*, Vol. 20, No. 4/5, 1997, pp. 715-724.

[93] Goodrich, C.C. and Scudder, J.D., "The Adiabatic Energy Change of Plasma Electrons and the Frame Dependence of the Cross-Shock Potential at Collisionless Magnetosonic Shock Waves," *Journal of Geophysical Research*, Vol. 89, No. A8, 1984, pp. 6654-6662.

[94] Gedalin, M., Balikhin, M., and Krasnosselskikh, V., "Electron Heating in Quasiperpendicular Shocks," *Advances in Space Research*, Vol. 15, No. 8/9, 1995, pp. 225-233.

[95] Scudder, J.D., "A Review of the Physics of Electron Heating at Collisionless Shocks," *Advances in Space Research*, Vol. 15, No. 8/9, 1995, pp. 181-223.

[96] Sanderson, J.J., "Jump Conditions Across a Collisionless, Perpendicular Shock," *Journal of Applied Physics D: Applied Physics*, Vol. 9, 1976, pp. 2327-2330.

[97] Morse, D.L., “Electrostatic Potential Rise Across Perpendicular Shocks,” *Plasma Physics*, Vol. 15, 1973, pp. 1262-1264.

[98] Schwartz, S.J., Thomsen, M.F., Bame, S.J., and Stansberry, J., “Electron Heating and the Potential Jump Across Fast Mode Shocks,” *Journal of Geophysical Research*, Vol. 93, No. A11, 1988, pp. 12,923-12,931.

[99] Manzella, D.H., “Stationary Plasma Thruster Ion Velocity Distribution,” AIAA-94-3141, 30th AIAA/ASME/SAE/ASEE Joint Propulsion Conference & Exhibit, Indianapolis, IN, July 1994.

[100] Keidar, M. and Boyd, I.D., “Effect of a Magnetic Field on the Plasma Plume from Hall Thrusters,” *Journal of Applied Physics*, Vol. 86, No. 9, 1999, pp. 4786-4791.

[101] Morozov, A.I., Esipchuk, Y.V., Kapulkin, A.M., Nevrovskii, V.A., and Smirnov, V.A., “Effect of the Magnetic Field on a Closed-Electron-Drift Accelerator,” *Soviet Physics – Technical Physics*, Vol.17, No.3, 1972, pp. 482-486.

[102] Gallimore, A.D., “Near- and Far-Field Characterization of Hall Thruster Plumes,” *Journal of Spacecraft and Rockets*, Vol. 38, No. 3, 2001, pp. 441-453.

[103] Boyd, I.D. and Dressler, R.A., “Far field modeling of the plasma plume of a Hall thruster,” *Journal of Applied Physics*, Vol. 92, No. 4, 2002, pp. 1764-1774.

[104] Gombosi, T.I., *Gaskinetic Theory*, Cambridge University Press, Cambridge, Great Britain, 1994.

[105] Tilley, D.A., de Grys, K.H., and Myers, R.M., “Hall Thruster – Cathode Coupling,” AIAA-99-2865, 35th AIAA/ASME/SAE/ASEE Joint Propulsion Conference & Exhibit, Los Angeles, CA, June 1999.

[106] Katz, I., Anderson, J.R., Polk, J.E., and Brophy, J.R., “One-Dimensional Hollow Cathode Model,” *Journal of Propulsion and Power*, Vol. 19, No. 4, 2003, pp. 595-600.

[107] Randolph, T., Kim, V., Kaufman, H., Kozubsky, K., Zhurin, V., and Day, M., “Facility Effects on Stationary Plasma Thruster Testing,” IEPC-93-93, 23rd International Electric Propulsion Conference, Seattle, WA, Sept. 1993.

[108] Moore, J.H., Davis, C.C., and Coplan, M.A, *Building Scientific Apparatus: Second Edition*, Perseus Books Publishing, LLC, Cambridge, MA, 1991.

[109] Oh, D.Y., Hastings, D.E., Marrese, C.M., Haas, J.M., and Gallimore, A.D., “Modeling of Stationary Plasma Thruster-100 Thruster Plumes and Implications for Satellite Design,” *Journal of Propulsion and Power*, Vol. 15, No. 2, 1999, pp. 345-357.

[110] Boyd, I.D. and Yim, J.T., “Modeling of the Near Field Plume of a Hall Thruster,” submitted to *Journal of Applied Physics*, 2003.

[111] Haas, J.M., Gulczinski III, F.S., Gallimore, A.D., Spanjers, G.G., and Spores, R.A., “Performance Characteristics of a 5-kW Laboratory Hall Thruster,” AIAA-98-3503, 34th AIAA/ASME/SAE/ASEE Joint Propulsion Conference & Exhibit, Cleveland, OH, July 1998.

[112] Tverdokhlebov, S.O., "Study of Double-Stage Anode Layer Thruster Using Inert Gas," IEPC-93-232, 23rd International Electric Propulsion Conference, Seattle, WA, Sept. 1993.

[113] Yamagiwa, Y. and Kuriki, K., "Performance of Double-Stage-Discharge Hall Ion Thruster," *Journal of Propulsion and Power*, Vol. 7, No. 1, 1991, pp. 65-70.

[114] Solodukhin, A.E., Semenkin, A.V., Tverdokhlebov, S.O., and Kochergin, A.V., "Parameters of D-80 Anode Layer Thruster in One- and Two-Stage Operation Modes," IEPC-2001-032, 27th International Electric Propulsion Conference, Pasadena, CA, Oct. 2001.

[115] Kaufman, H., *Operation of Broad-Beam Sources*, Commonwealth Scientific, Alexandria, VA, 1987.

[116] Sovey, J.S., "Improved Ion Containment Using a Ring-Cusp Ion Thruster," *Journal of Spacecraft and Rockets*, Vol. 21, No. 5, 1984, pp. 488-495.

[117] Morozov, A.I., Esipchuk, Y.V., Kapulkin, A.M., Nevrovskii, V.A., and Smirnov, V.A., "Effect of the Magnetic Field on a Closed-Electron-Drift Accelerator," *Soviet Physics – Technical Physics*, Vol. 17, No. 3, 1972, pp. 482-486.